Early stage precipitation in aluminum alloys
An ab initio study

Zhang, Xi

DOI
10.4233/uuid:349c75cd-11cb-41b2-a403-ce4b1dd3be0d

Publication date
2017

Document Version
Final published version

Citation (APA)
Zhang, X. (2017). *Early stage precipitation in aluminum alloys: An ab initio study*. [Dissertation (TU Delft), Delft University of Technology]. https://doi.org/10.4233/uuid:349c75cd-11cb-41b2-a403-ce4b1dd3be0d

Early stage precipitation in aluminum alloys

An *ab initio* study

Early stage precipitation in aluminum alloys

An *ab initio* study

Proefschrift

ter verkrijging van de graad van doctor
aan de Technische Universiteit Delft,
op gezag van de Rector Magnificus prof. ir. K.C.A.M. Luyben,
voorzitter van het College voor Promoties,
in het openbaar te verdedigen op maandag 27 november 2017 om 12:30 uur

door

Xi ZHANG

Master of Engineering in Materials Science
Central South University, Changsha, China
geboren te Anyang, Henan, China.

This dissertation has been approved by the

promotor: Prof. dr. B.J. Thijsse
copromotor: Dr. ir. M.H.F. Sluiter

Composition of the doctoral committee:

Rector Magnificus,	chairman
Prof. dr. B.J. Thijsse,	Delft University of Technology
Dr. ir. M.H.F. Sluiter,	Delft University of Technology
Independent members:	
Prof. dr. H. Zandbergen	Delft University of Technology
Prof. dr. M. Dijkstra	Utrecht University
Prof. dr. B. Partoens	University of Antwerp / Belgium
Prof. dr. ir. J. Sietsma,	Delft University of Technology

This work is financially supported by the China Scholarship Council (CSC, No. 2011637005).

Keywords: precipitation, aluminum alloys, *ab* initio, cluster expansion, kinetic Monte Carlo simulation

Printed by: Ipskamp Drukkers BV

Front & Back: Beautiful cover art that captures the entire content of this thesis in a single illustration.

ISBN 978-94-028-0881-0

An electronic version of this dissertation is available at
`http://repository.tudelft.nl/`.

To my parents
my wife
and all of my friends.

Xi Zhang

Contents

1

Introduction

Objective of the present thesis:

Thanks to the explosive growth of computational power and model development, multiscale computational materials science has reached a stage where many complicated phenomena or properties that are of great importance to manufacturing can be predicted or explained. The word "ab initio study" becomes commonplace as the development of density functional theory has enabled the predictions to be independent of experimental data or empirical parameters. For some crucial phenomena, e.g., precipitation processes in multicomponent alloys, however, challenges exist due to the requirement of an accurate and efficient description of both energetics and kinetics of a complex system. Therefore a systematic methodology needs to be established to predict the morphology and realistic formation kinetics of precipitates in multicomponent alloys, which is the main contribution of the present work. Aluminum alloys are chosen as prototype applications of the present methodology, because of the well-known strengthening mechanism—age or precipitation hardening which is a typical and important precipitation process utilized in industrial materials. Especially the realistic precipitation kinetics in multicomponent Al-based alloys is far from being understood.

1.1. Aluminum and its alloys

As the most abundant metallic element on this planet, aluminum has become one of the most widely used materials in the industry since the beginning of the 20th century. Compared with, e.g., iron, the relatively low specific mass ($2.70 g/cm^3$) of aluminum significantly reduces the weight of the products [1]. However, pure aluminum suffers from its softness and the low strength, limiting its structural applications. A typical strategy to tackle this problem is to add alloying elements into the pure aluminum matrix that can yield both satisfactory strength and ductility for general usage in automobile and aerospace industries [2–4].

Since Alfred Wilm discovered the age hardening phenomenon in aluminum alloys [5, 6], the design of aluminum alloys has been focusing on increasing the strength without losing the ductility. In order to get the desired microstructure, a typical strategy is to find an optimal combination of different alloying elements before proper heat treatments. Such aluminum alloys are, therefore, typically described as *heat treatable* alloys [5, 7]. Elements that are most commonly present in aluminum alloys (in various combinations) include copper, magnesium, zinc, silicon and manganese. They are labeled commercially with different four-digit numbers, e.g., 2xxx series with Cu as the principal alloying element, 6xxx series in which Mg and Si are the principal alloying elements [1, 8, 9]. Typical commercial aluminum alloys are listed in table 1.1.

Table 1.1: Commercial aluminum alloys and their applications.

Series	Principal alloying elements	Applications
1xxx	pure Al	Electrical and chemical industries
2xxx	Al-Cu (Mg)	Aircraft
3xxx	Al-Mn	Architectural applications and various containers
4xxx	Al-Si	Welding rods and brazing sheet
5xxx	Al-Mg	Boat hulls, gangplanks and other products exposed to marine environments
6xxx	Al-Mg-Si	Architectural extrusions
7xxx	Al-Zn (Cu,Mg,Cr,Zr)	Aircraft and other high-strength applications
8xxx	Al-Sn-Li	-

1.2. Age hardening: diffusional transformation in solids

It is well-known that the strength of aluminum alloys can be considerably increased after proper aging. [10, 11]. This type of transformation usually occurs when the high temperature homogenous solid solution is quenched into a two- or multi-phase region where it becomes supersaturated. The whole heat treatment process is schematically described in the Al-rich part of the Al-X phase diagram (figure 1.1, X refers to the alloying element) with the following reaction [12],

$$\alpha \rightarrow \alpha' + \beta$$

where α refers to the homogeneous aluminum solid solution, α' indicates a solid solution α with a lower concentration of the alloying element, β is the second phase (precipitates).

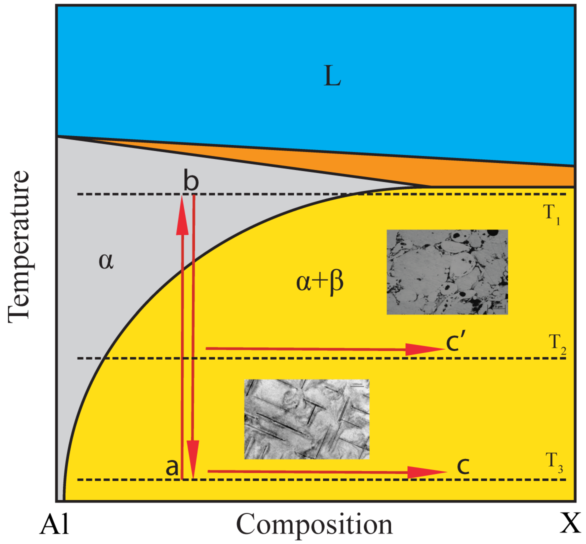

Figure 1.1: Schematic diagram of the heat treatment processes of age-hardened aluminum alloys. The Al-rich part of an Al-X phase diagram (X can refer to Cu, Mg, Zn etc.) is shown where L, α, and β refer to three different phases: the liquid phase, the Al-rich solid solution and the precipitation phase. Arrows represent iso-composition or isothermal transitions: $a \rightarrow b$, homogenization treatment; $b \rightarrow a$, quenching; $\rightarrow c$, natural aging; $\rightarrow c'$, artificial aging. T_1, T_2 and T_3 are temperatures at which homogenization, artificial aging and natural aging are performed. Insets show examples of the typical microstructure after the aging process.

In spite of additional machining steps or multiple heating or cooling processes, the main heat treatment process from figure 1.1 can be summarized by the following three steps:

Step 1. Homogenization treatment. Alloys are solutionized at a high temperature (T_1) for a sufficient time. The aim is to get a homogeneous solid solution α containing as many alloying atoms as possible. A high vacancy concentration is desired to accelerate the diffusion process at temperatures where diffusion is expected to be slow.

Step 2. Quenching to room temperature T_3 at which the solubility of the X atom in α is smaller than that at T_1. As a result, the supersaturated solid solution as well as the number of vacancies are preserved in a region where the equilibrium state is composed of the two phases α+β (yellow region in figure 1.1).

Step 3. Isothermally aging at either room temperature T_3 (*natural aging*) or at an elevated temperature T_2 (T_3<T_2<T_1, *artificial aging*) to acquire a sufficient number of uniformly distributed precipitates.

During the precipitation process most of the supersaturated solid solutions evolve through several intermediate states or metastable phases before reaching the equilibrium state. Typically, at an early stage precipitates are fully coherent with the parent matrix whereas a great structural mismatch between precipitates and matrix occurs at the final stage. Precipitation hardening is achieved via the obstruction of the motion of dislocations due to the occurrence of these multiple phases (precipitates). The very first coherent precipitates (clusters) fail to impede dislocations (too small) whereas the coarsened incoherent ones (too few) can be easily bypassed or sheared by dislocations (so-called *overaged*) [5, 10, 13]. Optimal mechanical properties are thus generally associated with the presence of precipitates with appropriate size and distribution. As being largely responsible for the optimal morphology and distribution of the precipitates at the later stage, early stage precipitations, i.e., the formation of Guinier-Preston zones (see the following section), in aluminum alloys have been the focus of alloy microstructure studies either experimentally or theoretically.

1.3. Early stage precipitation: Guinier-Preston zones

The precipitation sequence in aluminum alloys starts typically with the formation of Guinier-Preston (GP) zones (named after Guinier and Preston [14, 15]). GP zones are solute-rich clusters with diameters ranging from 1 to 10 nm. In transmission electron micrographs or field ion micrographs one can observe GP zones in different shapes. The shape of GP zones depends on the degree of mismatch between solute and solvent atoms as well as the elastic anisotropy of the matrix [16, 17]. If solute atoms are almost of the same size as the solvent atoms (e.g., Al-Ag, Al-Zn systems), spherical GP zones are usually expected [18–20]. When the sizes of the solute and solvent atoms differ more, disk-like GP zones can be observed [7, 16, 21, 22]. These planes are usually parallel to low-index planes of the matrix lattice (e.g. Al-Cu $\{100\}$ plane) where the elastic mismatch gives the lowest energetic cost.

At the early stage of precipitation the appearance of GP zones is the consequence of a homogeneous nucleation due to the low interfacial energy or a spinodal decomposition within a metastable miscibility gap. The formation of GP zones is also promoted by the excess quenched-in vacancies. Since the equilibrium vacancy concentration decreases exponentially with temperature, precipitation processes proceed slowly at relatively low ageing temperatures. It is the high temperature solution treatment and the rapid quenching that retain a significant number of vacancies to speed up the precipitation [6].

The formation of GP zones improves the strength of alloys even though they are small in size. While GP zones are fully coherent with the matrix, a size mismatch between solute and solvent atoms often results in a large strain within the local area [7, 10]. Such a strain field around the coherent precipitates retards the movement of dislocations whereby the strength and hardness of alloys are appreciably increased. Since GP zones are thermodynamically metastable, they subsequently transform to more stable transient precipitates that may further enhance the mechanical properties [10]. Optimal mechanical properties may be achieved, as mentioned before, by a mixture made up of multiple metastable precipitates. The precipitation sequences in some of the most important aluminum alloys are listed in table 1.2 [10].

Table 1.2: Precipitation sequence in some of the most important aluminum alloys.

Aluminum alloy	**Precipitation sequence**
Al-Ag	GP zone(spheres) $\rightarrow \gamma'$(plates) $\rightarrow \gamma(Ag_2Al)$
Al-Cu	GP zone(discs) $\rightarrow \theta''$(discs) $\rightarrow \theta'$(plates) $\rightarrow \theta(CuAl_2)$
Al-Cu-Mg	GP zone(rods) $\rightarrow S'$(laths) $\rightarrow S(CuMgAl_2)$
Al-Zn-Mg	GP zone(spheres) $\rightarrow \eta'$(plates) $\rightarrow \eta(MgZn_2)$
Al-Mg-Si	GP zone(rods) $\rightarrow \beta'$(rods) $\rightarrow \beta(Mg_2Si)$

1.4. Multiscale computational materials science

Since modern high-resolution transmission electron microscopy (HRTEM) and atom probe tomography (APT) became available, detailed information about the relationship between the microstructure and mechanical properties has been obtained. In order to obtain the desired mechanical properties, one must firstly investigate the microstructure evolution [23]. Although early stage precipitation can be experimentally observed it is challenging to theoretically predict the structures of GP zones as well as their realistic evolution kinetics. Moreover, as the realistic aluminum alloys are typically multicomponent alloys, obtaining new physical insight from “trial and error” experiments becomes intractable and costly.

With the rapid increase in available computing resources, computational modeling is becoming an indispensable tool to efficiently study the microstructural evolution and kinetics in alloys [23, 24]. One can flexibly isolate different physical effects—switch on/off one or several variables to monitor their corresponding consequences, individually. After being verified by available experimental results, the established computational methodologies can serve as a guide for manufacturing processes or further experimental investigations.

To this end, first of all, the physical model should capture the characteristic of the topic to be studied. The aluminum alloys that are of importance to industrial applications typically contain multiple alloying elements, which means that multicomponent systems must be taken into account. The challenge is then to accurately and efficiently describe both energetics and kinetics in systems with multiple species which is a highly non-trivial task. Precipitation processes in aluminum alloys are essentially governed by the vacancy mediated substitutional atomic diffusion. At the very early stage of the diffusion, precipitates, i.e., GP zones, are generally coherent with the alloy matrix. Such a feature greatly reduces the degrees of freedom in describing the interatomic potential. Atom-vacancy exchanges can therefore be restricted on a fixed (fcc) crystalline lattice. Moreover, as aging must be carried out at low temperatures to get sufficient supersaturation, long-time annealing is generally required because of the low kinetics. Calculations or simulations must therefore be designed in a computationally feasible and efficient way without losing the underlying physics.

Simplicity and universality have been long pursued for physical modeling. To date, unfortunately, no simple model is capable of describing phenomena in materials at arbitrary length or time scale [25]. For instance, although density functional theory (DFT) and Hartree-Fock methods solve ground state problems at the quantum level, they are challenged by problems involving thousands of atoms or more [26]. Therefore multiscale modeling is necessary. Considering the different elementary processes in materials (e.g., electrons, atoms, dislocations, grains, ...), a variety of materials properties have been computed or predicted with satisfactory accuracy by multiscale computational modeling [27]. Numerous computational approaches have been maturely developed, ranging from atomic scale to macroscopic scale, from nanosecond to hours (see Fig. 1.2). A brief review of their pros and cons is crucial before any development of a new model.

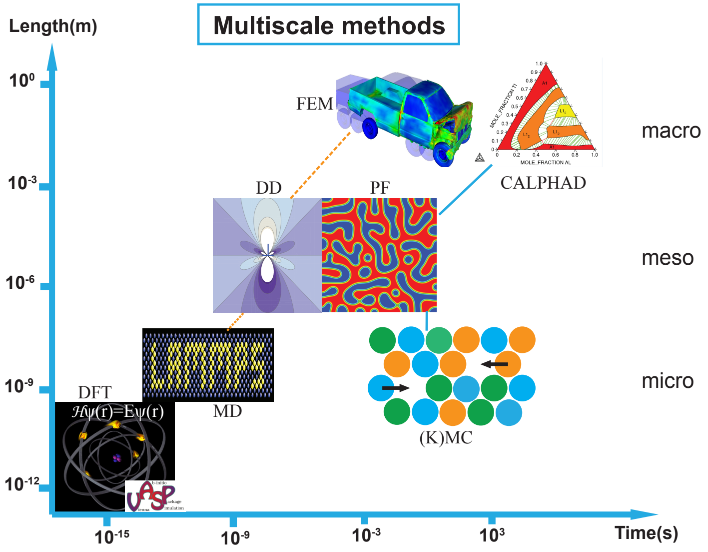

Figure 1.2: Multiscale methods for materials design. DFT=Density Functional Theory; MD=Molecular Dynamics; (K)MC=(Kinetic) Monte Carlo simulation; PF=Phase Field method; DD=Discrete Dislocation method; FEM=Finite Element Method; CALPHAD=CALculation PHAse Diagram.

1.4.1. Energetics from a quantum description

Ab initio calculations based on density functional theory (DFT) have been regarded as a standard treatment for ground-state energetics at T = 0K for metallic systems although the extension to finite temperatures is also available. Using only structural information DFT extracts ground state properties from the electronic density by solving the many-body Schrödinger equation in a self-consistent way [28]. In recent years accurate finite temperature free energies have become available from first principles by taking all of thermal excitation contributions into account, i.e., electronic contributions, quasi- and anharmonic vibrational contributions and/or magnetic contributions [29, 30]. In section 2.1 the DFT method will be explained in detail.

Although satisfactory ground state energies and free energies can be predicted, the application of DFT is limited by the requirement of expensive computing power. Nowadays *ab initio* predicted properties, e.g., total energies, elastic constants, electronic structures etc., serve as crucial energy paramenters for larger scale models, e.g., the CALPHAD approach [31–33].

1.4.2. Properties at finite temperatures

Only properties predicted at finite temperatures are of practical use for industry applications. Finite-temperature transitions at atomic or molecular scale in materials, e.g., solute atom precipitation [5], magnetic transitions [34], adsorption and desorption [35], and chemical reactions in polymer materials [36] were shown to have a significant impact on macroscopic mechanical properties [10]. Monte Carlo (MC) or molecular dynamic (MD) simulations have been widely used to elucidate thermodynamics and kinetics involved in these transitions driven by interatomic or intermolecular interactions. The predictive ability of these simulations relies on the accuracy of the potential energy derived from the electronic and atomic interactions. It is therefore generally necessary to first establish the potential energy that reflects the real interactions among the atoms (molecules). The system driven by the potential energy physically evolves then following a computationally efficient algorithm. The remainder of this section will briefly introduce the main feature of MC and MD simulations.

- **(K)MC simulation**

  Monte Carlo simulation is one of the most efficient methods to solve problems in materials science whose fundamental nature is stochastic, e.g., atomic diffusion, surface adsorption and desorption, grain growth [37], film deposition (or growth) [38, 39]. Specifically MC enables one to extract properties from the ensemble average of a system described under specific thermodynamic conditions [40–42].

  A variety of Monte Carlo algorithms have been developed during the past 50 years. The *Metropolis algorithm* is generally considered as the pioneer for sampling equilibrium properties [43, 44]. The key feature of the Metropolis sampling is the improvement of the efficiency by applying importance sampling in the phase space [45–47]. Another breakthrough in the development of Monte Carlo algorithms is the combination of kinetics with MC, which is now generally called **kinetic Monte Carlo** (kMC), although it was originally called "n-fold way algorithm" by its developers Bortz et al. [48, 49]. The KMC algorithm unconditionally accepts every attempt transition with known transition rate [50]. An event with a higher rate is typically associated with a larger occurrence probability. Such a feature enables studies of realistic kinetics in alloys at a long-time scale [51, 52]. The phase space, or say the total number of configurations should also be a finite value. A priori known transition probabilities are, however, necessary before implementing either the Metropolis or n-fold way sampling. Therefore efficient evaluation of all transition probabilities becomes important.

- **Molecular dynamics**

  The generation of a new configuration in MD is driven by Newton's equations of motion [53]. From the gradient of the potential energy forces acting on each atom are calculated. The time evolution of the system is characterized by the instantaneous positions and velocities updated after a finite time interval. Numerical integration of Newton's equations of motion, e.g., using the Verlet algorithm, is applied to propagate positions and velocities as a function of time. MD benefits from the explicit knowledge of the classical trajectory while suffers from the limited time scale (typically less than 100 ns) [54]. Therefore modeling rare events such as the thermally-excited vacancy diffusion goes far beyond the capability of MD simulations.

1.4.3. Models for larger scale descriptions

Phenomena at the meso- or macro-scale require models which focus on larger scale objects in materials, i.e., phases, domains, dislocations, grains or even continuum medium. Only interactions among these objects are considered. The predictive power of these models gets greatly enhanced when the "objects" are discretized because one can then keep track of the detailed evolution of each unit instead of obtaining an "averaged" image only. This advantage can be found in various models e.g., discrete dislocation method [55], phase field model [56, 57]) and finite element method.

It should be mentioned that since the 1970s, the CALPHAD (CALculation PHAse Diagrams) approach has become one of the most important methods to study phase equilibria [58, 59]. Gibbs energies of each phase are described as polynomials of composition, pressure and temperature where parameters are to be fitted to available experimental data. Optimized Gibbs energies are then used to calculate equilibrium phase diagrams as well as thermodynamic quantities. With reliable binaries it is feasible to extend to multinaries by adding additional parameters describing interactions among multiple species [60, 61]. However, the predictive ability of the CALPHAD model is limited by its intrinsic approximations for alloy mixing behavior and the amount of available experimental data [62]. To model problems involving non-equilibrium transitions one should go beyond CALPHAD.

1.5. Outline of the thesis

This thesis is divided into three main parts: (1) general background (chapter 1), (2) related theory and methods (chapters 2 and 3) and (3) applications of the methods (chapters 4–7). They are organized as follows:

The theory and the main methodologies used in this work will be introduced in chapter 2, including the discussion of the technical issues in detail. Specifically, chapter 3 is devoted to the cluster expansion (CE) method in particular addressing the issues arising in multicomponent alloys.

In chapter 4 one of the applications of the CE method in equilibrium thermodynamics will be presented—vacancy properties in concentrated alloys. The developed simple model is applied to extract vacancy properties in concentrated Cu-Ni alloys.

In chapter 5 precipitation thermodynamics and kinetics for dilute Al-Cu alloys are investigated by CE for configurational energies and for diffusion activation barriers. A significant change in kinetics will be found when local atomic environment dependent diffusion barriers are considered. A remarkable finding when studying the impact of the local atomic environment dependent diffusion barriers will be shown in chapter 6: In purely phase-separating alloys ordered pattern can be kinetically driven to appear as a transient phase.

As an extension of DFT at T = 0 K, electronic contribution at finite temperatures to the free energy for all the transition metals will be computed and presented in chapter 7.

References

[1] J. R. Davis, *Introduction to aluminum and aluminum alloys,* in *Aluminum and aluminum alloys*, ASM Specially Handbook (ASM International, Materials Park, Ohio, 1993) Chap. 1, pp. 3–17.

[2] J. R. Davis, *Selection and application of aluminum alloys,* in *Aluminum and aluminum alloys*, ASM Specially Handbook (ASM International, Materials Park, Ohio, 1993) Chap. 2, pp. 59–198.

[3] J. Hirsch, *Automotive trends in aluminium–the european perspective,* in *Materials Forum*, Vol. 28, edited by J. F. Nie, A. J. Morton, and B. C. Muddle (Institute of Materials Engineering Australasia Ltd, 2004) pp. 15–23.

[4] A. S. Warren, *Developments and challenges for aluminum–a boeing perspective,* in *Materials Forum*, Vol. 28, edited by J. F. Nie, A. J. Morton, and B. C. Muddle (Institute of Materials Engineering Australasia Ltd, 2004) pp. 24–31.

[5] I. J. Polmear, *Aluminium alloys–a century of age hardening,* in *Materials Forum*, Vol. 28, edited by J. F. Nie, A. J. Morton, and B. C. Muddle (Institute of Materials Engineering Australasia Ltd, 2004) pp. 1–14.

[6] M. Epler, *Structures by precipitation from solid solution,* in *ASM Handbook, Volume 09— Metallography and Microstructures*, edited by G. F. Vander Voort (ASM International, Materials Park, Ohio, 2004) pp. 134–139.

[7] J. R. Davis, *Fabrication and finishing of aluminum alloys,* in *Aluminum and aluminum alloys*, ASM Specially Handbook (ASM International, Materials Park, Ohio, 1993) Chap. 3, pp. 290–327.

[8] M. Warmuzek, *Metallographic techniques for aluminum and its alloys,* in *ASM Handbook, Volume 09—Metallography and Microstructures*, edited by G. F. Vander Voort (ASM International, Materials Park, Ohio, 2004) pp. 711–751.

[9] J. Kaufman, *Introduction to aluminum alloys and tempers,* (ASM International, 2000) Chap. 6, pp. 87–118.

[10] D. A. Porter, K. E. Easterling, and M. Y. Sherif, *Phase transformations in metals and alloys,* (CRC press, 2009) Chap. 5, pp. 288–302, 3rd ed.

[11] R. J. Naumann, *Introduction to the physics and chemistry of materials,* (CRC press, 2008) Chap. 14, pp. 279–285.

[12] D. A. Porter, K. E. Easterling, and M. Y. Sherif, *Phase transformations in metals and alloys,* (CRC press, 2009) Chap. 5, pp. 261–262, 3rd ed.

[13] J. R. Davis, *Physical metallurgy,* in *Aluminum and aluminum alloys*, ASM Specially Handbook (ASM International, Materials Park, Ohio, 1993) Chap. 1, pp. 31–46.

[14] A. Guinier, *Structure of age-hardened aluminium-copper alloys,* Nature **142**, 569 (1938).

[15] G. D. Preston, *Structure of age-hardened aluminium-copper alloys,* Nature **142**, 570 (1938).

[16] T. Konno, K. Hiraga, and M. Kawasaki, *Guinier-preston (GP) zone revisited: atomic level observation by HAADF-TEM technique,* Scripta Materialia **44**, 2303 (2001).

[17] M. Murayama, K. Hono, M. Saga, and M. Kikuchi, *Atom probe studies on the early stages of precipitation in Al-Mg-Si alloys,* Materials Science and Engineering: A **250**, 127 (1998).

[18] E. A. Marquis, F. Leonard, and N. C. Bartelt, *GP Zone Evolution in Al-Ag Alloys,* Microscopy and Microanalysis **13**, 1620 (2007).

[19] K. Matsuda, H. Daichou, G. J. Shiflet, and S. Ikeno, *HRTEM Observation of GP Zones in Al-Ag Alloy,* Materials Science Forum **331-337**, 1019 (2000).

[20] S. Müller, L. Wang, and A. Zunger, *First-principles kinetic theory of precipitate evolution in Al-Zn alloys,* Modelling and Simulation in Materials Science and Engineering **10**, 131 (2002).

[21] M. Karlík, B. Jouffrey, and S. Belliot, *The copper content of Guinier-Preston (GP1) zones in Al-1.84 at.% Cu alloy,* Acta metallurgica **46**, 1817 (1998).

[22] S. Son, M. Takeda, M. Mitome, Y. Bando, and T. Endo, *Precipitation behavior of an Al-Cu alloy during isothermal aging at low temperatures,* Materials Letters **59**, 629 (2005).

[23] K. Janssens, D. Raabe, E. Kozeschnik, M. Miodownik, and B. Nestler, *Computational materials engineering: An introduction to microstructure evolution,* (Elsevier Science, 2010) Chap. 1, pp. 1–6.

[24] W. Duan, *Computational materials science,* Current Opinion in Solid State and Materials Science **10**, 1 (2006).

[25] M. Ashby, *Physical modelling of materials problems,* Materials Science and Technology **8**, 102 (1992).

[26] J. Kohanoff and N. I. Gidopoulos, *Density functional theory: Basics, new trends and applications,* in *Handbook of Molecular Physics and Quantum Chemistry*, Vol. 2, edited by S. Wilson, P. F. Bernath, and R. McWeeny (WILEY-VCH Verlag, 2003) Chap. 26, pp. 532–568.

[27] M. F. Horstemeyer, *Multiscale modeling: A review,* in *Practical Aspects of Computational Chemistry: Methods, Concepts and Applications*, Chemistry and Materials Science, edited by J. Leszczynski and M. Shukla (Springer Netherlands, 2009) pp. 87–136.

[28] G. Kresse, M. Marsman, and J. Furthmüller, *Vienna Ab-initio Simulation Package the guide*, Computational Materials Physics, Faculty of Physics, Universität Wien, Sensengasse 8/12, A-1090 Wien, Austria, 2014th ed. (2014).

[29] C. K. Ande, *First-principles calculations on the stabilization of iron carbides(Fe_3C, Fe_5C_2 and η-Fe_2C) in steels*, Ph.D. thesis, Delft University of Technology (2013).

[30] A. Glensk, B. Grabowski, T. Hickel, and J. Neugebauer, *Understanding anharmonicity in fcc materials: From its origin to ab initio strategies beyond the quasiharmonic approximation,* Physical Review Letters **114**, 195901 (2015).

[31] C. Domain and C. Becquart, *Diffusion of phosphorus in α-Fe: An ab initio study,* Physical Review B **71**, 214109 (2005).

[32] S. Choudhury, L. Barnard, and J. Tucker, *Ab-initio based modeling of diffusion in dilute bcc Fe-Ni and Fe-Cr alloys and implications for radiation induced segregation,* Journal of Nuclear Materials **411**, 1 (2011).

[33] Y. S. Meng and M. E. Arroyo-de Dompablo, *First principles computational materials design for energy storage materials in lithium ion batteries,* Energy & Environmental Science **2**, 589 (2009).

[34] L. Mañosa, A. Planes, E. Vives, E. Bonnot, and R. Romero, *the Use of Shape-Memory Alloys for Mechanical Refrigeration,* Functional Materials Letters **02**, 73 (2009).

[35] J. W. Evans, *Kinetic monte carlo simulation of non-equilibrium lattice-gas models: Basic and refined algorithms applied to surface adsorption processes,* in *Handbook of Materials Modeling*, edited by S. Yip (Springer Netherlands, 2007) pp. 1753–1767.

[36] D. van Krevelen and K. te Nijenhuis, *Properties of Polymers: Their Correlation with Chemical Structure; their Numerical Estimation and Prediction from Additive Group Contributions* (Elsevier Science, 2009).

[37] G. H. Gilmer, *Computer models of crystal growth,* Science **208**, 355 (1980).

[38] P. Maksym, *Fast Monte Carlo simulation of MBE growth,* Semiconductor science and technology **3**, 594 (1988).

[39] Y. Yang, R. Johnson, and H. Wadley, *Kinetic Monte Carlo simulation of heterometal epitaxial deposition,* Surface Science **499**, 141 (2002).

[40] D. Landau and K. Binder, *A Guide to Monte Carlo Simulations in Statistical Physics,* (Cambridge University Press, 2009) Chap. 1, pp. 1–6, 3rd ed.

[41] D. Frenkel and B. Smit, *Understanding molecular simulation: From algorithms to applications,* (Elsevier Science, 2001) Chap. 1, pp. 1–6, 2nd ed.

[42] P. Allen and D. Tildesley, *Computer Simulation of Liquids*, Oxford Science Publ (Clarendon Press, 1989).

[43] N. Metropolis, A. W. Rosenbluth, M. N. Rosenbluth, A. H. Teller, and E. Teller, *Equation of state calculations by fast computing machines,* The Journal of Chemical Physics **21**, 1087 (1953).

[44] N. Metropolis, *The Beginning of the Monte Carlo Method,* Los Alamos Science **15**, 125 (1987).

[45] D. Landau and K. Binder, *A Guide to Monte Carlo Simulations in Statistical Physics,* (Cambridge University Press, 2009) Chap. 4, pp. 68–134, 3rd ed.

[46] D. Frenkel and B. Smit, *Understanding molecular simulation: From algorithms to applications,* (Elsevier Science, 2001) Chap. 3, pp. 23–58, 2nd ed.

[47] J. Amar, *The Monte Carlo method in science and engineering,* Computing in Science & Engineering **8**, 9 (2006).

[48] A. Bortz, M. Kalos, J. Lebowitz, and M. Zendejas, *Time evolution of a quenched binary alloy: Computer simulation of a two-dimensional model system,* Physical Review B **10**, 535 (1974).

[49] A. Bortz, M. Kalos, and J. Lebowitz, *A new algorithm for Monte Carlo simulation of Ising spin systems,* Journal of Computational Physics **17**, 10 (1975).

[50] D. Landau and K. Binder, *A Guide to Monte Carlo Simulations in Statistical Physics,* (Cambridge University Press, 2009) Chap. 2, pp. 7–46, 3rd ed.

[51] C. C. Battaile, *The Kinetic Monte Carlo method: Foundation, implementation, and application,* Computer Methods in Applied Mechanics and Engineering **197**, 3386 (2008).

[52] A. F. Voter, *Introduction to the kinetic monte carlo method,* in *Radiation Effects in Solids*, NATO Science Series, Vol. 235, edited by K. Sickafus, E. Kotomin, and B. Uberuaga (Springer Netherlands, 2007) pp. 1–23.

[53] D. Frenkel and B. Smit, *Understanding molecular simulation: From algorithms to applications,* (Elsevier Science, 2001) Chap. 4, pp. 63–107, 2nd ed.

[54] B. J. Alder and T. E. Wainwright, *Studies in molecular dynamics. i. general method,* The Journal of Chemical Physics **31**, 459 (1959).

[55] F. Sun, E. Van der Giessen, and L. Nicola, *Plastic flattening of a sinusoidal metal surface: A discrete dislocation plasticity study,* Wear **296**, 672 (2012).

[56] N. Moelans, B. Blanpain, and P. Wollants, *An introduction to phase-field modeling of microstructure evolution,* Calphad **32**, 268 (2008).

[57] L.-Q. Chen, *Phase-field models for microstructure evolution,* Annual Review of Materials Research **32**, 113 (2002).

[58] L. Kaufman, *Current and future applications of calphad technology,* in *Complex Inorganic Solids*, edited by P. Turchi, A. Gonis, K. Rajan, and A. Meike (Springer US, 2005) pp. 73–85.

[59] M. Hillert, *Phase Equilibria, Phase Diagrams and Phase Transformations: Their Thermodynamic Basis*, 2nd ed. (Cambridge University Press, 2007).

[60] X. Zhang, Y. F. Cui, G. L. Xu, W. J. Zhu, H. S. Liu, B. Y. Yin, and Z. P. Jin, *Thermodynamic assessment of the U-Mo-Al system,* Journal of Nuclear Materials **402**, 15 (2010).

[61] Y. F. Cui, X. Zhang, G. L. Xu, W. J. Zhu, H. S. Liu, and Z. P. Jin, *Thermodynamic assessment of Co-Al-W system and solidification of Co-enriched ternary alloys,* Journal of Materials Science **46**, 2611 (2011).

[62] H. Lukas, S. G. Fries, and B. Sundman, *Computational Thermodynamics: The Calphad Method* (Cambridge University Press, 2007).

2

Theory and Method

Multiscale computational materials science can unveil intrinsic physics in materials. By a proper use of multiscale computational methods, intricate properties or transformations in materials can be computed or simulated. Monitoring early stage precipitation in aluminum alloys requires simulations at the atomic scale. An accurate description of interatomic potentials in such simulations is the premise for obtaining trustworthy results that can be connected with experimental observations. Cluster expansions which provide a bridge between ab initio calculations and configurational energetics have proven to be accurate and efficient not only in thermodynamics but also in kinetics. Moreover, precipitates observed in simulations should be carefully identified both in the real space and in the reciprocal space.

2.1. Density functional theory: A brief introduction

Nowadays *ab* initio calculations based on density functional theory (DFT) are routinely applied to determine the ground state properties of materials. Excellent agreement has been found where experimental data are available for comparison [1–3]. With the fast development of the computer hardware, DFT calculations show an increasing power in predicting more properties when coupled with multiscale high-throughput computational methods [4]. In this section, the essence of the DFT method will be introduced.

2.1.1. Schrödinger equation

The study of the ground state structural and electronic properties of materials can be physically described as finding the ground state of an ensemble of interactive nuclei and electrons [5]. In order to obtain the energy as well as wavefunctions one needs to solve the many-body time-independent Schrödinger equation [6–8],

$$\hat{H}\Psi_i(\mathbf{r},\mathbf{R}) = E_i\Psi_i(\mathbf{r},\mathbf{R}) \tag{2.1}$$

where **r** and **R** represent the sets of coordinate vectors $\{\mathbf{r}_i\}(i = 1, 2, 3, ..., n)$ of n electrons and coordinate vectors $\{\mathbf{R}_I\}(I = 1, 2, 3, ..., N)$ of N nuclei. The Hamiltonian operator is a linear combination of the kinetic energy and the potential energy of interactive nuclei and electrons,

$$\begin{aligned}
\hat{H} &= \hat{T}_N + \hat{T}_e + \hat{V}_{N-N}(\mathbf{R}) + \hat{V}_{e-e}(\mathbf{r}) + \hat{V}_{N-e}(\mathbf{r},\mathbf{R}) \\
&= -\sum_{I=1}^{N}\frac{\hbar^2}{2M_I}\nabla_I^2 - \sum_{i=1}^{n}\frac{\hbar^2}{2m_i}\nabla_i^2 + \frac{e^2}{2}\sum_{I=1}^{N}\sum_{J\neq I}^{N}\frac{Z_I Z_J}{|\mathbf{R}_I - \mathbf{R}_J|} \\
&\quad + \frac{e^2}{2}\sum_{i=1}^{n}\sum_{j\neq i}^{n}\frac{1}{|\mathbf{r}_i - \mathbf{r}_j|} - e^2\sum_{I=1}^{N}\sum_{i=1}^{n}\frac{Z_I}{|\mathbf{R}_I - \mathbf{r}_i|}
\end{aligned} \tag{2.2}$$

where M (m) and Z (e) refer to the mass and the charge of the nucleus (electron).

Practically it is impossible to solve this equation without any approximations because it is a $3(n+N)$ dimensional correlated system. Exceptions are only limited to the cases with a small number of particles, e.g., hydrogen atom. Simplifications for solving the Schrödinger equation have several common features. They either (1) eliminate negligible correlations in order to orthogonalize the vectors, or (2) reduce the number of degrees of freedom, or (3) replace the real correlations with approximations.

2.1.2. Born-Oppenheimer (adiabatic) approximation

The Born-Oppenheimer approximation is based on separating the different time scales of the motion of nuclei and electrons. The velocities of electrons are much larger than that of the nuclei due to their difference in mass. Approximately the motion of electrons can be regarded to be adiabatically independent, which means that the low-mass electrons can catch up instantaneously with the movement of the nuclei [9]. In other words, we only need to solve the Schrödinger equations for electrons with the nuclei assumed to be stationary. By applying the Born-Oppenheimer approximation the wavefunction expression can therefore be decoupled as,

$$\Psi(\mathbf{r},\mathbf{R}) = \Theta(\mathbf{R})\Phi(\mathbf{r},\mathbf{R}) \tag{2.3}$$

where $\Theta(\mathbf{R})$ is the nuclear wavefuntion and $\Phi(\mathbf{r},\mathbf{R})$ is the electronic wavefunction. The decoupled adiabatic Schrödinger equations for electrons and nuclei can be then written as,

$$[\hat{T}_e + \hat{V}_{e-e}(\mathbf{r}) + \hat{V}_{N-e}(\mathbf{r},\mathbf{R})]\Phi_i(\mathbf{r},\mathbf{R}) = \varepsilon_i(\mathbf{R})\Phi_i(\mathbf{r},\mathbf{R}) \tag{2.4}$$

$$[\hat{T}_N + \hat{V}_{N-N} + \varepsilon_i(\mathbf{R})]\Theta_I(\mathbf{R}) = E_I\Theta_I(\mathbf{R}) \tag{2.5}$$

where ε_i are the eigenvalues of electrons which depend parametrically on the positions of nuclei. Since classical nuclear approximations [10] have successfully been developed to solve Eq. 2.5, we are now left with the most challenging problem of solving the many-body Schrödinger equations for electrons based on fixed positions of nuclei, Eq. 2.4 [11, 12].

2.1.3. Hohenberg-Kohn theorem

The key aspect of the density functional theory lies in replacing the multi-dimensional wavefunction with a 3D electron density from which all ground state properties can be derived, as proposed by Hohenberg and Kohn [13]. The theorem states the following:

- The ground state energy of an n-electron system is a unique functional of the electronic density $n(\mathbf{r})$: $E_0 \sim E[n(\mathbf{r})]$.
- The ground state energy can be obtained at the equilibrium charge density $n_0(\mathbf{r})$ by minimizing the energy functional with respect to the electronic density, which is

$$E_0 = \min\{E[n(\mathbf{r})]\} = E[n_0(\mathbf{r})] \tag{2.6}$$

According to the Hohenberg-Kohn theorem, the ground state total energy functional of an n-electron system can be written as

$$E_0[n_0] = T[n_0] + V_{N-e}[n_0] + V_{e-e}[n_0] \tag{2.7}$$

where T, V_{N-e} and V_{e-e} represent the electronic kinetic energy, electron-nucleus interactions and electron-electron interactions, respectively. The effect of nuclei on the electrons, $V_{N-e}[n_0]$, can be regarded as an external field which is also determined by the electronic density,

$$V_{N-e}[n_0] = \int n_0(\mathbf{r})v_{\text{ext}}(\mathbf{r})\mathrm{d}\mathbf{r} \tag{2.8}$$

Eq. 2.7 can then be rewritten as,

$$E_0[n_0] = \int n_0(\mathbf{r})v_{\text{ext}}(\mathbf{r})\mathrm{d}\mathbf{r} + F[n_0] \tag{2.9}$$

where a functional $F[n_0]$ $(= T[n_0] + V_{e-e}[n_0])$ which is independent of the external potential is defined [8].

The Hohenberg-Kohn theorem opened up a way to search for the ground state energy. However, two unsolved problems are still left: (1) how can we find the ground state electronic density n_0 and (2) how to solve $F[n_0]$.

2.1.4. Kohn-Sham method

The Hohenberg-Kohn theorem sheds light on where the ground state properties are hidden. The Kohn-Sham method introduced next gives then a practical way to carry out the search [14, 15]. The strategy within the Kohn-Sham method can be summarized as:

(1) One can simplify a problem of an n-body system to n problems of one-body systems.

(2) One can separate an interactive system into an effective non-interacting system and extra correction terms.

First a reference system with n non-interacting electrons is introduced. The electronic density $n^r(\mathbf{r})$ of the reference system is assumed to be the same as the ground state electronic density of the interacting system[1]. Each of these n non-interacting electrons lies in the same external potential as that in the interacting system. The Hamiltonian of the reference system is then written as,

$$\hat{H}^r = \sum_{i=1}^{n} \hat{h}_i^r = \sum_{i=1}^{n} \Big[-\frac{\hbar^2}{2m_i}\nabla_i^2 + v_{\text{eff}}^r(\mathbf{r}_i) \Big] \tag{2.10}$$

where $\hat{h}^r$ refers to the one-electron Kohn-Sham Hamiltonian. Then the Schrödinger equation for each electron in the reference system is,

$$\hat{h}_i^r \psi_i^r = \varepsilon_i^r \psi_i^r \tag{2.11}$$

Based on the reference system, the functional $F[n_0]$ of the interacting system in Eq. 2.9 can be rewritten as,

$$\begin{aligned} F[n_0] &= T[n_0] + V_{e-e}[n_0] \\ &= (T^r[n_0] + T'[n_0]) + (\frac{e^2}{2}\iint \frac{n_0(\mathbf{r})n_0(\mathbf{r}')}{|\mathbf{r}-\mathbf{r}'|}\mathbf{drdr}' + V'_{e-e}[n_0]) \\ &= (T^r[n_0] + \frac{e^2}{2}\iint \frac{n_0(\mathbf{r})n_0(\mathbf{r}')}{|\mathbf{r}-\mathbf{r}'|}\mathbf{drdr}') + E_{\text{xc}}[n_0] \end{aligned} \tag{2.12}$$

where the kinetic energy $T[n_0]$ and the electron-electron interaction $V_{e-e}[n_0]$ can be explicitly divided into a reference term and an extra term, respectively. Two extra terms, $T'[n_0]$ and $V'_{e-e}[n_0]$, constitute the exchange-correlation energy functional,

$$E_{\text{xc}}[n_0] = T'[n_0] + V'_{e-e}[n_0] \tag{2.13}$$

Then the ground state energy functional in Eq. 2.9 with the assumption that

$$n^r(\mathbf{r}) = n_0(\mathbf{r}) \tag{2.14}$$

will be,

$$E_0[n^r] = T^r[n^r] + \int n^r(\mathbf{r})v_{\text{ext}}(\mathbf{r})\mathbf{dr} + \frac{e^2}{2}\iint \frac{n^r(\mathbf{r})n^r(\mathbf{r}')}{|\mathbf{r}-\mathbf{r}'|}\mathbf{drdr}' + E_{xc}[n^r] \tag{2.15}$$

In the reference system it is trivial to compute the electronic density from one-electron wavefunctions. Then we are left with the problem of finding the proper one-electron

---

[1] superscript "r" in this section indicates the reference system

wavefunctions ψ_i^r which minimize the total energy functional of the system we are interested in. According to the Kohn-Sham algorithm, the ground state energy E_0 can be obtained from Eq. 2.6 via solving n one-particle Schrödinger equations (Kohn-Sham equations) [14, 16]:

$$\Big\{-\frac{\hbar^2}{2m_i}\nabla_i^2 + v_{\text{eff}}^r(\mathbf{r})\Big\}\psi_i^r(\mathbf{r}) = \varepsilon_i^r\psi_i^r(\mathbf{r}) \tag{2.16}$$

by setting

$$n^r(\mathbf{r}) = \sum_{i=1}^{n}|\psi_i^r(\mathbf{r})|^2 \tag{2.17}$$

where

$$v_{\text{eff}}^r(\mathbf{r}) = v_{\text{ext}}(\mathbf{r}) + e^2\int\frac{n^r(\mathbf{r}')}{|\mathbf{r}-\mathbf{r}'|}\mathbf{dr}' + \mu_{\text{xc}}[n^r(\mathbf{r})] \tag{2.18}$$

and

$$\mu_{\text{xc}}[n^r(\mathbf{r})] = \frac{\delta E_{xc}[n^r(\mathbf{r})]}{\delta n^r(\mathbf{r})} \tag{2.19}$$

is called the exchange-correlation potential [5, 17].

Eqs. 2.16–2.19 should be solved in a self-consistent way [14, 15, 18] (see also Fig. 2.1). To begin with, an initial trial electronic density $n^r(\mathbf{r})$ is generated. The exchange-correlation potential $\mu_{\text{xc}}[n^r(\mathbf{r})]$ and the effective Kohn-Sham potential $v_{\text{eff}}^r(\mathbf{r})$ are then calculated from Eqs. 2.19 and 2.18. An updated electronic density is subsequently computed by Eqs. 2.16 and 2.17. This process repeats until a self-consistent electronic density is obtained. The ground state total energy is then given by,

$$E_0 = \sum_{i=1}^{n}\varepsilon_i^r - \frac{e^2}{2}\iint\frac{n^r(\mathbf{r})n^r(\mathbf{r}')}{|\mathbf{r}-\mathbf{r}'|}\mathbf{drdr}' + E_{\text{xc}}[n^r(\mathbf{r})] - \int n^r(\mathbf{r})\mu_{\text{xc}}[n^r(\mathbf{r})]\mathbf{dr}. \tag{2.20}$$

The remaining problem is to find the exact expression of the exchange-correlation functional $E_{\text{xc}}[n]$. This is also where the accuracy of DFT calculations gets limited. A hierarchy of exchange-correlation functionals based on various approximations has been developed.

2.1.5. Exchange-correlation functionals

According to the sequence of an increasing accuracy, four rungs of the "Jacob's ladder" within the family of DFT exchange-correlation functionals have been established [19, 20].

- **Local density approximation (LDA)**

  The LDA simply assumes that the exchange-correlation energy depends on the local electronic density only,

  $$E_{\text{xc}}^{\text{LDA}}[n(\mathbf{r})] = \int n(\mathbf{r})\varepsilon[n(\mathbf{r})]\mathbf{dr} \tag{2.21}$$

  where $\varepsilon[n(\mathbf{r})]$ is the exchange-correlation energy per electron of a homogeneous electron gas with the local density $n(\mathbf{r})$. It is exact only for systems whose electronic

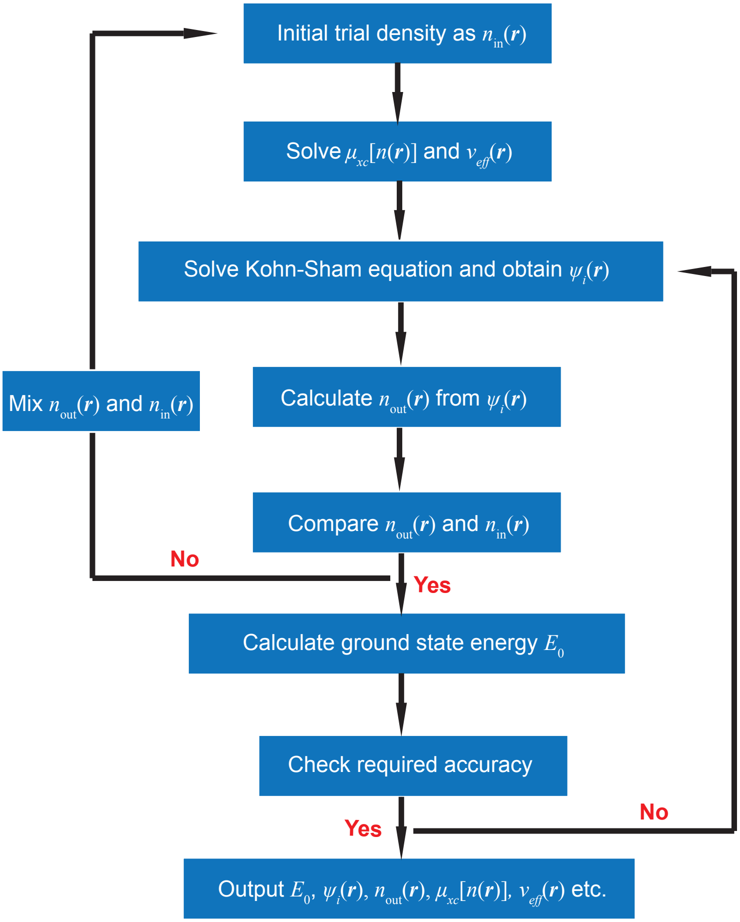

Figure 2.1: The flow chart of self-consistently solving Kohn-Sham equations to obtain the ground state energy.

density variation is sufficiently slow [21, 22]. The actual performance shows that the LDA can yield satisfactory results for systems with covalent, ionic and metallic bonds, especially for those with homogeneous electronic density. However, a well-known deficiency of the LDA is the overestimation of the bond strength [5, 19, 20]. Lattice constants and atomic ground state energies obtained with LDA are therefore generally underestimated whereas cohesive energies are overestimated. Band gaps in semiconductors and insulators are seriously underestimated.

- **Generalized gradient approximation (GGA)**

  The GGA improves the LDA with an additional assumption that the exchange-correlation energy depends also on the gradient of the electronic density $\nabla n(\mathbf{r})$,

$$E_{\mathrm{xc}}^{\mathrm{GGA}}[n(\mathbf{r})] = \int n(\mathbf{r})\varepsilon[n(\mathbf{r})]\mathrm{d}\mathbf{r} + \int F_{\mathrm{xc}}[n(\mathbf{r}), \nabla n(\mathbf{r})]\mathrm{d}\mathbf{r} \tag{2.22}$$

where a functional F_{xc} which may not be designed in a unique way is required to satisfy several conditions for the exchange correlations of electrons. Several exchange-correlation functionals in the "GGA family" have been developed in recent years:

PW91 the functional proposed by Perdew et al. in 1991 [23].

PBE the Perdew-Burke-Ernzerhof functional [24, 25].

AM05 the functional designed to include surface effects by Armiento and Mattson in 2005 [26].

PBEsol A revised PBE functional that improves predictions of equilibrium properties in solids [27].

Generally speaking, the GGA corrects the over-binding deficiency of the LDA and yields better results in predicting correct ground state properties of metals. However, besides the problem of underestimation for band gaps, it was reported that the GGA overcorrects the over-binding problem, resulting in an overestimation of lattice constants, bulk moduli, phonon frequencies etc. More comparison among different GGAs can be found in Refs. [5, 19, 20, 28].

- **Meta-GGA and hybrid functionals**

  More accurate descriptions can be achieved by adding higher order approximations. In the meta-GGA both the Laplacian of the electronic density $\nabla^2 n(\mathbf{r})$ and the local kinetic energy density which is the sum of all the occupied Kohn-Sham eigenstates,

  $$\tau(\mathbf{r}) = \frac{1}{2}\sum_{i=1}^{n} |\nabla\psi_i(\mathbf{r})|^2, \tag{2.23}$$

  are taken into account. In addition, accuracy may also be increased by mixing non-local and local functionals. As an example, the B3LYP functional consists of 80% of the LDA and 20 % of the exact Hartree-Fork exchange functional as well as other functionals wherein empirical parameters may exist [29, 30].

It should be noticed that the choice of the exchange-correlation functional depends on the features of the system under study and properties to be evaluated. For instance, for metallic solid solutions, it is unwise to choose the B3LYP functional which is designed for molecules. Likewise if the electronic density of the system deviates from homogeneous distribution, the GGA or the meta-GGA yields a better description than the LDA. Interestingly, sometimes LDA can also give excellent results for inhomogeneous systems [19]. The reason might be the cancelation of errors induced by two opposite deficiencies.

2.1.6. Limitations of DFT

Although DFT has been successful in the prediction of properties in materials from first principles, its limitations still exist due to the intrinsic approximations in the exchange-correlation functionals. The deficiencies of the current widely used exchange-correlation functionals lead to several failures such as [16, 31]:

- Incorrect prediction of the exited states, e.g., the underestimation of band gaps in semiconductors and insulators.
- Dissatisfying description of the binding behavior.
- Poor predictions for elements with strongly correlated *d*- and *f*-bands.
- Failure for predicting van der Waals interactions.

Fortunately, for the present study—ground state total energies of multi-component metallic systems without strong *d*- or *f*- bands, the GGA-PBE can give reasonable results with satisfactory accuracy.

2.2. Lattice gas model

As multicomponent alloys in a solid solution state are generally in the form of a certain crystalline structure, it is reasonable to study phenomena in terms of configurational order by a lattice gas model. The definition of the "lattice gas" refers to the assumption that species (atoms as well as vacancies) are confined to a **fixed lattice**. For substitutional solid solutions it is also assumed that each lattice site is associated with one and only one type of the species [32]. This approximation applies for one-, two-, or three-dimensional lattices.

2.2.1. Generalized mean field approximations

Based on the lattice gas model, the degrees of freedom of a many-body system are discretized into a finite mesh. By doing this the system becomes tractable, but the problems are still far from solved. Further approximations are necessary to achieve an efficient description of interactions among particles at a low computational cost. To simplify a many-body problem to "one-body" problems mean field approximations (MFAs) introduce "averaged effective interactions" acting on a single particle generated by all the other particles [33]. Specifically fluctuations of the system can be expanded around the mean of an effective field with different "order" [34].

- **Bragg-Williams approximation**

  The *Bragg-Williams approximation*, also called the single-site or "zeroth order" approximation, is the simplest mean field approximation. It is assumed that the occupation of one lattice site is not influenced by any of the other lattice positions. In other words, the probabilities of single-site occupations by atoms of type i are exclusively determined by the atomic concentration x_i [35–37]. For example, in binary A-B alloys, the configurational energy described by the Bragg-Williams approximation can be expressed as,

  $$E(x_A) = \sum_i \sum_j n_{ij} J_{ij} = \frac{z}{2}[x_A^2 J_{AA} + 2x_A x_B J_{AB} + x_B^2 J_{BB}], \tag{2.24}$$

  where J_{ij} is the bonding energy between nearest neighbor sites i-j, z is the coordination number and $x_{A(B)}$ is the atomic concentration of A (B) atom. The corresponding configurational mixing entropy has the form,

$$S = -k_B[x_A \ln x_A + x_B \ln x_B], \tag{2.25}$$

where k_B is the Boltzmann's constant.

- **Quasi-chemical approximation**

  Within the quasi-chemical approximation (also called the pair approximation) nearest neighbor pairs correlate with each other by a certain degree of short range order. Solid solutions with phase separating or ordering tendency exhibit non-random distributions of i-j pairs. At finite temperatures equilibrium states can be reached by minimizing Gibbs energies with respect to each pair correlation function. If we define a short-range-order interaction parameter, $\omega = J_{AB} - (J_{AA} + J_{BB})/2$ [38–40], then the Gibbs energy can be expressed as,

$$\begin{aligned} G &= E - TS \\ &= \frac{z}{2}\sum_{i,j} x_{ij}J_{ij} + k_B T \ln W(x_i, x_{ij}) \\ &= \frac{z}{2}(x_A J_{AA} + x_B J_{BB} + 2x_{AB}\omega) + k_B T \ln W(x_i, x_{ij}), \end{aligned} \tag{2.26}$$

  where x_{ij} is the concentration of pair i-j and $W(x_i, x_{ij})$ represents the total number of possible arrangements of A and B atoms. It is apparent that the Gibbs energy is a function of point and pair correlation functions.

- **Cluster variation method (CVM)**

  The cluster variation method, proposed by Kikuchi [41, 42] more than 50 years ago, is derived based on a generalized mean field approximation. It generalizes correlations in terms of n-body clusters which is expected to be exact if clusters of infinite size are included [43]. The formalism of the CVM is based on the establishment of a cluster algebra on fixed lattices decorated by different occupation variables assigned to each species i ($i = A, B, C...$). The configurational energy functional (or Hamiltonian) $[E]$ is written as a weighted summation of effective cluster interactions (ECIs)[1] while the configurational entropy functional $[S]$ is expressed as a sum of generalized "$x \ln x$" terms [44, 45],

$$[S] = k_B \sum_{i=1}^{M} \gamma_i \sum_{\sigma_i} [p_i(\sigma_i)] \ln[p_i(\sigma_i)], \tag{2.27}$$

  Where γ_i is the Kikuchi-Barker coefficient associated with the cluster of type i, $p_i(\sigma_i)$ refers to the density function of the cluster of type i with decoration σ_i and M the maximal clusters used in one expansion, i.e., four-body clusters in the tetrahedron-triangle (TT) approximation and six-body clusters in the tetrahedron-octahedron (TO) approximation [46]. It is generally believed that by including larger maximal clusters higher accuracy can be reached. For most of the alloys, convergence can be nicely achieved with maximal clusters including four atoms.

---

[1] See section 2.4 for more details

2.2.2. Case study: The Ising model

The Ising model is a prototype case of the lattice gas model originally proposed for modeling magnetic transitions. It was afterwards generalized to study the configuration dependent properties in solid solutions. In the Ising model spins which are either up (+1) or down (–1) are arranged on the lattice sites of an n-dimensional lattice. Nearest neighbor interactive spin pairs are associated with an interaction $-J$ if they are parallel or $+J$ if they are antiparallel [32, 46–48]. The total energy under an external magnetic field can be expressed as [49],

$$E = -J\sum_{i,j}^{N}\sigma_i\sigma_j - H\sum_{i=1}^{N}\sigma_i, \tag{2.28}$$

where σ_i represents the spin variable of site i with value $+1$ or -1, "i,j" corresponds to the nearest neighbor spin pair, N is the total number of spins and H the magnetic field intensity.

Although simple the Ising model is non-trivial with respect to analytical solutions. For a one-dimensional Ising model an exact solution had been obtained where no transitions were found. Phase transitions have been observed in two- or three-dimensional cases [50].

2.3. Vacancy-assisted substitutional diffusion in solid solution

One application of the lattice gas model is to model phase transformations on a fixed crystalline lattice, e.g., fcc alloys. From a microscopic point of view, precipitation processes in substitutional solid solutions are the consequence of atomic diffusion via vacancies on the lattice. Substitutional atoms may exchange their positions with neighboring vacancies once they acquire enough excitations at finite temperatures [51–53] (see Fig. 2.2). However, oftentimes aging treatment for aluminum alloys is performed at low temperatures where the diffusion kinetics is typically very slow.

2.3.1. Transition state theory for thermal activation processes

Substitutional diffusion can be regarded as stochastic walks of diffusing atoms on a certain lattice. In close packed structures diffusion can hardly happen without vacancies. Most of the time atoms keep oscillating on their equilibrium lattice positions at certain vibrational frequencies. By chance vacancy-atom swapping may occur if one atom next to a vacancy gets thermally activated and overcomes a certain activation energy barrier [54]. Such a description suggests that diffusion at the atomic level depends not only on the number of available vacancies but also on the activation energy. According to the transition state theory (TST) [55], the rate of the thermally activated jumps of the diffusing atom follows an Arrhenius relation [54, 56]:

$$\nu(V,T) = \frac{k_BT}{h}\exp\Big(-\frac{\Delta F^{\text{act}}(V,T)}{k_BT}\Big) \tag{2.29}$$

where $\Delta F^{\text{act}}(V,T)$ is the thermal activation free energy, i.e., free energy difference between the saddle point and the end point and h is the Planck constant. To facilitate the

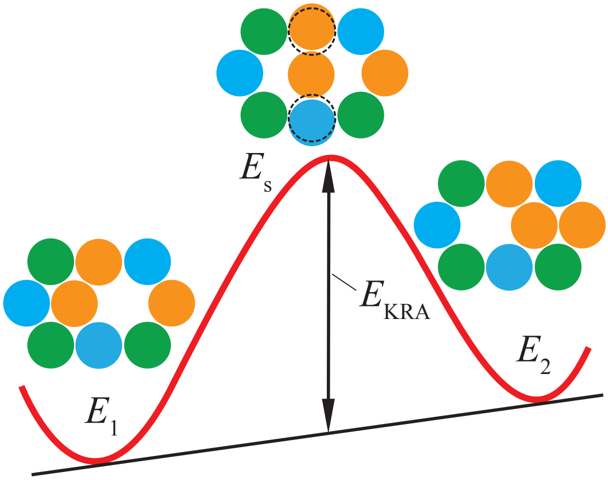

Figure 2.2: Vacancy-assisted substitutional diffusion in fcc ternary alloys. The energy profile is shown by the thick red curve where the two valleys are energies of the end points (E_1 and E_2) and the peak is the energy at the saddle point (E_s). The corresponding configurations are also attached. Blue, orange and green solid circles refer to three alloying elements (the close-packed [110] plane is shown). Dashed open circles indicate the original positions of atoms without the diffusing atom sitting at the saddle point. The kinetically resolved activation (KRA) barrier is illustrated by the black double-headed arrow.

standard T=0 K DFT calculations, it is generally preferred to separate the activation energy at T=0 K from $\Delta F^{\text{act}}(V,T)$ in the exponential and put all relevant thermal excitations (mainly the vibrational contributions) into a prefactor $\nu_0(V,T)$ [57]. Eq. 2.29 then becomes,

$$\nu(V,T) = \nu_0(V,T)\exp\Big(-\frac{Q}{k_BT}\Big) \tag{2.30}$$

where $Q = \Delta E^{\text{act}}_{0K}(V)$ referring to the activation barrier at T=0 K and $\nu_0(V,T)$ is the so-called effective attempt frequency. The activation energies at $T = 0$ K in Eq. 2.30 are nowadays routinely calculated via the nudged elastic band (NEB) method which will be discussed in Sec. 2.3.3.

Several approaches are available for evaluating $\nu_0(V,T)$. A simplest estimation is based on an Einstein frequency which is the frequency of the jumping atom when all the atoms are at the equilibrium positions:

$$\nu_0^{\text{Ein}} = \frac{1}{2\pi}\sqrt{k/M} \tag{2.31}$$

where M is the mass of the jumping atom and k is the spring constant of the jumping atom at the equilibrium position. A more accurate calculation using a high-temperature approximation of phonon modes at the Gamma point is the Vineyard formula [58, 59]

$$\nu_0^{\text{Vin}} = \frac{\prod_j^N \nu_j}{\prod_j^{N-1} \nu_j'} \tag{2.32}$$

where ν_j (ν_j') are normal frequencies at the Gamma point in the equilibrium (transition) state. Of course, if one aims at accurate calculations of the temperature and volume dependent effective attempt frequency, all thermal excitations should be included in Eq. 2.29.

2.3.2. Kinetically resolved activation (KRA) barrier

Due to the multiple local atomic configurations in multi-component alloys, the activation barrier Q depends on the jumping direction, i.e., from Fig. 2.2 it is apparent that $Q(1 \rightarrow 2) \neq Q(2 \rightarrow 1)$. A problem then rises that the energy barrier is not a state function anymore. Van de Ven et al. [60, 61] solved this problem by introducing the so-called **kinetically resolved activation** (KRA) barrier which is defined as,

$$E_{\text{KRA}} = E_s - \frac{1}{2}(E_1 + E_2), \tag{2.33}$$

as is also schematically shown in Fig. 2.2. Then the activation barrier can be rewritten for jump $1 \rightarrow 2$ as,

$$Q = E_{\text{KRA}} + (E_2 - E_1)/2. \tag{2.34}$$

2.3.3. Saddle point energy calculations

It is essential to know the saddle point energy before calculating activation barriers. In multi-component alloys the saddle point may not necessarily be right at the middle point between two end points because symmetry may be broken due to the multiple interactions [54]. The most widely used and efficient method for searching the saddle point is called the **nudged elastic band** (NEB) method. It is also applied to compute the minimum-energy path (MEP) [62, 63]. The schematic description of the NEB method is shown in Fig. 2.3. To perform NEB calculations initial and final structures should firstly be fully relaxed. An initial guess for the transition path (called the elastic band, labeled by "NEB" in Fig. 2.3) is then made by interpolating several intermediate "images" between initial and final states. Finally the saddle point (or the MEP) can be found by minimizing the total energy of the elastic band with respect to atomic displacements under the nudge of the band (i.e., perturbations to different components of spring forces). An improved NEB method called **the climbing image nudged elastic band** (CI-NEB) method has also been developed (see Ref. [64, 65] for more details). In the present thesis the CI-NEB method is used for all the calculations of the saddle point energy.

2.4. Cluster expansion

The cluster expansion (CE) method is designed specifically to treat problems related to the configurational order in materials. The advantage of the CE is particularly evident for the

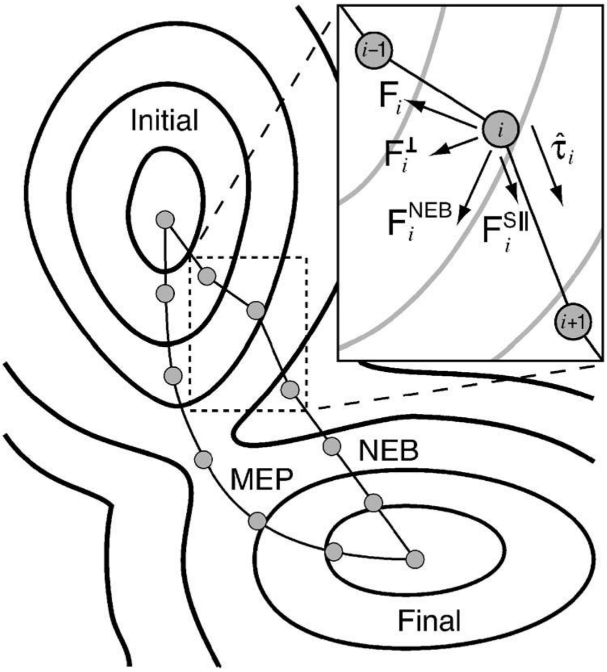

Figure 2.3: Schematic diagram of the nudged elastic band (NEB) method. Large open circles and curves in thick black lines represent the contours of the potential energy surface where the initial and the final states are labeled. Grey solid circles are intermediate "images" connected by the elastic band. Inset shows different force components acting on a specific "image" from its neighbor "images". The nudged elatic band and the minimum-energy path are labeled by "NEB" and "MEP", respectively. (from: http://theory.cm.utexas.edu/henkelman/research/saddle/)

case when *ab initio* DFT calculations are challenged by cumbersome energy evaluations. In Monte Carlo simulations, for example, the most time-consuming step is the computation of the configurational energy for every iteration. It is therefore impractical to rely on DFT calculations only, especially when the system is large. Readers can refer to section 3.2.1 for the basics of the CE in detail. In the following sections computation details of the CE will be explained and discussed.

2.4.1. Calculation of effective cluster interactions

Effective cluster interactions (ECIs) can be extracted by the structure inversion method (see section 3.2.1 for details). One should firstly establish an energy database of several known structures typically by *ab initio* DFT calculations. For each structure in the energy database the correlation function of each selected cluster is then examined by evaluating the Connolly-Williams matrix [66]. With the Connolly-Williams matrix the structure inversion can be applied by either (a) the direct inversion method or (b) a least-squares procedure. If the Connolly-Williams matrix is a square matrix, direct inversion might be efficient. Otherwise the Connollly-Williams matrix is a pseudo-inverse which requires a least-squares fit. ECIs are then extracted after minimizing the fitting error [43, 67],

$$\sum_s w[s][E_{\mathrm{DFT}}[s] - \sum_\alpha \tilde{J}_\alpha \langle \sigma_\alpha [s] \rangle]^2 = \mathrm{min}, \tag{2.35}$$

Where $E_{\mathrm{DFT}}[s]$ is the energy of structure s obtained with DFT and $w[s]$ is a weight factor assigned to each structure to make sure that ground-state structures have higher weight than metastable ones,

$$w[s] = \frac{1}{1 + \omega \left(\frac{d[s]}{\langle d \rangle} \right)^2}, \tag{2.36}$$

where $d[s]$ is the energy difference between structure s and the ground state structure at the same composition (convex hull), $\langle d \rangle$ is the expectation value of $d[s]$ and ω is a scale factor.

2.4.2. Criteria for a good CE

The performance of a CE can be tested with some fitness criteria. Common fitness criteria are (a) the root mean square **fitting error** for known structural energies and (b) a measure of the "predictive ability"—the **leave-one-out cross validation** (LOOCV) score [43, 67–71],

$$\mathrm{LOOCV} = \sqrt{\frac{1}{N_s} \sum_{s=1}^{N_s} (E_{\mathrm{DFT}}[s] - E_{\mathrm{CE}}[s^*])^2}, \tag{2.37}$$

Where N_s is the number of structures, $E_{\mathrm{CE}}[s^*]$ is the predicted energy by a CE extracted from a least-squares fit based on the energy database excluding structure s.

By adding more ECIs in a CE the fitting error will always go down as a result of an increasing degree of freedom. The LOOCV predictive error, on the other hand, increases after arriving at a minimum (see Fig. 2.4). Similarly as for a polynomial fitting a more accurate fit is always achieved at the cost of the predictive ability.

2.4.3. Ground-state search: Towards an optimized CE

The structure inversion method makes it possible to effortlessly calculate both the predicted energies from one set of ECIs and ECIs from an *ab initio* energy database. The ground-state search can therefore be efficiently performed within a pre-defined "structure pool" (SP), i.e., a set of structures with restricted size and/or maximal length of the translation vectors. Since a "good" CE is generally judged by how accurately the convex hull is reproduced instead of all structures, the performance of the CE can therefore be improved by a ground-state-search procedure [43, 72]. The whole procedure (schematically shown in Fig. 2.5) can be described by the following steps:

1. Compute energies of a group of small supercell structures via *ab initio* DFT calculations since they are not computationally expensive. These energies can be regarded as the initial "energy pool" (EP).

2. Calculate the correlation functions for all possible structures within the SP.

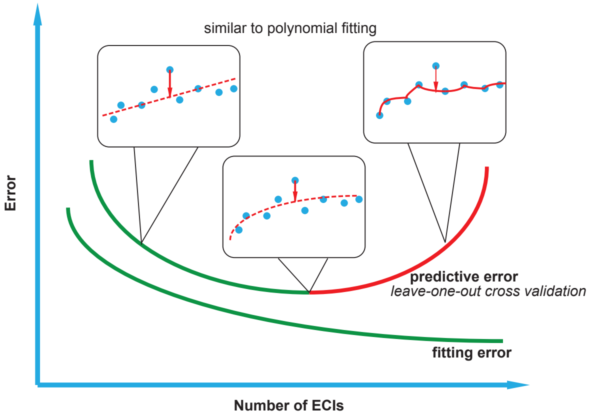

Figure 2.4: A comparison of the fitting error and the “LOOCV” predictive error. The fitting error decreases with an increasing number of ECIs (purely thick green line) while the “LOOCV” predictive error exhibits a parabolic behavior (line with the first half in green and the second half in red). The similarity of the predictive error and the polynomial fitting is also illustrated (insets) where either underfitting or overfitting gives relatively large error.

3. Obtain a CE from the current EP and use these ECIs to predict energies of all the possible structures in the SP. If ground state candidates with predicted total energies below the convex hull are found, these candidates should then be computed *ab initio*.
4. Update the EP by adding the newly-calculated *ab initio* energies and obtain an updated CE from the expanded EP.
5. Repeat the last two steps.

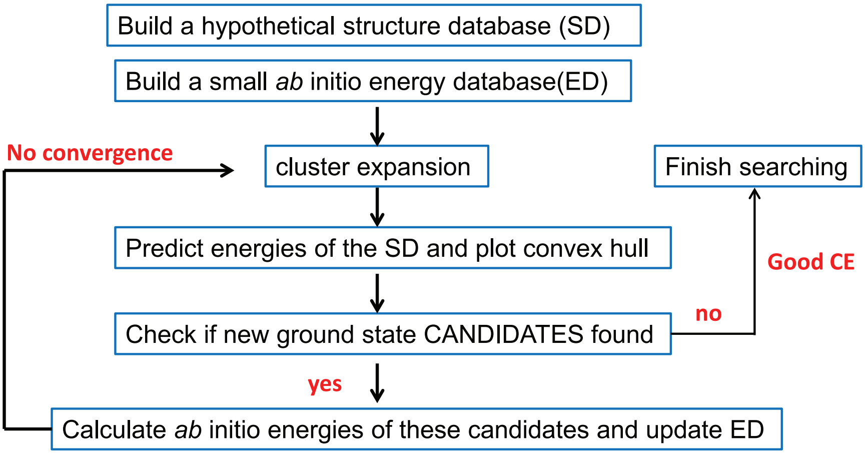

Figure 2.5: A flow chart for the ground-state search process using the CE.

Every iteration from step 3 to 5 can spontaneously increase the “volume” of the EP as well as the accuracy of the CE. As the performance of the CE gets improved new ground state structures become less likely to be found. Eventually the ground-state search converges when no more new ground-state structures are discovered and the LOOCV score is sufficiently small [73]. The criteria for the convergence may also be found by (1) checking the LOOCV score for structures which are not used for extracting the CE or by (2) repeating the algorithm with a different initial EP.

2.5. Monte Carlo simulation

Monte Carlo simulations (MC) provide efficient algorithms to evaluate properties which are sensitive to atomic configurations at finite temperatures, e.g., configurational energies, heat capacities, correlation functions etc. The MC with the residence time algorithm implemented, also called the kinetic Monte Carlo (kMC), enables one to keep track of the evolution kinetics. In the following sections the (kinetic) Monte Carlo theory and algorithms used in the present thesis will be discussed.

2.5.1. Partition function

The partition function of a system represents all the statistical information when the system reaches thermodynamic equilibrium,

$$Z = \sum_{\sigma} e^{-\beta E^{(\sigma)}}, \tag{2.38}$$

where $\beta = \frac{1}{k_B T}$ with k_B representing the Boltzmann's constant and T the temperature[1], $E^{(\sigma)}$ is the energy associated with configuration σ. The sum goes over all possible microstates that the system can visit [49, 74, 75]. If an energetic degeneracy exits, or say multiple microstates take the same energy $E^{(s)}$, the partition function is then,

$$Z = \sum_{s} g_s e^{-\beta E^{(s)}}, \tag{2.39}$$

where g_s is the density of states associated with energy $E^{(s)}$. The temperature independent density of states can be evaluated by the algorithm proposed by Wang and Landau. [76]. With the definition of the partition function it is evident that the probability of the occurrence of any particular microstate σ at thermodynamic equilibrium can be written as the Bolzmann distribution,

$$P^{(\sigma)} = \frac{e^{-\beta E^{(\sigma)}}}{Z}, \tag{2.40}$$

As a result it is required to obey the detailed-balance for sampling equilibrium properties in the MC algorithm, see also section 2.5.3.3.

2.5.2. Thermodynamic quantities

Since the partition function has been well defined its connection to a variety of thermodynamic quantities is straightforward, i.e.,

---

[1] Without specification, β in this thesis has the same meaning as here.

- **Free energy**

$$F = -\frac{1}{\beta}\text{ln}Z \tag{2.41}$$

All the other thermodynamic quantities can be derived from the free energy, i.e.,

- **internal energy**

$$U = \langle E\rangle = \frac{\partial(\beta F)}{\partial\beta} \tag{2.42}$$

- **Heat capacity**

$$\begin{aligned} C_v &= \frac{\partial U}{\partial T} \\ &= -\frac{\beta}{T}\frac{\partial U}{\partial\beta} \\ &= \frac{\beta}{T}\frac{\partial^2(\beta F)}{\partial\beta^2} \\ &= \frac{\beta}{T}\frac{\partial^2 lnZ}{\partial\beta^2} \\ &= \frac{\beta}{T}\frac{\partial}{\partial\beta}\Big(\frac{1}{Z}\frac{\partial Z}{\partial\beta}\Big) \\ &= \frac{\beta}{T}\Big[\frac{1}{Z}\frac{\partial^2 Z}{\partial\beta^2} - \frac{1}{Z^2}\Big(\frac{\partial Z}{\partial\beta}\Big)^2\Big] \\ &= \frac{\beta}{T}[\langle E^2\rangle - \langle E\rangle^2], \end{aligned} \tag{2.43}$$

For magnetic systems similar equations in terms of magnetization can be derived as,

- **Magnetic susceptibility**

$$\begin{aligned} \chi_v &= \frac{\partial\langle M\rangle}{\partial H} \\ &= \beta[\langle M^2\rangle - \langle M\rangle^2], \end{aligned} \tag{2.44}$$

Where M is the magnetization of the material and H is the magnetic field intensity.

- **Entropy**

It should be noticed that some thermodynamic quantities, e.g., the free energy and the entropy cannot be readily measured directly from Monte Carlo simulations. This is because they are not simply quantities that measure the average fluctuations of microstates but are dependent on the available size of the phase space [77, 78]. However, as one can obtain the internal energy U directly from the MC, the entropy can be derived from the integration of the heat capacity,

$$S(T) = S(T_0) + \int_{T_0}^{T}\frac{C_p}{\tau}d\tau, \tag{2.45}$$

Alternatively, one can also firstly compute the free energy from the integration of Eq. 2.42,

$$\beta F(\beta) = -S(\infty) + \int_0^\beta U d\beta', \tag{2.46}$$

Where $S(\infty)$ refers to the entropy at the high temperature limit with the value $-k_B[x\ln x + (1-x)\ln(1-x)]$ (x is the composition) for binary systems. Then the entropy can be obtained from the derivative of the free energy,

$$S = -\Big(\frac{\partial F}{\partial T}\Big)_v. \tag{2.47}$$

2.5.3. Markov chains

States $\sigma_1, \sigma_2, \sigma_3, ..., \sigma_n ...$ generated in the MC form a so-called **Markov chain**. One of the most important properties is that the newly-generated state is only dependent on the present state and has no relation to the previous states [49, 79], which is expressed as,

$$P(\sigma_{n+1}|\sigma_1, \sigma_2, \sigma_3, ..., \sigma_n) = P(\sigma_{n+1}|\sigma_n). \tag{2.48}$$

2.5.3.1. Transition matrix

For finite size systems with the total number of states N_m, an N_m-dimensional row vector **v** describing the probability distribution is defined so that entries of the vector sum up to unity. For any two states $i, j \in N_m$ there is a transition probability $p_{ij} = p(\sigma_i \to \sigma_j)$. It follows that transition probabilities among different states form an $N_m \times N_m$ **transition matrix P** with elements p_{ij}.

The transition matrix is a stochastic matrix that has the following important properties [79, 80]:

1. The value of each element is between 0 and 1.
2. The sum of the row elements should be unity, i.e. $\sum_j p_{ij} = 1$.
3. If $\mathbf{v}_0$ is assumed to be the initial probability distribution and **P** is the transition matrix of a time-homogeneous Markov chain (i.e., the transition matrix is always the same for each transition), the probability distribution after t steps will be $\mathbf{v}_0 \cdot \mathbf{P}^t$.

2.5.3.2. Equilibrium probability distribution

The transition matrix **P** of a Markov chain is *regular* and *ergodic* if all entries are definitely positive over time and any state can be visited from any other state within a finite amount of steps. There is a limiting probability distribution $\mathbf{v}_s$ called the equilibrium (or stationary) probability distribution which satisfies [81]

$$\mathbf{v}_s \cdot \mathbf{P} = \mathbf{v}_s, t \to \infty \tag{2.49}$$

The equilibrium probability distribution is also defined as

$$\mathbf{v}_s = \lim_{t\to\infty} \mathbf{v}_0 \cdot \mathbf{P}^t, \tag{2.50}$$

where $\mathbf{v}_0$ is an arbitrary initial probability distribution vector which implies that the stationary distribution is independent of the initial state. As t goes towards infinity the powers $\mathbf{P}^t$ approach a limiting matrix $\mathbf{P}_s$ whose column elements are of the same vector $\mathbf{v}_s$. Once the equilibrium state has been reached, the probability distribution becomes invariant in any number of steps,

$$\mathbf{v}_s \cdot \mathbf{P}_s^t = \mathbf{v}_s. \tag{2.51}$$

It immediately follows that, comparing Eq. 2.51 with 2.49,

$$\mathbf{P}_s^t = \mathbf{P}_s \tag{2.52}$$

which indicates an important property of the limiting matrix $\mathbf{P}_s$: it is an idempotent matrix which is always diagonalizable with eigenvalues either 0 or 1. From Eq. 2.49 it is also evident that the equilibrium probability distribution $\mathbf{v}_s$ is an eigenvector of the transition matrix associated with the eigenvalue 1.

2.5.3.3. Master equation and detailed balance

The flux of the probability density with respect to the time can be described by the **master equation**, which is given by [49, 79],

$$\frac{\partial p(\sigma_j, t)}{\partial t} = \sum_{\sigma_i} p_t(\sigma_i \to \sigma_j) p(\sigma_i, t) - \sum_{\sigma_i} p_t(\sigma_j \to \sigma_i) p(\sigma_j, t), \tag{2.53}$$

where $p_t(\sigma_i \to \sigma_j)$ is the transition probability from state σ_i to σ_j per unit time and $p(\sigma, t)$ is the probability that the system stays at σ at time t. Under the steady-state condition (not necessarily the equilibrium state) where there is no net probability transition flux the LHS of Eq. 2.53 should be zero

$$\sum_{\sigma_i} p_t(\sigma_i \to \sigma_j) p(\sigma_i, t) = \sum_{\sigma_i} p_t(\sigma_j \to \sigma_i) p(\sigma_j, t). \tag{2.54}$$

Eq. 2.54 is a description of the so-called **detailed balance**. As $t \to \infty$ detailed balance can also be written as

$$p_t(\sigma_i \to \sigma_j) p(\sigma_i, t = \infty) = p_t(\sigma_j \to \sigma_i) p(\sigma_j, t = \infty). \tag{2.55}$$

It is possible to use different transition probabilities in MC algorithms for either equilibrium properties or kinetics. When designing a Markov chain without the knowledge of the transition matrix one is required to satisfy the detailed balance described by Eq. 2.54 or 2.55 [82]. The imposed detailed balance guarantees that the system can be driven towards the equilibrium Boltzmann distribution (Eq. 2.40).

2.5.3.4. Convergence of Markov chains

If we assume that the transition matrix $\mathbf{P}$ is (a) diagonalizable and (b) its N_m eigenvalues satisfy $1 = |\lambda_1| \geq |\lambda_2| \geq ... \geq |\lambda_{N_m}|$, $\mathbf{P}$ can be then rewritten as

$$\mathbf{P} = \mathbf{V}\Lambda\mathbf{V}^{-1}, \tag{2.56}$$

where $\mathbf{V}$ is a matrix made up of N_m orthonormal column eigenvectors of $\mathbf{P}$, $\mathbf{v}_1$, $\mathbf{v}_2$, ..., $\mathbf{v}_{N_m}$(normalized with $||\mathbf{v}_i|| = 1$) and Λ is the diagonalized $\mathbf{P}$ with items λ_1, λ_2,..., λ_{N_m} on the diagonal. Therefore $\mathbf{v}_1$, $\mathbf{v}_2$,..., $\mathbf{v}_{N_m}$ can also be viewed as a basis into which state functions are expanded. Any arbitrary state $\mathbf{s}$ can be described as a linear combination of $\mathbf{v}_i(i = 1, 2, ..., N_m)$ with coefficients c_i:

$$\mathbf{s} = \sum_{i=1}^{N_m} c_i \mathbf{v}_i^T. \tag{2.57}$$

Eq. 2.50 is then applied as $t \to \infty$

$$\begin{aligned} \mathbf{s}_s &= \mathbf{s} \cdot \mathbf{P}^t \\ &= \mathbf{s}(\mathbf{V}\Lambda\mathbf{V}^{-1})(\mathbf{V}\Lambda\mathbf{V}^{-1})...(\mathbf{V}\Lambda\mathbf{V}^{-1}) \\ &= \mathbf{s}\mathbf{V}\Lambda^t\mathbf{V}^{-1} \\ &= \sum_{i=1}^{N_m}[c_i\mathbf{v}_i^T\mathbf{V}\Lambda^t\mathbf{V}^{-1}] \\ &= c_1\lambda_1^t\mathbf{v}_1^T + c_2\lambda_2^t\mathbf{v}_2^T + ... + c_{N_m}\lambda_{N_m}^t\mathbf{v}_{N_m}^T \\ &= \lambda_1^t\Big[c_1\mathbf{v}_1^T + c_2\Big(\frac{\lambda_2}{\lambda_1}\Big)^t\mathbf{v}_2^T + c_3\Big(\frac{\lambda_3}{\lambda_1}\Big)^t\mathbf{v}_3^T \\ &\quad +... + c_{N_m}\Big(\frac{\lambda_{N_m}}{\lambda_1}\Big)^t\mathbf{v}_{N_m}^T\Big]. \end{aligned} \tag{2.58}$$

Obviously, from Eq. 2.58, the equilibrium distribution $\mathbf{s}_s$ gradually converges to $c_1\mathbf{v}_1^T$ as $t \to \infty$ since each term $\frac{\lambda_i}{\lambda_1}$ is smaller than 1. Because $|\lambda_2| \geq |\lambda_3| \geq ... \geq |\lambda_{N_m}|$ the second largest eigenvalue λ_2 dominates the speed of the convergence [83, 84].

2.5.4. Conventional Monte Carlo simulations

In order to obtain the equilibrium distribution, as mentioned before, the detailed balance must be obeyed,

$$\frac{p_t(\sigma_i \to \sigma_j)}{p_t(\sigma_j \to \sigma_i)} = \frac{p(\sigma_j, t = \infty)}{p(\sigma_i, t = \infty)}. \tag{2.59}$$

The substitution of Eq. 2.40 into the above equation yields

$$\frac{p_t(\sigma_i \to \sigma_j)}{p_t(\sigma_j \to \sigma_i)} = e^{-\beta(E_{\sigma_j} - E_{\sigma_i})}, \tag{2.60}$$

where the unknown partition function Z cancels out and only the energy difference between two states needs to be computed. Transition probabilities that satisfy the detailed balance can be realized in various ways [85]. Two of them are of great popularity:

- **Glauber transition probability**

$$P_G = \frac{e^{-\beta\Delta E}}{1 + e^{-\beta\Delta E}} \tag{2.61}$$

where ΔE is the energy difference before and after a transition, e.g., a spin reversal or two spins exchange or an A atom "flips" to a B atom.

- **Metropolis transition probability**

$$P_M = \min\{1, e^{-\beta \Delta E}\} \tag{2.62}$$

which means if $\Delta E \leq 0$ the transition probability equals unity, otherwise the transition probability follows $e^{-\beta \Delta E}$.

The algorithm of the conventional MC can be summarized as following:

Conventional Monte Carlo algorithm

1. Choose an initial state, e.g., configurational random state.
2. Generate a new configuration, e.g., species "Q" at site i is replaced by "M" or species at i and j are swapped
3. Calculate the probability P for the transition.
4. Generate a random number $r \in$ [0,1).
5. If $r < P$, perform the transition, otherwise keep the current state.

It should be noticed that in step 3 either the Metropolis or the Glauber transition probability can give the correct dynamics. If the time evaluation is necessary, however, the Glauber dynamics is preferred since it is still possible to build the connection to the real time from the transition probability. One may speed up the search for the equilibrium state via the Metropolis transition probability at the cost of losing the track of the time. The Metropolis algorithm accelerates the convergence by accepting all the transitions that result in the energy decrease. Fig. 2.6 shows a comparision between these two transition probabilities at relatively high temperature.

2.5.5. Kinetic Monte Carlo simulations

2.5.5.1. The n-fold way algorithm

In some cases, e.g., at low temperatures or near critical temperatures, the probability of accepting a transition becomes quite low. Most of the attempt transitions are rejected and no transitions occur for many steps. This can also be seen from Fig. 2.6 where $\beta \Delta E$ is large. To overcome this inefficiency the kinetic Monte Carlo (kMC) method based on the n-fold way algorithm was proposed by ensuring that an event must occur at each time step. The time increment is calculated with the assumption that no transition occurs among successive steps (see Fig. 2.7) [86, 87]. The most important feature of the kMC method is the integration of the realistic transition rate that enables the investigation of the realistic kinetics.

To perform the kMC simulations, first of all, transition rates of all possible transitions are a priori required. For thermal activation processes transition rates are estimated by Eq. 2.30. In fcc alloys vacancy-assisted substitutional diffusion is realized by vacancies exchanging

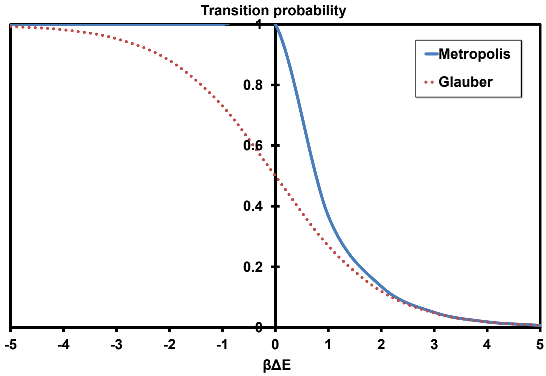

Figure 2.6: A comparison of the transition probability given by the Metropolis formula and the Glauber formula at high temperatures. It should be noticed that for transitions with the energy decreasing and with the energy slightly increasing the Metropolis dynamics (blue solid line) gives higher transition probability than the Glauber dynamics (red dotted line).

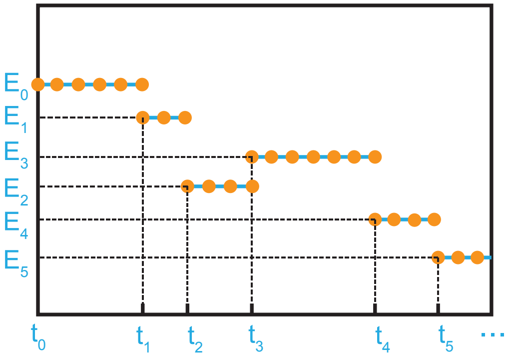

Figure 2.7: Schematic description of the (energy) state evolution in the kMC as a function of the time. The orange solid circles refer to transitions in the conventional MC. E_i and t_i ($i = 0$–5) exemplify the evolution of the energy state and the time in the kMC. Unlike the conventional MC, for each kMC time step (which is not necessarily equal), there must be a transition. The distance between orange solid circles shows one conventional MC step which is uniformly distributed.

their positions with one of 12 nearest neighbor atoms at a certain rate [see Fig. 2.8(a)]. Each nearest neighbor atom is not equiprobably chosen but biasedly selected in proportion to their swapping rates with the vacancy. The higher the swapping rate is the larger the probability for the transition to occur.

An illustration of the kMC algorithm is shown in Fig. 2.8(b) using a casino wheel. Transition rates $r_i (i = 1, 2, 3, ..., n)$ of n possible events are distributed along the circumference of the casino wheel. The size of the area associated with each rate indicates the relative magnitude of the transition probability. R_i are cumulative sums of rates from 1 to i, i.e., $R_2 = r_1 + r_2$; $R_n = \sum_{i=1}^{n} r_i$. Every attempt transition is similar to triggering the pointer of the wheel—the transition where the pointer stops will occur.

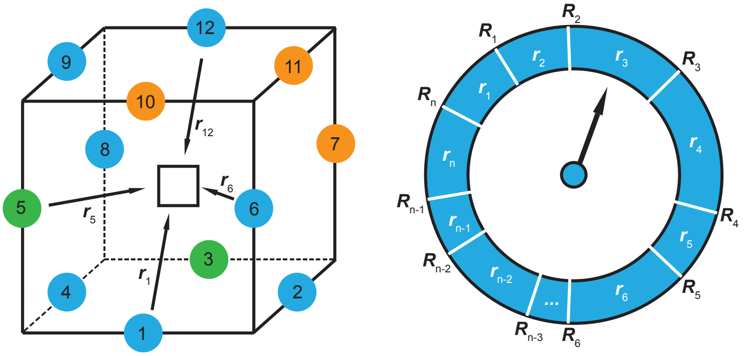

Figure 2.8: Schematic illustration of (a) the substitutional diffusion on the fcc lattice and (b) the kMC algorithm. Vacancy (atoms) represented as an open square (colored circles), the vacancy-atom exchange rate (the cumulative sum of rates) is referred by r_i (R_i). The casino wheel shown in (b) is divided by areas in different size, indicating the different probabilities associated with different transitions.

The algorithm of kMC simulations can be summarized as following:

The *n*-fold way algorithm

1. Make a list of all possible transition rates r_i of the system.
2. Calculate the cumulative sums $R_i = \sum_{i=1}^{i} r_i$ for $i = 1, 2, 3, ..., n$.
3. Generate a random number $x \in [0,1)$.
4. Perform the ith transition if $R_{i-1} \le R_n x < R_i$.
5. Update the time increment with $t = t + \Delta t$, where $\Delta t = \frac{1}{R_n}$.

2.5.5.2. Time increment: A Poisson process

The number of transitions occuring within a fixed time interval follows a *Poisson distribution* because each transition rate is independent of both the last transition and the time [82, 85, 87]. Therefore the probability that transition i occurs n times within Δt can be written as,

$$P_n(\Delta t) = \frac{(r_i \Delta t)^n}{n!} e^{-r_i \Delta t} \tag{2.63}$$

A group of independent Poisson processes forms an expanded Poisson process, which means the total number of the occurrence of transitions with different rates $r_1, r_2, r_3, ..., r_n$ within Δt follows also a Poisson distribution

$$P_N(\Delta t) = \frac{(R_n \Delta t)^N}{N!} e^{-R_n \Delta t}, \tag{2.64}$$

where $R_n = \sum_{i=1}^{n} r_i$. Therefore the time interval between two successive transitions can be obtained via assuming there are no transitions within Δt,

$$P_0(\Delta t) = e^{-R_n \Delta t} \tag{2.65}$$

Since it is a stochastic process, a random number $z \in [0, 1)$ is set to be equal to $P_0(\Delta t)$ before the time increment is extracted as

$$\Delta t = -\frac{lnz}{R_n}. \tag{2.66}$$

Alternatively with the property that $\langle \Delta t \rangle = \frac{1}{R_n}$ one may also update the time increment via $\Delta t = \frac{1}{R_n}$.

2.5.6. Efficiency improvement: Removing oscillations in the kMC

2.5.6.1. Origin of oscillations

The diffusion activation barrier E_{KRA} described in section 2.3.2 (see Fig. 2.2) is sensitive to the local atomic arrangement. Sometimes barriers between different swaps can differ significantly, leading to an exponential difference in swapping probability (see Eq. 2.30). It is therefore very likely that the barrier of one specific swap might be dramatically lower than all of the neighboring swapping barriers, see Fig. 5.4, e.g., the barrier between position p_2 and p_3. It follows that the vacancy may keep exchanging the position with the same neighboring atom for a long time until it escapes by chance. Such non-productive oscillations greatly reduce the efficiency of the simulation. It is firstly good to try to find a solution to the oscillation problem from a simplified four-state model in one dimension since the extension to fcc crystalline structures is trivial. The simplified four-state model is

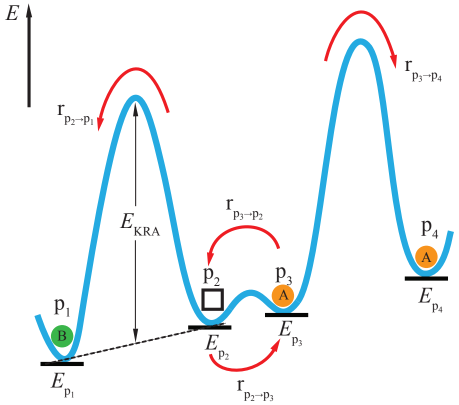

Figure 2.9: Schematic diagram of an energy landscape with low barriers between states 2 and 3. Black square represents a vacancy, species C, while orange and green solid circles refer to atomic species A and B.

schematically shown in Fig. 5.4 where the vacancy can jump only between four positions p_1, p_2, p_3 and p_4. At each time the vacancy is only allowed to move left or right by overcoming a certain barrier. The rates from state i to j, $r_{i \to j}$, are evaluated by Eq. 2.30. It is obvious that the barrier between p_2 and p_3 is much lower than the others, which means the vacancy oscillation will occur between p_2 and p_3. Once the vacancy escapes from the oscillation and arrives at either position p_1 or p_4 it is supposed that it has no chance to get back to position p_2 or p_3. In order to remove these oscillations it is crucial to find the answer to the following two questions: (a) the average time the vacancy gets involved in the oscillation and (b) the probability distribution after the vacancy escapes.

2.5.6.2. Average oscillation time

To evaluate the average oscillation time it is essential to examine the characteristic time the vacancy spends on each oscillation state. Therefore let us start from the transition matrix $\mathbf{M}$ for oscillation state p_2 and p_3,

$$\mathbf{M} = \begin{pmatrix} 1 - r_{p_2 \to p_1} - r_{p_1 \to p_3} & r_{p_3 \to p_2} \\ r_{p_2 \to p_3} & 1 - r_{p_3 \to p_2} - r_{p_3 \to p_4} \end{pmatrix} \tag{2.67}$$

where the entry m_{ij} in matrix $\mathbf{M}$ refers to the probability of the transition from state j to state i. If we define a 2×1 column vector $\mathbf{s}^{(t)}$ whose entry $s_i^{(t)}$ $(i = 1, 2)$ refers to the probability that the vacancy stays at position $p_{(i+1)}$ at time t, it then follows that

$$\mathbf{s}^{(t)} = \mathbf{M} \cdot \mathbf{s}^{(t-1)}. \tag{2.68}$$

Repeated substitutions of Eq. 2.68 yields

$$\mathbf{s}^{(t)} = \mathbf{M}^t \cdot \mathbf{s}^{(0)}. \tag{2.69}$$

Since the vacancy will anyhow arrive at either position p_1 or p_4 it is obvious that the (long time) limit of $\mathbf{M}^t$ is a zero matrix. The expected time that the vacancy stays at position p_i $(i = 2, 3)$ can be defined as,

$$t_{p_i} = \int_0^\infty s_{i-1}^{(t)} dt = \sum_{t=0}^{\infty} s_{i-1}^{(t)}, i = 2, 3 \tag{2.70}$$

If we assume that $\mathbf{s}^{(0)} = (1, 0)^T$ which means the vacancy initially stays at position p_2 it then follows that the sum in Eq. 2.70 can be written as,

$$t_{p_i} = \sum_{t=0}^{\infty} m_{(i-1)1}^{(t)}, i = 2, 3 \tag{2.71}$$

where $m^{(t)}$ is the corresponding entry in the $\mathbf{M}^t$ matrices. From Eq. 2.71 it is obvious that t_{p_i} can be obtained from the first entry of the $(i-1)$th row in matrix $\mathbf{N} = \mathbf{I} + \mathbf{M} + \mathbf{M}^2 + \mathbf{M}^3 + ... = (\mathbf{I} - \mathbf{M})^{-1}$. The average oscillation time is then obtained by summing over the residence time at positions p_2 and p_3.

2.5.6.3. Probability distribution after the oscillation

At each time t the probability that the vacancy jumps to position p_1 from p_2 is

$$P^{(t)} = s_1^{(t)} r_{p_2 \to p_1}. \tag{2.72}$$

The overall probability that the vacancy can finally escape to position p_1 should therefore be the sum of all contributions from each time step,

$$\mathbb{P} = \sum_{t=0}^{\infty} P^{(t)} = r_{p_2 \to p_1} t_{p_2}. \tag{2.73}$$

Similarly, the overall probability that the vacancy can finally arrive at position p_4 is $r_{p_3 \to p_4} t_{p_3}$.

2.5.7. Error analysis of the simulation data

In statistics, for a series of uncorrelated data $x_1, x_2, x_3, ..., x_n$, a good estimator of their deviation from the expectation value is the variance,

$$\sigma^2(x) = \langle x - \langle x \rangle \rangle^2 = \langle x^2 \rangle - \langle x \rangle^2 \tag{2.74}$$

where $\langle x \rangle$ is the expectation value of the data estimated as,

$$\langle x \rangle = \frac{1}{n} \sum_{i=1}^{n} x_i. \tag{2.75}$$

The variance of $\langle x \rangle$ can be estimated by

$$\sigma^2(\langle x \rangle) = \frac{1}{n} \sigma^2(x). \tag{2.76}$$

However, this is not the case for the correlated data generated from a Markov chain [88, 89]. Larger error may occur if less independent data are collected.

Suppose we collect n measurements of a thermodynamic quantity, say energy, E_1, E_2, E_3,...,E_n and let the expectation value $\langle E \rangle$ be an estimate of the desired energy of the system. How accurately does the $\langle E \rangle$ represent the real energy value of the system is typically estimated by the variance given by [90],

$$\sigma^2(\langle E \rangle) = \frac{1}{n} \sum_{i=1}^{n} \sum_{j=1}^{n} C_{ij} \tag{2.77}$$

where C_{ij} is the covariance between E_i and E_j defined as,

$$C_{ij} = \langle E_i E_j \rangle - \langle E_i \rangle^2 \tag{2.78}$$

If we define $d = |i - j|$ as the distance between two data points, C_{ij} can also be viewed as a correlation function which depends on the correlation distance d, especially when the system has reached thermodynamic equilibrium:

$$\begin{aligned} C(d) &= \langle E_0 E_d\rangle - \langle E\rangle^2 \\ &= \Big(\frac{1}{n-d}\sum_{i=1}^{n-d} E_i E_{i+d}\Big) - \langle E\rangle^2 \end{aligned} \tag{2.79}$$

The asymptotic behavior of the normalized correlation function $c(d)$ as $d \to \infty$ is given by,

$$c(d) = \frac{C(d)}{C(0)} \sim (e^{-\frac{1}{\tau_e}})^d, \tag{2.80}$$

where τ_e is called the exponential correlation time. It is related to the second largest eigenvalue λ_2 in Eq. 2.58 by,

$$\lambda_2 = e^{-\frac{1}{\tau_e}} \tag{2.81}$$

The variance of $\langle E\rangle$, compared with Eq. 2.76, is then increased as a result of the correlation [91],

$$\begin{aligned} \sigma^2(\langle E\rangle) &= \frac{\sigma^2(E)}{n}\tau_{\text{int}} \\ &= \frac{\sigma^2(E)}{n}\Big(\frac{1+\lambda_2}{1-\lambda_2}\Big) \end{aligned} \tag{2.82}$$

where

$$\begin{aligned} \tau_{\text{int}} &= 1 + 2\sum_{d=1}^{\infty} c(d) \\ &= \frac{1+\lambda_2}{1-\lambda_2} \end{aligned} \tag{2.83}$$

is called the integrated correlation time. From Eq. 2.82 it is apparent that $\sigma^2(\langle E\rangle)$ of the correlated data points is larger than that of the uncorrelated data by a factor of τ_{int}. Besides, the integrated correlation time has a limiting value of $2\tau_e$ at the large τ_e limit.

For a Gaussian distribution with expectation value $\langle E\rangle$ and variance $\sigma^2(\langle E\rangle)$ the probability p that the data are located within a confidence interval $[\langle E\rangle - \epsilon, \langle E\rangle + \epsilon]$ is given by

$$p = \text{erf}\Big(\frac{q}{\sqrt{2}}\Big), \tag{2.84}$$

where $\epsilon = q\sigma(\langle E\rangle)$. One can set $p = 0.99$ which means the certainty of the error bar is 99%. Then the error bar is estimated as

$$\epsilon = \sqrt{2}\sigma(\langle E\rangle)\text{erf}^{-1}(0.99) \tag{2.85}$$

with $\sigma(\langle E\rangle)$ calculated by Eq. 2.82.

2.6. Identification of precipitates

One of the most important analyses of the simulation results is the determination of the structure of precipitates. Firstly, it is straightforward to observe the structure in real space since positions of each atom are available. However, for most of the ordering or phase separating phenomena, it is necessary to examine the diffraction pattern in reciprocal space by Fourier analysis.

2.6.1. Bragg diffraction of the single species

Bragg diffractions reflect the long-range order in alloys whose diffraction pattern is characterized by Bragg peaks. The scattered intensity I_s is proportional to the structure factor S_G by

$$I_s \sim S_G S_G^* \tag{2.86}$$

where the "*" refers to the complex conjugate [92]. The structure factor S_G is defined as

$$S_G = \sum_j f_j \text{exp}(-i\mathbf{G} \cdot \mathbf{r}_j), \tag{2.87}$$

where f_j is an atomic property called the atomic form factor.

If the position of atom j in the real space $\mathbf{r}_j$ and the reciprocal vector $\mathbf{G}$ are described as

$$\mathbf{r}_j = x_j\mathbf{a}_1 + y_j\mathbf{a}_2 + z_j\mathbf{a}_3 \tag{2.88}$$

and

$$\mathbf{G} = h\mathbf{b}_1 + k\mathbf{b}_2 + l\mathbf{b}_3, \tag{2.89}$$

where $\mathbf{a}_1$, $\mathbf{a}_2$, $\mathbf{a}_3$ and $\mathbf{b}_1$, $\mathbf{b}_2$, $\mathbf{b}_3$ are primitive vectors in real and reciprocal space, then Eq. 2.87 becomes

$$\begin{aligned} S_G(hkl) &= \sum_j f_j \text{exp}[-i(x_j\mathbf{a}_1 + y_j\mathbf{a}_2 + z_j\mathbf{a}_3) \cdot (h\mathbf{b}_1 + k\mathbf{b}_2 + l\mathbf{b}_3)] \\ &= \sum_j f_j \text{exp}[-i2\pi(x_jh + y_jk + z_jl)]. \end{aligned} \tag{2.90}$$

Since the basis for fcc structures is (0,0,0), (1/2,1/2,0), (1/2,0,1/2) and (0,1/2,1/2) it is trivial to find that $S(hkl) = 4f$ if h, k, l are either all odd or all even number and $S(hkl) = 0$ if they are mixed (assuming pure fcc with the uniform atomic form factor f). It is apparent that the reciprocal diffraction pattern of an fcc structure is bcc [93].

In MC simulations it is trivial to separate the diffraction intensity of any single species. Such a possibility increases the chance to find more features that might not be easily observed in the experiment. Some superstructures with special periodicity can show obviously strong peaks among successive Bragg peaks.

2.6.2. Diffuse scattering pattern

A good measure of the short-range order (SRO) exhibited by precipitates is the diffuse scattering pattern. The scattering intensity for binary A-B fcc alloys is calculated as

$$I_{\text{SRO}} = I_f \sum_l \sum_m \sum_n \alpha_{lmn} \text{exp}(-i\mathbf{g} \cdot \mathbf{r}_{lmn}), \tag{2.91}$$

where $I_f = Nx_Ax_B(f_A - f_B)^2$ (x_i is the atomic concentration of species i, f_i the atomic form factor and N the number of atoms), $\mathbf{g} = h_1\mathbf{b}_1 + h_2\mathbf{b}_2 + h_3\mathbf{b}_3$ is a vector in the reciprocal lattice, $\mathbf{r}_{lmn} = l\mathbf{a}_1 + m\mathbf{a}_2 + n\mathbf{a}_3$ represents an interatomic vector with an arbitrary atom at the origin and position (l, m, n) as the end. Substitution of **g** and $\mathbf{r}_{lmn}$ in Eq. 2.91 yields

$$I_{\text{SRO}} = I_f \sum_l \sum_m \sum_n \alpha_{lmn} \cos 2\pi(h_1 l + h_2 m + h_3 n). \tag{2.92}$$

For cubic systems such as fcc, Eq. 2.92 can be further simplified via symmetry [94],

$$I_{\text{SRO}} = I_f \sum_l \sum_m \sum_n \alpha_{lmn} \cos(2\pi h_1 l) \cos(2\pi h_2 m) \cos(2\pi h_3 n). \tag{2.93}$$

The parameter α_{lmn} in Eq. 2.91 is called the Warren-Cowley SRO parameter [95, 96] which is defined as

$$\alpha_{lmn} = 1 - (P_{lmn}^{AB}/x_B) = (P_{lmn}^{BB} - x_B)/(1 - x_B) \tag{2.94}$$

where P_{lmn}^{AB} is the conditional probability that a B atom can be found at position (l, m, n) if an A atom is at the origin. The Warren-Cowley SRO parameter can also be determined experimentally from the diffuse scattering intensity measured from X-ray diffraction [97, 98].

References

[1] M. H. F. Sluiter, C. Colinet, and A. Pasturel, *Ab initio calculation of the phase stability in Au-Pd and Ag-Pt alloys,* Physical Review B **73**, 174204 (2006).

[2] M. H. F. Sluiter, Y. Kawazoe, P. Sharma, A. Inoue, A. R. Raju, C. Rout, and U. V. Waghmare, *First principles based design and experimental evidence for a ZnO-based ferromagnet at room temperature,* Physical Review Letters **94**, 187204 (2005).

[3] M. van Huis, J. Chen, H. Zandbergen, and M. Sluiter, *Phase stability and structural relations of nanometer-sized, matrix-embedded precipitate phases in Al-Mg-Si alloys in the late stages of evolution* , Acta Materialia **54**, 2945 (2006).

[4] V. Vaithyanathan, C. Wolverton, and L. Chen, *Multiscale modeling of θ' precipitation in Al-Cu binary alloys* , Acta Materialia **52**, 2973 (2004).

[5] J. Kohanoff and N. I. Gidopoulos, *Density functional theory: Basics, new trends and applications,* in *Handbook of Molecular Physics and Quantum Chemistry*, Vol. 2, edited by S. Wilson, P. F. Bernath, and R. McWeeny (WILEY-VCH Verlag, 2003) Chap. 26, pp. 532–568.

[6] P. Atkins and R. Friedman, *Molecular quantum mechanics,* (Oxford University Press, 2005) Chap. 9, p. 287, 4th ed.

[7] D. Sholl and J. Steckel, *Density functional theory: A practical introduction,* (Wiley, 2011) Chap. 1, pp. 7–16.

[8] I. Levine, *Quantum Chemistry*, 5th ed. (Prentice-Hall Of India Pvt. Limited, 2006).

[9] P. Atkins and R. Friedman, *Molecular quantum mechanics,* (Oxford University Press, 2005) Chap. 8, pp. 249–252, 4th ed.

[10] J. M. Ziman, *Electrons and phonons: the theory of transport phenomena in solids* (Clarendon, Oxford, 2001).

[11] D. McQuarrie and J. Simon, *Physical Chemistry: A Molecular Approach* (University Science Books, 1997).

[12] J. Hafner, *VASP Workshop Lectures: Ab-initio simulation in materials science*, Institut für Materialphysik and Center for Computational Material Science, Universität Wien, Sensengasse 8/12, A-1090 Wien, Austria (2003).

[13] P. Hohenberg and W. Kohn, *Inhomogeneous electron gas,* Physical review **136**, B864 (1964).

[14] W. Kohn and L. Sham, *Self-consistent equations including exchange and correlation effects,* Physical Review **140**, A1133 (1965).

[15] W. Kohn, *Nobel lecture: Electronic structure of matter—wave functions and density functionals,* Reviews of Modern Physics **71**, 1253 (1999).

[16] J. Hafner, *VASP Workshop Lectures: Foundations of Density-Functional Theory*, Institut für Materialphysik and Center for Computational Material Science, Universität Wien, Sensengasse 8/12, A-1090 Wien, Austria (2003).

[17] R. Hirschl, *VASP Workshop Lectures: DFT in depth—the exchange-correlation term*, Institut für Materialphysik and Center for Computational Material Science, Universität Wien, Sensengasse 8/12, A-1090 Wien, Austria (2003).

[18] G. Kresse, M. Marsman, and J. Furthmüller, *Vienna Ab-initio Simulation Package the guide*, Computational Materials Physics, Faculty of Physics, Universität Wien, Sensengasse 8/12, A-1090 Wien, Austria, 2014th ed. (2014).

[19] S. F. Sousa, P. A. Fernandes, and M. J. Ramos, *General performance of density functionals,* The Journal of Physical Chemistry A **111**, 10439 (2007).

[20] J. Hafner, *Ab-initio simulations of materials using vasp: Density-functional theory and beyond,* Journal of Computational Chemistry **29**, 2044 (2008).

[21] P. A. M. Dirac, *Note on exchange phenomena in the thomas atom,* Mathematical Proceedings of the Cambridge Philosophical Society **26**, 376 (1930).

[22] J. C. Slater, *A simplification of the hartree-fock method,* Physical Review **81**, 385 (1951).

[23] J. P. Perdew, *Unified theory of exchange and correlation beyond the local density approximation,* in *Electronic Structure of Solids '91*, Physical Research, Vol. 17, edited by P. Ziesche and H. Eschrig (Akademie Verlag, Berlin, 1991) pp. 11–20.

[24] J. Perdew, K. Burke, and M. Ernzerhof, *Generalized gradient approximation made simple,* Physical Review Letters **77**, 3865 (1996).

[25] J. P. Perdew, K. Burke, and M. Ernzerhof, *Generalized gradient approximation made simple,* Physical Review Letters **78**, 1396 (1997).

[26] R. Armiento and A. E. Mattsson, *Functional designed to include surface effects in self-consistent density functional theory,* Physical Review B **72**, 085108 (2005).

[27] J. P. Perdew, A. Ruzsinszky, G. I. Csonka, O. A. Vydrov, G. E. Scuseria, L. A. Constantin, X. Zhou, and K. Burke, *Restoring the density-gradient expansion for exchange in solids and surfaces,* Physical Review Letters **100**, 136406 (2008).

[28] A. J. Cohen and N. C. Handy, *Assessment of exchange correlation functionals,* Chemical Physics Letters **316**, 160 (2000).

[29] C. Lee, W. Yang, and R. G. Parr, *Development of the colle-salvetti correlation-energy formula into a functional of the electron density,* Physical Review B **37**, 785 (1988).

[30] A. D. Becke, *Density-functional thermochemistry. iv. a new dynamical correlation functional and implications for exact-exchange mixing,* The Journal of Chemical Physics **104**, 1040 (1996).

[31] A. J. Cohen, P. Mori-Sánchez, and W. Yang, *Insights into current limitations of density functional theory,* Science **321**, 792 (2008).

[32] T. Lee and C. Yang, *Statistical theory of equations of state and phase transitions. II. Lattice gas and Ising model,* Physical Review **87**, 410 (1952).

[33] J.-F. Gouyet, M. Plapp, W. Dieterich, and P. Maass, *Description of far-from-equilibrium processes by mean-field lattice gas model,* Advances in Physics **52**, 523 (2003).

[34] L. Kadanoff, *More is the same; phase transitions and mean field theories,* Journal of Statistical Physics **137**, 777 (2009).

[35] D. de Fontaine, *Cluster variation and cluster statics,* in *Theory and Applications of the Cluster Variation and Path Probability Methods*, edited by J. Morán-López and J. Sanchez (Springer US, 1996) pp. 125–144.

[36] T. Hill, *The bragg-williams or mean-field approximation in steady-state systems,* in *Cooperativity Theory in Biochemistry*, Springer Series in Molecular and Cell Biology (Springer New York, 1985) pp. 429–455.

[37] M. Hillert, *Phase equilibria, phase diagrams and phase transformations: Their thermodynamic basis,* (Cambridge University Press, 2007) Chap. 22, pp. 476–478, 2nd ed.

[38] Y.-Y. Li, *Quasi-chemical method in the statistical theory of regular mixtures,* Physical Review **76**, 972 (1949).

[39] A. Sher, M. van Schilfgaarde, A.-B. Chen, and W. Chen, *Quasichemical approximation in binary alloys,* Physical Review B **36**, 4279 (1987).

[40] M. Hillert, *Phase Equilibria, Phase Diagrams and Phase Transformations: Their Thermodynamic Basis*, 2nd ed. (Cambridge University Press, 2007).

[41] R. Kikuchi, *A theory of cooperative phenomena,* Physical review **81**, 988 (1951).

[42] R. Kikuchi, *Problems in the foundation of the path probability method: Path probability function and entropy production,* in *Theory and Applications of the Cluster Variation and Path Probability Methods*, edited by J. Morán-López and J. Sanchez (Springer US, 1996) pp. 1–20.

[43] M. H. F. Sluiter and Y. Kawazoe, *Cluster expansion method for adsorption: Application to hydrogen chemisorption on graphene,* Physical Review B **68**, 085410 (2003).

[44] D. de Fontaine, *Cluster approach to order-disorder transformations in alloys,* in *Solid State Physics*, Vol. 47, edited by H. Ehrenreich and D. Turnbull (Academic Press, 1994) pp. 33–176.

[45] J. Sanchez, F. Ducastelle, and D. Gratias, *Generalized cluster description of multicomponent systems,* Physica A: Statistical Mechanics and its Applications **128**, 334 (1984).

[46] J. M. Sanchez and D. de Fontaine, *The fcc Ising model in the cluster variation approximation,* Physical Review B **17**, 2926 (1978).

[47] G. Ceder, *A derivation of the Ising model for the computation of phase diagrams,* Computational Materials Science **1**, 144 (1993).

[48] A. Gonis, P. Singh, P. Turchi, and X. G. Zhang, *Use of the Ising model in the study of substitutional alloys,* Physical Review B **51**, 2122 (1995).

[49] D. Landau and K. Binder, *A Guide to Monte Carlo Simulations in Statistical Physics,* (Cambridge University Press, 2009) Chap. 2, pp. 7–46, 3rd ed.

[50] A. Bortz, M. Kalos, and J. Lebowitz, *A new algorithm for Monte Carlo simulation of Ising spin systems,* Journal of Computational Physics **17**, 10 (1975).

[51] M. Glicksman, *Diffusion in solids: Field theory, solid-state principles, and applications,* (Wiley, 1999) Chap. 13, pp. 213–233.

[52] D. A. Porter, K. E. Easterling, and M. Y. Sherif, *Phase transformations in metals and alloys,* (CRC press, 2009) Chap. 2, pp. 65–111, 3rd ed.

[53] H. Mehrer, *Diffusion mechanisms,* in *Diffusion in Solids*, Springer Series in Solid-State Sciences, Vol. 155 (Springer Berlin Heidelberg, 2007) pp. 95–104.

[54] Y. Mishin, *Atomistic computer simulation of diffusion,* in *Diffusion Processes in Advanced Technological Materials*, edited by D. Gupta (Springer Berlin Heidelberg, 2005) pp. 113–171.

[55] H. Eyring, *The activated complex in chemical reactions,* The Journal of Chemical Physics **3**, 107 (1935), http://dx.doi.org/10.1063/1.1749604 .

[56] A. F. Voter, *Introduction to the Kinetic Monte Carlo Method,* in *Radiation Effects in Solids*, NATO Science Series, Vol. 235, edited by K. Sickafus, E. Kotomin, and B. Uberuaga (Springer Netherlands, 2007) pp. 1–23.

[57] J. Koettgen, T. Zacherle, S. Grieshammer, and M. Martin, *Ab initio calculation of the attempt frequency of oxygen diffusion in pure and samarium doped ceria,* Phys. Chem. Chem. Phys. **19**, 9957 (2017).

[58] G. H. Vineyard, *Frequency factors and isotope effects in solid state rate processes,* Journal of Physics and Chemistry of Solids **3**, 121 (1957).

[59] C. D. Versteylen, N. H. van Dijk, and M. H. F. Sluiter, *First-principles analysis of solute diffusion in dilute bcc fe-X alloys,* Phys. Rev. B **96**, 094105 (2017).

[60] A. Van der Ven, G. Ceder, M. Asta, and P. Tepesch, *First-principles theory of ionic diffusion with nondilute carriers,* Physical Review B **64**, 184307 (2001).

[61] A. Van der Ven and G. Ceder, *Vacancies in ordered and disordered binary alloys treated with the cluster expansion,* Physical Review B **71**, 054102 (2005).

[62] H. Jónsson, G. Mills, and K. W. Jacobsen, *Nudged elastic band method for finding minimum energy paths of transitions,* in *Classical and Quantum Dynamics in Condensed Phase Simulations*, edited by B. J. Berne, G. Ciccotti, and D. F. Coker (World Scientific, 1998) pp. 385–404.

[63] G. Henkelman and H. Jónsson, *A dimer method for finding saddle points on high dimensional potential surfaces using only first derivatives,* The Journal of Chemical Physics **111**, 7010 (1999).

[64] G. Henkelman, B. P. Uberuaga, and H. Jónsson, *A climbing image nudged elastic band method for finding saddle points and minimum energy paths,* The Journal of Chemical Physics **113**, 9901 (2000).

[65] G. Henkelman and H. Jónsson, *Improved tangent estimate in the nudged elastic band method for finding minimum energy paths and saddle points,* The Journal of Chemical Physics **113**, 9978 (2000).

[66] J. Connolly and A. Williams, *Density-functional theory applied to phase transformations in transition-metal alloys,* Physical Review B **27**, 5169 (1983).

[67] K. Govaerts, M. H. F. Sluiter, B. Partoens, and D. Lamoen, *Homologous series of layered structures in binary and ternary Bi-Sb-Te-Se systems: Ab initio study,* Physical Review B **89**, 054106 (2014).

[68] K. Baumann, *Cross-validation as the objective function for variable-selection techniques,* Trends in Analytical Chemistry **22**, 395 (2003).

[69] N. Zarkevich and D. Johnson, *Reliable First-Principles Alloy Thermodynamics via Truncated Cluster Expansions,* Physical Review Letters **92**, 255702 (2004).

[70] Y. S. Meng and M. E. Arroyo-de Dompablo, *First principles computational materials design for energy storage materials in lithium ion batteries,* Energy & Environmental Science **2**, 589 (2009).

[71] J. M. Sanchez, *Cluster expansion and the configurational theory of alloys,* Physical Review B **81**, 224202 (2010).

[72] A. Díaz-Ortiz, H. Dosch, and R. Drautz, *Cluster expansions in multicomponent systems: precise expansions from noisy databases.* Journal of physics: Condensed matter **19**, 406206 (2007).

[73] G. L. W. Hart, V. Blum, M. J. Walorski, and A. Zunger, *Evolutionary approach for determining first-principles hamiltonians.* Nature materials **4**, 391 (2005).

[74] J. Amar, *The Monte Carlo method in science and engineering,* Computing in Science & Engineering **8**, 9 (2006).

[75] Y. N. Kaznessis, *Statistical thermodynamics and stochastic kinetics: An introduction for engineers,* (Cambridge University Press, 2011) Chap. 4, pp. 66–90.

[76] F. Wang and D. P. Landau, *Determining the density of states for classical statistical models,* Physical Review E **64**, 056101 (2001).

[77] D. Frenkel and B. Smit, *Understanding molecular simulation: From algorithms to applications,* (Elsevier Science, 2001) Chap. 7, pp. 167–200, 2nd ed.

[78] D. Landau and K. Binder, *A Guide to Monte Carlo Simulations in Statistical Physics,* (Cambridge University Press, 2009) Chap. 5, pp. 174–176, 3rd ed.

[79] Y. N. Kaznessis, *Statistical thermodynamics and stochastic kinetics: An introduction for engineers,* (Cambridge University Press, 2011) Chap. 15, pp. 255–272.

[80] C. M. Grinstead and J. L. Snell, *Introduction to probability,* (American Mathematical Society, 2012) Chap. 11, pp. 405–470.

[81] J. Norris, *Markov Chains*, Cambridge Series in Statistical and Probabilistic Mathematics (Cambridge University Press, 1998).

[82] D. Johnson, *Kinetic Monte Carlo: Bare Bones and a Little Flesh*, Tech. Rep. (Computational Materials Science Summer School, UIUC Materials Computation Center, 2001).

[83] F. Schmitt, F. Schmitt, F. Rothlauf, and F. Rothlauf, *On the Importance of the Second Largest Eigenvalue on the Convergence Rate of Genetic Algorithms*, Tech. Rep. (Proceedings of the 14th Symposium on Reliable Distributed Systems, 2001).

[84] B. Franzke and B. Kosko, *Noise can speed convergence in Markov chains,* Physical Review E **84**, 041112 (2011).

[85] P. Kratzer, *Monte Carlo and Kinetic Monte Carlo Methods—A Tutorial,* in *Multiscale Simulation Methods in Molecular Sciences: Lecture Notes*, edited by J. Grotendorst, N. Attig, S. Blügel, and D. Marx (Jülich Supercomputing Centre, Jülich, 2009) pp. 51–76.

[86] D. Landau and K. Binder, *A Guide to Monte Carlo Simulations in Statistical Physics,* (Cambridge University Press, 2009) Chap. 5, pp. 146–148, 3rd ed.

[87] R. Y. Rubinstein and D. P. Kroese, *Simulation and the Monte Carlo Method*, Wiley Series in Probability and Statistics (Wiley, 2008).

[88] H. Flyvbjerg and H. G. Petersen, *Error estimates on averages of correlated data,* The Journal of Chemical Physics **91**, 461 (1989).

[89] M. Kikuchi, N. Ito, and Y. Okabe, *Statistical dependence analysis,* International Journal of Modern Physics C **07**, 379 (1996).

[90] B. A. Berg, *Markov Chain Monte Carlo Simulations and Their Statistical Analysis: With Web-based Fortran Code,* (World Scientific, 2004) Chap. 4, pp. 196–235.

[91] A. Van de Walle and M. Asta, *Self-driven lattice-model Monte Carlo simulations of alloy thermodynamic properties and phase diagrams,* Modelling and Simulation in Materials Science and Engineering **10**, 521 (2002).

[92] R. J. Naumann, *Introduction to the physics and chemistry of materials,* (CRC press, 2008) Chap. 6, pp. 121–139.

[93] C. Kittel, *Introduction to solid state physics,* (Wiley, 1987) Chap. 2, pp. 23–45, 8th ed.

[94] L. H. Schwartz and J. B. Cohen, *Diffraction from materials,* (Springer-Verlag, 1987) Chap. 7, pp. 402–406, 2nd ed.

[95] F. Ducastelle, *Order and phase stability in alloys,* (North Holland, 1991) Chap. 1, pp. 1–45.

[96] W. Schweika, *Disordered Alloys: Diffuse Scattering and Monte Carlo Simulations*, Springer Tracts in Modern Physics No. 141 (Springer, 1998).

[97] E. Matsubara and J. B. Cohen, *The GP zones in Al-Cu alloys—I,* Acta Metallurgica **33**, 1945 (1985).

[98] T. Hasegawa, K. Osaka, T. Takama, and H. Chen, *Short-range order structure and effective pair-interaction energy in Ni-Si alloys,* Acta Materialia **55**, 5382 (2007).

3

Cluster Expansions for Thermodynamics and Kinetics of Multicomponent Alloys

Cluster expansions have proven a very useful tool to model thermodynamics and kinetics of substitutional alloys in metallic, ionic, and even covalently bonded systems. Cluster expansions are usually obtained with the structure inversion method in which the energies, or other relevant property, of a set of structures are used to obtain expansion coefficients. The expansion coefficients are multipliers of correlation functions which pertain to clusters of sites on the parent lattice. There are significant practical issues associated with obtaining a cluster expansion, such as selecting which structures and especially which correlation functions are required for an adequate description of the energy. While these issues are significant for binary alloys, they become much more daunting when dealing with multicomponent alloys. Moreover, oftentimes interest is not limited to the energetics of the thermodynamic equilibrium state, but the evolution of quenched alloys with time is just as important. The treatment of diffusion within the context of cluster expansions is then another challenge. The article describes a formal method for utilizing cluster expansions for transition states as occur during vacancy mediated diffusion in substitutional alloys. The methods are illustrated with some applications to the prediction of initial coherent precipitates in Al-Cu and Al-Mg-Si alloys.

3.1. Introduction

Cluster expansions (CEs) have become a ubiquitous tool in computational alloy theory [1–21] and even in seemingly completely unrelated fields such and electronic band gap engineering and protein sequencing [22–25]. It is used to express thermodynamic and other properties as function of the configurational order of alloys. Most of the applications focus on binary alloys. However, the most interesting and the most realistic alloys are generally multi-component alloys. Although there are several CE studies on ternary alloys [26–32], usually a presupposed cluster, such as the irregular tetrahedron in the case of bcc lattices, is selected while ignoring convergence issues. On the other hand, more recent ab initio studies on multinary alloys are not so clear on the formal basis and the actual implementation of the CE [13, 33–36] so that a comprehensive derivation, such as given here, might be desirable. In particular, the generalized Ising model for binary alloys cannot be easily extended to multinary alloys [37]. The specific treatment in the literature of vacancy mediated diffusion in alloys [12, 38, 39] too, is scant and not very detailed on practical implementation. In the current work we try to present a comprehensive and detailed formalism that trivially extends to multi-component alloys. An important special feature is that CEs for multinary systems can be built-up from expansions with fewer components. We will first define a general framework for substitutional alloys, next describe how to add atomic species to a CE with re-use of already determined expansion coefficients. Then a generalization of the cluster expansion to treating the environmentally dependent energetics of transition states for vacancy mediated diffusion in concentrated alloys will be presented. Finally some applications to multi-components alloys are presented as illustrations.

3.2. Theory

3.2.1. cluster probabilities, sum rules, and correlation functions

Here, without loss of generality, we will assume that the expanded property is the energy E. The CE assumes that the energy can be written as a rapidly converging sum over cluster contributions where contributions from larger clusters become negligible. A practical example of this idea is common in organic chemistry where the formation enthalpy of a molecule can be expressed approximately as a sum of contributions from nearest neighbor pairs (read bonds) only. In the case of ethane one would count one C-C pair and six C-H pairs and estimate that the formation energy with respect to the isolated atoms is given as the sum of the single C-C bond energy and the six C-H bond energies. Contributions from larger clusters such as triplets usually provide minor corrections only. We will now return to the case of crystalline bulk alloys and limit ourselves to the case where every atom can be uniquely identified with one and only one atomic position. That is, the alloy becomes perfectly periodic with a relatively small unit cell when all atoms were to become indistinguishable. There is a well-defined “fixed” underlying grid of atomic sites. In such a case clusters can be uniquely identified without any ambiguity on how to classify any group of atomic sites. There would then never be any doubt whether a given pair is a 1st or a 2nd nearest neighbor pair. Another aspect of a “fixed” underlying grid is that the configuration of the alloy would be completely specified by the atomic occupation for every site, as in the case of e.g. the Ising model. In analogy with the Ising model we could assign the occupation of every site with a site occupation variable,

$$\sigma_i^{(P)} = \begin{cases} 1 & P \text{ atom at site } i \\ 0 & \text{no } P \text{ atom at site } i \end{cases} \tag{3.1}$$

where P designates a particular atomic species, the parentheses remind us it does not refer to exponentiation [27, 40, 41]. To be completely general we will consider a vacancy also as an atomic species. If there are N atomic species in the alloy, only $N-1$ need to be specified because of a sum rule:

$$\sum_{P=1}^{N} \sigma_i^{(P)} = 1 \quad \forall i \tag{3.2}$$

It signifies that every site is occupied by one and only one atom. The occupation of an arbitrary pair cluster consisting of sites i and j with occupations P and Q can be described in terms of site occupation variables

$$\sigma_{ij}^{(PQ)} = \sigma_i^{(P)} \sigma_j^{(Q)} \tag{3.3}$$

Here again, sum rules apply for every individual pair

$$\sum_{P=1}^{N} \sum_{Q=1}^{N} \sigma_{ij}^{(PQ)} = 1 \quad \forall ij \quad \text{and} \quad \sum_{P=1}^{N} \sigma_{ij}^{(PQ)} = \sigma_j^{(Q)} \tag{3.4}$$

Therefore, it is necessary to only specify the $N-1$ occupations of sites i and j and to only specify the pair occupations that contain exclusively the $N-1$ atomic species in order to fully determine the specific atomic occupancy of the ij pair cluster. It is not necessary to specify the occupation of a point or pair cluster that contains one or more atoms of type N. This generalizes to clusters of multiple sites: a three body cluster consisting of sites i, j, k with occupations P, Q, R can be described in terms site occupation variables

$$\sigma_{ijk}^{(PQR)} = \sigma_i^{(P)} \sigma_j^{(Q)} \sigma_k^{(R)}. \tag{3.5}$$

The value of any σ_{ijk}^{PQR} where an N type atom occurs follows from sum rules and occupations of contained points, contained pairs, and triangle involving $N-1$ species exclusively.

The specific occupation of any particular cluster is generally not of interest in an infinitely large crystal. Then, the cluster probabilities are much more informative. Cluster probabilities are averages over equivalent clusters, where equivalence derives from the symmetry of the underlying grid of atomic sites. Angle brackets are used to designate cluster probabilities. $< \sigma_{ij}^{PQ} >$ with sites i and j nearest neighbors, thus indicates the probability that any nearest neighbor pair in the infinite crystal is occupied by a PQ pair of atoms. Obviously, this probability shall always be in the interval [0,1]. The previously mentioned sum rules also apply to cluster probabilities so that probabilities exclusively pertaining to the $N-1$ atomic species only are needed for a full description of probabilities. In other words, the cluster probabilities pertaining to $N-1$ atomic species present a complete set of independent basis functions of the alloy configuration. Therefore, unlike the complete set of cluster probabilities involving all N atomic species, the subset of the cluster probabilities pertaining to the $N-1$ atomic species is a suitable basis for expanding properties that depend on the alloy configuration. This subset is a non-unique choice as a definition of correlation functions. Non-unique for several reasons; site occupations expressed as 0 or 1 instead of e.g. the Ising definition of +1 and -1; and because in our definition any one of the N atomic species can be declared redundant. In the following we proceed with the assumption that the Nth species has been declared redundant [42].

The correlation function expansion of the energy per atom can now be expressed as

$$E[s] = \sum_{\alpha} J_\alpha m_\alpha < \sigma_\alpha[s] > \tag{3.6}$$

$E[s]$ is the energy per atom of the structure s, α is the short-hand notation for the index of a particular correlation function $< \sigma_\alpha >=< \sigma_{ij...k}^{(PQ...R)} >$, J_α is the effective cluster interaction (ECI) pertaining to correlation α per occurrence, and m_α is the multiplicity, or the number of clusters α per atom. It is to be noted that considering crystal structures with interstitials may benefit from defining multiplicities and structural energies with reference to a lattice point of the disordered structure. However, here we shall avoid such complications and assume we are dealing with simple underlying lattices with just one atom per lattice point in the disordered state as for common fcc- and bcc-based alloys. Often, it is handier to combine m_α and J_α into one term, $\tilde{J}_\alpha = m_\alpha \, J_\alpha$, the ECI per atom.

In the case of a binary A-B alloy the probabilities of the pure A clusters only are required for an expansion of $E[s]$. So for every cluster there is one and only one correlation function. It is now apparent why the actually correct term “correlation function expansion” is usually replaced with the much more common “cluster expansion” as initially binary alloys only were considered.

Expansions based on cluster probabilities can be much more efficient than those based on the Ising convention—even in the case of binary alloys. When the majority type atom is considered as the redundant species, there will be very few clusters consisting of minority atoms only. In fact, in a large simulation cell, say for a Monte Carlo simulation, one can maintain a list of the minority atoms to count quickly how many of those pure minority atom clusters are present. In contrast, using the Ising definition, the particular sign of every instance of a cluster must be evaluated before the value of the corresponding correlation function is known. The more dilute an alloy, the greater the advantage of the current definition [42].

3.2.2. Inheritance of expansion coefficients

Another advantage of the current description is that it is quite trivial to build up an N component CE using, and retaining exactly, the CEs of $N-1$ subsystems comprised of $N-1$ components. In other words, when modeling a ternary alloy A-B-C one can reuse the ECIs of the A-C and B-C binaries. The reason for this is that the correlation functions as defined here form an independent basis. In the case of an A-B-C ternary it is quite simple to rationalize the preservation of ECIs from the A-C and B-C binaries:

$$\begin{aligned}
E[s] &= \sum_{\alpha} \tilde{J}_{\alpha} < \sigma_{\alpha}[s] > \\
&= \sum_{\alpha} \tilde{J}_{\alpha}^{(AB)} < \sigma_{\alpha}^{(AB)}[s] > \\
&= \sum_{\alpha,n\neq 0} \tilde{J}_{\alpha}^{(A_nB_0)} < \sigma_{\alpha}^{(A_nB_0)}[s] > + \sum_{\alpha,m\neq 0} \tilde{J}_{\alpha}^{(A_0B_m)} < \sigma_{\alpha}^{(A_0B_m)}[s] > \\
&\quad + \sum_{\alpha,n\neq 0\forall m\neq 0} \tilde{J}_{\alpha}^{(A_nB_m)} < \sigma_{\alpha}^{(A_nB_m)}[s] > \qquad (3.7)
\end{aligned}$$

The RHS contains three sums over correlation functions deriving from clusters α. The 1st of the three sums refers to correlation functions pertaining to A-C alloys only because there is no B present. Likewise the 2nd term refers to BC alloys only because there are zero A atoms. The last term only contains correlations that pertain to both A and B atoms. It follows that for a ternary alloy A-B-C the pure A ECIs can be copied from the AC binary and the pure B ECIs can be copied from the B-C binary provided that the C species is chosen as the redundant species. This can be formulated as:

$$\begin{aligned}
\tilde{J}_{\alpha A_n/AB(C)} &= \tilde{J}_{\alpha A_n/A(C)} \\
\tilde{J}_{\alpha B_n/AB(C)} &= \tilde{J}_{\alpha B_n/B(C)}, \qquad (3.8)
\end{aligned}$$

where the notation $\alpha PQ/AB(C)$ refers to the ECI of cluster type α(here pair only) with decoration PQ in the alloy A-B-C with the species C as eliminated species, and where the subscript n indicates that it is valid for all n-body pure A and pure B clusters. ECIs from the A-B binary are not as trivially preserved exactly. If the CE is limited to pair-wise terms only, i.e. clusters α contain two sites at most, it requires a minor algebraic operation only. The AB pair interactions of the A-B-C ternary can be obtained simply from $\tilde{J}_{\alpha AB/AB(C)} = \tilde{J}_{\alpha AA/A(C)} + \tilde{J}_{\alpha BB/B(C)} - \tilde{J}_{\alpha AA/A(B)}$. The reason that it is more complicated to derive a similar equation when the CE contains 3-site and larger clusters, is that the 3-site and larger cluster interactions of mixed AB type all contain energy terms that include all three species simultaneously. Of course, such energy terms cannot originate from a description of any binary. It follows that in the case of pair clusters, and it then does not matter up to which neighbor shell the pairs are considered, all three atomic species cannot be present in one cluster. By induction it then follows that for a quaternary alloy A-B-C-D with D as the eliminated species the A-B-C ternary ECIs can be exactly preserved provided that the ECIs are limited to clusters of 3 sites or fewer. For a penternary alloy A-B-C-D-E all subsystem quaternary CE coefficients can be preserved if no clusters larger than 4-sites are considered. Generally, ECIs pertaining to 4-site clusters are already quite small, and generally it is not necessary to go to 5-site or larger clusters. The implication is that CEs of many-component alloys are completed determined by their subsystems. Another important consequence is that once CEs for all quaternary systems are known, no new CEs need to be performed for penternary or higher component systems because the ECIs are already known from their quaternary subsystems. This is quite a remarkable conclusion given that generally it is believed that determining CEs for many component alloys is impossibly complicated due to the combinatorial explosion of possible combinations of correlation functions that such a CE entails.

It should also be pointed out that the inheritance of ECIs to higher order alloy systems is analogous to the extrapolation methods well-known to CALPHAD practitioners [43].

To fully take advantage of this inheritance of ECIs from subsystems, it is of course necessary that consistently the same set of underlying clusters is used for all the subsystems. Then a new question arises, one may determine the optimal set of clusters for a CE in some specific binary, but how can one find the optimal set of clusters for a large group of binaries?

3.2.3. Completeness

Another question that arises is how a change of basis, say for re-using the ECIs of the A-B-C-D quaternary in the A-B-C-D-E penternary, affects the selection of correlation functions to be used in the CE. This question has been addressed already earlier where it was concluded that a completeness criterion must be met [42]: When a certain cluster is included in the CE all its subclusters must be included as well [44, 45]. In multicomponent alloys this completeness criterion must be generalized for a CE to remain invariant under transformation of the occupation variable. For a multicomponent alloy the completeness criterion can be shown to require that if a certain correlation function is included in a CE, a) all correlations associated with that cluster must be included, and 2) all correlations associated with the subclusters must be included also. The multicomponent completeness criterion can be derived in a completely analogous way as was done for a binary [42].

3.2.4. Pools of correlation functions

In the following sections we will therefore focus on the issue of selecting the optimal set of clusters for a series of binaries. We will limit ourselves to fcc Al-based alloys. The set of cluster will be selected from a certain “pool”. This pool is defined by two criteria: a) only clusters with up to and including 4 sites are considered, and b) in such clusters no two sites shall be further apart than the 8th nearest neighbor. We designate this pool as N4R8. The justification of these criteria is as follows: the enthalpy of mixing is generally represented as a polynomial in the composition. The highest power in this polynomial is an indication of the number of sites in the largest cluster that significantly contributes to the alloy energy. E.g. a parabolic enthalpy of mixing, symmetric around equiatomic composition, indicates that only 2 body (i.e. pairwise) interactions are needed and three- four- and larger body interaction terms can be neglected. Extensive experience in fitting binary phase diagrams has shown that usually a sub-regular (i.e. a third order polynomial) or more rarely, a fourth order polynomial in the composition is completely adequate to represent the enthalpy of mixing accurately. Therefore, ECIs with 4 sites (N4) should generally be adequate. With the exception of long-period superstructures, such as in Cu-Pd, all experimentally observed fcc superstructures can be stabilized by pairwise interactions with ranges up to the 8th nearest neighbor (R8). The experimentally observed Al_3Zr phase(StructurBericht notation:$D0_{22}$) is stabilized by the 8th nearest neighbor ($<2\ 0\ 0>$ a_{fcc}, see Fig. 3.1). The N4R8 pool contains 1 point cluster, 8 pair clusters, 50 three body, and 427 four body clusters for a total of 486 clusters. In addition we must count the so-called empty cluster with zero sites. The “cluster interaction” corresponding to the empty cluster represents a constant off-set in the energy. Including this empty cluster there are 487 clusters in the N4R8 pool. The versatility of the N4R8 set of clusters is nicely illustrated by the accurate representation of the GP morphology. A particularly challenging issue for any CE without explicit treatment for long-ranged elastic interactions is the prediction of GP zone shapes [46]. In Al-Cu with about 2 a/o Cu, GP zones are known to form as pure Cu on 100 planes separated by 2 or 3 atomic planes of pure Al. Initially, it is believed that there are 3 intermediary Al planes, but absorption of vacancies and concomitant relaxation rapidly reduces this to 2 atomic Al layers [47–49]. Describing the Cu-Al-Al-Al sandwich morphology requires a highly optimized CE with a LOOCV of just 1 meV/atom, with about 200 fitted structural energies and 80 ECIs. see Fig. 3.2.

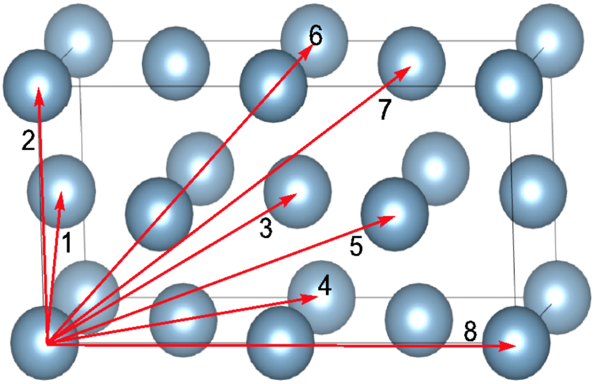

Figure 3.1: The 8 neighbor pairs included in the N4R8 cluster pool.

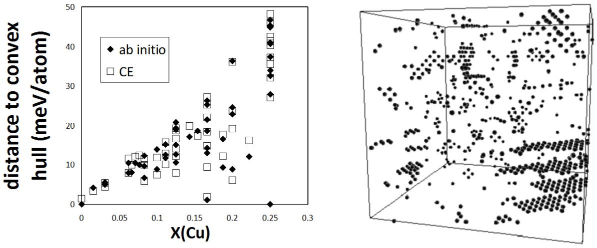

Figure 3.2: (left) Distance to the convex hull as function of the Cu atomic concentration in Al-rich Al-Cu alloys according to ab initio calculations and as obtained with a N4R8 CE using 80 ECIs and about 200 structural energies representing the whole Al-Cu composition range. The stability of the transitory GP zones consisting of single Cu (100) planes separated by 3 Al planes is readily apparent at X(Cu) =0.25. At right only Cu atoms are displayed in a box formed by 20 × 20 × 20 fcc cubes with 2 a/o Cu. In the kinetic Monte Carlo simulation using the CE the early stages of precipitation are simulated at 300 K. A GP zone can be recognized in the lower RHS of the box.

3.2.5. On the impossibility of finding the best expansion

Finding the best CE for a certain alloy, using a large set of structural energies, and using a pool of clusters with N members is a daunting task. The total number of combinations

$P(N)$ that can be generated by selecting arbitrarily a set of clusters with anywhere from 1 to N members can be calculated as follows:

$$P(N) = \frac{N!}{(N-1)!\,(1)!} + \frac{N!}{(N-2)!\,(2)!} + ... + \frac{N!}{(N-N)!\,(N)!} = \sum_{i=1}^{N} \left(\begin{array}{c} N \\ i \end{array} \right) = 2^N - 1 \tag{3.9}$$

The value of $P(N)$ is easily understood because each cluster either is included, or is not included, which gives 2^N, but we explicitly excluded the possibility of a completely empty combination so that one has to be subtracted. When $N = 487$ the value of P is approximately 4×10^{146}, and this is considering a single binary only! It is not feasible to evaluate all possible CEs and select the best performing one exactly. One has to settle for a "good" CE, rather than expect to find the "best" CE. How well a CE performs can be judged with some fitness criterion. Common fitness criteria are (a) the root mean square fitting error in for the known structural energies, sometimes modified by other criteria such as whether or not correct ground states are produced by the CE [50]; (b) a measure of "predictive ability" of a CE [5, 50, 51], such as the leave-one-out cross-validation score [44] or leave-many-out cross-validation score [14].

Several methods for finding "good" CE have been proposed. Various statistical methodologies have been discussed in e.g. Refs. [44, 52, 53] and [54]. Here we mention 4 methods.

- **"aufbau"**

  where a given CE is expanded with a single new cluster, one at a time [55]. All not yet included clusters are considered. Among the set of not yet included clusters the one that gives the best improvement in the fitness criterion is selected. Now, a new CE has been generated and the process is repeated. Repetitions stop either when the maximal number of clusters in the CE is reached, or when the fitness criterion improves too little, or deteriorates.

- **Singular value decomposition(SVD)** [56]

  When there are not precisely N structural energies available, the $< \sigma_\alpha[s] >$ matrix is not square and only a pseudo-inverse can be defined. Usually, the number of structural energies is less than N, so that there is an under-determined set of equations to be solved. Oftentimes the $< \sigma_\alpha[s] >$ matrix is ill-conditioned for various reasons which to some extent can be mitigated by adding very small random numbers. Generally, this methods works best when the set of equations is over-determined, i.e. when the number of structural energies is larger than N. This is in practice rarely the case. When this method succeeds in generating a CE it is optimal in the sense that it produces a small fitting error. The SVD method can be modified in order to better utilize insight in underlying physical properties, see Ref. [57].

- **Genetic algorithm** [16] A population of distinct CEs is allowed to "mate" (i.e. exchange expansion terms) and the resulting offspring is then culled on the basis of the fitness criterion. This procedure of is repeated for a number of generations, till the fitness criterion no longer improves.

- **Enumeration in combination with completeness and mandatory clusters** [55]

  Imposition of the completeness criterion drastically reduces the number of acceptable CEs. If furthermore it is imposed that certain clusters, such as the empty cluster, the single point and nearest neighbor pair clusters are always required in a valid CE the number of CEs can be reduced further. A complete CE is fully characterized by its maximal clusters only. When only CEs are considered with a limited number of maximal clusters their total number remains relatively small. In the case of binary fcc alloys with the N4R8 cluster pool and imposition of completeness and mandatory inclusion of the empty, point, nearest and next nearest pair clusters, and considering only CEs with 4 or fewer maximal clusters, there remain just 2,018,401,138 ($\approx 2 \times 10^9$) CEs only. While this number is still very large, it can be evaluated in a number of weeks to months on a single CPU core.

This 4th method is used below.

It should be remarked that enumeration with a limited number of maximal clusters biases CEs with completeness towards the clusters with larger numbers of sites. Larger clusters are favored because they contain several subclusters and thus yield a greater improvement in the "fitting criterion" than smaller clusters. With a handicap or weighting function this bias can be ameliorated to some extent.

To illustrate that a single set of clusters can yield acceptable CEs across a range of alloys, we considered all major alloying elements in Al-base alloys. Leave-one-out cross-validation scores (LOOCV) have been determined for CEs of 9 binary Al alloys, Al-Cu, Al-Fe, Al-Li, Al-Mg, Al-Mn, Al-Si, Al-Ti, Al-Zn, Al-Zr. The CEs are complete as discussed in section 3.2.3. The CEs are based on the N4R8 pool with up to 4 maximal clusters. For each binary a set of 100 *ab* initio computed structural energies was used for fitting. Enumeration gave 2,018,401,138 CEs for each binary. To find the optimal CE across all 9 binaries we computed the product of all 9 LOOCVs for a given set of maximal clusters. The resulting set of clusters is shown in Fig. 3.3. Including the empty cluster, the maximal clusters shown in figure 3 have 20 subclusters, thus there are 24 ECIs in our optimal CE for Al-alloys, Al-optimal for brevity. For a ternary alloys the number of ECIs in Al-optimal is 146 out of the more than 7000 that occur within the N4R8 pool for ternaries. Al-optimal gives small LOOCV values for binaries (Al-Mg: 1.3 meV/atom, Al-Si: 2.8 meV/atom) by design, but for the Al-Mg-Si ternary also, the LOOCV has a small value of just 2.2 meV/atom. Of course, as mentioned in section 3.2.2 the interactions of the Al-Mg and Al-Si binaries were inherited in describing the ternary. It should be remarked that with 100 structural energies per binary, while extracting only 24 ECIs, the CE is very overdetermined and as

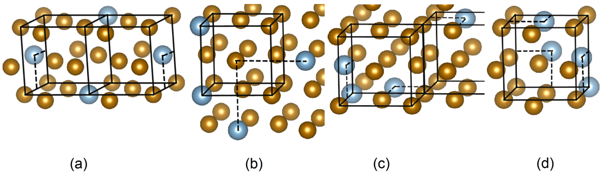

Figure 3.3: The 4 maximal clusters (blue spheres) that minimize the product of LOOCVs of 9 binary Al alloys. Fcc cubes and dashed lines have been added for clarity.

a consequence the LOOCV takes values that are very close to the root of the mean square error of the fit. In addition to using 100 structural energies for each of the three constituent binaries, an additional 100 structural energies pertaining to truly ternary compounds were used. The Al-Mg-Si CE was used to predict plausible initial coherent, i.e. fcc-based, stages of precipitation and resulting structures are displayed in Fig. 3.4.

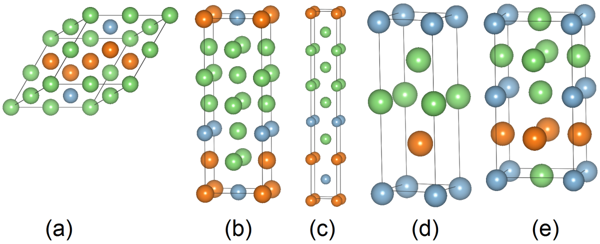

Figure 3.4: fcc-based superstructures predicted by the Al-optimal CE for Al-Mg-Si: (a) Al_4Mg_3Si, (b) $Al_8Mg_2Si_2$, (c) $Al_6Mg_2Si_2$, (d) Al_2MgSi, (e) $Al_4Mg_2Si_2$. Al: green spheres, Mg: orange spheres, and Si: blue spheres.

3.2.6. Cluster expansions for vacancy-mediated diffusion in substitutional alloys

When vacancies trade places with neighboring atoms in an alloy, a certain activation barrier must be overcome, see Fig. 3.5. When the vacancy is considered as an additional atomic species, it is apparent that the energies of state $1(E_1)$ and state $2(E_2)$ can be described by a multinary CE. However, for the activated state between states 1 and 2 problems arise. In the activated state the atom that trades places with the vacancy is no longer uniquely associated with a single lattice site. This is a problem because the cluster expansion is built upon the concept of there being a lattice gas where every site is associated with one, and only one, atomic species. A second problem is that the energy barrier is not purely a “state function” because the height of the barrier depends on the direction of the swap, the transition $1 \rightarrow 2$ has a different barrier than transition $1 \leftarrow 2$. This last problem is elegantly solved by van der Ven et al. by defining the kinetically resolved activation barrier [12], defined as

$$E_{KRA} = E_{tr} - \frac{1}{2}(E_1 + E_2) \tag{3.10}$$

Where E_{tr} is the highest energy along the lowest energy path connecting the states 1 and 2. When E_{KRA}, E_1 and E_2 are known it is trivial to extract the energy barriers for transitions $1 \rightarrow 2$ and $1 \leftarrow 2$.

The first problem, the lattice gas violation, can also be resolved by introducing a new atomic species for the vacancy-swapping atom pair, “swapping pair” for brevity, as displayed in Fig. 3.6. When a single vacancy is present only in an N-component alloy (here $N = 3$: orange species, blue species, and vacancy), replacing the swapping pair by two “atoms” of a new atomic species, results in $N - 1$ new N component systems. Thus the complexity of the problem is not significantly increased. When the value of E_{KRA} is computed in actual alloys, it is found to vary strongly with atomic occupancy right around

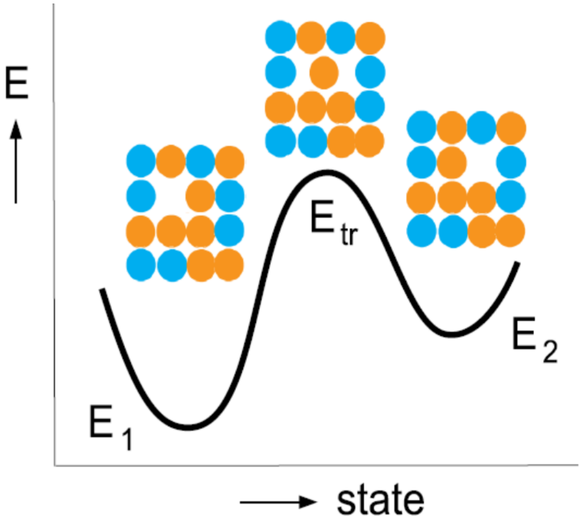

Figure 3.5: Schematic view of vacancy-mediated diffusion of substitutional atom. E1 (E2) is the energy in state 1(2), E_{tr} is the energy is the transition state. For movement from state 1 to 2 (2 to 1) an energy barrier $E_{tr} - E_1$ ($E_{tr} - E_2$) must be overcome.

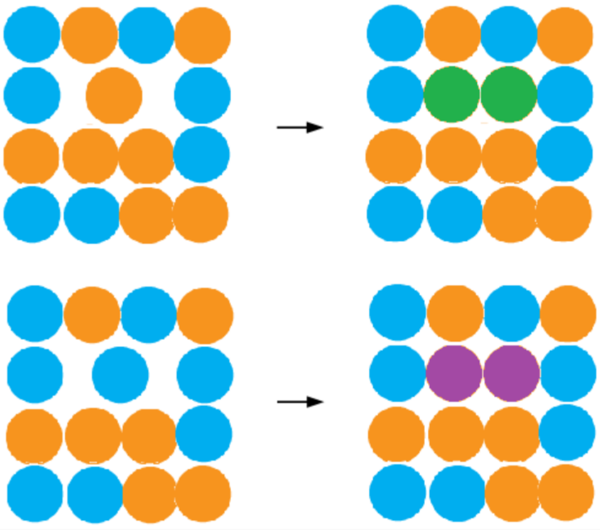

Figure 3.6: Transition states (left side) in a binary alloy with vacancies are mapped onto a lattice gas featuring two distinct ternaries (top: orange, blue, and an orange jumping atom represented as a green swapping pair; bottom: orange, blue and and an blue jumping atom represented as a purple swapping pair).

the swapping pair. In Al-Cu alloys the largest and smallest values might easily differ by a factor 3. To illustrate the significant local neighborhood dependence of the KRA energies, some Al-Cu supercells are shown with the corresponding values of E_{KRA} in Fig. 3.7.

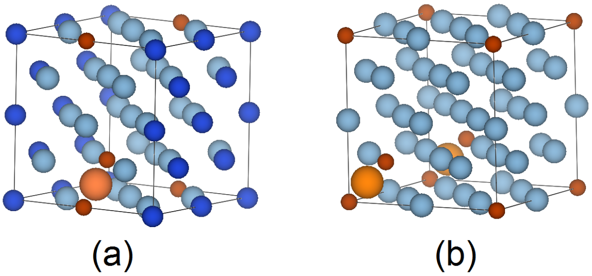

Figure 3.7: Supercells with transition states. Dark (light) blue spheres: Cu (Al), large orange sphere: Al in transition state, small brown spheres: half vacancy. The kinetically resolved activation barrier is (a) 0.22 eV in $Al_{23}Cu_8$Vac and (b) 0.65 eV in Al_{31}Vac.

As E_{KRA} is a strong function of the local environment, a local CE appears a sensible approach. A local CE should depend only on atomic occupancy right near the swapping pair and this expansion should not describe the average energetics of the alloy, which is already covered in the CE for states 1 and 2. This is easily achieved by selecting only correlation functions that encompass the swapping pair. We emphasize that the whole pair should be included because otherwise correlation functions may not be properly distinguished, as illustrated in Fig. 3.8. The reason for this is that the introduction of the swapping pair has eliminated many operations from the symmetry group of the underlying disordered crystal structure. Only operations that preserve the swapping pair can be retained. As the local CE retains only correlations that contain the swapping pair, it is apparent that such a local CE is NOT complete in a strict sense, because subclusters that contain only one or no sites of the swapping pair are excluded. Of course, one can retain the completeness property with regard to the local environment of the swapping pair. The local CE can be expressed as

$$E_{KRA} = \sum_{\alpha} \sigma_{\alpha\cup\beta}\, J_{\alpha\cup\beta} \tag{3.11}$$

Where α represents a cluster decoration corresponding to the empty cluster, or a point cluster, etc. but not part of the swapping pair, β represents the swapping pair, $\sigma_{\alpha\cup\beta}$ is a counter for the number of cluster decorations of type $\alpha \cup \beta$, and J is the corresponding ECI. $\sigma_{\alpha\cup\beta}$ has a maximum value $\mu_{\alpha\cup\beta}$ that is determined by its symmetry, e.g. for the decorations encircled by the blue oval in figure 4 it is 4(left side) and 2(right side).

3.2.7. Positive definite local cluster expansions

Another aspect of the E_{KRA} local CE is that it should generally yield positive values for all local neighborhoods. Unlike configurational energies which can be both positive and negative, here only positive energies are desired. In the local CE occurrences of cluster decorations are counted. As these occurrences can be counted using positive numbers only, it is tempting to assume that a strictly positive expansion can be obtained by requiring all ECI non-negative. However, this is a severe restriction that makes it generally too difficult to obtain a good CE. A less severe restriction can be designed. For α is empty a positive interaction J_β must exist. The sum of all negative valued interactions, times their maximal

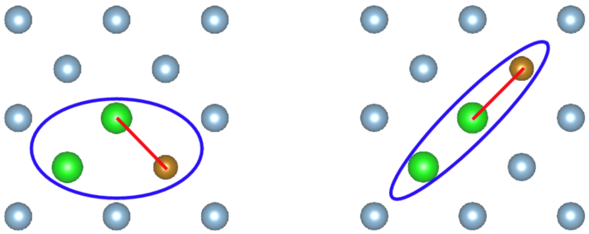

Figure 3.8: Green spheres indicate the swapping pair on a (100) plane in fcc. In the local CE, the pair (indicated by the red line) on the left and the pair on the right are not equivalent but are not properly distinguished when applying the symmetry of the underlying lattice gas. However, when the swapping pair is completely included, as in the clusters enclosed by the blue lines, the inequivalence is readily apparent.

multipliers $\mu_{\alpha\cup\beta}$, plus the J_β should thus be positive,

$$J_\beta + \frac{1}{2}\sum_{\alpha*} \mu_{\alpha\cup\beta}\left(J_{\alpha\cup\beta} - |J_{\alpha\cup\beta}|\right) > 0 \tag{3.12}$$

where α^* in the sum indicates that the empty cluster is excluded. This less restrictive condition is easily implemented in the aufbau and enumeration methods. The most effective method we have found however, is another method; Immediately screening every CE for a large number of pre-selected local environments and requiring that for all these test environments the E_{KRA} exceeds zero or some small positive value.

3.3. Conclusion

It has been shown that the definition of the correlation functions is a crucial aspect of cluster expansions. Particularly for multicomponent alloys, the current definition of the correlation functions allows inheritance, i.e. effective cluster interactions from constituent systems can be directly re-used. This assures that a good description of the alloy energetics in constituent systems is carried forth in more complex alloys. It also great facilitates determining cluster expansions in alloys with many components because it was shown that if N-body terms in a CE suffice for describing the energetics of an alloy, then alloys with N+1 components do not require any interactions beyond those present in the N+1 constituent systems with N components. As generally CEs with 4-body terms are capable of describing alloy energetics to within the meV/atom range, it follows that penternary alloys already, can be fully described using the energetics of the constituent quaternaries only. This observation is also an indication why there are so very few multicomponent superstructures in metallic alloys. Another aspect of the current formulation of correlation coefficients is the great efficiency in evaluating the energy in dilute binaries and multicomponent alloys generally. Efficient algorithms for determining CEs were presented. These methods were illustrated by determining a set of clusters that yields good CEs for multiple Al-based alloys. Finally, the peculiarities of strictly local CEs, e.g. for KRA energy barriers for vacancy mediated diffusion in substitutional alloys, were discussed. A method to impose that such local CEs yield only positive energy barriers was presented.

References

[1] J. Connolly and A. Williams, *Density-functional theory applied to phase transformations in transition-metal alloys,* Physical Review B **27**, 5169 (1983).

[2] J. Sanchez, F. Ducastelle, and D. Gratias, *Generalized cluster description of multicomponent systems,* Physica A: Statistical Mechanics and its Applications **128**, 334 (1984).

[3] A. A. Mbaye, L. G. Ferreira, and A. Zunger, *First-principles calculation of semiconductor-alloy phase diagrams,* Physical Review Letters **58**, 49 (1987).

[4] M. H. F. Sluiter, D. de Fontaine, X. Q. Guo, R. Podloucky, and A. J. Freeman, *First-principles calculation of phase equilibria in the aluminum lithium system,* Physical Review B **42**, 10460 (1990).

[5] Z. W. Lu, S.-H. Wei, A. Zunger, S. Frota-Pessoa, and L. G. Ferreira, *First-principles statistical mechanics of structural stability of intermetallic compounds,* Physical Review B **44**, 512 (1991).

[6] M. Asta, D. de Fontaine, M. van Schilfgaarde, M. Sluiter, and M. Methfessel, *First-principles phase-stability study of fcc alloys in the Ti-Al system,* Physical Review B **46**, 5055 (1992).

[7] D. de Fontaine, *Cluster Approach to Order-Disorder Transformations in Alloys ,* in *Solid State Physics*, Vol. 47, edited by H. Ehrenreich and D. Turnbull (Academic Press, 1994) p. 84.

[8] G. D. Garbulsky and G. Ceder, *Linear-programming method for obtaining effective cluster interactions in alloys from total-energy calculations: Application to the fcc Pd-V system,* Physical Review B **51**, 67 (1995).

[9] M. Asta, S. M. Foiles, and A. A. Quong, *First-principles calculations of bulk and interfacial thermodynamic properties for fcc-based Al-Sc alloys,* Phys. Rev. B **57**, 11265 (1998).

[10] A. Van der Ven, M. K. Aydinol, G. Ceder, G. Kresse, and J. Hafner, *First-principles investigation of phase stability in* Li_xCoO_2, Physical Review B **58**, 2975 (1998).

[11] D. Morgan, A. van de Walle, G. Ceder, J. D. Althoff, and D. de Fontaine, *Vibrational thermodynamics: coupling of chemical order and size effects,* Modelling and Simulation in Materials Science and Engineering **8**, 295 (2000).

[12] A. Van der Ven, G. Ceder, M. Asta, and P. Tepesch, *First-principles theory of ionic diffusion with nondilute carriers,* Physical Review B **64**, 184307 (2001).

[13] M. H. F. Sluiter and Y. Kawazoe, *Cluster expansion method for adsorption: Application to hydrogen chemisorption on graphene,* Physical Review B **68**, 085410 (2003).

[14] V. Blum and A. Zunger, *Structural complexity in binary bcc ground states: The case of bcc Mo-Ta,* Physical Review B **69**, 020103 (2004).

[15] R. Drautz and M. Fähnle, *Spin-cluster expansion: Parametrization of the general adiabatic magnetic energy surface with ab initio accuracy,* Physical Review B **69**, 104404 (2004).

[16] G. Hart, V. Blum, M. Walorski, and A. Zunger, *Ordering and segregation processes in transition metal alloys in relation to their electronic structures,* Nature materials **4**, 391 (2005).

[17] J. Z. Liu, A. van de Walle, G. Ghosh, and M. Asta, *Structure, energetics, and mechanical stability of Fe-Cu bcc alloys from first-principles calculations,* Physical Review B **72**, 144109 (2005).

[18] A. Díaz-Ortiz, H. Dosch, and R. Drautz, *Cluster expansions in multicomponent systems: precise expansions from noisy databases,* Journal of Physics: Condensed Matter **19**, 406206 (2007).

[19] G. Ghosh, A. van de Walle, and M. Asta, *First-principles calculations of the structural and thermodynamic properties of bcc, fcc and hcp solid solutions in the Al-TM (TM = Ti, Zr and Hf) systems: A comparison of cluster expansion and supercell methods,* Acta Materialia **56**, 3202 (2008).

[20] D. Lerch, O. Wieckhorst, G. L. W. Hart, R. W. Forcade, and S. Müller, *UNCLE: a code for constructing cluster expansions for arbitrary lattices with minimal user-input,* Modelling and Simulation in Materials Science and Engineering **17**, 055003 (2009).

[21] S. Curtarolo, W. Setyawan, G. L. Hart, M. Jahnatek, R. V. Chepulskii, R. H. Taylor, S. Wang, J. Xue, K. Yang, O. Levy, M. J. Mehl, H. T. Stokes, D. O. Demchenko, and D. Morgan, *AFLOW: An automatic framework for high-throughput materials discovery,* Computational Materials Science **58**, 218 (2012).

[22] R. Magri and A. Zunger, *Real-space description of semiconducting band gaps in substitutional systems,* Physical Review B **44**, 8672 (1991).

[23] F. Zhou, G. Grigoryan, S. R. Lustig, A. E. Keating, G. Ceder, and D. Morgan, *Coarse-graining protein energetics in sequence variables,* Physical Review Letters **95**, 148103 (2005).

[24] G. Grigoryan, F. Zhou, S. R. Lustig, G. Ceder, D. Morgan, and A. E. Keating, *Ultra-fast evaluation of protein energies directly from sequence,* PLoS Computational Biology **2**, e63 (2006).

[25] A. Kutana, E. S. Penev, and B. I. Yakobson, *Engineering electronic properties of layered transition-metal dichalcogenide compounds through alloying,* Nanoscale **6**, 5820 (2014).

[26] R. Kikuchi, *Ternary phase diagram calculations—i general theory,* Acta Metallurgica **25**, 195 (1977).

[27] M. H. F. Sluiter and Y. Kawazoe, *Site preference of ternary additions in* Ni_3Al*,* Physical Review B **51**, 4062 (1995).

[28] I. Ohnuma, C. Schön, R. Kainuma, G. Inden, and K. Ishida, *Ordering and phase separation in the b.c.c. phase of the Fe–Al–Ti system* , Acta Materialia **46**, 2083 (1998).

[29] V. Chaumat, F. Moret, and C. Colinet, *Study of phase equilibria in the Nb-Ti-Al system theoretical study: CVM calculation of the phase diagram of bcc Nb-Ti-Al,* Journal of Phase Equilibria **20**, 389 (1999).

[30] P. R. Alonso and G. H. Rubiolo, *Relative stability of bcc structures in ternary alloys with* $\mathrm{ti}_{50}\mathrm{al}_{25}\mathrm{mo}_{25}$ *composition,* Physical Review B **62**, 237 (2000).

[31] S. Bein, C. Colinet, and M. Durand-Charre, *CVM calculation of the ternary system Co–Cu–Fe* , Journal of Alloys and Compounds **313**, 133 (2000).

[32] C. Schön, *Order-disorder transformations and diffusion in ternary bcc alloys: The role of second-order boundaries,* Journal of Phase Equilibria **22**, 287 (2001).

[33] F. Lechermann, M. Fähnle, and J. Sanchez, *First-principles investigation of the Ni–Fe–Al system* , Intermetallics **13**, 1096 (2005).

[34] K. Yuge, *First-principles study of phase equilibria in Cu–Pt–Rh disordered alloys,* Journal of Physics: Condensed Matter **21**, 415401 (2009).

[35] T. Hoshino, N. Fujima, and M. Asato, *Ab initio study for magnetism in* Ni_2MnAl *full-Heusler alloy: A cluster expansion approach for total energy* , Journal of Alloys and Compounds **504, Supplement 1**, S534 (2010), 16th International Symposium on Metastable, Amorphous and Nanostructured Materials.

[36] J. S. Wróbel, D. Nguyen-Manh, M. Y. Lavrentiev, M. Muzyk, and S. L. Dudarev, *Phase stability of ternary fcc and bcc Fe-Cr-Ni alloys,* Physical Review B **91**, 024108 (2015).

[37] C. Wolverton and D. de Fontaine, *Cluster expansions of alloy energetics in ternary intermetallics,* Physical Review B **49**, 8627 (1994).

[38] A. Van der Ven and G. Ceder, *First principles calculation of the interdiffusion coefficient in binary alloys,* Physical Review Letters **94**, 045901 (2005).

[39] A. Van der Ven and G. Ceder, *Vacancies in ordered and disordered binary alloys treated with the cluster expansion,* Physical Review B **71**, 054102 (2005).

[40] F. Gautier, F. Ducastelle, and J. Giner, *Ordering and segregation processes in transition metal alloys in relation to their electronic structures,* Philosophical Magazine **31**, 1373 (1975).

[41] F. Ducastelle and F. Gautier, *Generalized perturbation theory in disordered transitional alloys: Applications to the calculation of ordering energies,* Journal of Physics F: Metal Physics **6**, 2039 (1976).

[42] M. H. F. Sluiter and Y. Kawazoe, *Invariance of truncated cluster expansions for first-principles alloy thermodynamics,* Physical Review B **71**, 212201 (2005).

[43] H. Lukas, S. G. Fries, and B. Sundman, *Computational Thermodynamics: The Calphad Method* (Cambridge University Press, 2007).

[44] A. Van de Walle and G. Ceder, *Automating first-principles phase diagram calculations,* Journal of Phase Equilibria **23**, 348 (2002).

[45] N. Zarkevich and D. Johnson, *Reliable First-Principles Alloy Thermodynamics via Truncated Cluster Expansions,* Physical Review Letters **92**, 255702 (2004).

[46] C. Wolverton, *First-principles prediction of equilibrium precipitate shapes in Al-Cu alloys,* Philosophical Magazine Letters **79**, 683 (1999).

[47] T. Sato and A. Kamio, *High resolution electron microscopy of phase decomposition microstructures in aluminium-based alloys,* Materials Science and Engineering: A **146**, 161 (1991).

[48] A. Bigot, F. Danoix, P. Auger, D. Blavette, and A. Menand, *3D reconstruction and analysis of GP zones in Al-1.7Cu (at%): a tomographic atom probe investigation,* Applied Surface Science **94–95**, 261 (1996), proceedings of the 42nd International Field Emission Symposium.

[49] M. STARINK and A. M ZAHRA, *Mechanisms of combined GP zone and θ' precipitation in an Al-Cu alloy,* Journal of Materials Science Letters **16**, 1613 (1997).

[50] M. Sluiter and P. E. A. Turchi, *Electronic theory of phase stability in substitutional alloys: The generalized perturbation method versus the Connolly-Williams method,* Physical Review B **40**, 11215 (1989).

[51] M. H. F. Sluiter, Y. Watanabe, D. d. Fontaine, and Y. Kawazoe, *First-principles calculation of the pressure dependence of phase equilibria in the Al-Li system,* Physical Review B **53**, 6137 (1996).

[52] R. Drautz and A. Díaz-Ortiz, *Obtaining cluster expansion coefficients in ab initio thermodynamics of multicomponent lattice-gas systems,* Physical Review B **73**, 224207 (2006).

[53] A. van de Walle, *Multicomponent multisublattice alloys, nonconfigurational entropy and other additions to the Alloy Theoretic Automated Toolkit ,* Calphad **33**, 266 (2009), tools for Computational Thermodynamics.

[54] A. van de Walle, *Methods for first-principles alloy thermodynamics,* JOM **65**, 1523 (2013).

[55] M. H. F. Sluiter, C. Colinet, and A. Pasturel, *Ab initio calculation of the phase stability in Au-Pd and Ag-Pt alloys,* Physical Review B **73**, 174204 (2006).

[56] M. H. F. Sluiter, K. Esfarjani, and Y. Kawazoe, *Site occupation reversal in the* $\mathrm{Fe}-\mathrm{Cr}\sigma$ *phase,* Physical Review Letters **75**, 3142 (1995).

[57] E. Cockayne and A. van de Walle, *Building effective models from sparse but precise data: Application to an alloy cluster expansion model,* Physical Review B **81**, 012104 (2010).

4

Ab initio prediction of vacancy properties in concentrated alloys: the case of fcc Cu-Ni

Vacancy properties in concentrated alloys continue to be of great interest because nowadays ab initio supercell simulations reach a scale where even defect properties in disordered alloys appear to be within reach. We show that vacancy properties cannot generally be extracted from supercell total energies in a consistent manner without a statistical model. Essential features of such a model are knowledge of the chemical potential and imposition of invariants. In the present work, we derive the simplest model that satisfies these requirements and we compare it with models in the literature. As illustration we compute ab initio vacancy properties of fcc Cu-Ni alloys as function of composition and temperature.

Ab initio density functional calculations were performed for SQS supercells at various compositions with and without vacancies. Various methods of extracting alloy vacancy properties were examined. A ternary cluster expansion yielded effective cluster interactions (ECIs) for the Cu-Ni-Vac system. Composition and temperature dependent alloy vacancy concentrations were obtained using statistical thermodynamics models with the ab initio ECIs. An Arrhenius analysis showed that the heat of vacancy formation was well represented by a linear function of temperature. The positive slope of the temperature dependence implies a negative configurational entropy contribution to the vacancy formation free energy in the alloy. These findings can be understood by considering local coordination effects.

4.1. Introduction

Nowadays, ab initio prediction of point defects and diffusivities in pure metals has become commonplace. Especially for self-diffusion and for impurity diffusion in dilute alloys generally good agreement has been found with experimental data [1–8]. For point defects in pure metals, generally excellent agreement with high temperature experimental data can be achieved provided that sufficient thermal excitation effects are included [9–11]. Point defects in alloys are more complicated than point defects in pure metals due to the multiple local environments. In so far alloys have been considered it is usually in the low-point defect concentration limit so that point defects can be assumed to be non-interacting. Within these limitations, point defect properties in ordered structures such as B2-AlNi [12–16], B2-FeAl [12, 17, 18], and L12-Ni3Al [19] have been theoretically studied. As described in Refs. [14, 19], special attention should be paid to the definition of the single defect formation energy for ordered alloys because it is non-trivial to define and compute supercell energy differences under the constraints of constant number of atoms and constant degree of order. Therefore, the common strategy to solve this problem is to minimize a grand canonical potential (i.e. fixed number of lattice sites and varying number of atomic species). In this approach chemical potentials are used as Lagrange multipliers to preserve composition. Oftentimes in energy considerations little thought is given then to the requirement of preservation of e.g. volume as atoms in the reservoir are exchanged with the supercell. Likewise other parameters are oftentimes not clearly defined with respect to what state variables are held fixed (pressure or volume; entropy or temperature, order parameter, or ordering energy). Nevertheless, this method has found widespread use when dealing with ordered structures.

In disordered crystalline materials, such as substitutional alloys, experimental information on vacancies and diffusivities is scarce (see e.g. ref. [20, 21]), and from the theoretical side also, there have been rather few studies that deal with specific alloy systems. Initially using empirical potentials [22–25], and later through ab initio approaches, both through supercell calculations [26–29] and ab initio based cluster expansions [30–33], it has been established that the local atomic environment around a vacancy plays a significant role. While the influence of vacancies on phase stability [30, 34] and kinetics [31–33] received some attention for Al-Ni [30], Sc-S [34], and Al-Li [31–33] alloys, the actual vacancy properties in specific alloys were mostly neglected with the exception of an empirical potential study of Cu-Ni alloys by Zhao et al. [24]. In the latter study [24] vacancies were studied with an embedded atom method (EAM) potential and structural relaxation, vibrational and configurational effects were included. This very comprehensive approach did not lead to a clear identification of how the structural, configurational and vibrational effects individually contributed to vacancy properties, and the complexity of the treatment did not allow one to extract rules of thumb that might be extrapolated to other alloy systems. On the other hand, there are various lattice gas models that treat vacancies through Bragg-Williams, or quasi-chemical approaches [14, 35–41] that are transparent enough to extract rules of thumb. But these studies suffer from a too simple representation of the energetics, such as including pairwise nearest neighbor interactions only, that are applicable to very few actual alloys. Vacancy properties in disordered alloys were investigated also by studying vacancies embedded in an effective medium, such as that defined by the coherent potential approximation (CPA). CPA implementations such as the self-consistent Green's function(LSGF) method [42] or exact muffin-tin orbital (EMTO) method [43], were shown to give composition dependent vacancy properties in alloys at T=0K. However, the CPA based methods consider the local vacancy environment only in an averaged way, and tend to neglect the temperature dependence of the local environment and oftentimes neglect local structural relaxations or limit relaxation to the nearest neighbor shell.

Therefore, in the current work we will consider structural relaxation and configurational effects realistically, and attempt to describe the alloy-vacancy system in a simple enough model so that vacancy properties emerge as function of a small number of intuitive parameters. As the vacancy concentration in disordered alloys is generally very low, we neglect intra-vacancy interactions and do not concern ourselves with vacancy clusters. In the following, we introduce a formalism to extract vacancy properties from supercell and cluster expansion approaches. We show how a simple cluster expansion can give rise to non-trivial vacancy properties in the alloy, such as negative configurational vacancy formation entropies and vacancy induced short range order. Finally, we give some general tendencies for vacancies in alloys based on phase separation and ordering tendencies in substitutional alloys.

4.2. Theory

We consider the problem of vacancy formation energies in disordered alloys, a problem that recently is receiving increased attention [27, 28, 31, 33]. We limit ourselves initially to configurationally random alloys, i.e. the reference state is the configurationally random state without vacancies. This is not only for simplicity, but also, because it uniformly applies to all substitutional alloys far enough above the transition temperature. The extension to alloys with short range order is briefly discussed later. To describe a defect formation energy, it is good to make a brief sojourn to the basic definition via the 1^{st} law of thermodynamics

$$\begin{aligned} \mathrm{d}E &= \sum Y \mathrm{d}X \\ &= TdS - PdV + \sum_i \mu_i \mathrm{d}N_i + \epsilon_{sro}\mathrm{d}\eta_{sro} + \Delta E_d \mathrm{d}N_d + \ldots, \end{aligned} \tag{4.1}$$

where Y represents intensive variables that are system size independent while X represents extensive variables that are proportional to system size. A matching pair of "Y and X" are usually referred to as conjugates. Subscript i refers to an atomic species, ϵ_{sro} is an effective interaction energy associated with short range order (SRO). η_{sro} is an extensive short range order parameter, which could simply be a combination of the number of like atom pairs and of unlike atom pairs, while ΔE_d is the energy and N_d is the number of a particular kind of defect. It then follows that the defect energy may be defined as

$$\Delta E_d = \frac{\mathrm{d}E}{\mathrm{d}N_d}|_{S,V,N_i,\eta_{sro},\ldots}, \tag{4.2}$$

where the interest lies in the parameters that are held constant, the "invariants". As we generally are more apt to work at constant pressure this equation can be conveniently rewritten in terms of the enthalpy. At finite temperatures eqn. 4.2 needs a modification because the configurational entropy is non-analytic in the low (defect) concentration limit. Then, the configurational entropy contribution due to the defect species under consideration must be explicitly excluded. In the case of substitutional point defects this gives

$$\Delta\widetilde{G}_d = \frac{\mathrm{d}\widetilde{G}}{\mathrm{d}N_d}|_{T,P,N_i,\eta_{sro},\ldots}, \tag{4.3}$$

where the excess Gibbs energy is defined in the usual way, namely by excluding the ideal mixing contribution.

$$\widetilde{G} = G - Nk_BT[x_d\ln(x_d) + (1-x_d)\ln(1-x_d)], \tag{4.4}$$

with N representing the total number of atomic positions, and $x_d = N_d/N$ being the fraction of atomic positions that is occupied by the point defects.

4.2.1. Problematic supercell calculations

In order to facilitate the link with ab initio supercell calculations, we consider how the defect formation enthalpy ΔH_d might be extracted from periodic supercell calculations by replacing a derivative with a finite difference. Moreover, the T=0 K case will be considered here which is typical for ab initio calculations. It should be emphasized that the result of this exercise is that vacancy properties in disordered, or less than perfectly ordered, alloys cannot be derived from supercell calculations alone. An additional statistical thermodynamic model is essential. At T=0 K the entropy contribution vanishes so that H takes the same value as the free energies G and $\widetilde{G}$.

$$\Delta H_d = \frac{\mathrm{d}H}{\mathrm{d}N_d}|_{T=0,P,N_i,\eta_{sro},\ldots} = [H_{sc+d} - H_{sc}]_{T=0,P,N_i,\eta_{sro},\ldots}. \tag{4.5}$$

Below, the invariants will be omitted for brevity. When the defect is a vacancy, the requirement of keeping the number of atoms constant means that an appropriate term for compensating the energy loss of the vacated atom must be included

$$\Delta H_{vac} = [H_{sc+vac} - H_{sc} + \mu], \tag{4.6}$$

where μ is the chemical potential of the vacated atom. For a pure metal μ is simply the energy of the supercell divided by the number of atoms in the supercell. However, in a disordered alloy, say with atomic species A and B, the μ term depends on the type of atom removed to make the vacancy. Moreover, μ_i is the chemical potential of atomic species i (i=A or B) in the alloy, which generally differs from μ_i in the pure element, as was erroneously assumed in eqn. 5 in ref. [27]. It is now apparent also why an enthalpy formulation is preferable over an energy formulation because maintaining equal pressure is much easier than maintaining equal volume in the supercell with vacancy plus that of the i-atom vis-a-vis the supercell without the vacancy.

In binary A-B random alloys, vacancies can be surrounded by a various numbers of A and B atoms unlike the pure element case. In the nearest neighbor shell of an fcc alloy the 12 nearest neighbors of a vacancy can range from 12 A and 0 B atoms all the way to 0 A and 12 B atoms. The composition of the nearest neighbor shell, and of more distant neighbor shells, affects the vacancy formation enthalpy. It is then apparent that “the vacancy formation enthalpy” in a disordered alloy requires a careful definition because the vacancy formation enthalpy must be a function of the atomic neighborhood of the vacancy, the composition of the alloy and other factors. In order to preserve the composition of the alloy, A and B atoms need to be removed according to their composition, that is x_A times an A atom and x_B times a B atom. It follows that a weighted average over A and B removed supercells must be considered,

$$\begin{aligned} \Delta H_{vac}(x_A, x_B) &= x_A[H_{sc+vac_A} + \mu_A - H_{sc}] + x_B[H_{sc+vac_B} + \mu_B - H_{sc}] \\ &= x_A[H_{sc+vac_A} - H_{sc}] + x_B[H_{sc+vac_B} - H_{sc}] + H_{sc}/N \\ &= [x_A H_{sc+vac_A} + x_B H_{sc+vac_B} - \frac{N-1}{N} H_{sc}], \end{aligned} \tag{4.7}$$

where N is the number of atoms in the supercell without vacancy. Of course, actual supercells contain small numbers of atoms only, and therefore they poorly satisfy the invariants. Removing a certain atom from a supercell changes the composition and the state of order. For solid solutions without any short- or long range order, the most configurationally representative supercells are constructed as special quasi-random structures (SQSs) which, for all presupposed important correlation functions in the alloy reproduce the values for truly random structures [44]. In such a supercell one can then remove one atom at a time, and define the vacancy formation enthalpy as an appropriate average

$$\Delta H_{vac}(x_A, x_B) = \frac{1}{N} \sum_{i=1}^{N} [H_{SQS-atom_i} - \frac{N-1}{N} H_{SQS}]. \tag{4.8}$$

However, the above equation is actually not physically relevant because it averages over vacancy neighborhoods. In an actual alloy vacancies would occur where favorable local neighborhoods exist, so that the effective vacancy formation enthalpy should be tilted towards the lowest enthalpy neighborhoods. In a random alloy with low A concentration, it is improbable to find neighborhoods with exclusively A atoms, even if that type of neighborhood were to give the lowest vacancy formation enthalpy. Therefore, the tilting towards the lowest enthalpy configurations is limited by combinatorial factors. If the effective interactions between vacancies and A or B atoms are limited to the near neighbors, the sum in eqn. 4.8 could be limited to those atomic positions which have a particular neighborhood α only,

$$\Delta H^{\alpha}_{vac}(x_A, x_B) = \frac{1}{N_\alpha} \sum_{i_\alpha=1}^{N_\alpha} [H_{SQS-atom_{i_\alpha}} + \mu_i - H_{SQS}]. \tag{4.9}$$

Where N_α refers to the number of sites in the SQS supercells with neighborhood α. This definition is akin to ref. [24, 43, 45, 46]. The chemical potentials of the A and B atomic species in the solid solution (at T=0 K) can be obtained by fitting an interpolation formula, usually some low-order polynomial in the composition, to the solid solution enthalpy. In the earlier work [45, 46] the chemical potential was obtained by averaging over various ordered structures, which for disordered alloys is likely to be less reliable than using SQSs.

In practice, it is rather cumbersome to generate SQS supercells that contain all types of neighborhoods. Just considering the nearest neighbor shell in fcc solid solutions alone gives 144 distinct configurations [47] in a binary alloy. Therefore, it is usually more efficient to compute neighborhood dependent vacancy formation enthalpies through cluster expansions [31–33].

4.2.2. Cluster expansion

In the cluster expansion approach the A-B alloy with vacancies is treated as a ternary with the vacancy as an additional species [30–33, 48, 49]. As the vacancy concentration in actual disordered alloys is usually very low, and vacancy clusters in thermally equilibrated alloys are rare, such cluster expansions typically do not require determination of vacancy-vacancy interaction terms. This significantly reduces the number of effective cluster interactions (ECIs) that are needed for a good representation of the energetics of alloys with vacancies.

Here, we follow the site occupation variable definition **p** as in ref. [50–52], where the site occupation is represented as a vector with as many components as there are species in the alloy, here vacancy, A, and B atoms. For convenience the vacancy could be designated as a type “C” atom, an idea already expressed earlier in refs. [30, 34, 48, 49, 53, 54]. The occupation variable for every site i thus has vector components $p^{(C)}$, $p^{(B)}$, and $p^{(A)}$. $p^{(Q)}$ is the probability that a site is occupied by the species Q. For a particular site i, $p^{(Q)}$ takes the value zero, except when the actual occupancy at that site is “Q” in which case it equals unity.

As every site is occupied by one and only one of these three species, it follows that for every site there exists a “sumrule:” $p^{(C)}+p^{(B)}+p^{(A)}=1$. Therefore, one of the components is redundant. Specifying $p^{(C)}$ and $p^{(B)}$ fully determines the value of $p^{(A)}$ through $p^{(A)}=1-p^{(C)}-p^{(B)}$.

Sumrules apply not just to individual sites but to clusters also. In a cluster each site is occupied by one of the species in the alloy, giving rise to the concept of a “cluster decoration” where each site in a cluster is decorated with an atomic species. The sum of the probabilities for all the cluster decorations is unity for each cluster in the alloy. For instance the sum of probabilities for pair decorations, here for a ternary alloy: $p^{(AA)}+p^{(AB)}+p^{(AC)}+p^{(BA)}+p^{(BB)}+p^{(BC)}+p^{(CA)}+p^{(CB)}+p^{(CC)}=1$.

Using these sum rules, it can be trivially shown that redundancy can be removed by eliminating the cluster decoration probabilities involving one of the species in the alloy. In other words, all cluster decoration probabilities in a ternary A-B-C alloy can be completely determined by specifying the probabilities of decorations involving the species C and B only. Generally, in an alloy with N_{sp} species, the cluster decoration probabilities involving N_{sp}-1 species can be used as a basis set of non-redundant variables, i.e. as correlation functions, to fully describe the probabilities, i.e. the configuration [55]. In the case of a binary alloy, this means that the cluster decoration probabilities of pure B cluster decorations p_γ (where we have eliminated the B superscripts for brevity) fully describes the configurational order, so that the enthalpy of a binary alloy with structure σ can be given as

$$H^\sigma = \sum_\gamma J_\gamma p_\gamma^\sigma, \tag{4.10}$$

where γ indicates a cluster and J_γ is an effective interaction enthalpy associated with a pure B cluster decoration, as was formally proven in ref. [55]. Considering vacancies as a ternary species, and considering isolated vacancies only, eqn. 4.10 can be adapted to include vacancies in alloys,

$$H^\sigma = \sum_\gamma J_\gamma p_\gamma + \sum_{\gamma'} J_{\gamma'} p_{\gamma'}, \tag{4.11}$$

where the second term involves cluster decorations γ' in which one B species is substituted by a vacancy. The single site term in the second sum, $\gamma' = C$ (vacancy), pertains to the vacancy formation enthalpy in pure A J_C and the probability of finding a vacancy p_C. Of course, eqns. 4.10 and 4.11 can be written equally well in terms of the Gibbs energy excluding the configurational entropy part in terms of temperature dependent effective interactions [56].

The enthalpy of the random binary alloy is easily obtained from the cluster expansion because all the cluster decoration probabilities are products of single site decoration probabilities, that is, atomic concentrations. On the fcc lattice, considering nearest neighbor pair and nearest neighbor equilateral triangle ECIs only, this gives

$$H_{rnd}(x_B) = J_0 + x_B J_1^{(B)} + x_B^2 n_{2,1} J_{2,1}^{(BB)} + x_B^3 n_{3,1} J_{3,1}^{(BBB)}, \tag{4.12}$$

where J_0 is a so-called empty cluster "interaction" which serves to define the enthalpy of pure A and n_γ is the number of clusters of type γ per lattice site; γ indicates the number of sites in a cluster, followed by a type, e.g. (2,1) for a nearest neighbor pair, (2,2) for a second nearest neighbor pair [57]. For the fcc lattice, $n_{2,1} = 6$ and $n_{3,1} = 8$. The enthalpy of mixing and the formation energy of any structure σ, is obtained by subtracting the enthalpy from the pure end members $H_A(H_B)$,

$$\begin{aligned} H_{mix}(x_B) &= H_{rnd}(x_B) - x_B H_B - x_A H_A, && (4.13)\\ H_{form,\sigma}(x_B) &= H_\sigma(x_B) - x_B H_B - x_A H_A. && (4.14) \end{aligned}$$

The T=0 K chemical potentials of A and of B are extracted from the random enthalpy,

$$\mu_A(x_B) = J_0 - 6x_B^2 J_{2,1}^{(BB)} - 16x_B^3 J_{3,1}^{(BBB)} \tag{4.15}$$

$$\mu_B(x_B) = J_0 + J_1^{(B)} + 6x_B(2 - x_B) J_{2,1}^{(BB)} + 8x_B^2(3 - 2x_B) J_{3,1}^{(BBB)}. \tag{4.16}$$

If the solid solution is not random, one can generate configurations that satisfy predefined degrees of long- or short range order [58], e.g. through Monte Carlo algorithms. The ECIs are obtained by inverting eqn. 4.10, through the so-called structure inversion method, described in detail elsewhere [57, 59, 60]. An expression for the formation enthalpy of a vacancy in an alloy is derived from eqn. 4.11, by considering which bonds are broken and which bonds are created when an A or B atom is replaced by a vacancy while imposing the requirement of keeping the number of atoms constant. To include the effect of the neighborhood, we consider an atom surrounded by a particular neighborhood α formed by 1^{st}, and optionally more distant neighbor shells, embedded in the alloy. Considering the nearest neighbor shell only as a neighborhood, this gives

$$\begin{aligned}\Delta H^{(\alpha)}_{vac(A)}(x_B) &= J_1^{(C)} + n_1^{(\alpha)} J_{2,1}^{(BC)} + n_2^{(\alpha)} J_{3,1}^{(BBC)} + \mu_A(x_B) - J_0 \\ \Delta H^{(\alpha)}_{vac(B)}(x_B) &= J_1^{(C)} + n_1^{(\alpha)} J_{2,1}^{(BC)} + n_2^{(\alpha)} J_{3,1}^{(BBC)} + \mu_B(x_B) \\ &- (J_0 + J_1^{(B)} + n_1^{(\alpha)} J_{2,1}^{(BB)} + n_2^{(\alpha)} J_{3,1}^{(BBB)}), \qquad (4.17)\end{aligned}$$

where the subscript $vac(i)(i = A$ or $B)$ indicates whether the vacated central atom is A (or B), $J_1^{(C)}$ is the enthalpy needed for forming a vacancy in pure A, $J_{2,1}^{(PQ)}$ is the effective nearest neighbor pair interaction per PQ atom pair, $J_{3,1}^{(PQR)}$ is the effective nearest neighbor equilateral triangle interaction per PQR atom triangle and $n_1^{(\alpha)}(n_2^{(\alpha)})$ is the number of B atoms (BB nearest neighbor pairs) in the nearest neighbor shell around the vacancy with neighborhood α. It is trivial to include more neighbor shells, and clusters with more sites. The 144 distinct nearest neighbor shell configurations [47] in fcc solid solutions in a binary alloy in this approximation are actually energetically distinguished by the numbers $n_1^{(\alpha)}$ and $n_2^{(\alpha)}$ only. Therefore, just 41 distinct vacancy formation enthalpies emerge for each central vacated atom A (or B) from eqn. 4.17, see table 4.1. Of course, eqn. 4.17 can be generalized to the Gibbs energy of vacancy formation by using temperature dependent ECIs that account for thermal excitation effects provided that the contribution from the ideal configurational entropy is excluded. Moreover, within the cluster expansion approach the effect of short range order can be incorporated by using the cluster expansion within a lattice gas model, which can be solved using Monte Carlo [31, 32] or cluster variation methods [30, 48].

Table 4.1: Types of nearest neighbor shells (α) in an fcc A-B alloy: corresponding indices k from table XIII in Ref. [47], degeneracy ($m^{(\alpha)}$), number of B atoms and BB pair ($n_1^{(\alpha)}$ and $n_2^{(\alpha)}$) in the nearest neighbor shell.

α	index **k** [47]	$m^{(\alpha)}$	$n_1^{(\alpha)}$	$n_2^{(\alpha)}$
1	1	1	0	0
2	2	12	1	0
3	3–5	42	2	0
4	6	24	2	1
5	7–9	44	3	0
6	10–12	120	3	1
7	13,14	48	3	2
8	15	8	3	3
9	16,17	9	4	0
10	18,19	96	4	1
11	20–28	240	4	2
12	29–31	96	4	3
13	32,33	54	4	4
14	34–38	108	5	2
15	39–44	264	5	3
16	45–52	264	5	4
17	53–55	120	5	5
18	56,57	36	5	6

Table 4.1 (*continued*)

α	index **k** [47]	$m^{(\alpha)}$	$n_1^{(\alpha)}$	$n_2^{(\alpha)}$
19	58–66	216	6	4
20	67–72	240	6	5
21	73–83	336	6	6
22	84,85	96	6	7
23	86,87	36	6	8
24	$\overline{34}$–$\overline{38}$	108	7	6
25	$\overline{39}$–$\overline{44}$	264	7	7
26	$\overline{45}$–$\overline{52}$	264	7	8
27	$\overline{53}$–$\overline{55}$	120	7	9
28	$\overline{56}$,$\overline{57}$	36	7	10
29	$\overline{16}$,$\overline{17}$	9	8	8
30	$\overline{18}$,$\overline{19}$	96	8	9
31	$\overline{20}$–$\overline{28}$	240	8	10
32	$\overline{29}$–$\overline{31}$	96	8	11
33	$\overline{32}$,$\overline{33}$	54	8	12
34	$\overline{7}$–$\overline{9}$	44	9	12
35	$\overline{10}$–$\overline{12}$	120	9	13
36	$\overline{13}$,$\overline{14}$	48	9	14
37	$\overline{15}$	8	9	15
38	$\overline{3}$–$\overline{5}$	42	10	16
39	$\overline{6}$	24	10	17
40	$\overline{2}$	12	11	20
41	$\overline{1}$	1	12	24

As seen above in eqns. 4.17, the enthalpy of a vacancy defect depends on the environment α, and on which atom species *i* is removed, A or B. The vacancy formation enthalpy in the alloy is therefore a weighted sum over environments and over removed atom species,

$$\Delta H = \sum_{\alpha,i} x^{(\alpha)}_{vac(i)} \Delta H^{(\alpha)}_{vac(i)}, \tag{4.18}$$

where $x^{\alpha}_{vac(i)}$ is the concentration of each type of vacancy. It is now evident also that the removed atom species index *i* is really needed, because the likelihood of finding an A or a B atom in environment α is not the same for the two atom species. Of course, after the atom *i* is removed, it is no longer possible to determine what species originally was there. The concentration of vacancy types $x^{\alpha}_{vac(i)}$ is a product of concentration (or probability) $x^{(\alpha)}_i$ of finding an *i* atom in an α environment and of the probability of removing that *i* atom from that environment $f^{(\alpha)}_{vac(i)}$. Naturally, $f^{(\alpha)}_{vac(i)}$ should be a function of $\Delta H^{(\alpha)}_{vac(i)}$ because if the latter is large the corresponding probability should be low. There must also be an entropy associated with $f^{(\alpha)}_{vac(i)}$. As the vacancy defects are few and generally far apart, the entropy can be represented by an ideal entropy,

$$\Delta S = -\sum_{\alpha,i} k_B x^{(\alpha)}_i \Xi(f^{(\alpha)}_{vac(i)}), \tag{4.19}$$

with

$$\Xi(f^{(\alpha)}_{vac(i)}) = f^{(\alpha)}_{vac(i)} \ln(f^{(\alpha)}_{vac(i)}) + (1 - f^{(\alpha)}_{vac(i)}) \ln(1 - f^{(\alpha)}_{vac(i)}). \tag{4.20}$$

It then follows that at finite temperature, the Gibbs energy due to the formation of vacancies can be written as,

$$\Delta G = \sum_{\alpha,i} x^{(\alpha)}_{vac(i)} \Delta H^{(\alpha)}_{vac(i)} + k_B T x^{(\alpha)}_i \Xi(f^{(\alpha)}_{vac(i)}). \tag{4.21}$$

Once $\Delta H^{(\alpha)}_{vac(i)}$ and the short range order as given by $x^{(\alpha)}_i$ are known, the concentration of each type of vacancy $x^{\alpha}_{vac(i)}$ can be computed by minimizing eqn. 4.21. However, the minimization of ΔG_{vac} with respect to $x^{(\alpha)}_{vac(i)}$ does not generally satisfy preservation of both A and B atoms. The apparent number of vacated A atoms might differ from what is to be expected on the basis of the composition. Hence, a constraint must be imposed:

$$\frac{\sum_\alpha x^{(\alpha)}_{vac(B)}}{\sum_\alpha x^{(\alpha)}_{vac(A)}} = \frac{x_B}{x_A}. \tag{4.22}$$

Using a Lagrange multiplier λ this gives a Lagrangian

$$\Lambda = \Delta G + \lambda[x_A \sum_\alpha x^{(\alpha)}_{vac(B)} - x_B \sum_\alpha x^{(\alpha)}_{vac(A)}], \tag{4.23}$$

and the values of $x^{\alpha}_{vac(i)}$ are then found by solving

$$\frac{\partial \Lambda}{\partial x^{(\alpha)}_{vac(i)}} = \Delta H^{(\alpha)}_{vac(i)} - \lambda[\delta_{iA} x_B - \delta_{iB} x_A] + k_B T \ln(\frac{f^{(\alpha)}_{vac(i)}}{1 - f^{(\alpha)}_{vac(i)}}) = 0, \tag{4.24}$$

where δ is the Kronecker delta. When vacancy concentrations are small, the denominators inside the logarithm can be neglected, yielding

$$x^{(\alpha)}_{vac(i)} = x^{(\alpha)}_i \exp(-\beta\{\Delta H^{(\alpha)}_{vac(i)} - \lambda[\delta_{iA} x_B - \delta_{iB} x_A]\}), \tag{4.25}$$

where $\beta = (k_B T)^{-1}$. By substituting eqns. 4.25 into eqn. 4.22 an analytical solution for λ is obtained,

$$\lambda = \frac{1}{\beta} \ln(\frac{x_A \sum_\alpha x^{(\alpha)}_B e^{-\beta \Delta H^{(\alpha)}_{vac(B)}}}{x_B \sum_\alpha x^{(\alpha)}_A e^{-\beta \Delta H^{(\alpha)}_{vac(A)}}}). \tag{4.26}$$

In the random alloy case, $x^{(\alpha)}_i$ is a simple function of the composition

$$x^{(\alpha)}_i = m^{(\alpha)} x_i x_A^{12 - n^{(\alpha)}_1} x_B^{n^{(\alpha)}_1}, \tag{4.27}$$

where $m^{(\alpha)}$ is the degeneracy of a particular neighborhood, see table 4.1. In non-random alloys, a Monte Carlo method can be used to impose a certain degree of short- or long range order on the probabilities $x_i^{(\alpha)}$. Of course, the sum of $x_i^{(\alpha)}$ over all α yields the concentration x_i. The total vacancy concentration is obtained from

$$x_{vac}(x_B, T) = \sum_{\alpha,i} x_{vac(i)}^{(\alpha)}. \tag{4.28}$$

It is evident that the total vacancy concentration does not necessarily follow a simple Arrhenius equation because each neighborhood has its own vacancy formation enthalpy, see eqn. 4.25. At low temperature, only those α with the lowest formation enthalpies contribute, while at high temperature α with higher formation enthalpies contribute also. Therefore, when the total vacancy concentration is fit to an Arrhenius equation, it is to be expected that the effective vacancy formation energy shifts towards higher values as the temperature increases. Although $\Delta H_{vac(A)}^{(\alpha)}$ is in this derivation temperature independent, the effective energy for vacancy formation is better represented as a temperature dependent Gibbs energy

$$\Delta G_{vac}^{eff}(x_B, T) = -k_B T \ln(x_{vac}(x_B, T)) \tag{4.29}$$

The temperature dependence of ΔG_{vac}^{eff} can be used to determine an effective vacancy formation entropy ΔS_{vac}^{eff} and enthalpy ΔH_{vac}^{eff},

$$\Delta S_{vac}^{eff}(x_B) = -[\Delta G_{vac}^{eff}(x_B, T_1) - \Delta G_{vac}^{eff}(x_B, T_2)]/[T_1 - T_2], \tag{4.30}$$

$$\Delta H_{vac}^{eff}(x_B) = \Delta G_{vac}^{eff}(x_B, T_1) + T_1 \Delta S_{vac}^{eff}(x_B), \tag{4.31}$$

where T_1 and T_2 indicate the temperature range of interest. Another vacancy property of interest is the average number of B neighbors around a vacancy,

$$\langle n_B \rangle = \frac{1}{x_{vac}} \sum_{\alpha,i} x_{vac(i)}^{(\alpha)} n_1^{(\alpha)}, \tag{4.32}$$

In the above derivation, it is assumed that the fraction of neighborhoods $x_i^{(\alpha)}$ is not affected by the vacancy concentrations $x_{vac(i)}^{\alpha}$. This should be true as long as $x_{vac(i)}^{\alpha}$ is much smaller than $x_i^{(\alpha)}$, i.e. $f_{vac(i)}^{\alpha} << 1$. It breaks down when e.g. the lowest energy neighborhood α' is very rare. Say, if an all A surrounded vacancy is strongly favored in an almost pure B alloy. In such a case we must expect a coupling of short- or long range ordering with the occurrence of vacancies. Fortunately one can explicitly verify whether $f_{vac(i)}^{\alpha}$ is small.

4.3. Method

The thermodynamics of fcc Cu-Ni solid solutions was investigated by means of SQSs with 16 atoms per cell with compositions Cu_4Ni_{12} , $Cu_{12}Ni_4$ (both structures listed as SQS-1 in ref.[61]), and Cu_8Ni_8 (two variants listed as SQS-2 and SQS-3 in ref.[61]). The pure Cu and Ni phases are considered also using the same type cell as for the Cu_4Ni_{12} and $Cu_{12}Ni_4$ compositions. Generalized gradient approximation [62, 63] projector augmented wave pseudopotentials as implemented in VASP [64–66], version 4.6, are used with collinear spin polarization. Integrations in reciprocal space use a Γ-centered Monkhorst-Pack grid with the number of k-points determined through $N_{atom}N_{k-point} \approx$10000 in the 1^{st} Brillouin zone. Precision was set to "accurate." In all calculations, the electronic wave functions were expanded in terms of plane waves up to a cutoff kinetic energy of 320 eV. The Hermite-Gauss smearing method of Methfessel and Paxton of order 1 has been used, with a smearing parameter of 0.1 eV. All structures are fully relaxed. The convergence criteria for energy, force magnitude, and stress component, were 0.1 meV, 10 meV/nm, and 1 kBar respectively. Structural optimizations were reinitiated at least twice. With these convergence settings energy changes between the last ionic iterations are a few μeV/atom only. All ab initio calculations pertain to T=0 K with zero-point vibrational corrections being neglected. In the 4 types of SQSs every site was once replaced by a vacancy, giving rise to 4x16=64 supercells with a single vacancy. A cluster expansion using point, nearest neighbor pair, and nearest neighbor equilateral triangle clusters was fit to in total 71 structures; 2 pure elements, vacuum,4 SQSs, and 64 single vacancy SQS derived structures. The ECIs were used in a ternary cluster variation method [67, 68] (CVM) calculation in the tetrahedron approximation to determine the Cu-Ni phase diagram, and the vacancy concentration as function of composition and temperature. In the CVM calculations the ratio of Cu to Ni atoms is held constant, but the concentration of the vacancy species is freely varied. The equilibrium vacancy concentration is determined by minimizing the Gibbs energy with respect to the vacancy concentration.

4.4. Results and Discussion

Vacancy properties in concentrated Cu-Ni alloys are reported and discussed. Next, we seek to generalize our findings to other alloy types, where we consider alloys that are of ordering type, unlike Cu-Ni, and alloys in which the vacancy formation enthalpy in the end members differs even more, or significantly less than for Cu-Ni.

4.4.1. Alloy with phase separation: the case of fcc Cu-Ni

The ab initio computed supercell properties are listed in table 4.2. In the supercells with vacancies, the letters following the structure indicate which atom has been vacated, "a" ("p") indicates that the 1^{st} (16^{th}) atom in the structure is vacated. Enthalpy of formation of the SQS, computed as described in ref.[61], is used as a proxy for the mixing enthalpy ΔH_{mix}. Figure 4.1 illustrates that the compositional dependence of the mixing enthalpy can be approximated by subregular solution model. The chemical potential of Cu and Ni is extracted from the mixing enthalpy as function of the alloy composition. It should be remarked that small 16 atom supercells do not give very accurate vacancy formation energies, but the objective here is not high accuracy but insight in vacancy properties in alloys. For the pure elements a comparison with literature values is given in table 4.3. It is evident that the results are comparable to other PBE-GGA [62, 63] calculations with small supercells. We chose the PBE implementation of the GGA because a recent study [69] suggests that the PBE-GGA xc-potential performs at least as well as the newer AM05-GGA [70] xc-potential in describing vacancy formation energies.

Table 4.2: Computed enthalpies (ΔH) and magnetic moments (M) for supercells as described in the text, the number of Cu atoms in the nearest neighbor shell around the vacant site, the chemical potentials, and the vacancy formation enthalpy according to eqn 4.6.

Structure	formula	ΔH (eV/cell)	M (μ_B/cell)	$n_1^{(Cu)}$	μ_{Ni} (eV/atom)	μ_{Cu} (eV/atom)	ΔH_{vac}^{α} (eV)
SQS-1	$Ni_{16}Cu_0$	-89.167	10.031		-5.573	-3.538	
SQS-1	$Ni_{15}Cu_0$	-82.185	9.499	0	-5.573		1.409
SQS-1	Ni_0Cu_{16}	-59.563	0.000		-5.585	-3.723	
SQS-1	Ni_0Cu_{15}	-54.781	0.000	12		-3.723	1.059
SQS-1	$Ni_{12}Cu_4$	-81.381	6.054		-5.555	-3.674	
SQS-1a	$Ni_{11}Cu_4$	-74.489	5.529	3	-5.555		1.337
SQS-1b	$Ni_{11}Cu_4$	-74.438	5.658	1	-5.555		1.388
SQS-1c	$Ni_{11}Cu_4$	-74.388	5.531	1	-5.555		1.437
SQS-1d	$Ni_{11}Cu_4$	-74.588	5.613	4	-5.555		1.237
SQS-1e	$Ni_{11}Cu_4$	-74.607	5.688	6	-5.555		1.219
SQS-1f	$Ni_{11}Cu_4$	-74.534	5.680	5	-5.555		1.292
SQS-1g	$Ni_{11}Cu_4$	-74.430	5.623	3	-5.555		1.395
SQS-1h	$Ni_{11}Cu_4$	-74.342	5.741	1	-5.555		1.483
SQS-1i	$Ni_{11}Cu_4$	-74.424	5.635	2	-5.555		1.402
SQS-1j	$Ni_{11}Cu_4$	-74.410	5.680	2	-5.555		1.415
SQS-1k	$Ni_{11}Cu_4$	-74.392	5.664	3	-5.555		1.434
SQS-1l	$Ni_{11}Cu_4$	-74.536	5.736	5	-5.555		1.289
SQS-1m	$Ni_{12}Cu_3$	-76.343	6.588	2		-3.674	1.363
SQS-1n	$Ni_{12}Cu_3$	-76.352	6.580	3		-3.674	1.354
SQS-1o	$Ni_{12}Cu_3$	-76.359	6.537	4		-3.674	1.347
SQS-1p	$Ni_{12}Cu_3$	-76.304	6.606	3		-3.674	1.402
SQS-1	Ni_4Cu_{12}	-66.873	0.000	12	-5.524	-3.730	
SQS-1a	Ni_4Cu_{11}	-61.879	0.000	9		-3.730	1.264
SQS-1b	Ni_4Cu_{11}	-62.044	0.001	11		-3.730	1.099
SQS-1c	Ni_4Cu_{11}	-62.032	0.000	11		-3.730	1.111
SQS-1d	Ni_4Cu_{11}	-61.842	0.000	8		-3.730	1.301
SQS-1e	Ni_4Cu_{11}	-61.777	0.054	6		-3.730	1.366
SQS-1f	Ni_4Cu_{11}	-61.859	0.000	7		-3.730	1.283
SQS-1g	Ni_4Cu_{11}	-61.959	0.000	9		-3.730	1.184
SQS-1h	Ni_4Cu_{11}	-62.113	0.000	11		-3.730	1.030
SQS-1i	Ni_4Cu_{11}	-61.987	0.000	10		-3.730	1.156
SQS-1j	Ni_4Cu_{11}	-62.023	0.000	10		-3.730	1.120
SQS-1k	Ni_4Cu_{11}	-61.968	0.000	9		-3.730	1.175
SQS-1l	Ni_4Cu_{11}	-61.866	0.000	7		-3.730	1.277
SQS-1m	Ni_3Cu_{12}	-60.160	0.000	10	-5.524		1.188
SQS-1n	Ni_3Cu_{12}	-60.113	0.000	9	-5.524		1.235
SQS-1o	Ni_3Cu_{12}	-60.043	0.000	8	-5.524		1.305
SQS-1p	Ni_3Cu_{12}	-60.192	0.000	9	-5.524		1.157
SQS-2	Ni_8Cu_8	-73.990	2.243		-5.527	-3.726	1.297
SQS-2a	Ni_8Cu_7	-68.865	3.081	3		-3.726	1.400
SQS-2b	Ni_8Cu_7	-68.864	3.081	3		-3.726	1.400
SQS-2c	Ni_8Cu_7	-68.989	2.801	7		-3.726	1.275
SQS-2d	Ni_8Cu_7	-69.013	2.834	7		-3.726	1.252
SQS-2e	Ni_8Cu_7	-68.973	2.764	7		-3.726	1.291
SQS-2f	Ni_8Cu_7	-68.989	2.810	7		-3.726	1.275
SQS-2g	Ni_8Cu_7	-68.974	2.760	7		-3.726	1.290
SQS-2h	Ni_8Cu_7	-69.013	2.827	7		-3.726	1.251
SQS-2i	Ni_7Cu_8	-67.081	1.886	5	-5.527		1.382

Table 4.2 (*continued*)

Structure	formula	ΔH (eV/cell)	M (μ_B/cell)	$n_1^{(Cu)}$	μ_{Ni} (eV/atom)	μ_{Cu} (eV/atom)	ΔH^{α}_{vac} (eV)
SQS-2j	Ni_7Cu_8	-67.116	2.117	5	-5.527		1.347
SQS-2k	Ni_7Cu_8	-67.125	1.990	5	-5.527		1.338
SQS-2l	Ni_7Cu_8	-67.081	1.876	5	-5.527		1.382
SQS-2m	Ni_7Cu_8	-67.127	1.980	5	-5.527		1.336
SQS-2n	Ni_7Cu_8	-67.117	2.108	5	-5.527		1.347
SQS-2o	Ni_7Cu_8	-67.368	2.124	9	-5.527		1.095
SQS-2p	Ni_7Cu_8	-67.368	2.124	9	-5.527		1.095
SQS-3	Ni_8Cu_8	-73.995	2.208		-5.527	-3.726	
SQS-3a	Ni_8Cu_7	-68.849	3.071	3		-3.726	1.420
SQS-3b	Ni_8Cu_7	-68.848	3.070	3		-3.726	1.422
SQS-3c	Ni_8Cu_7	-69.045	2.847	7		-3.726	1.225
SQS-3d	Ni_8Cu_7	-69.045	2.838	7		-3.726	1.224
SQS-3e	Ni_8Cu_7	-69.043	2.882	7		-3.726	1.226
SQS-3f	Ni_8Cu_7	-69.044	2.844	7		-3.726	1.225
SQS-3g	Ni_8Cu_7	-69.043	2.882	7		-3.726	1.226
SQS-3h	Ni_8Cu_7	-69.044	2.841	7		-3.726	1.225
SQS-3i	Ni_7Cu_8	-67.149	2.010	5	-5.527		1.319
SQS-3j	Ni_7Cu_8	-67.149	1.991	5	-5.527		1.319
SQS-3k	Ni_7Cu_8	-67.155	2.206	5	-5.527		1.314
SQS-3l	Ni_7Cu_8	-67.149	2.010	5	-5.527		1.320
SQS-3m	Ni_7Cu_8	-67.154	2.206	5	-5.527		1.314
SQS-3n	Ni_7Cu_8	-67.149	1.989	5	-5.527		1.320
SQS-3o	Ni_7Cu_8	-67.422	1.993	9	-5.527		1.047
SQS-3p	Ni_7Cu_8	-67.420	1.978	9	-5.527		1.049

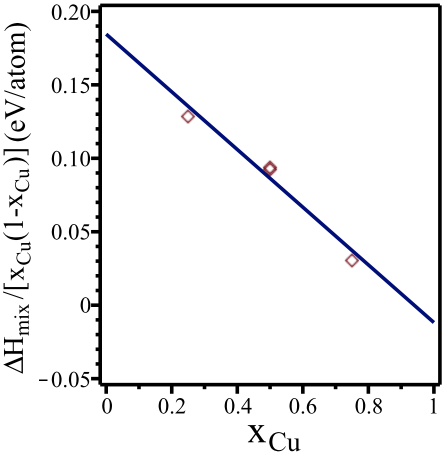

Figure 4.1: $\Delta H_{mix}/[x_{Cu}(1-x_{Cu})]$ as function of the atomic concentration Cu; a) as computed with eqn 4.14 using SQS formation enthalpies (diamond symbols), b) as interpolated through a least squares linear fit (solid line).

In the SQSs single vacancies were introduced by removing a single atom at a time, followed by a structural relaxation. The computed enthalpies are used in eqn. 4.6 to extract vacancy formation enthalpies for various vacancy neighborhoods, see figure 4.2. It is evident that the greater the number of Cu atoms in the nearest neighbor shell, the smaller the

Table 4.3: Vacancy formation enthalpy in fcc Cu and fcc Ni as computed with eqn 4.9, and as reported in the literature.

method	H_{vac}^{Cu}(eV)	H_{vac}^{Ni}(eV)	reference
LDA	1.26		[69]
PW91	0.99		[69]
PBE [62, 63]	1.06	1.41	this work
PBE [62, 63] 16-atom cell	1.03	1.46	[71]
PBE [62, 63] 32-atom cell	1.02	1.46	[71]
PBE [62, 63] 32-atom cell	1.04	1.44	[72]
PBE [62, 63] 108-atom cell	1.06		[69]
AM05 [70] 32-atom cell	1.28	1.75	[71]
AM05 [70] 32-atom cell	1.26	1.69	[72]
AM05 [70] 108-atom cell	1.29		[69]
experiment	0.92∼1.27	1.45∼1.8	[20]
experiment	1.04∼1.49		[73]
experiment		1.2∼1.68	[74]
experiment(LGT DD+PAS)	1.06		[69]

vacancy formation enthalpy. This is in keeping with the greater vacancy formation enthalpy in pure Ni in comparison with that in pure Cu.

The SQS calculations with, and without vacancies, are used also for obtaining a cluster expansion. The computed ECIs, shown in table 4.4, have been extracted in terms of n-body clusters($n = 1, 2, 3$). Although a much smaller number of ECIs is used than there are structural energies to be fitted to, nevertheless a rather good fit is obtained with a predictive error [67], or cross-validation score [75] of less than 4.5 meV/atom. The good performance of the CE is apparent also, when the formation energies are computed from the ECIs, listed in table 4.4, using eqn. 4.11 and plotted versus the ab initio computed formation energies from eqn. 4.14, as shown in figure 4.3. The CE reproduces the ab initio data with a root mean square error of less than 4 meV/atom.

Table 4.4: Effective cluster interactions (ECIs) in Cu-Ni system from cluster expansion.

Cluster	ECI(meV/cluster)
J_v	1505.5
J_{Cu}	166.7
$J_{v\text{-}Cu}$	-53.5
$J_{Cu\text{-}Cu}$	-50.0
$J_{v\text{-}Cu\text{-}Cu}$	4.08
$J_{Cu\text{-}Cu\text{-}Cu}$	16.3

The mixing enthalpy of Cu-Ni alloys as function of composition is computed using the ECIs with eqn. 4.13. Figure 4.4 illustrates that the mixing enthalpy as estimated through figure 4.1, as computed through the formation energy of SQS, and as obtained by a phase diagram assessment using experimental data [76], are all in fair agreement. The tendency

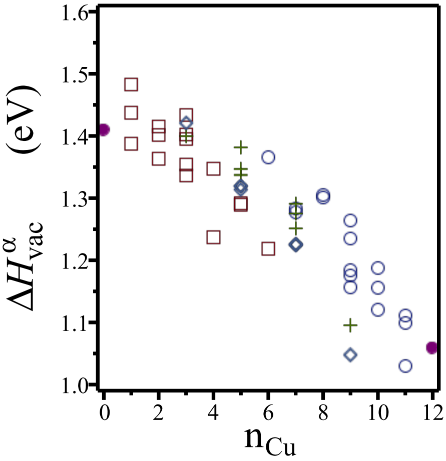

Figure 4.2: Vacancy formation enthalpy ΔH^{α}_{vac} as function of the number of Cu atoms in the nearest neighbor shell (n_{Cu}) as computed with eqn. 4.6 at various compositions; solid circles: in pure Cu and Ni; squares: in SQS-1 at x_{Cu}=0.25; crosses: in SQS-2 at x_{Cu}=0.5; diamonds: in SQS-3 at x_{Cu}=0.5; open circles: in SQS-1 at x_{Cu}=0.75.

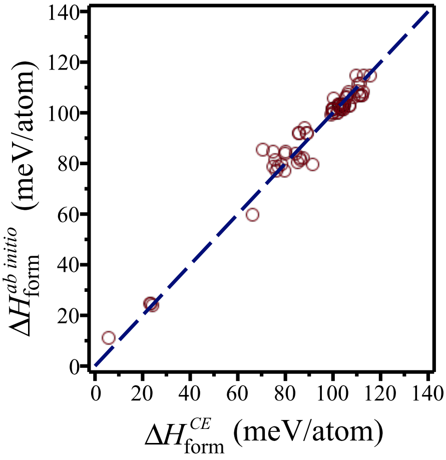

Figure 4.3: A comparison of formation energies calculated ab initio through eqn. 4.14 and as calculated with the cluster expansion.

towards phase separation is strongest at about $x_{Cu} = 0.4$.

The ECIs can be used also in a cluster variation method calculation of the phase diagram, see figure 4.5. The ab initio computed phase diagram displays a miscibility gap with a maximum temperature of 680 K at $Cu_{0.35}Ni_{0.65}$ in excellent agreement with the assessement of experimental data by an Mey in figure 7 of Ref. [76], which gives a maximum temperature of 640 K at $Cu_{0.4}Ni_{0.6}$, and as assessed by Chakrabarti et al. [77] which gives a maximum temperature of 628 K at $Cu_{0.33}Ni_{0.67}$. It should be remarked that

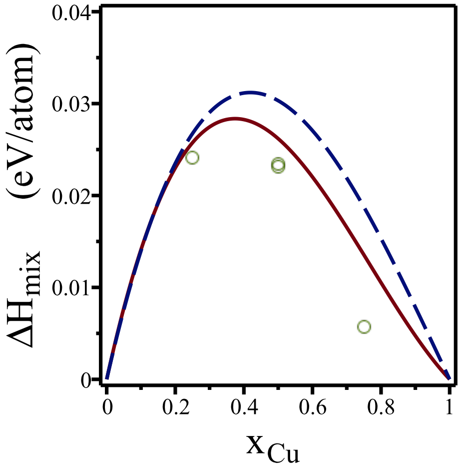

Figure 4.4: Mixing enthalpy of fcc Cu-Ni alloys as function of the atomic fraction Cu; using the cluster expansion through eqn. 4.13 (solid line), using the SQS formation enthalpies from eqn. 4.14 (circles), and the mixing enthalpy at T=298 K as assessed on the basis of experimental data by an Mey [76] (dashed line).

the concentration of vacancies is so low, that even when the phase diagram were computed strictly as a binary Cu-Ni alloy without considering vacancies, the changes would have been completely imperceptible.

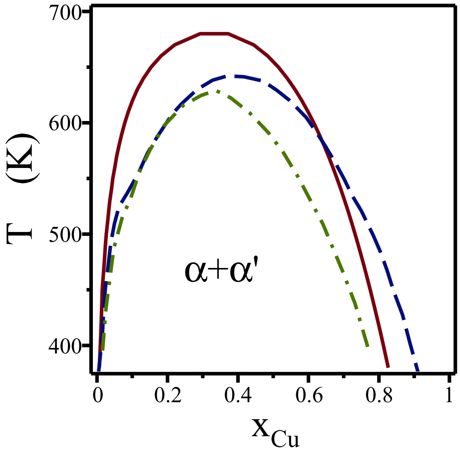

Figure 4.5: Low temperature part of Ni-Cu phase diagram as computed with the ECI in table 4.4 in the tetrahedron approximation of the CVM (solid line), as assessed by an Mey [76] (dashed line), and as assessed by Chakrabarti et al. [77] (dash-dotted line).

Local environment dependent vacancy formation enthalpies $\Delta H^{(\alpha)}_{vac(i)}(x_{Cu})$ at T = 0 K can be obtained by substituting the ECIs into eqn. 4.17, see figure 4.6. It is evident that two energy terms contribute to the formation enthalpy of a vacancy: a) the energy to break the bonds between the vacated atom and its neighbor atoms; b) the chemical potential of the vacated atom. The chemical potential represents the energy for putting the vacated atom back into the alloy, and this term makes the vacancy formation enthalpy composition dependent, see eqn. 4.17. As the mixing enthalpy is concave with respect to composition in Cu-Ni, it follows that the chemical potential of Cu (Ni) decreases as the composition gets richer in Cu (Ni), see figure 4.7. In other words, putting back a Cu (Ni) atom in a Cu-rich alloy is less (more) costly than putting it back in a Ni-rich alloy. For this reason all the Cu-vacated vacancy formation enthalpies are rigidly shifted higher in $Cu_{0.25}Ni_{0.75}$ in comparison to $Cu_{0.75}Ni_{0.25}$.

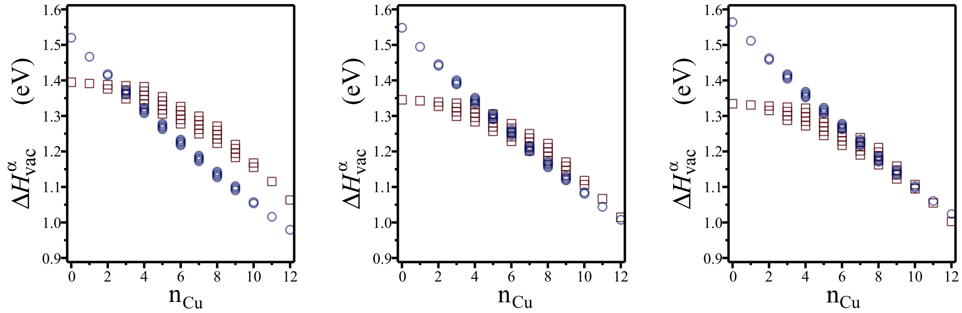

Figure 4.6: Vacancy formation enthalpy $\Delta H^{(\alpha)}_{vac(i)}$ at T = 0 K as a function of the number of Cu atoms in the nearest neighbor shell n_{Cu}, Ni-vacated (open circles), Cu-vacated (open squares): (a) in $Cu_{0.25}Ni_{0.75}$, (b) in $Cu_{0.50}Ni_{0.50}$, (c) in $Cu_{0.75}Ni_{0.25}$.

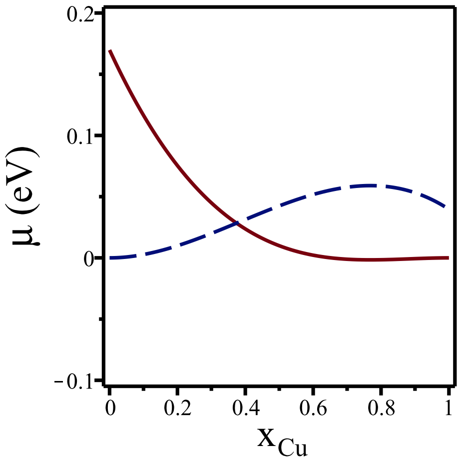

Figure 4.7: Chemical potential of Cu (solid line) and Ni (dashed line) as a function of composition at T = 0 K

Of course, the distinction between Cu- and Ni vacancies is artificial: in the alloy one cannot know what atom has previously occupied the position of the vacancy site. Therefore the λ Lagrange multiplier must be considered. Considering $Cu_{0.50}Ni_{0.50}$ (figure 4.6b) it is clear that vacancies are most favorable at Ni occupied sites surrounded by many Cu atoms. The λ parameter makes sure that just as many Ni atoms get vacated as Cu atoms (in an equiatomic alloy). Therefore, the λ parameter should make the Cu-vacated vacancies energetically a little less costly, and the Ni-vacated ones a little more costly. Eqn. 4.25 shows that this occurs when λ takes a negative value. At very high temperature, the Boltzmann factor for all vacancy types moves towards unity. Then, the combinatorial factor $x_i^{(\alpha)}$ (eqn. 4.27) plays a dominant role. For the random alloys this implies that λ moves towards zero, as is seen in figure 4.8. The λ parameter is a function of composition also. At a given, not too high, temperature, λ is strongly negative at Ni-rich compositions while λ is weakly positive at Cu-rich compositions. Looking at figure 4.6a, it is evident that the high Cu coordinated Ni sites are much more likely to be vacated in $\mathrm{Cu}_{0.25}\mathrm{Ni}_{0.75}$ than in the equiatomic alloy, so that an even more negative λ value is required to balance Ni and Cu vacated sites. Figure 4.6c, on the other hand, shows that for Cu-rich alloys the favorable high Cu coordinated Ni and Cu sites have about equal vacancy formation enthalpies. Therefore, λ must take very small values, and it needs to be slightly positive because the majority of vacancies must derive from Cu vacated sites.

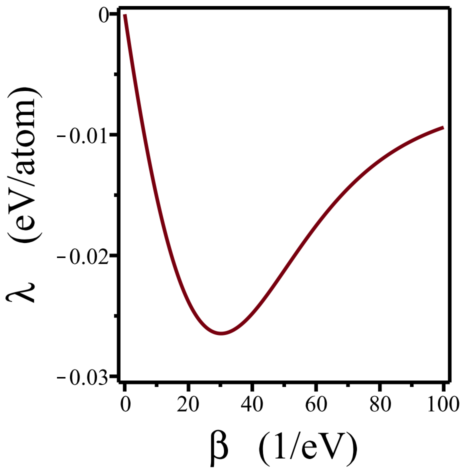

Figure 4.8: Lagrange multiplier λ in $\mathrm{Cu}_{0.50}\mathrm{Ni}_{0.50}$ as given by eqn. 4.26 as function of the inverse temperature β.

Now that λ behaviour has been rationalized, the total vacancy concentration $x_{vac}(x_B, T)$ is examined. Figure 4.9 displays the Cu- and Ni-vacated vacancy concentrations $x_{vac(i)}$ summed over all neighborhoods α, and it shows the total vacancy concentration $x_{vac} = x_{vac(Ni)} + x_{vac(Cu)}$, as function of the composition. Clearly, in the equiatomic alloy $x_{vac(Ni)} = x_{vac(Cu)}$, as imposed by the Lagrange multiplier λ. It is also obvious that at higher Cu content, the vacancy concentration is much larger because the vacancy formation energies decrease as the number of Cu nearest neighbors around a vacancy increases.

Fitting the total vacancy concentrations to an Arrhenius equation, eqn. 4.29, yields the effective vacancy formation Gibbs energy, $\Delta G_{vac}^{\mathrm{eff}}$, see figure 4.10. It should be emphasized that only configurational excitations have been considered here so that for the pure elements (x_{Cu}=0,x_{Cu}=1) ΔG_{vac}^{eff} is found to be temperature independent. ΔG_{vac}^{eff} is not well represented by a linear interpolation w.r.t. composition between the pure

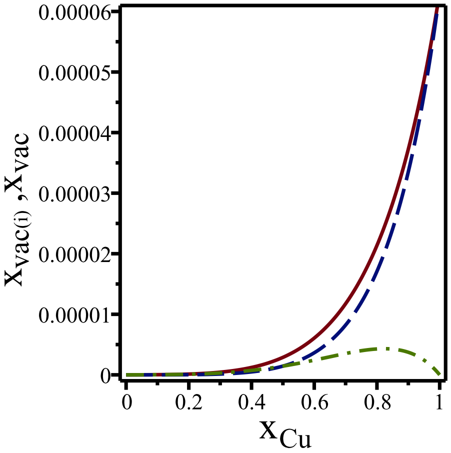

Figure 4.9: Vacancy concentration $x_{vac(i)}$ (dashed line: Cu-vacated; dash-dotted line: Ni-vacated) and x_{vac} (solid line) at T=1200 K as given by eqn. 4.28 as function of the Cu concentration x_{Cu}.

element values because it takes significantly lower values in concentrated alloys than the concentration weighted average. This is explained by the multitude of local neighborhoods that exist within an alloy, so that vacancies will be formed in the most favorable locations. Moreover, the deviation of ΔG_{vac}^{eff} from the linear interpolated value, ΔG_{vac}^{eff-xs}, gets smaller when temperature increases because there is then a weaker preference for low energy neighborhood vacancies. Nevertheless, ΔG_{vac}^{eff-xs} remains negative for alloys with phase separation tendency. The high temperature limit of ΔG_{vac}^{eff} is the statistical average of the vacancy formation enthalpy of all types of vacancies $\sum_{\alpha,i} x_i^{(\alpha)} \Delta H_{vac(i)}^{(\alpha)}(x_{Cu})$, which may be above the linear interpolation value for Cu-rich alloys.

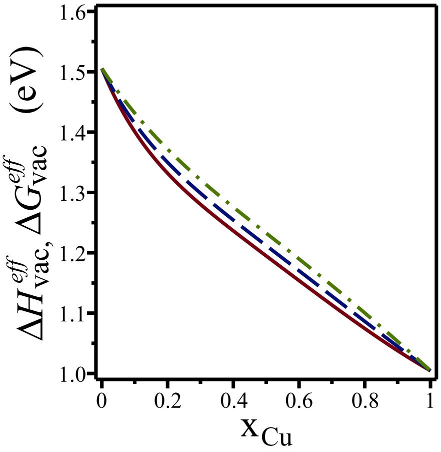

Figure 4.10: Effective vacancy formation enthalpy at T=0 K (solid line) and Gibbs energies at T=600 K (dashed line) and at T=1200 K (dash-dotted line) as function of composition.

In concentrated alloys, ΔG^{eff}_{vac} increases with temperature which suggests a negative effective vacancy formation entropy ΔS^{eff}_{vac}. ΔS^{eff}_{vac} is computed with eqn. 4.30 using T_1 = 600 K and T_2 = 1200 K. The negative value of ΔS^{eff}_{vac} too, is a consequence of the multitude of local vacancy neighborhoods in concentrated alloys. At low temperature vacancies occur in the most favorable neighborhoods only, while at elevated temperature less favorable neighborhoods also provide vacancies. Of course, this concerns the configurational aspect only. Non-configurational excitations, such as the vibrational contribution to the entropy of vacancy formation, tend to give significantly positive effective vacancy formation entropy contributions, see e.g. table 2 in ref. [11]. Nevertheless, the configurational contribution to $\Delta S^{\mathrm{eff}}_{vac}$ is quite large at about 0.4 k_B in $\mathrm{Cu}_{0.25}\mathrm{Ni}_{0.75}$, see figure 4.11. The magnitude of ΔS^{eff}_{vac} is decided by the formation energy difference between vacancies at most and least favorable positions. For this reason, ΔS^{eff}_{vac} increases when the vacancy formation energy in the pure end-member elements differ strongly or when the SRO tendency gets stronger.

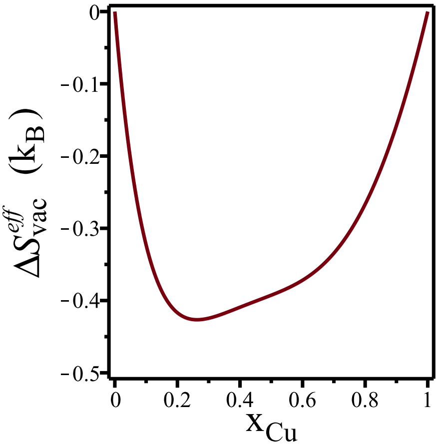

Figure 4.11: Effective vacancy formation entropy as a function of composition as computed with eqn. 4.30.

The effective vacancy formation enthalpy, as computed with eqn. 4.31, is displayed in figure 4.10. Like ΔG^{eff}_{vac}, it shows the strongest deviation from a linear composition dependence near x_{Cu}=0.25 because at the Ni-rich side the strongest shift of vacancy neighborhood occurs when the temperature is changed. At low temperature only high Cu coordinated vacancies can occur because they are energetically favored, but in a Cu-poor alloy such neighborhoods are rare. At high temperature also energetically much less favorable, but combinatorially much more prevalent, high Ni-coordinated vacancies occur. Thus in Ni-rich alloys the largest change in vacancy formation energies occurs as the temperature increases. This is illustrated in figure 4.12 where the average number of Cu nearest neighbors around a vacancy $\langle n_{Cu} \rangle$ in $\mathrm{Cu}_{0.25}\mathrm{Ni}_{0.75}$, as computed with eqn. 4.32, is shown as function of the inverse temperature β. In the vicinity of β=0, the number of Cu neighbors converges to the random value of 12×0.25=3, but at large values of β vacancies occur only there where they are exclusively surrounded by 12 Cu atoms, in spite of Cu atoms being in the minority.

The strong preference of vacancies for Cu coordination occurs across the whole

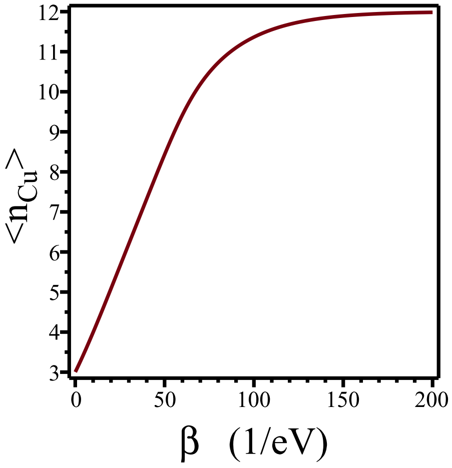

Figure 4.12: The average number of Cu neighbors around a vacancy $\langle n_{Cu} \rangle$ in $\mathrm{Cu}_{0.25}\mathrm{Ni}_{0.75}$ as a function of the inverse temperature β.

composition range, as is shown in figure 4.13. Our findings agree very well with an earlier embedded atom method (EAM) study [24], which included vibrational effects also. Apparently the vibrational effects play a minor role.

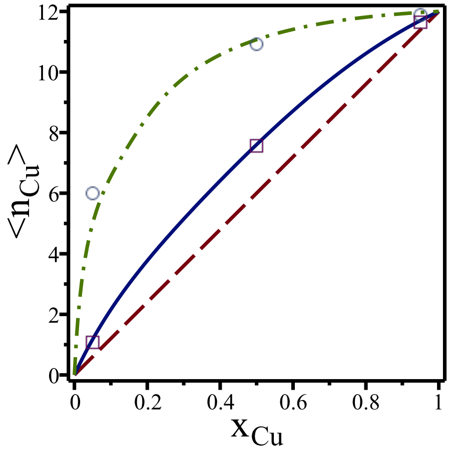

Figure 4.13: The average number of Cu neighbors around a vacancy $\langle n_{Cu} \rangle$ at T=200 K (dash-dotted line), at T=800 K (solid line), and as extrapolated to infinite temperature (dashed line), as function of the composition. The results predicted by Zhao et al. [24] are indicated as symbols: T=200 K data (circles); T=800 K data (squares).

Instead of using the model introduced here, the CVM can be used to compute the vacancy concentration. The CVM in the tetrahedron approximation was used in conjuction with the CE listed in table 4.4. The computed vacancy concentrations differ a few percent only from those computed with the current random model over a wide range of temperatures and compositions, see figure 4.14, in spite of the fact that the CVM includes the effect of short-range order. The current model can be compared also with the quasi-chemical model as studied in much detail by Schapink [38]. The quasi-chemical approach too, like the CVM, yields vacancy concentrations that differ by a few percent from the values obtained with the current model. Other properties differ little between current and quasi-chemical, in the case of the vacancy formation free energy the difference is just 5 meV or less. In contrast to the earlier work [24, 30, 36, 38], the current model can be implemented using a spreadsheet, no special software required.

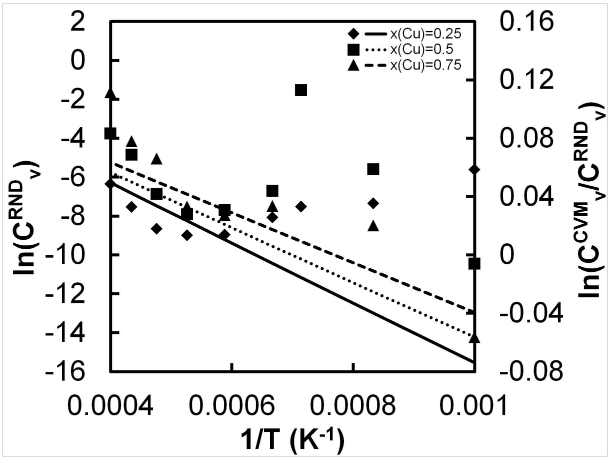

Figure 4.14: Vacancy concentration C_v^{RND} as computed with the current model as function of inverse temperature β in $\mathrm{Cu}_{0.25}\mathrm{Ni}_{0.75}$ (solid line), $\mathrm{Cu}_{0.5}\mathrm{Ni}_{0.5}$ (dotted line), $\mathrm{Cu}_{0.75}\mathrm{Ni}_{0.25}$ (dashed line). Comparison between current model and CVM is indicated with symbols with reference to the axis on the right: $\mathrm{Cu}_{0.25}\mathrm{Ni}_{0.75}$ (diamonds), $\mathrm{Cu}_{0.5}\mathrm{Ni}_{0.5}$ (squares), $\mathrm{Cu}_{0.75}\mathrm{Ni}_{0.25}$ (triangles).

4.4.2. Alloy with ordering tendency

It is of interest to examine whether the trends revealed for vacancy formation in phase separating alloys, such as Cu-Ni, also apply to alloys with ordering tendencies. Therefore, we examine an alloy with nearest neighbor pair interactions between A and B atoms such that the enthalpy of mixing at equiatomic composition is -300 meV/atom. These interactions, listed in table 4.5, are not *ab initio* and do not pertain to any real alloy system. They are selected to serve as illustration only. The interactions give the "classical" fcc phase diagram [78–81] for the solid state A-B alloy with a critical order-disorder temperature of about 1100 K at equiatomic composition. Concerning the vacancy formation energies in pure A and B, we consider two cases: a) the strong asymmetric case with vacancy formation energies in pure A (B) of 2 (1) eV; and b) the weak asymmetric case with vacancy formation energies in pure A (B) of 1.2 (1) eV.

The vacancy formation enthalpies $\Delta H_{vac(i)}^{(\alpha)}$ at equiatomic composition as computed with eqn. 4.17 are shown in figure 4.15. Due to the elimination of nearest neighbor equilateral triangle ECIs, $\Delta H_{vac(i)}^{(\alpha)}$ of A-vacated and B-vacated vacancies for different α have become linear functions of the number of B atoms in the nearest neighbor shell, n_B,

Table 4.5: Effective cluster interactions (ECIs) in a hypothetical ordering A-B alloy.

Cluster	ECI(meV/cluster)	
	Case (a)	Case (b)
J_v	2000	1200
J_B	-1200	-1200
$J_{v\text{-}B}$	16.7	83.3
$J_{B\text{-}B}$	200	200

crossing at $n_B = 6$. Unlike a phase separating system like Cu-Ni, for a specific shell, $\Delta H^{(\alpha)}_{vac(i)}$ of A-vacated vacancies is higher (lower) than that of B-vacated vacancies in B-rich (A-rich) shells because A-B bonds require more energy to be broken than the weighted average of A-A and B-B bonds. Furthermore, as expected, in case b) the A and B vacated energies are much more similar than in case a).

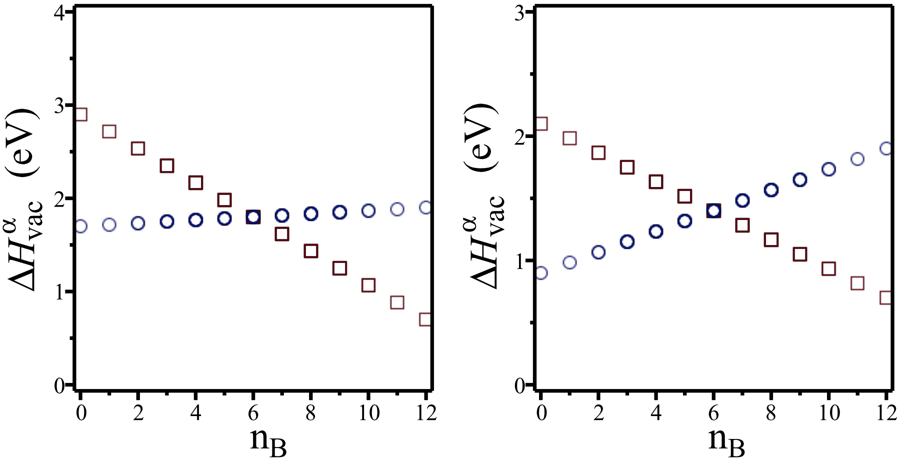

Figure 4.15: Vacancy formation enthalpy $\Delta H^{(\alpha)}_{vac(i)}(x_B = 0.5)$ at T = 0 K according to eqn. 4.17 as a function of the number of B atoms in the nearest neighbor shell n_B, A-vacated (open circles), B-vacated (open squares) vacancy. Panels correspond to cases a) and b) described in the text.

The effective Gibbs energy of vacancy formation, ΔG^{eff}_{vac} (eqn. 4.29) as function of the composition is curved upward, quite unlike the phase separating case, from the linear interpolation between the pure A and B end members. The deviation is rather similar in magnitude to the negative of the mixing enthalpy, $-\Delta H_{mix}$, both for case (a) and for case (b)(Fig.4.16). As in the phase separating Cu-Ni alloy, the configurational contribution to the vacancy formation entropy (eqn. 4.30) is negative. The reason for this is entirely the same as in the case of phase separation, at higher temperatures energetically less favorable configurations come into play.

The asymmetry in the endmember vacancy formation energy does have a very pronounced effect on the short range order around a vacancy. Vacancy properties such as the configurational contribution to the entropy shift to more negative value when the pure end

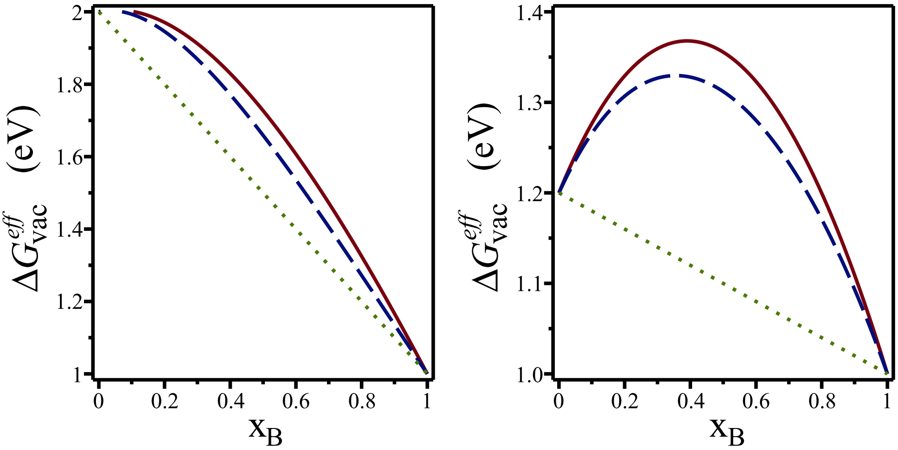

Figure 4.16: Effective vacancy formation Gibbs energy in an A-B ordering alloy as a function of the composition at T = 4000 K (solid line) and T = 2000 K (dashed line). Dotted line is the linear interpolation between the pure elements. Panels correspond to cases a) and b) described in the text.

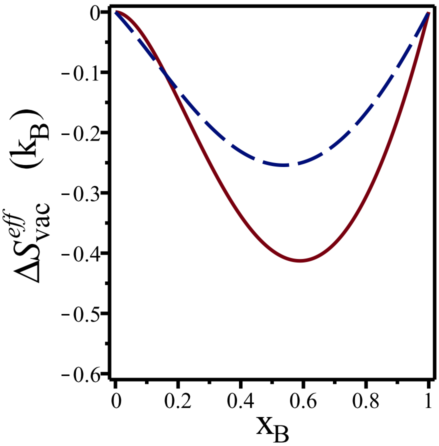

Figure 4.17: Effective vacancy formation entropy of an A-B ordering alloy as function of composition: case a) (solid line) and case b) (dashed line).

member difference is larger (see figure. 4.17).

Ordering systems, with interactions of the same magnitude as phase separating systems, develop vacancy-vacancy-pairs already at a lower temperature. Therefore, the comparison between the current model and a more accurate methodology such as the cluster variation method or lattice Monte Carlo begins to break down at a lower temperature than was the case for phase separating systems. For alloys with ordering tendencies vacancy-vacancy-pairs begin to play a role above about twice the highest order-disorder temperature.

4.5. Conclusions

A formalism for the computation of vacancy formation energies in substitutional alloys has been presented. It is shown that composition and temperature play an important role in the thermodynamics of vacancies in alloys. The current approach, consisting of a cluster expansion coupled with a simple statistical thermodynamics model, has been shown to reproduce accurately the features of more sophisticated lattice gas models such a the quasi-chemical or cluster variation methods. The effective vacancy formation free energy deviates from the linear interpolation between that of the terminal pure phases in a manner opposite to the mixing enthalpy between those end members. Therefore, phase separating alloys have vacancy formation free energies that are less than the composition-weighted average of the end members, while the opposite holds in ordering type alloys. At low temperatures, the configurational contribution to the vacancy formation entropy is negative. This is caused by the fact that at low temperature vacancies will occur only in the energetically most favorable local neighborhoods in the alloy, while at higher temperatures also less energetically favorable neighborhoods come into play. In addition to ordering and phase separating tendencies, the asymmetry in the vacancy formation energy in the pure end-members plays a significant role also. When the vacancy formation energies of the pure end members differ more strongly from one another, the excess vacancy properties in the alloy become more significant. Particularly, the configurational contribution to the entropy of vacancy formation becomes more negative, and the vacancy coordination departs stronger from the average, as the asymmetry in vacancy formation energies between the pure end-members increases. In the current model pure vacancy clusters are not considered, so that at high temperature deviations from more accurate lattice gas models occur. These deviations are more significant for ordering type alloys than for phase separating alloys. It must be noted that in order to understand vacancy formation in substitutional alloys a few arbitrarily selected ab initio calculations on alloy supercells with vacancies generally will not suffice. A proper statistical thermodynamic analysis is required. As this work has shown, such a thermodynamic analysis need not be very complex fortunately.

Vacancies in the Cu-Ni system were shown to prefer Cu neighbors, regardless of the composition of the alloy. The vacancy formation free energy was shown to be strongly composition dependent, with lower values towards the Cu-rich side. Since the vacancy formation energy in binary disordered alloys strongly depends on local environment, a cluster expansion was shown to be the optimal approach. Effective cluster interactions(ECIs) in terms of point, nearest neighbor pair and nearst neighbor equilateral triangle clusters were extracted from a ternary cluster expansion by fitting the energies of 71 structures. The ECIs were used also to calculate the mixing enthalpy of the solid solution and the solid portion of the Cu-Ni phase diagram, which both agreed well with previous assessments. The CE approach coupled with a simple thermodynamic model made it possible to compute vacancy concentrations as a continuous function of temperature and composition. Fitting the vacancy concentration to an Arrhenius equation allowed us to extract the effective Gibbs energy of vacancy formation as function of temperature and composition. The effective Gibbs energy of vacancy formation was found to be a non-linear function of composition with a deviation from linearity between the endmembers that was roughly equal to the negative value of the mixing enthalpy. The effective configurational entropy of vacancy formation was found to be composition dependent and negative with values ranging from about 0 to -0.5$\times k_B$.

References

[1] A. Janotti, M. Krčmar, C. L. Fu, and R. C. Reed, *Solute diffusion in metals: Larger atoms can move faster,* Physical Review Letters **92**, 085901 (2004).

[2] C. Domain and C. Becquart, *Diffusion of phosphorus in α-Fe: An ab initio study,* Physical Review B **71**, 214109 (2005).

[3] N. Sandberg and R. Holmestad, *First-principles calculations of impurity diffusion activation energies in Al,* Physical Review B **73**, 014108 (2006).

[4] D. Simonovic and M. H. F. Sluiter, *Impurity diffusion activation energies in Al from first principles,* Physical Review B **79**, 054304 (2009).

[5] M. Mantina, Y. Wang, L. Q. Chen, Z. K. Liu, and C. Wolverton, *First principles impurity diffusion coefficients,* Acta Materialia **57**, 4102 (2009).

[6] T. R. Mattsson, N. Sandberg, R. Armiento, and A. E. Mattsson, *Quantifying the anomalous self-diffusion in molybdenum with first-principles simulations,* Physical Review B **80**, 224104 (2009).

[7] S. Huang, D. L. Worthington, M. Asta, V. Ozolins, G. Ghosh, and P. K. Liaw, *Calculation of impurity diffusivities in α-Fe using first-principles methods,* Acta Materialia **58**, 1982 (2010).

[8] S. Choudhury, L. Barnard, and J. Tucker, *Ab-initio based modeling of diffusion in dilute bcc Fe-Ni and Fe-Cr alloys and implications for radiation induced segregation,* Journal of Nuclear Materials **411**, 1 (2011).

[9] K. M. Carling, G. Wahnström, T. R. Mattsson, N. Sandberg, and G. Grimvall, *Vacancy concentration in Al from combined first-principles and model potential calculations,* Physical Review B **67**, 054101 (2003).

[10] B. Grabowski, L. Ismer, T. Hickel, and J. Neugebauer, *Ab initio up to the melting point: Anharmonicity and vacancies in aluminum,* Physical Review B **79**, 134106 (2009).

[11] B. Grabowski, T. Hickel, and J. Neugebauer, *Formation energies of point defects at finite temperatures,* Physica Status Solidi (b) **248**, 1295 (2011).

[12] C. L. Fu, Y.-Y. Ye, M. H. Yoo, and K. M. Ho, *Equilibrium point defects in intermetallics with the B2 structure: NiAl and FeAl,* Physical Review B **48**, 6712 (1993).

[13] Y. Mishin and D. Farkas, *Atomistic simulation of point defects and diffusion in B2 NiAl,* Philosophical Magazine A **75**, 169 (1997).

[14] M. Hagen and M. W. Finnis, *Point defects and chemical potentials in ordered alloys,* Philosophical Magazine A **77**, 447 (1998).

[15] B. Meyer and M. Fähnle, *Atomic defects in the ordered compound B2-NiAl: A combination of ab initio electron theory and statistical mechanics,* Physical Review B **59**, 6072 (1999).

[16] P. A. Korzhavyi, A. V. Ruban, A. Y. Lozovoi, Y. K. Vekilov, I. A. Abrikosov, and B. Johansson, *Constitutional and thermal point defects in B2 NiAl,* Physical Review B **61**, 6003 (2000).

[17] J. Mayer, C. Elsässer, and M. Fähnle, *Concentrations of Atomic Defects in B2-* Fe_xAl_{1-x}*. An ab initio study,* physica status solidi (b) **191**, 283 (1995).

[18] R. Krachler and H. Ipser, *Application of the grand canonical ensemble to the study of equilibrium point defect concentrations in binary intermetallic phases with the B2-structure,* Intermetallics **7**, 141 (1999).

[19] S. Foiles and M. Daw, *Application of the embedded atom method to* Ni_3Al*,* Journal of Materials Research **2**, 5 (1987).

[20] P. Ehrhart, P. Jung, H. Schultz, and H. Ullmaier, *Concentrated alloys,* in *Atomic Defects in Metals*, Landolt-Börnstein - Group III Condensed Matter, Vol. 25, edited by H. Ullmaier (Springer Berlin, 1991).

[21] Y. Kraftmakher, *Equilibrium vacancies and thermophysical properties of metals,* Physics Reports-Review Section of Physics Letters **299**, 80 (1998).

[22] J. Dorn and J. Mitchell, *Vacancies in binary alloys,* Acta Metallurgica **14**, 70 (1966).

[23] S. Tanigawa and M. Doyama, *The formation energy of a vacancy in disordered binary alloys,* Physics Letters A **54**, 455 (1975).

[24] L. Zhao, R. Najafabadi, and D. J. Srolovitz, *Statistical mechanical-atomistic determination of vacancy formation free energies in Cu-Ni alloys,* Philosophical Magazine A **70**, 519 (1994).

[25] L. Zhao, R. Najafabadi, and D. Srolovitz, *Determination of vacancy and atomic diffusivities in solid solution alloys,* Acta materialia **44**, 2737 (1996).

[26] P. Venezuela, G. M. Dalpian, A. J. R. da Silva, and A. Fazzio, *Vacancy-mediated diffusion in disordered alloys: Ge self-diffusion in* $\mathrm{Si}_{1-x}\mathrm{Ge}_x$, Physical Review B **65**, 193306 (2002).

[27] M. Muzyk, D. Nguyen-Manh, K. J. Kurzydłowski, N. L. Baluc, and S. L. Dudarev, *Phase stability, point defects, and elastic properties of W-V and W-Ta alloys,* Physical Review B **84**, 104115 (2011).

[28] E. del Rio, J. M. Sampedro, H. Dogo, M. J. Caturla, M. Caro, A. Caro, and J. M. Perlado, *Formation energy of vacancies in FeCr alloys: Dependence on Cr concentration,* Journal of Nuclear Materials **408**, 18 (2011).

[29] J. B. Piochaud, T. P. C. Klaver, G. Adjanor, P. Olsson, C. Domain, and C. S. Becquart, *First-principles study of point defects in an fcc Fe-10Ni-20Cr model alloy,* Physical Review B **89**, 024101 (2014).

[30] F. Lechermann and M. Fähnle, *Ab initio statistical mechanics for alloy phase diagrams and ordering phenomena including the effect of vacancies,* Physical Review B **63**, 012104 (2000).

[31] A. Van der Ven and G. Ceder, *Vacancies in ordered and disordered binary alloys treated with the cluster expansion,* Physical Review B **71**, 054102 (2005).

[32] A. Van der Ven and G. Ceder, *First principles calculation of the interdiffusion coefficient in binary alloys,* Physical Review Letters **94**, 045901 (2005).

[33] A. Van der Ven, H.-C. Yu, G. Ceder, and K. Thornton, *Vacancy mediated substitutional diffusion in binary crystalline solids,* Progress in Materials Science **55**, 61 (2010).

[34] G. L. W. Hart and A. Zunger, *Origins of Nonstoichiometry and Vacancy Ordering in* $\mathrm{Sc}_{1-x}\Box_x S$, Physical Review Letters **87**, 275508 (2001).

[35] W. M. Lomer, *Point defects and diffusion in metals and alloys,* in *Vacancies and other point defects in metals and alloys, Monograph and Report Series 23* (Institute of Metals (London), 1958) pp. 79–98.

[36] L. Girifalco, *Vacancy concentration and diffusion in order-disorder alloys,* Journal of Physics and Chemistry of Solids **25**, 323 (1964).

[37] R. E. Howard and A. B. Lidiard, *Matter transport in solids,* Reports on Progress in Physics **27**, 161 (1964).

[38] F. W. Schapink, *Thermodynamics of vacancies in binary alloys,* Philosophical Magazine **12**, 1055 (1965).

[39] S. Masharov, *Equilibrium vacancy concentration in disordered binary alloys,* Soviet Physics Journal **15**, 694 (1972).

[40] S. M. Kim, *Vacancy formation energies in disordered alloys,* Physical Review B **30**, 4829 (1984).

[41] A. R. Allnatt and A. B. Lidiard, *Atomic Transport in Solids* (Cambridge University Press, 1993).

[42] O. Gorbatov, P. Korzhavyi, A. Ruban, B. Johansson, and Y. Gornostyrev, *Vacancy-solute interactions in ferromagnetic and paramagnetic bcc iron: Ab initio calculations,* Journal of Nuclear Materials **419**, 248 (2011).

[43] L. Delczeg, B. Johansson, and L. Vitos, *Ab initio description of monovacancies in paramagnetic austenitic Fe-Cr-Ni alloys,* Physical Review B **85**, 174101 (2012).

[44] A. Zunger, S.-H. Wei, L. G. Ferreira, and J. E. Bernard, *Special quasirandom structures,* Physical Review Letters **65**, 353 (1990).

[45] S. B. Zhang and J. E. Northrup, *Chemical potential dependence of defect formation energies in GaAs: Application to Ga self-diffusion,* Physical Review Letters **67**, 2339 (1991).

[46] L. E. Ramos, J. Furthmüller, F. Bechstedt, L. M. R. Scolfaro, and J. R. Leite, *Ab initio theory of native defects in alloys: application to charged N vacancies in* $Al_xGa_{1-x}N$, Journal of Physics: Condensed Matter **14**, 2577 (2002).

[47] P. C. Clapp, *Atomic configurations in binary alloys,* Physical Review B **4**, 255 (1971).

[48] J. Sanchez and J. Moran-Lopez, *Pseudo-three dimensional model of oxygen ordering in* $YBa_2Cu_3O_{6+\delta}$, Solid State Communications **79**, 151 (1991).

[49] C. Wolverton and A. Zunger, *Cation and vacancy ordering in* $\mathrm{Li}_x\mathrm{CoO}_2$, Physical Review B **57**, 2242 (1998).

[50] F. Ducastelle and F. Gautier, *Generalized perturbation theory in disordered transitional alloys: Applications to the calculation of ordering energies,* Journal of Physics F: Metal Physics **6**, 2039 (1976).

[51] M. H. F. Sluiter and Y. Kawazoe, *Site preference of ternary additions in* Ni_3Al, Physical Review B **51**, 4062 (1995).

[52] M. H. F. Sluiter and Y. Kawazoe, *Cluster expansion method for adsorption: Application to hydrogen chemisorption on graphene,* Physical Review B **68**, 085410 (2003).

[53] G. Ceder, M. Asta, W. C. Carter, M. Kraitchman, D. de Fontaine, M. E. Mann, and M. H. F. Sluiter, *Phase diagram and low-temperature behavior of oxygen ordering in* $\mathrm{YBa_2Cu_3O}_z$ *using ab initio interactions,* Physical Review B **41**, 8698 (1990).

[54] P. A. Korzhavyi, L. V. Pourovskii, H. W. Hugosson, A. V. Ruban, and B. Johansson, *Ab Initio study of phase equilibria in* TiC_x, Physical Review Letters **88**, 015505 (2001).

[55] M. H. F. Sluiter and Y. Kawazoe, *Invariance of truncated cluster expansions for first-principles alloy thermodynamics,* Physical Review B **71**, 212201 (2005).

[56] G. D. Garbulsky and G. Ceder, *Effect of lattice vibrations on the ordering tendencies in substitutional binary alloys,* Physical Review B **49**, 6327 (1994).

[57] D. de Fontaine, *Cluster approach to order-disorder transformations in alloys,* in *Solid State Physics*, Vol. 47, edited by F. Seitz, H. Ehrenreich, and D. Tumbull (Academic Press, New York, 1994) pp. 33–176.

[58] J. Epperson, *Determination of local atomic configurations for binary substitutional alloys,* Journal of Applied Crystallography **12**, 351 (1979).

[59] J. Connolly and A. Williams, *Density-functional theory applied to phase transformations in transition-metal alloys,* Physical Review B **27**, 5169 (1983).

[60] M. H. F. Sluiter, D. de Fontaine, X. Q. Guo, R. Podloucky, and A. J. Freeman, *First-principles calculation of phase equilibria in the aluminum lithium system,* Physical Review B **42**, 10460 (1990).

[61] M. H. F. Sluiter and Y. Kawazoe, *Prediction of the mixing enthalpy of alloys,* Europhysics Letters **57**, 526 (2002).

[62] J. Perdew, K. Burke, and M. Ernzerhof, *Generalized gradient approximation made simple,* Physical Review Letters **77**, 3865 (1996).

[63] J. P. Perdew, K. Burke, and M. Ernzerhof, *Generalized gradient approximation made simple,* Physical Review Letters **78**, 1396 (1997).

[64] G. Kresse and J. Furthmüller, *Efficiency of ab-initio total energy calculations for metals and semiconductors using a plane-wave basis set,* Computational Materials Science **6**, 15 (1996).

[65] G. Kresse and J. Furthmüller, *Efficient iterative schemes for ab initio total-energy calculations using a plane-wave basis set,* Physical Review B **54**, 11169 (1996).

[66] G. Kresse and D. Joubert, *From ultrasoft pseudopotentials to the projector augmented-wave method,* Physical Review B **59**, 1758 (1999).

[67] M. H. F. Sluiter, Y. Watanabe, D. de Fontaine, and Y. Kawazoe, *First-principles calculation of the pressure dependence of phase equilibria in the Al-Li system,* Physical Review B **53**, 6137 (1996).

[68] M. H. F. Sluiter, C. Colinet, and A. Pasturel, *Ab initio calculation of the phase stability in Au-Pd and Ag-Pt alloys,* Physical Review B **73**, 174204 (2006).

[69] A. Glensk, B. Grabowski, T. Hickel, and J. Neugebauer, *Breakdown of the Arrhenius Law in Describing Vacancy Formation Energies: The Importance of Local Anharmonicity Revealed by Ab initio Thermodynamics,* Physical Review X **4**, 011018 (2014).

[70] R. Armiento and A. E. Mattsson, *Functional designed to include surface effects in self-consistent density functional theory,* Physical Review B **72**, 085108 (2005).

[71] L. Delczeg, E. K. Delczeg-Czirjak, B. Johansson, and L. Vitos, *Assessing common density functional approximations for the ab initio description of monovacancies in metals,* Physical Review B **80**, 205121 (2009).

[72] R. Nazarov, T. Hickel, and J. Neugebauer, *Vacancy formation energies in fcc metals: Influence of exchange-correlation functionals and correction schemes,* Physical Review B **85**, 144118 (2012).

[73] H.-E. Schaefer, *Investigation of thermal equilibrium vacancies in metals by positron annihilation,* Physica Status Solidi (a) **102**, 47 (1987).

[74] E. H. Megchiche, S. Pérusin, J.-C. Barthelat, and C. Mijoule, *Density functional calculations of the formation and migration enthalpies of monovacancies in Ni: Comparison of local and nonlocal approaches,* Physical Review B **74**, 064111 (2006).

[75] A. Van de Walle, M. Asta, and G. Ceder, *The alloy theoretic automated toolkit: A user guide,* Calphad-Computer Coupling of Phase Diagrams and Thermochemistry **26**, 539 (2002).

[76] S. an Mey, *Thermodynamic Reevaluation of the Cu-Ni System,* Calphad-Computer Coupling of Phase Diagrams and Thermochemistry **16**, 255 (1992).

[77] D. J. Chakrabarti, D. E. Laughlin, S. W. Chen, and Y. A. Chang, *Cu-Ni (copper-nickel),* in *Phase Diagrams of Binary Copper Alloys*, edited by P. R. Subramanian, D. J. Chakrabarti, and D. E. Laughlin (ASM International, Materials Park, OH, 1994) pp. 276–286.

[78] C. van Baal, *Order-disorder transformations in a generalized Ising alloy,* Physica **64**, 571 (1973).

[79] R. Kikuchi, *Superposition approximation and natural iteration calculation in cluster variation method,* The Journal of Chemical Physics **60**, 1071 (1974).

[80] J. M. Sanchez, D. de Fontaine, and W. Teitler, *Comparison of approximate methods for the study of antiferromagnetism in the fcc lattice,* Physical Review B **26**, 1465 (1982).

[81] A. Finel and F. Ducastelle, *On the phase diagram of the fcc Ising model with antiferromagnetic first-neighbour interactions,* Europhysics Letters **1**, 135 (1986).

5

Cluster expansions for realistic precipitation kinetics: An application to Guinier-Preston zone formation in an Al-Cu alloy

A method for performing kinetic lattice gas Monte Carlo simulations for the early stages of clustering and precipitation in substitutional alloys is presented and applied. Cluster expansions are used both for the thermodynamic states and for configuration dependent diffusion activation barriers in order to simulate realistically both thermodynamic driving forces and kinetic pathways. The method is applied to an aluminium 2 atomic percent copper alloy. The cluster expansion is shown to be capable of describing the morphology of Guinier-Preston (GP) zones of type I and II although it requires a large set of effective cluster interactions. The configuration dependence, and thereby the local composition dependence, of diffusivities is investigated in detail. It is found that in Al-Cu diffusion activation energies vary by a factor of five depending on the local distribution of Al and Cu atoms. The kinetics and evolution of clustering and precipitation is shown to differ significantly when modeled using constant or local configuration dependent activation barriers for diffusion. Although both constant and local configuration dependent activation diffusion barriers yield the experimentally observed succession of GP-I and GP-II zones in Al-Cu alloys, the details of the early stages of precipitation differ significantly.

5.1. Introduction

Understanding and realistically modeling the kinetics of precipitation has been an objective for many years in part because of precipitation hardening is used is many metallic materials [1, 2]. A great variety of computational approaches exist, range from continuum [3–5] to atomistic [6]. Experimentally too, it has been realized that still, important improvements in the precipitation hardening are possible [7–9]. Recent focus has been on temporarily trapping and later controlled releasing of excess vacancies that are retained in the solid solution after quenching from the solutionizing treatment [9–11]. Especially for retardation of natural aging vacancy trapping by impurity atoms has proven useful, such as via Sn impurities in Al-Mg-Si alloys. The idea is that vacancies are trapped at room temperature and below, and are released again when the alloy, after quenching and storage at ambient, is brought to aging temperature. It requires an impurity with a specific vacancy binding energy, neither too weak nor too strong, and with sufficient solubility in the matrix without overly strong intermetallic formation with the other constituents of the alloy. Clearly, impurity-vacancy binding must be included into an atomistic description of precipitation kinetics to get realistic results. Therefore, precipitation in an alloy with two constituents must be considered as a ternary, the two atomic species, and the vacancy as a third species [12, 13].

The energetics of distributing various atomic species on a lattice is nowadays routinely modeled using cluster expansions (CEs) [14–17] which provides an expedient coupling between ab initio electronic density functional energy calculations and configurational thermodynamics [18]. It has become also possible to model diffusion activation barriers through local CEs [19–21]. It has been found that diffusion in solid solutions is highly dependent on the local configuration around a vacancy [20, 21]. This makes a common assumption [3, 6, 22] that diffusivity in an alloy can be approximated by dilute impurity diffusion highly suspect. Van der Ven and Ceder [20] showed that vacancy concentrations varied with alloy composition and with state of order. Moreover, recently it was shown that the local configurational dependence of diffusion activation barriers can give rise to transient ordered states even if thermodynamically the alloy is of pure phase separating type [23]. These findings suggest that modeling precipitation with knowledge of configurational thermodynamics of the alloy and of vacancy-impurity interaction is not sufficient.

In this study we will consider a particularly challenging alloy, Al-Cu, that has been well studied from both the experimental [24, 25] and the thermodynamic aspects [6, 26, 27]. A proper description of the configurational thermodynamics of Guinier-Preston (GP) [25, 28] zones that form during the initial stages of precipitation requires a complicated CE [26, 27], while the local atomic configuration near a vacancy is known to strongly affect the kinetics in this alloy [21]. Although describing the GP zones properly is a *sine qua non*, our main focus will be on a proper accounting of the configurational dependence of the diffusivity in the alloy and how this affects both the time scale of the precipitation process and the morphology. These latter two are also, of course, of great practical importance for all precipitation hardened alloys.

5.2. Theory and methodology

We use the cluster expansion formalism to efficiently evaluate the energetics of atomic configurations *and* of activation barriers for diffusion [20, 21]. Although the formalism is applied to a binary alloy, it is applicable to multicomponent systems without much additional computational effort [21].

The kinetics of the precipitation evolution is determined by the rate at which configurations evolve. According to the transition state theory (TST), the transition rates between state i and state j are computed as,

$$r_{i\leftrightarrow j} = \nu \exp[-\beta(E_{\text{KRA}} + \frac{1}{2}\Delta E^{i\leftrightarrow j}_{\text{conf}})], \tag{5.1}$$

where ν is the atomic jump attempt frequency, β is the reciprocal temperature $\frac{1}{k_B T}$, $\Delta E^{i\leftrightarrow j}_{\text{conf}}$ refers to the configurational energy change between state i and state j and E_{KRA} is the kinetically resolved activation (KRA) barrier [19, 20]. When transition rates are known, the configuration evolution and the kinetics can be monitored by tracking the vacancy in a kinetic Monte Carlo (KMC) simulation with n-fold way algorithm [29].

5.2.1. Cluster expansion for the configurational energetics,

At the early stages of precipitation in fcc Al-based alloys, GP zones are generally coherent with the parent matrix. Such a feature greatly reduces the degrees of freedom in describing the interatomic potential. Atom-vacancy exchanges can therefore be restricted on a fixed (fcc) crystalline lattice. It follows that the effective interatomic interactions can be obtained by cluster expansions. Therefore we elaborate the A-B-C ternary CE to describe the configurational energy, E_{conf}.

$$E_{\text{conf}} = \sum_{\alpha} n^{ABC}_{\alpha} J^{ABC}_{\alpha}, \tag{5.2}$$

where A refers to aluminum, B to copper and C to vacancies [13, 19], α indicates a particular cluster selected from an “N4R8” cluster pool [21], n_α is a counter for the number of α-type clusters per lattice site, and J_α is the corresponding effective cluster interaction (ECI). We neglect vacancy-vacancy interactions since multi-vacancy clusters are rare at the early stages of precipitation.

The structures used for extracting ECIs are selected through an “evolutionary” procedure. Initially, energies of a small set of about 60 supercell structures are obtained via *ab initio* DFT calculations. An initial CE is then obtained from the set of structural energies (SSE). This CE is then used to search for low energy structures in a pre-defined “structure pool” (SP), i.e., a large set of some 30000 structures. The SP is generated automatically with the restrictions that a) each primitive unit cell contains 16 atoms or less, and b) that all three primitive translations can be selected simultaneously such that their length is two fcc lattice parameters or less. When low energy structures are found, their energies are computed *ab initio* and the ab initio energies are added to the SSE. The new, expanded SSE is used to generate a new CE, and again we search for low energy structures in the SP. We repeat this, until no new low energy structures are found and the leave-one-out cross validation

(LOOCV) score of the CE is sufficiently small. Using this procedure, 80 ECIs are extracted from 228 *ab initio* energies; 160 structures without vacancy and 68 structures with a single vacancy. The LOOCV score of the CE is less than 2.8 meV/atom.

5.2.2. Local cluster expansions for KRA barriers

Having addressed the calculation of the configurational energetics, the main remaining issue in Eq. (6.3) is the evaluation of the kinetically resolved activation barriers E_{KRA} which play a critical role in the kinetics. Eq. (6.3) reveals that decreasing the KRA barrier by 0.1 eV accelerates the exchange between atom and vacancy by a factor of 50 at room temperature. To determine the local configurational dependence of the KRA barriers as reported in Ref. [19, 21, 30], we examined the KRA barriers for 42 typical structures in Al-Cu alloys using the climbing image nudged elastic band (CI-NEB) method [31, 32] and show the results in Fig. 5.1. Fig. 5.1 shows that KRA barriers vary over a wide range from about 0.2 eV to 1 eV. This means that for different local atomic configurations the KRA barriers in Al-Cu alloys are likely to vary by a factor of 5 or more. The constant activation barrier assumption employed in previous studies [33–35] is therefore quite severe. The diffusion activation barriers for Al self diffusion and Cu impurity diffusion in pure fcc Al have been reported theoretically as 0.51 eV and 0.44 eV respectively [36]. In this study slightly larger barriers were found, 0.64 eV and 0.55 eV for Al self diffusion and Cu impurity diffusion in pure fcc Al, respectively. It is apparent that the local configuration can both decrease and increase the KRA barriers in concentrated alloys.

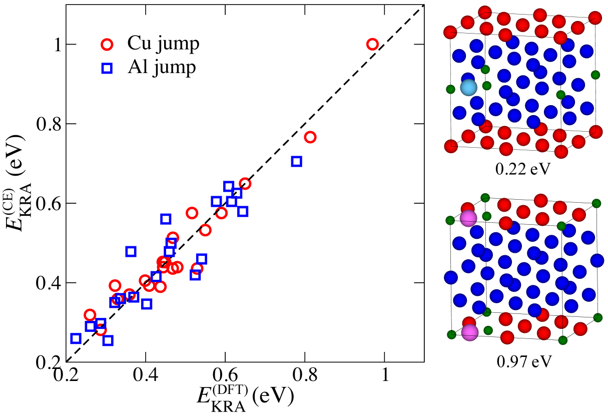

Figure 5.1: A comparison of KRA barriers from *ab initio* DFT calculations and as calculated with the local cluster expansion in Al-Cu alloys. Red open circles (blue open squares) represent the KRA barriers for Cu (Al) as the jumping atom. Two examples of supercells with very small and very high KRA barriers are shown also. Red (blue) spheres: Cu (Al), large pink (light blue) spheres: Cu (Al) in a transition state, small green spheres: half vacancy. The numbers below the supercells are the corresponding KRA barriers.

To achieve an accurate and computationally efficient description of local configuration dependent KRA barriers, a local cluster expansion appears a sensible approach. However, in the activated state the jumping atom is positioned at the saddle point between two lattice sites (see Fig. 5.2), and it is no longer uniquely associated with a single lattice site. This violates the lattice gas concept, that forms the basis for CEs, where every site is associated with one, and only one, atomic species. Fortunately, such a lattice gas violation problem can also be resolved by introducing a new atomic species for the vacancy-jumping atom pair, “swapping pair” for brevity, as displayed in Fig. 5.2. In the present low vacancy concentration simulations, it is reasonable to introduce only a single vacancy in the alloy because the number vacancy-vacancy pairs are assumed to be negligible. When a single vacancy is present in an N-component alloy (here N=3: species A, B and vacancy “C”), replacing the swapping pair by two “atoms” of a new atomic species, results in $N-1$ new N-component systems. Thus the complexity of the problem is not significantly increased. Namely, the “A(B)-vac” pair is replaced by a “D-D” (“E-E”) pair to establish an A-B-D(E) ternary system (see Fig. 5.2, right side). A local CE should depend only on atomic occupancy right near the swapping pair. This is easily achieved by selecting only correlation functions that encompass the swapping pair. We emphasize that the whole pair should be included because otherwise correlation functions may not be properly distinguished, as illustrated in Fig. 5.3. The reason for this is that the introduction of the swapping pair has eliminated many operations from the symmetry group of the underlying disordered crystal structure. Only symmetry operations that preserve the swapping pair can be retained. As the local CE retains only correlations that contain the swapping pair, it is apparent that such a local CE is NOT complete [37], because subclusters that contain only one or no sites of the swapping pair, are excluded. The local CE can be expressed as

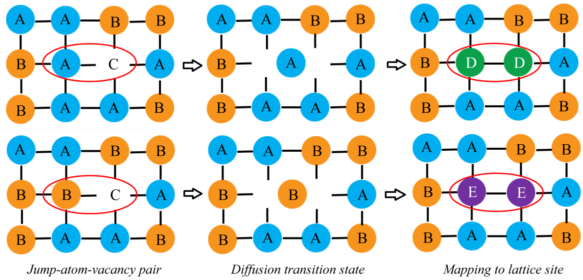

Figure 5.2: schematic diagram of the concept “*vacancy-jumping atom pair*”(left side). Transition states (middle side) in a binary alloy with vacancies are mapped onto a lattice gas featuring two distinct ternaries(right side).

$$E_{\text{KRA}} = \sum_{\alpha} \sigma_{\alpha\cup\gamma} J_{\alpha\cup\gamma} \tag{5.3}$$

Where α represents a cluster decoration corresponding to the empty cluster, or a point cluster, etc. but not part of the swapping pair, γ represents the swapping pair, $\sigma_{\alpha\cup\gamma}$ is a counter for the number of cluster decorations of type $\alpha\cup\gamma$, and J is the corresponding ECI. $\sigma_{\alpha\cup\gamma}$ has a maximum value $\mu_{\alpha\cup\gamma}$ that is determined by its symmetry, e.g. for the decorations encircled by the blue oval in Fig. 5.3 it is 4 (left side) and 2 (right side).

Another aspect of the E_{KRA} local CE is that it should generally yield positive values for all possible local neighborhoods. Unlike configurational energies which can be both positive and negative, here only positive energies are desired. In the local CE occurrences of cluster decorations are counted. As these occurrences can be counted using positive

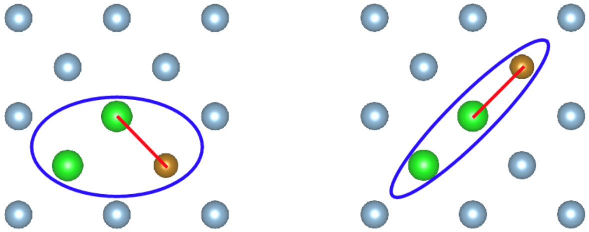

Figure 5.3: Green spheres indicate the swapping pair on a (100) plane in fcc. In the local CE, the pair (indicated by the red line) on the left and the pair on the right are not equivalent but are not properly distinguished when applying the symmetry of the underlying lattice gas. However, when the swapping pair is completely included, as in the clusters enclosed by the blue lines, the inequivalence is readily apparent.

numbers only, it is tempting to assume that a strictly positive expansion can be obtained by requiring all ECI non-negative. However, this is a too severe restriction for obtaining a good CE. A less severe restriction can be designed when it is recognized that in pure Al a positive E_{KRA} exists. It implies that interaction J_{α^*} corresponding to the empty cluster α^* must be positive. Now, we can assure positive definite E_{KRA} provided that

$$J_{\alpha^*} + \frac{1}{2}\sum_{\alpha}{}' \mu_{\alpha\cup\gamma}\left(J_{\alpha\cup\gamma} - |J_{\alpha\cup\gamma}|\right) > 0 \tag{5.4}$$

where prime in the sum indicates that the empty cluster is excluded. This condition is easily implemented in the so-called aufbau and enumeration methods for finding good CEs [21].

An alternate method is to generate a testing set: a large number of local configurations around the swapping pair, and test that each configuration yields a positive E_{KRA}. One then determines a CE that optimally represents the *ab initio* E_{KRA} while satifying that the testing set gives positive CE predicted E_{KRA} only. The testing set configurations that yield the most extreme predicted E_{KRA} values can then be calculated *ab initio*. When the *ab initio* and CE predicted E_{KRA} are not sufficiently close to one another, the new *ab initio* computed extreme configurations are added to the fitting set and a new CE is generated and the loop repeats. The iterations stop when the most extreme CE predicted E_{KRA} are sufficiently close to the *ab initio* values. In our calculations a testing set with a thousand local configurations was used.

5.2.3. Efficiency improvement: removing oscillations

The strong configuration dependence of E_{KRA} leads frequently to anomalously low barriers during the KMC simulations such as sketched in Fig. 5.4 between states o_1 and o_2. This causes rattling, rapid but unproductive back and forth oscillations, that greatly reduce the efficiency of the simulation. Efficiency can be restored with the “absorbing Markov chain” algorithm [38]. Namely, two positions (o_1 and o_2 in Fig. 5.4) between which the vacancy oscillates are transient positions while the other neighboring positions (e.g., position 1 and 2) are absorbing positions. Then the average residence oscillation time can be calculated as,

$$\mathbf{t}_{\mathrm{osc}} = \mathbf{c} \cdot \mathbf{F} \tag{5.5}$$

where $\mathbf{t}_{\text{osc}}$ is a 1×2 row vector whose ith entry t_i is the average oscillation time given that the chain starts in state i, $\mathbf{c}$ is also a 1×2 row vector with each element equals to unity and $\mathbf{F}$ is the fundamental matrix given by,

$$\begin{aligned} \mathbf{F} &= (\mathbf{I} - \mathbf{Q})^{-1} \\ &= \begin{pmatrix} \sum_j r_{o_1 \to j} & -r_{o_2 \to o_1} \\ -r_{o_1 \to o_2} & \sum_k r_{o_2 \to k} \end{pmatrix}^{-1} \end{aligned} \tag{5.6}$$

Where $\mathbf{I}$ is a 2×2 identity matrix, o_1 and o_2 are two oscillation positions, j and k represent the $n-1$ nearest neighbor positions associated with o_1 and o_2(for fcc, $n = 12$) respectively. The probabilities that the vacancy can escape to one of the absorbing positions s given that its initial position is at o_1 or o_2 are calculated by,

$$\mathbf{P} = (p_{o_1}, p_{o_2}) = \mathbf{R} \cdot \mathbf{F} \tag{5.7}$$

Where $\mathbf{R}$ is a $d \times 2$ matrix (d is number of absorbing positions, $d = 18$ for fcc) whose ith column is composed by the rate $r_{o_i \to s}$. Once rattling has been detected during the simulation, the inefficiency is removed by directly forwarding the vacancy to one of the absorbing positions with the probability computed by Eq. (5.7). The corresponding elapsed time is evaluated with Eq. (5.5).

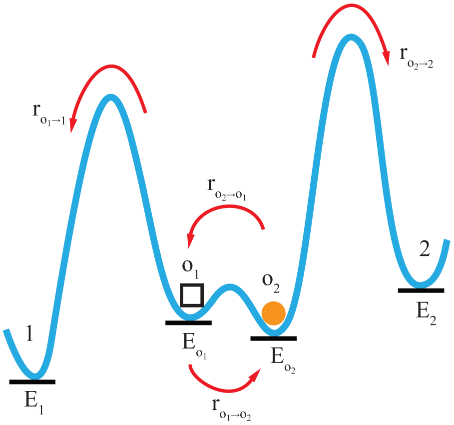

Figure 5.4: Schematic description of rattling of a jumping atom. Vacancy (jumping atom) represented as ☐ (●), E_{p} and $r_{\text{p}\to\text{q}}$ (p, q $= 1, 2, o_1, o_2$) refer to energy of state p and transition rate between p and q, the curved arrows indicate the directions of jumps. Rattling occurs when the vacancy-jumping atom energy barrier is much smaller than surrounding barriers.

5.3. Results and discussion

We apply the aforementioned formalism to a dilute Al-Cu alloy with 2 a/o Cu and simulate the GP zones morphology and precipitation kinetics at room temperature (300 K). The simulation is performed in a supercell with periodic boundary conditions containing 20 ×

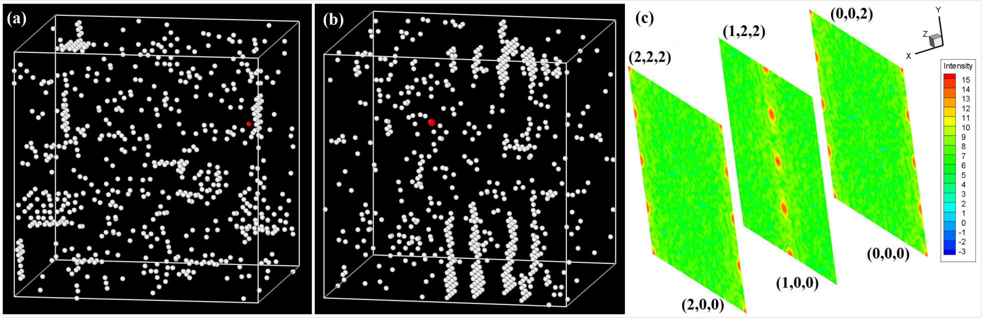

Figure 5.5: Kinetic Monte Carlo simulation of early stage precipitation in Al-2at.%Cu alloy at 300 K. Only Cu atoms(white balls) and vacancy(red ball) are shown within a simulation box formed by 20 × 20 × 20 fcc cubes. (a) GP-I (single pure Cu (100) plane) after about 1 ks; (b) GP-II (sandwich structure consisted by (100) planes with sequence “Cu-Al-Al-Al-Cu”) after about 6 ks; (c) calculated structure factor of Cu pertaining to (b).

20 × 20 conventional fcc cubes with $4 \times 20^3 = 32000$ lattice sites. The quenched-in vacancy concentration inherited from solutionizing (usually around 800 K) is estimated to be $\sim 4{\cdot}10^{-5}$. Introducing a single vacancy in the supercell is therefore a reasonable estimate of the real vacancy concentration. The jump attempt frequencies for Al atom and Cu atoms have been estimated from the Einstein vibrational frequency ν as follows: $\nu = \frac{1}{2\pi}\sqrt{k/M}$, where M is the mass of the atom, and k the spring constant. We obtained ν_{Al} (ν_{Cu}) = 7.4 (2.7) THz. For local CEs of the KRA barriers, ECIs are extracted by fitting for each type of jumping atom 20 CI-NEB KRA barriers. Only clusters up to and including four sites (including the “swapping pair”) are selected with the restriction that no two sites within a cluster are further apart than the 4th nearest neighbor. Optimized positive definite local CE for Al yields a fitting error of 55 meV and 40 meV for Cu.

Figures. 5.5(a) and 5.5(b) show the morphology of GP zones in Al-2 a/o Cu alloy at 300 K from the present kMC simulation. A particularly challenging issue for any CE without explicit treatment for long-ranged elastic interactions is the prediction of GP zone shapes [39]. In dilute Al-Cu alloys GP-I zones are known to be single pure Cu on {100} planes while GP-II zones form as pure Cu on {100} planes separated by 3 atomic planes of pure Al [25, 28]. GP-II zones can rapidly evolve to θ’ precipitates by absorbing vacancies on the Al positions between the {100} Cu planes, so that then only 2 atomic Al layers remain between the Cu planes [40–42]. This evolution to θ’ violates the fcc underlying lattice and therefore we will restrain ourselves to GP-II formation. Describing the precipitation evolution from the single Cu {100}planes [GP-I, see Fig. 5.5(a)] to the Cu-Al-Al-Al-Cu sandwich morphology [GP-II, see Fig. 5.5(b)] requires a highly optimized CE with a LOOCV of just 2.78 meV/atom, with about 200 fitted structural energies and 80 ECIs. Consistency of the simulated GP-II structure with the experimental observation can also be verified, see Fig. 5.5(c), by the calculated Cu structure factor. The diffraction peaks are separated by a half bcc cube edge, right between the Bragg peaks, indicating that the spacing of consecutive {100}Cu planes is 2 fcc lattice parameters.

Fig. 5.6 shows the Cu clustering at the early stages of natural aging as obtained with local configuration dependent KRA barriers (CEKRA) and as obtained with constant KRA barriers (CKRA: $E_{\text{KRA}}[Al] = 0.58$ eV, $E_{\text{KRA}}[Cu] = 0.53$ eV). The CKRA values are

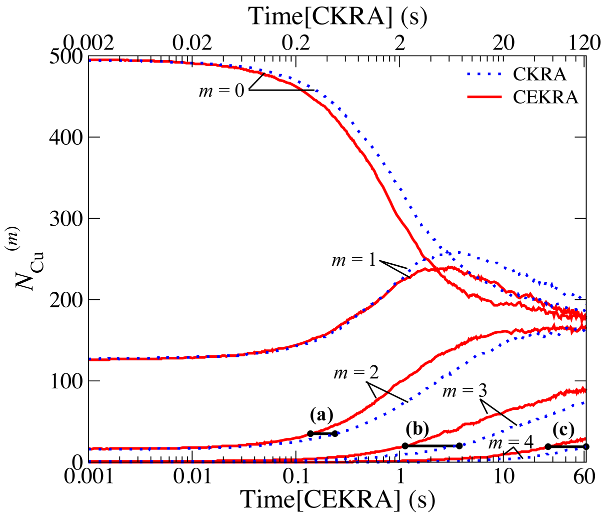

Figure 5.6: Clustering in Al-2 a/o Cu alloy at 300 K: a comparison of CEKRA and CKRA. $N_{Cu}^{(m)}$ (see text) for $m = 0, 1, 2, 3, 4$ is plotted as a function of time (s). Solid lines (CEKRA) and dotted lines (CKRA) correspond to lower horizontal axes and upper horizontal axes.

derived from the CEKRA values for the cases of Al self diffusion and Cu impurity diffusion in pure fcc Al. It should be remarked that the *ab initio* calculated CKRA barriers are about 0.06 eV higher, which at 300 K would retard the growth kinetics by a factor of 10. For each Cu atom the number of Cu nearest neighbors is determined. The number of Cu atoms with m ($m = 0, 1, 2, 3, 4$) Cu atoms in the nearest neighbor shell are indicated as $N_{Cu}^{(m)}$. In total there are $0.02 \times 32000 = 640$ Cu atoms. In order to minimize the statistical error, the Fig. 5.6 shows the average of 50 independent runs. Initially, after high temperature solutionizing at 800 K, most Cu atoms have 12 Al nearest neighbors and no Cu nearest neighbors, $m = 0$. Cu atoms that are part of $\{100\}$Cu planes have 4 Cu neighbors, so that $N_{Cu}^{(4)}$ is a measure for GP-I and GP-II formation.

As natural aging proceeds the number of isolated Cu atoms ($m = 0$) decreases and Cu atoms with one or more Cu neighbors ($m = 1, 2, 3, 4$) increases. The most remarkable feature in Fig. 5.6 is that clustering as computed with CEKRA proceeds more than twice as fast as with CKRA (note the distinct time scales below and above the figure). Except for an overlap of $N_{Cu}^{(1)}$ curve at the very beginning of the precipitation, CEKRA and CKRA curves corresponding to the same m-value diverge with time as is apparent from the horizontal gap between the curves. These horizontal gaps for $N_{Cu}^{(m)}$, m=2, 3, and 4, are shown as horizontal bars labelled (a), (b), and (c), respectively, in Fig. 5.6. The bars are drawn for $N_{Cu}^{(m)}$ values that are 19 greater than that for the competely random state, thus for $N_{Cu}^{(2)} = 33$, $N_{Cu}^{(3)} = 20$, and $N_{Cu}^{(4)} = 19$. It is apparent that this time gap increases at later times, and that larger m are more accelerated than smaller m. Thus the acceleration associated with CEKRA over CKRA is more pronounced for larger m and hence also for larger pure Cu clusters. This means that the CEKRA and CKRA show distinct evolutions of Cu clustering and GP zone formation. Therefore, it is not possible to rescale the time axis and the CKRA E_{KRA} values such that CEKRA evolution is reproduced as was confirmed by repeated attempts. This means that realistic modeling of clustering and precipitation cannot generally be achieved by using configuration independent KRA barriers. Specifically we conclude that it is not possible to reproduce precipitate evolution using KRA barriers from impurity diffusivities.

5.4. Summary

Summarizing, a method for atomistically simulating the early stages of clustering and precipitation is presented. The method is based on a local cluster expansion for the kinetically resolved activation barrier for diffusion, taking into account that this cluster expansion may yield positive barriers only. The method is applied to GP zone formation in Al-Cu alloys. The kinetically resolved activation barriers for diffusion is shown to be strongly dependent on the local configuration around the swapping vacancy-jumping atom pair, with highest and lowest barriers differing by a factor of five in fcc based Al-Cu alloys. The morphology of the GP zones in Al-Cu alloys is correctly predicted during the kinetic Monte Carlo simulations. Our results for precipitation kinetics in Al-Cu alloys show that the assumption of constant, configuration independent, diffusivity activation barriers does not yield the same kinetics as a local configuration dependent form.

References

[1] J. W. Martin, *Precipitation hardening: theory and applications* (Butterworth-Heinemann, 2012).

[2] R. Smallman and A. Ngan, *Chapter 13 - precipitation hardening,* in *Modern Physical Metallurgy (Eighth Edition)*, edited by R. Smallman and A. Ngan (Butterworth-Heinemann, Oxford, 2014) eighth edition ed., pp. 499 – 527.

[3] E. Clouet, A. Barbu, L. Laé, and G. Martin, *Precipitation kinetics of* Al_3Zr *and* Al_3Sc *in aluminum alloys modeled with cluster dynamics,* Acta Materialia **53**, 2313 (2005).

[4] D. Den Ouden, L. Zhao, C. Vuik, J. Sietsma, and F. Vermolen, *Modelling precipitate nucleation and growth with multiple precipitate species under isothermal conditions: Formulation and analysis,* Computational Materials Science **79**, 933 (2013).

[5] L. Barnard, N. Cunningham, G. Odette, I. Szlufarska, and D. Morgan, *Thermodynamic and kinetic modeling of oxide precipitation in nanostructured ferritic alloys,* Acta Materialia **91**, 340 (2015).

[6] K. Joshi and S. Chaudhuri, *Empirical force field-based kinetic Monte Carlo simulation of precipitate evolution and growth in Al-Cu alloys,* Modelling and Simulation in Materials Science and Engineering **24**, 075012 (2016).

[7] N. Vo, D. Dunand, and D. Seidman, *Improving aging and creep resistance in a dilute Al-Sc alloy by microalloying with Si, Zr and Er,* Acta Materialia **63**, 73 (2014).

[8] M. Zandbergen, Q. Xu, A. Cerezo, and G. Smith, *Study of precipitation in Al-Mg-Si alloys by Atom Probe Tomography I. Microstructural changes as a function of ageing temperature,* Acta Materialia **101**, 136 (2015).

[9] M. Werinos, H. Antrekowitsch, T. Ebner, R. Prillhofer, W. Curtin, P. Uggowitzer, and S. Pogatscher, *Design strategy for controlled natural aging in Al-Mg-Si alloys,* Acta Materialia **118**, 296 (2016).

[10] S. Pogatscher, H. Antrekowitsch, M. Werinos, F. Moszner, S. Gerstl, M. Francis, W. Curtin, J. Löffler, and P. Uggowitzer, *Diffusion on demand to control precipitation aging: application to Al-Mg-Si alloys,* Physical Review letters **112**, 225701 (2014).

[11] M. Werinos, H. Antrekowitsch, E. Kozeschnik, T. Ebner, F. Moszner, J. Löffler, P. Uggowitzer, and S. Pogatscher, *Ultrafast artificial aging of Al-Mg-Si alloys,* Scripta Materialia **112**, 148 (2016).

[12] F. Lechermann and M. Fähnle, *Ab initio statistical mechanics for alloy phase diagrams and ordering phenomena including the effect of vacancies,* Physical Review B **63**, 012104 (2000).

[13] X. Zhang and M. H. F. Sluiter, *Ab initio prediction of vacancy properties in concentrated alloys: The case of fcc Cu-Ni,* Physical Review B **91**, 174107 (2015).

[14] M. Sluiter and P. E. A. Turchi, *Electronic theory of phase stability in substitutional alloys: The generalized perturbation method versus the connolly-williams method,* Physical Review B **40**, 11215 (1989).

[15] S.-H. Wei, L. G. Ferreira, and A. Zunger, *First-principles calculation of temperature-composition phase diagrams of semiconductor alloys,* Physical Review B **41**, 8240 (1990).

[16] M. Asta, D. de Fontaine, M. van Schilfgaarde, M. Sluiter, and M. Methfessel, *First-principles phase-stability study of fcc alloys in the Ti-Al system,* Physical Review B **46**, 5055 (1992).

[17] A. Van De Walle, M. Asta, and G. Ceder, *The alloy theoretic automated toolkit: A user guide,* Calphad **26**, 539 (2002).

[18] G. Ceder, *A derivation of the Ising model for the computation of phase diagrams,* Computational Materials Science **1**, 144 (1993).

[19] A. Van der Ven, G. Ceder, M. Asta, and P. Tepesch, *First-principles theory of ionic diffusion with nondilute carriers,* Physical Review B **64**, 184307 (2001).

[20] A. Van der Ven and G. Ceder, *First principles calculation of the interdiffusion coefficient in binary alloys.* Physical Review Letters **94**, 045901 (2005).

[21] X. Zhang and M. H. F. Sluiter, *Cluster expansions for thermodynamics and kinetics of multicomponent alloys,* Journal of Phase Equilibria and Diffusion **37**, 44 (2016).

[22] J. Lepinoux and C. Sigli, *On the effect of concentrated solid solutions on properties of clusters in a model binary alloy,* Philosophical Magazine **96**, 955 (2016).

[23] X. Zhang and M. H. F. Sluiter, *Kinetically driven ordering in phase separating alloys,* xxx **xx**, xx (2017).

[24] S. Son, M. Takeda, M. Mitome, Y. Bando, and T. Endo, *Precipitation behavior of an Al-Cu alloy during isothermal aging at low temperatures,* Materials Letters **59**, 629 (2005).

[25] A. Biswas, D. J. Siegel, C. Wolverton, and D. N. Seidman, *Precipitates in Al-Cu alloys revisited: Atom-probe tomographic experiments and first-principles calculations of compositional evolution and interfacial segregation,* Acta Materialia **59**, 6187 (2011).

[26] C. Wolverton, *First-principles prediction of equilibrium precipitate shapes in al-cu alloys,* Philosophical magazine letters **79**, 683 (1999).

[27] J. Wang, C. Wolverton, S. Müller, Z.-K. Liu, and L.-Q. Chen, *First-principles growth kinetics and morphological evolution of Cu nanoscale particles in Al,* Acta Materialia **53**, 2759 (2005).

[28] T. Konno, K. Hiraga, and M. Kawasaki, *Guinier-Preston (GP) zone revisited: atomic level observation by HAADF-TEM technique,* Scripta Materialia **44**, 2303 (2001).

[29] A. Bortz, M. Kalos, and J. Lebowitz, *A new algorithm for Monte Carlo simulation of Ising spin systems,* Journal of Computational Physics **17**, 10 (1975).

[30] M. Leitner, D. Vogtenhuber, W. Pfeiler, and W. Püschl, *Monte-Carlo simulation of atom kinetics in intermetallics: Correcting the jump rates in* Ni_3Al*,* Intermetallics **18**, 1091 (2010).

[31] G. Henkelman, B. P. Uberuaga, and H. Jónsson, *A climbing image nudged elastic band method for finding saddle points and minimum energy paths,* The Journal of Chemical Physics **113**, 9901 (2000).

[32] G. Henkelman and H. Jónsson, *Improved tangent estimate in the nudged elastic band method for finding minimum energy paths and saddle points,* The Journal of Chemical Physics **113**, 9978 (2000).

[33] E. Vincent, C. Becquart, C. Pareige, P. Pareige, and C. Domain, *Precipitation of the FeCu system: A critical review of atomic kinetic Monte Carlo simulations* , Journal of Nuclear Materials **373**, 387 (2008).

[34] B. Swoboda, a. Ven, and D. Morgan, *Assessing Concentration Dependence of FCC Metal Alloy Diffusion Coefficients Using Kinetic Monte Carlo,* Journal of Phase Equilibria and Diffusion **31**, 250 (2010).

[35] N. Castin, G. Bonny, D. Terentyev, M. Lavrentiev, and D. Nguyen-Manh, *Modelling phase separation in Fe-Cr system using different atomistic kinetic Monte Carlo techniques* , Journal of Nuclear Materials **417**, 1086 (2011), proceedings of ICFRM-14.

[36] D. Simonovic and M. H. Sluiter, *Impurity diffusion activation energies in al from first principles,* Physical Review B **79**, 054304 (2009).

[37] M. H. F. Sluiter and Y. Kawazoe, *Invariance of truncated cluster expansions for first-principles alloy thermodynamics,* Physical Review B **71**, 212201 (2005).

[38] M. A. Novotny, *Monte carlo algorithms with absorbing markov chains: Fast local algorithms for slow dynamics,* Physical Review Letters **74**, 1 (1995).

[39] C. Wolverton, *First-principles prediction of equilibrium precipitate shapes in Al-Cu alloys,* Philosophical Magazine Letters **79**, 683 (1999).

[40] T. Sato and A. Kamio, *High resolution electron microscopy of phase decomposition microstructures in aluminium-based alloys,* Materials Science and Engineering: A **146**, 161 (1991).

[41] A. Bigot, F. Danoix, P. Auger, D. Blavette, and A. Menand, *3D reconstruction and analysis of GP zones in Al-1.7Cu (at%): a tomographic atom probe investigation,* Applied Surface Science **94–95**, 261 (1996), proceedings of the 42nd International Field Emission Symposium.

[42] M. Starink and A. M Zahra, *Mechanisms of combined GP zone and θ' precipitation in an Al-Cu alloy,* Journal of Materials Science Letters **16**, 1613 (1997).

6

Kinetically driven ordering in phase separating alloys

It is shown that in substitutional alloys peculiar ordered patterns can result from neighborhood dependent diffusion activation barriers even when there are no metastable ordered phases. Lattice gases with pure phase separation character are shown to exhibit transient ordered structures that can be retained almost indefinitely although not at thermodynamic equilibrium. It is shown that such structures can come about relatively easily by quenching from the high temperature configurationally random solid solution.

6.1. Introduction

The thermodynamic properties of the Ising model have been studied intensely for almost a century. The role of dimensionality, the occurrence of order-disorder transitions, and many other features of this model and its generalizations are now well understood [1, 2]. Among the most interesting applications of the Ising model and its generalizations is the study of substitutional alloys [3–5]. With the advent of *ab initio* methods to compute the effective interatomic interactions, the practical utility of the model has greatly expanded [6–12]. When the generalized Ising model is applied to alloys, the kinetics of these alloys is at least as interesting as the study of thermodynamic equilibrium. After all, real alloys are usually at a kinetically determined intermediary stage evolving towards thermodynamic equilibrium, rather than at equilibrium [13, 14]. Kinetics in substitutional alloys generally is driven by vacancy mediated diffusion. While vacancies, because of their typically low equilibrium concentration, rarely play a role in equilibrium thermodynamics, they are crucial for kinetics. Experimentally too, the intricate details of vacancy behavior in substitutional alloys has attracted attention again lately [15–19]. A number of studies exist on Ising model kinetics, some which neglect vacancies [20] and therefore unrealistic kinetics, others which include vacancies but which employ simplifying assumptions concerning diffusion activation energies [21–23], and recently some studies where multiple issues surrounding vacancies and diffusion barriers are considered [24–27]. These latter studies generally appear able to provide realistic time scales and evolution histories. Here, we take a special interest in the evolution history, particularly the occurrence of transient phases [28–31].

We define transient phases as non-equilibrium phases that can occur during the evolution towards equilibrium for an extended, but finite, period of time. It is well understood that transient ordered phases can form from a disordered, or random-like, solid solution with unmixing tendencies if they are metastable ordered phases that are much more stable than the disordered solid solution, such as occur in various semiconductor alloys [32]. These observations have been explained in terms of strain energy minimization by atomic size mismatch [32–34]. Even in the absence of strain effects, metastable ordered phases can be transient as has been found in Monte Carlo simulations of phase separating alloys [31, 35–37] or in concentration wave simulations [38]. In all these cases transient ordered phases appear under the constraint of limited atomic mobility, free energy can be reduced more quickly by metastable ordering, than by macro-scale phase separation. This explanation for the occurrence of transient phases has proven so alluring that quite generally transient phases in bulk alloys are ascribed to thermodynamic metastability, often in conjunction with limited atomic mobility [39–45]. The importance of purely kinetic effects in phase selection has been seen in colloidal system simulations [46] where metastable NaCl type ordering occurs prior to, or instead of stable CsCl type ordering. A less clear scenario occurs when preferred nucleation is in play, particularly when heterogeneous nucleation for a metastable phase happens more readily than nucleation of the stable phase [47]. However, here too, thermodynamic competition remains an important factor. Purely kinetic factors have not been reported for metallic alloys. With the increasing awareness that vacancy formation and substitutional diffusion in concentrated alloys is strongly dependent on the local environment [24, 25, 48–51], it is of interest to examine whether this local environment dependence of the kinetics could lead to new, hitherto not recognized, phenomena.

In this work we report transient order in a configurationally random alloy upon quenching into the two phase region pertaining to phase separation. Here, we show that without any thermodynamic causative factor, there also may be a purely kinetic origin of transient phases. For clarity, first we will analyze a 2-D case, and subsequently show that analogous phenomena occur in 3-D.

6.2. Kinetically driven ordering on two-dimensional square lattice

6.2.1. Model description

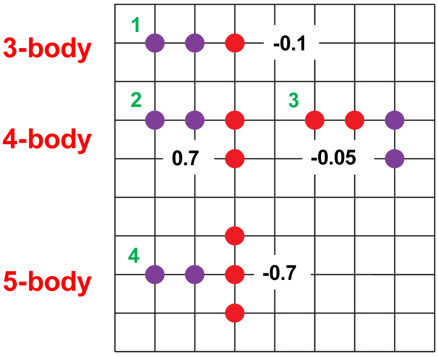

Figure 6.1: Clusters and effective cluster interactions (in eV) used for expanding the configuration dependence of the KRA barrier. Cluster type γ is indicated by the green digit, J_γ (in eV/cluster) by the number printed in black. Red circles indicate B species, purple circles E species, and A species are present at all grid points, but are not drawn for clarity.

Intentionally, the simplest thermodynamic model is used with two atomic species on a rigid lattice with effective interatomic interactions limited to the nearest neighbors. The interactions favor phase separation into the pure constituents, but configurational entropy leads to intermixing as temperature is raised. Vacancies are assumed to have the same effective interactions with both atomic species, so that their concentration is not dependent on (local) composition or order. However, the activation energy for atom-vacancy interchange is made dependent on the local environment. We employ the formalism of Ref. [51], where the kinetics of vacancy mediated diffusion in a binary A-B alloy can be described by resorting to a 5-component lattice gas: the atomic species A and B, the vacancy species C, the A atom and vacancy in the transition state represented as two D species, and finally the B atom and vacancy in the transition state represented as two E species. The D and E species must be introduced in order to account for the diffusion activation energetics. A great simplification can be made if we assume that within our material vacancies are so rare that they never exist within each others vicinity. Then, the C, D and E species can never occur simultaneously and their interactions are not needed.

The only interactions on the lattice gas are then those between A-B-C or A-B-D or A-B-E species, i.e. three ternaries. Furthermore, D (and E) species occur only as D-D (E-E) nearest neighbor pairs. If we assign the most abundant species to A, it turns out that a very sparse interaction Hamiltonian can account for the energetics of atomic configurations and their intermediary transition states [51]. First, we elaborate the A-B-C cluster expansion (CE) to describe the configurational energy E_{conf}.

$$E_{conf} = \sum_{\alpha=1}^{2} n_{\alpha}^{ABC} J_{\alpha}^{ABC}, \tag{6.1}$$

where α indicates a particular cluster, $\alpha = 1(2)$ refers to the B point cluster (BB nearest neighbor pair), n_α is a counter for the number of α-type clusters per lattice site, and J_α is the corresponding effective cluster interaction. In order to see if transient order occurs without there being a metastable ordered structure lurking just above the convex hull of ground states, we consider a square lattice (2D) with nearest neighbor interactions only. We arbitrarily select $J_1^{ABC} = +0.4$ eV/point and $J_2^{ABC} = -0.2$ eV/pair, so that E_{conf} is a parabola as function of the composition with a maximum of +0.1 eV/atom in the equiatomic A-B alloy, and $E_{conf} = 0$ eV for pure A and pure B. These interactions give rise to a miscibility gap with a critical temperature of about 10533 K at equiatomic composition [52]. To keep the model as simple as possible, the vacancy interactions between C and A, and C and B are all the same and equal to zero. The vacancy prefers neither A nor B neighbors. The vacancy formation energy is not of concern because we impose that there is but a single, conserved, vacancy in our system. Concerning the A-B-D local cluster expansion (LCE), needed to evaluate the kinetically resolved activation [24, 48] (KRA) barriers E_{KRA} for atoms trading places with the vacancy, we again select the simplest possibility: for all configurations around a DD pair $E_{KRA} = 0.7$ eV. It follows that E_{KRA} for a majority A atom trading places with a vacancy is always 0.7 eV. The A-B-E LCE describes the KRA barriers for B atom diffusion. We opt here for configuration dependence,

$$E_{KRA} = J_0 + \sum_{\gamma=1}^{4} n_{\gamma}^{ABE} J_{\gamma}^{ABE}, \tag{6.2}$$

where $J_0 = 0.6$ eV is the KRA barrier for a B atom surrounded by A atoms trading places with a vacancy and γ represents a cluster labeled 1 through 4, shown in figure 6.1. The clusters have been chosen carefully: the negative value for the $\gamma = 1$ cluster lowers the barriers for forming linear arrays of B atoms, while the other clusters are designed to limit the growth of side branches on such linear B arrays. The rate at which configurations evolve can be simulated by tracking the vacancy in a kinetic Monte Carlo simulation where the transition rate $r_{i\to j}$ between states i and j is given by

$$r_{i\to j} = \omega \exp[-\beta(E_{KRA} + \frac{1}{2}E_{conf}^{j} - \frac{1}{2}E_{conf}^{i})], \tag{6.3}$$

where ω is the jump attempt frequency, $\beta = 1/(k_B T)$, E_{KRA} is given by the ABD (ABE) LCE when an A (B) atom trades places with a vacancy, and $E_{conf}^{i(j)}$ is the configurational energy before (after) the jump as given by the ABC CE. For simplicity we assume that

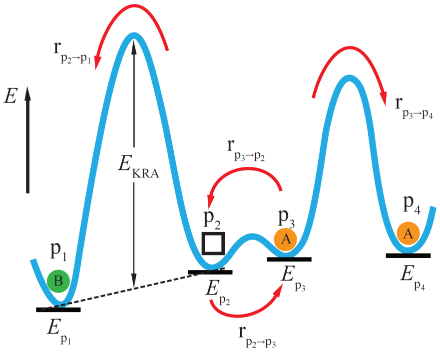

Figure 6.2: Schematic diagram of an energy landscape with low barriers between states 2 and 3. Black square represents a vacancy, species C, while orange and green solid circles refer to atomic species A and B.

ω is configuration and temperature independent and takes a value of 1 THz. When KRA barriers are configuration dependent, it follows that anomalously low barriers can occur such as sketched in Fig. 6.2 between states p_2 and p_3. This will give rise to many back and forth oscillations within the actual configuration evolving. Fortunately, to a large degree such “unproductive oscillations” can be integrated out by using the absorbing Markov chain algorithm [53]. Fig. 6.2 also illustrates the principle of kinetic ordering: while the lowest energy occurs for the vacancy jumping towards position p_1, the transient state represented by position p_4 is more likely to be reached within short time spans. In order to clearly identify the effect of the local environment dependence of the KRA (EDKRA) barrier of the B-vacancy swap as expressed in the ABE LCE, we compare results with the case where all E_{KRA} for a B-vacancy swap is set to 0.6 eV (CTKRA). Of course, as described above the E_{KRA} for an A-vacancy swap is always 0.7 eV. In order to describe the evolution of the state of order we define an order parameter $N_B^{(m)}$, which is the number of B atoms that has m B neighbors. As we have designed our ABE LCE such that linear arrays of B atoms are preferred, we will define a special order parameter $N_B^{(2*)}$ which counts the number of B atoms that have precisely two B atoms in a straight line as neighbors.

6.2.2. Results and discussion

Precipitation kinetics of an $A_{1279}B_{320}C$ alloy (T = 300 K) on a 2D 40×40 square lattice with periodic boundary conditions are shown in Fig. 6.3. Starting from a random configuration, the short range order in the alloy is monitored through the $N_B^{(m)}$ order parameters as function of time. The kinetics in the EDKRA and the CTKRA cases are remarkably different. The CTKRA case exhibits the expected kinetics of B clusters forming from the random mixture, isolated B atoms rather quickly connect with other B atoms to form clusters which coarsen over time. The number of 2-fold coordinated B atoms ($N_B^{(2*)}$) initially very rapidly increases, but then decreases as more B atoms join. The number of 4-fold coordinated B atoms ($N_B^{(4)}$) follows a similar trend, but at a much slower pace. The EDKRA case, on the other hand, follows a completely different path. The inset shows a characteristic

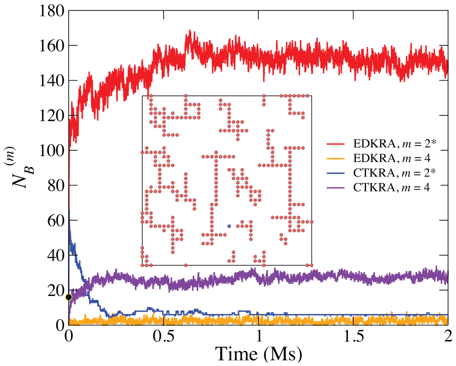

Figure 6.3: Kinetic Monte Carlo simulation of short range order evolution in an A-B-vac alloy on a square lattice. Order parameters $N_B^{(2*)}$ and $N_B^{(4)}$ are shown as function of time for environmentally dependent kinetically resolved activation barriers (EDKRA) and configuration independent kinetically resolved activation barriers (CTKRA). The black circle on the vertical axis indicates the initial value of $N_B^{(2*)}$. The inset shows a characteristic configuration that is obtained with EDKRA after 2 Ms.

configuration after 2 Ms which features the linear B arrays with rather few side branches. As the value of $N_B^{(2*)} \approx 160$ shows, about half of all the B atoms (320) are in a linear configuration. After 2 Ms $N_B^{(2*)}$ is about 30 times larger in the EDKRA than in the CTKRA case. The number of B atoms with 4 B neighbors in the inset is in the single digits and about one order of magnitude lower than in the CTKRA case. While there is no thermodynamic driving force that stabilizes the linear B arrays, these arrays nevertheless are robust for extremely long time periods, considering that 2 Ms corresponds to $2 \cdot 10^{18}$ jump attempts. The finding that the EDKRA kinetically drives the alloy towards transient states, motivated us to investigate whether it would persist in more realistic cases, such as on an fcc lattice in 3D.

6.3. Kinetically driven ordering on fcc lattice

6.3.1. Model description

Similarly as shown in Eq. (6.1) for the square lattice, we use an A-B-C (A=majority atom, B=minority atom and C=vacancy) ternary cluster expansion to describe the configurational energy of the phase separating system on fcc lattice. B point cluster ($\alpha = 1$) and BB nearest neighbor pair ($\alpha = 2$) are used to describe a parabolic type configurational energy as a function of composition. The corresponding effective cluster interactions are $J_1 = +1.2$ eV/point and $J_2 = -0.2$ eV/pair. The vacancy interactions between C and A, and C and B are all the same and equal to zero.

We use an A-B-D (A-B-E) local cluster expansion (LCE) to describe the kinetically resolved activation (KRA) barriers E_{KRA} for A (B) atom trading places with the vacancy.

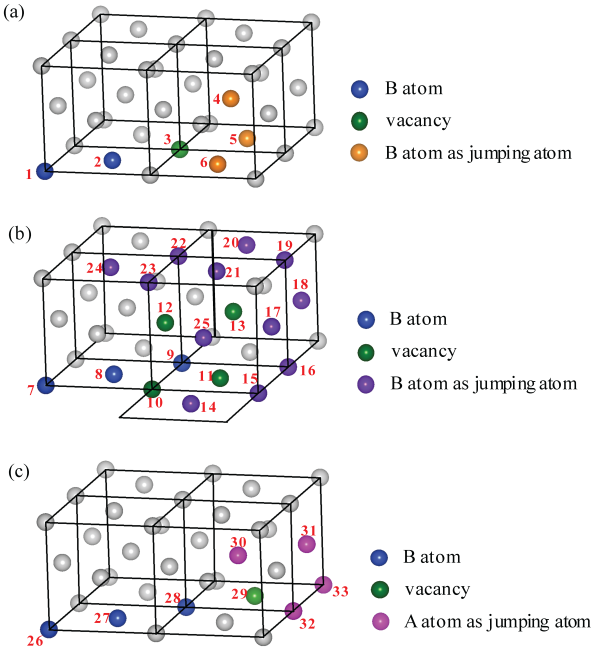

Figure 6.4: Illustration of the clusters (γ) and the corresponding decorations used in the local cluster expansions A-B-D and A-B-E for (c) A atom and (a, b) B atom as the jumping atom. The number attached to each colored atom is used for describing the corresponding clusters in Table 6.1. Fcc cubes (black solid lines) have been added for clarity.

Table 6.1: Effective cluster interactions (ECIs) in A-B-D and A-B-E local cluster expansions for kinetically resolved activation (KRA) barriers. Numbers connected by “-” indicate a cluster γ. The positions of the atoms within each cluster γ can be found in the corresponding figures.

Clusters (γ) for B atom diffusion	Figure	ECI (eV/cluster)
1 - 2 - 3 - 4	6.4(a)	-0.3
1 - 2 - 3 - 5		-0.2
1 - 2 - 3 - 6		-0.25
7 - 8 - 9 - 10 - 14	6.4(b)	0.4
7 - 8 - 9 - 10 - 25		
7 - 8 - 9 - 11 - 15		
7 - 8 - 9 - 11 - 16		
7 - 8 - 9 - 11 - 17		
7 - 8 - 9 - 11 - 25		
7 - 8 - 9 - 12 - 21		
7 - 8 - 9 - 12 - 22		
7 - 8 - 9 - 12 - 23		
7 - 8 - 9 - 12 - 24		
7 - 8 - 9 - 12 - 25		
7 - 8 - 9 - 13 - 16		
7 - 8 - 9 - 13 - 17		
7 - 8 - 9 - 13 - 18		
7 - 8 - 9 - 13 - 19		
7 - 8 - 9 - 13 - 20		
7 - 8 - 9 - 13 - 21		
7 - 8 - 9 - 13 - 22		
Clusters (γ) for A atom diffusion	Figure	ECI (eV/cluster)
26 - 27 - 28 - 29 - 30	6.4(c)	-0.1
26 - 27 - 28 - 29 - 31		-0.1
26 - 27 - 28 - 29 - 32		-0.15
26 - 27 - 28 - 29 - 33		-0.2

The configuration dependent of the KRA barriers are then written as,

$$E_{KRA} = J_0^{ABD(E)} + \sum_{\gamma} n_{\gamma}^{ABD(E)} J_{\gamma}^{ABD(E)}, \tag{6.4}$$

where $J_0^{ABD} = +0.8$ eV and $J_0^{ABE} = +1.0$ eV refer to the KRA barriers for an A (B) atom trading places with the vacancy when the jumping atom and the vacancy are surrounded purely by A atoms. γ represents a cluster illustrated in Fig. 6.4. All the clusters γ as well as the associated ECIs used in the present work are shown in Fig. 6.4 and Table 6.1.

6.3.2. Results and discussion

We found here too, a completely different behavior for EDKRA and CTKRA kinetics. Fig. 6.5 shows the short range order evolution starting from the random configuration in

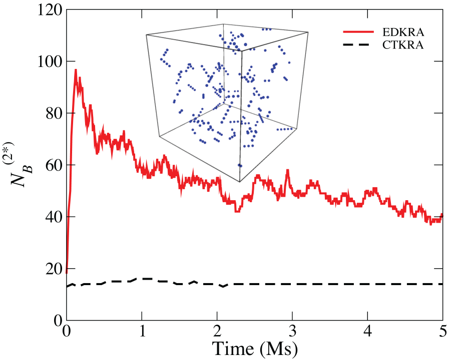

Figure 6.5: Kinetic Monte Carlo simulation of short range order evolution in a phase separating $A_{0.95}B_{0.05}$ alloy with a single vacancy at 300 K. The simulation box consists of 20 × 20 × 20 conventional fcc cubes. The inset shows B atoms that are part of linear arrays of B atoms along the $< 110 >$ direction after a simulation of 0.12 Ms in the EDKRA case.

a phase separating $A_{0.95}B_{0.05}$ alloy with a single vacancy at 300 K. The simulation is performed on a fixed fcc lattice containing 4×20^3 lattice sites with periodic boundary conditions. As shown in the inset of Fig. 6.5, there are many linear arrays of B atoms in $< 110 >$ directions. This feature can be seen also from the peak of $N_B^{(2*)}$ after a time of about 0.12 Ms. In the random configuration $N_B^{(2*)} \approx 1600 \cdot 6 \cdot (0.05^2) \cdot (0.95^{10}) \approx 14$, a number that is seen for the CTKRA case rather independent of time. As the barriers for B migration are not identical in the EDKRA and CTKRA case, it is worthwhile to consider if the two cases differ mostly in terms of time scale. Therefore the time required for the CTKRA case to reach the same order parameter $N_B^{(m)}$ as the EDKRA at a particular time was examined. Two times were considered: EDKRA at t = 42 Ms and at t = 150 Ms as shown in Fig. 6.6. Data points below (above) the horizontal axis occur for B-atom coordinations that occur faster (slower) with EDKRA kinetics than with CTKRA kinetics. It is readily apparent that most configurations occur more quickly with EDKRA than with CTKRA kinetics, while the isolated B atoms, as indicated by $m = 0$, decay more rapidly. These findings occur both after 42 Ms and after 150 Ms have passed. However, B atoms with 3 B neighbors occur much quicker with CTKRA than with EDKRA kinetics. Therefore EDKRA does not result in a general acceleration of kinetics, but in a different type of short range order evolution. The overall kinetics of the system described via EDKRA does not coincide with CTKRA, although initial and final equilibrium states are identical. This is similar to what was already observed for the 2D case.

From Eq.(6.3), it can be easily estimated that lowering the height of KRA barrier about 0.1 eV can speed up the vacancy-atom swapping by 50 times at room temperature. In several substitutional alloys, such as Al-Li [48, 54] and Al-Cu [51] *ab initio* calculations have shown that KRA barriers are very sensitive to local configuration. In Al-Cu alloys KRA barriers might vary by as much as a factor 3 [51]. Especially at lower temperatures this would result in kinetic pathways that strongly deviate from predictions obtained using configuration independent KRA barriers.

Another remarkable difference between EDKRA and CTKRA kinetics concerns va-

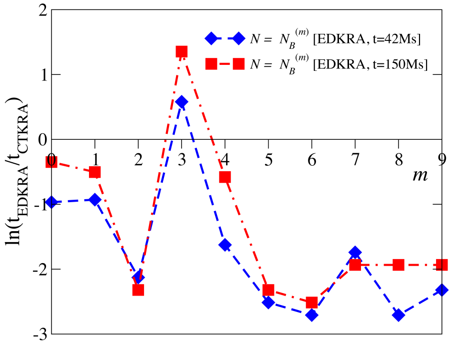

Figure 6.6: The ratio of time required for EDKRA and CTKRA reaching the same values of $N_B^{(m)}$ as a function of m after 42 Ms and after 150 Ms have passed with EDKRA kinetics.

cancy mobility. In Fig. 6.7 the distance that a vacancy has moved after 32000 atom swaps is shown for both EDKRA and CTKRA kinetics. It is apparent that the vacancy travels larger distances during CTKRA kinetics than during EDKRA kinetics. The reason for this behavior is that below average activation barriers in EDKRA kinetics have the tendency to trap vacancies while no such trapping occurs in CTKRA. An example of such trapping can be seen in Fig. 6.2 where the vacancy, at least initially, will spend more time in positions p_2, p_3, and p_4 than in position p_1. The below average barriers in EDKRA occur in the neighborhood of B atoms, and not in areas consisting purely of A atoms. As a consequence the unproductive vacancy presence in pure A areas is much less in EDKRA then in CTKRA kinetics and the attachment of B atoms to B clusters proceeds at a greater rate with EDKRA kinetics.

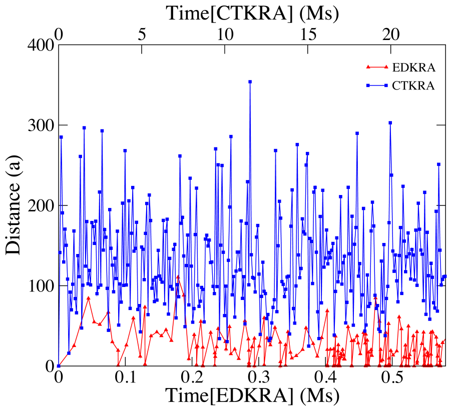

Figure 6.7: Distance traveled by a vacancy after every 32000 successive jumps in units of the fcc lattice parameter.

6.4. Conclusion

Summarizing, we proposed a new ordering mechanism in alloy systems where phase stability is thermodynamically characterized by phase separation. The essential requirement is that diffusion activation barriers in an alloy depend on the local environment. *Ab initio* density functional calculations support this claim [48, 51, 54]. Furthermore, specific features in the local environment dependence of the diffusion activation barriers can give rise to peculiar short range ordered patterns that are not in any way related to a (meta)stable thermodynamic state. Such short range ordered configurations can exist and appear stable for extended time periods and thus can be considered transient phases. Our results also show that configurationally dependent activation barriers give rise to short range order evolution that can not be reproduced by configuration independent activation barriers by e.g. rescaling of time. A purely kinetic phenomenon of vacancy trapping has emerged from these simulations that in itself accelerates the evolution of the short range order in the alloy. It appears that in order to obtain realistic descriptions of the kinetics of short range ordering and precipitation in substitutional alloys the environmental dependence of the diffusion activation barriers cannot be ignored.

References

[1] T. D. Lee and C. N. Yang, *Statistical Theory of Equations of State and Phase Transitions. II. Lattice Gas and Ising Model,* Phys. Rev. **87**, 410 (1952).

[2] J. G. Amar, F. E. Sullivan, and R. D. Mountain, *Monte Carlo study of growth in the two-dimensional spin-exchange kinetic Ising model,* Phys. Rev. B **37**, 196 (1988).

[3] S. G. Brush, *History of the Lenz-Ising Model,* Rev. Mod. Phys. **39**, 883 (1967).

[4] C. V. Baal, *Order-disorder transformations in a generalized Ising alloy,* Physica **64**, 571 (1973).

[5] R. Kikuchi, J. Sanchez, D. D. Fontaine, and H. Yamauchi, *Theoretical calculation of the Cu-Ag-Au coherent phase diagram,* Acta Metallurgica **28**, 651 (1980).

[6] J. W. D. Connolly and A. R. Williams, *Density-functional theory applied to phase transformations in transition-metal alloys,* Phys. Rev. B **27**, 5169 (1983).

[7] M. Sluiter and P. E. A. Turchi, *Electronic theory of phase stability in substitutional alloys: The generalized perturbation method versus the Connolly-Williams method,* Phys. Rev. B **40**, 11215 (1989).

[8] S.-H. Wei, L. G. Ferreira, and A. Zunger, *First-principles calculation of temperature-composition phase diagrams of semiconductor alloys,* Phys. Rev. B **41**, 8240 (1990).

[9] P. E. A. Turchi, M. Sluiter, F. J. Pinski, D. D. Johnson, D. M. Nicholson, G. M. Stocks, and J. B. Staunton, *First-principles study of phase stability in Cu-Zn substitutional alloys,* Phys. Rev. Lett. **67**, 1779 (1991).

[10] S. de Gironcoli, P. Giannozzi, and S. Baroni, *Structure and thermodynamics of* $\mathrm{Si}_x\mathrm{Ge}_{1-x}$ *alloys from ab initio Monte Carlo simulations,* Phys. Rev. Lett. **66**, 2116 (1991).

[11] M. Asta, D. de Fontaine, M. van Schilfgaarde, M. Sluiter, and M. Methfessel, *First-principles phase-stability study of fcc alloys in the Ti-Al system,* Phys. Rev. B **46**, 5055 (1992).

[12] G. Ceder, *A derivation of the Ising model for the computation of phase diagrams,* Computational Materials Science **1**, 144 (1993).

[13] K. N. Ishihara, *Chapter 2 thermodynamics and kinetics of metastable phase formation,* in *Non-equilibrium Processing of Materials*, Pergamon Materials Series, Vol. 2, edited by C. Suryanarayana (Pergamon, 1999) pp. 5–20.

[14] E. Bévillon, J. P. Colombier, B. Dutta, and R. Stoian, *Ab Initio Nonequilibrium Thermodynamic and Transport Properties of Ultrafast Laser Irradiated 316L Stainless Steel,* The Journal of Physical Chemistry C **119**, 11438 (2015).

[15] S. Pogatscher, E. Kozeschnik, H. Antrekowitsch, M. Werinos, S. Gerstl, J. L□ffler, and P. Uggowitzer, *Process-controlled suppression of natural aging in an Al-Mg-Si alloy,* Scripta Materialia **89**, 53 (2014).

[16] S. Pogatscher, H. Antrekowitsch, M. Werinos, F. Moszner, S. S. A. Gerstl, M. F. Francis, W. A. Curtin, J. F. Löffler, and P. J. Uggowitzer, *Diffusion on Demand to Control Precipitation Aging: Application to Al-Mg-Si Alloys,* Phys. Rev. Lett. **112**, 225701 (2014).

[17] S. Wenner, K. Nishimura, K. Matsuda, T. Matsuzaki, D. Tomono, F. L. Pratt, C. D. Marioara, and R. Holmestad, *Clustering and Vacancy Behavior in High- and Low-Solute Al-Mg-Si Alloys,* Metallurgical and Materials Transactions A **45**, 5777 (2014).

[18] M. Werinos, H. Antrekowitsch, E. Kozeschnik, T. Ebner, F. Moszner, J. L□ffler, P. Uggowitzer, and S. Pogatscher, *Ultrafast artificial aging of Al-Mg-Si alloys,* Scripta Materialia **112**, 148 (2016).

[19] M. Werinos, H. Antrekowitsch, T. Ebner, R. Prillhofer, W. Curtin, P. Uggowitzer, and S. Pogatscher, *Design strategy for controlled natural aging in Al-Mg-Si alloys,* Acta Materialia **118**, 296 (2016).

[20] A. J. Bray, *Theory of phase-ordering kinetics,* Advances in Physics **51**, 481 (2002).

[21] E. Vincent, C. Becquart, C. Pareige, P. Pareige, and C. Domain, *Precipitation of the FeCu system: A critical review of atomic kinetic Monte Carlo simulations* , Journal of Nuclear Materials **373**, 387 (2008).

[22] D. M. B. Swoboda, A. van der Ven, *Assessing Concentration Dependence of FCC Metal Alloy Diffusion Coefficients Using Kinetic Monte Carlo,* Journal of Phase Equilibria and Diffusion **31**, 250 (2010).

[23] N. Castin, G. Bonny, D. Terentyev, M. Lavrentiev, and D. Nguyen-Manh, *Modelling phase separation in Fe-Cr system using different atomistic kinetic Monte Carlo techniques ,* Journal of Nuclear Materials **417**, 1086 (2011), proceedings of ICFRM-14.

[24] A. Van der Ven, G. Ceder, M. Asta, and P. Tepesch, *First-principles theory of ionic diffusion with nondilute carriers,* Physical Review B **64**, 184307 (2001).

[25] M. Leitner, D. Vogtenhuber, W. Pfeiler, and W. Püschl, *Monte-Carlo simulation of atom kinetics in intermetallics: Correcting the jump rates in* Ni_3Al, Intermetallics **18**, 1091 (2010).

[26] D. R. Alfonso and D. N. Tafen, *Simulation of Diffusion in FCC NiFe Binary Alloys Using Kinetic Monte Carlo Method,* The Journal of Physical Chemistry C **118**, 22221 (2014).

[27] M. Francis and W. Curtin, *Microalloying for the controllable delay of precipitate formation in metal alloys,* Acta Materialia **106**, 117 (2016).

[28] H. M. Tawancy and M. O. Aboelfotoh, *Experimental observations of transient phases during long-range ordering to Ni4Mo in a Ni-Mo-Fe-Cr alloy,* physica status solidi (a) **99**, 461 (1987).

[29] L.-Q. Chen, Y. Wang, and A. G. Khachaturyan, *Transformation-induced elastic strain effect on the precipitation kinetics of ordered intermetallics,* Philosophical Magazine Letters **64**, 241 (1991).

[30] C. Bansal, Z. Q. Gao, L. B. Hong, and B. Fultz, *Phases and phase stabilities of Fe3X alloys (X=Al, As, Ge, In, Sb, Si, Sn, Zn) prepared by mechanical alloying,* Journal of Applied Physics **76**, 5961 (1994).

[31] J. Ni and B. Gu, *Transient Ordered States during Relaxation from a Quenched Disordered State to an Equilibrium Disordered State,* Physical Review Letters **79**, 3922 (1997).

[32] G. P. Srivastava, J. L. Martins, and A. Zunger, *Atomic structure and ordering in semiconductor alloys,* Physical Review B **31**, 2561 (1985).

[33] C. Wolverton, V. Ozolins, and A. Zunger, *Short-range-order types in binary alloys: a reflection of coherent phase stability,* Journal of Physics: Condensed Matter **12**, 2749 (2000).

[34] H. Reichert, A. Schöps, I. B. Ramsteiner, V. N. Bugaev, O. Shchyglo, A. Udyansky, H. Dosch, M. Asta, R. Drautz, and V. Honkimäki, *Competition between Order and Phase Separation in Au-Ni,* Physical Review Letters **95**, 235703 (2005).

[35] P. E. A. Turchi, L. T. Reinhard, and M. Sluiter, *First-principles approach to alloy phase stability,* International Journal of Modern Physics B **07**, 286 (1993).

[36] L. Reinhard and P. E. A. Turchi, *Transient ordered states in phase-separating alloys,* Physical Review Letters **72**, 120 (1994).

[37] F. Soisson and G. Martin, *Monte Carlo simulations of the decomposition of metastable solid solutions: Transient and steady-state nucleation kinetics,* Phys. Rev. B **62**, 203 (2000).

[38] L.-Q. Chen and A. Khachaturyan, *Computer simulation of structural transformations during precipitation of an ordered intermetallic phase,* Acta Metallurgica et Materialia **39**, 2533 (1991).

[39] B. S. Murty, D. H. Ping, and K. Hono, *Nanoquasicrystallization of binary Zr-Pd metallic glasses,* Applied Physics Letters **77**, 1102 (2000).

[40] T. Ziller, G. Le Caër, O. Isnard, P. Cénédèse, and B. Fultz, *Metastable and transient states of chemical ordering in Fe-V nanocrystalline alloys,* Phys. Rev. B **65**, 024204 (2001).

[41] M. Styles, R. Marceau, T. Bastow, H. Brand, M. Gibson, and C. Hutchinson, *The competition between metastable and equilibrium S (Al2CuMg) phase during the decomposition of AlCuMg alloys,* Acta Materialia **98**, 64 (2015).

[42] D. Ma, M. Yao, K. Pradeep, C. C. Tasan, H. Springer, and D. Raabe, *Phase stability of non-equiatomic CoCrFeMnNi high entropy alloys,* Acta Materialia **98**, 288 (2015).

[43] Y. Zheng, R. E. Williams, and H. L. Fraser, *Characterization of a previously unidentified ordered orthorhombic metastable phase in Ti-5Al-5Mo-5V-3Cr,* Scripta Materialia **113**, 202 (2016).

[44] R. Alert, P. Tierno, and J. Casademunt, *Formation of metastable phases by spinodal decomposition,* Nature Communications **7**, 13067 (2016).

[45] L. Gao, X. Ding, T. Lookman, J. Sun, and E. K. H. Salje, *Metastable phase transformation and hcp-? transformation pathways in Ti and Zr under high hydrostatic pressures,* Applied Physics Letters **109**, 031912 (2016).

[46] D. Bochicchio, A. Videcoq, and R. Ferrando, *Kinetically driven ordered phase formation in binary colloidal crystals,* Phys. Rev. E **87**, 022304 (2013).

[47] J. Perepezko, *Nucleation-controlled reactions and metastable structures,* Progress in Materials Science **49**, 263 (2004), a Festschrift in Honor of T. B. Massalski.

[48] A. Van der Ven and G. Ceder, *First principles calculation of the interdiffusion coefficient in binary alloys.* Physical Review Letters **94**, 045901 (2005).

[49] A. Van der Ven, H. Yu, G. Ceder, and K. Thornton, *Vacancy mediated substitutional diffusion in binary crystalline solids,* Progress in Materials Science **55**, 61 (2010).

[50] X. Zhang and M. H. F. Sluiter, *Ab initio prediction of vacancy properties in concentrated alloys: The case of fcc Cu-Ni,* Phys. Rev. B **91**, 174107 (2015).

[51] X. Zhang and M. H. F. Sluiter, *Cluster Expansions for Thermodynamics and Kinetics of Multicomponent Alloys,* Journal of Phase Equilibria and Diffusion **37**, 44 (2016).

[52] L. Onsager, *Crystal Statistics. I. A Two-Dimensional Model with an Order-Disorder Transition,* Phys. Rev. **65**, 117 (1944).

[53] M. A. Novotny, *Monte Carlo Algorithms with Absorbing Markov Chains: Fast Local Algorithms for Slow Dynamics,* Physical Review Letters **74**, 1 (1995).

[54] A. Van der Ven and G. Ceder, *Vacancies in ordered and disordered binary alloys treated with the cluster expansion,* Phys. Rev. B **71**, 054102 (2005).

7

Ab initio energetics beyond T=0K: Accurate electronic free energies of the transition metals at high temperatures

Free energies of bulk materials are nowadays routinely computed by density functional theory. In particular for metals, electronic excitations can significantly contribute to the free energy. For an ideal static lattice, this contribution can be obtained at low computational cost, e.g., from the electronic density of states derived at T=0K or by utilizing the Sommerfeld approximation. The error introduced by these approximations at elevated temperatures is rarely known. The error arising from the ideal lattice approximation is likewise unexplored, but computationally much more challenging to overcome. In order to shed light on these issues we have computed the electronic free energies for all 3d, 4d, and 5d transition elements on the ideal lattices of the bcc, fcc, and hcp structures using finite-temperature density-functional-theory. For a subset of elements we have explored the impact of explicit thermal vibrations on the electronic free energies by using ab initio molecular dynamics simulations. We provide an analysis of the observed chemical trends in terms of the electronic density of states and the canonical d band model, and quantify the errors in the approximate methods. The electronic contribution to the heat capacities and the corresponding errors due to the different approximations are studied as well.

7.1. Introduction

Free energies determine thermodynamic phase stabilities and phase diagrams and are, therefore, a key ingredient to materials design. In the past years extensive efforts have been undertaken to develop *ab initio* methods, mainly based on density-functional-theory (DFT), for computing accurate free energies [1–7]. A particular challenge in doing so is the inclusion of all relevant excitation mechanisms up to the melting temperature related to atomic, electronic, and, for magnetic materials, spin degrees of freedom. Neglecting the non-adiabatic coupling between the different degrees of freedom, such an approach can be systematically developed on top of the free energy Born-Oppenheimer approximation [8, 9]. Although atomic vibrations (quasiharmonic part) dominate the free energy at elevated temperatures, the neglect or an inaccurate evaluation of seemingly minor contributions (e.g., electronic, magnetic or anharmonic) can result in falsely predicted phase stabilities or inaccurate phase transition temperatures.

Table 7.1: Compilation of several previous *ab initio* studies on electronic free energies for ideal lattices, highlighting the employed methodology: SCF=self-consistent field method; DOS=fixed DOS approximation; SOM=Sommerfeld approximation; “x” indicates the used method, whereas “c” means that results by this method were shown for comparison only.

Year	Ref.	Material	Method		
			SCF	DOS	SOM
1986	[10]	Fe		x	
1995	[11]	Ni-V, Pd-V		x	c
1996	[12]	Fe		x	
1996	[13]	Sc, Ti, V, Cr, Y, Zr, Nb, Mo		x	
1998	[14]	Al-Mn-Pd, Al-Re-Pd			x
1998	[15]	Nb_3Sn	x		x
2002	[16]	Ce			x
2004	[17]	Al, Ni, NiAl, Ni_3Al		x	
2005	[18]	Ni-Al		x	
2005	[19]	Ni-Al		x	c
2006	[20]	YB_6			x
2007	[21]	Al, Pb, Cu, Ag, Au, Pd, Pt, Rh, Ir	x		
2007	[22]	Ti			x
2008	[23]	Al, Cu, Ag, Au, Ni, Pt, W, Ti		x	c
2010	[24]	Al, Cu, Ni, Mo, Ta, Ni-Al, Ni_3Al		x	
2011	[25]	Ca	x		
2011	[26]	Model study		x	x
2016	[27]	High entropy alloys			x

In this work we focus on approaches for computing electronic free energies. For atoms on ideal lattice positions the electronic free energy can be computed rather efficiently. Available approaches are (a) a self-consistent field (SCF) finite temperature DFT calculation, (b) the fixed density of states (DOS) approximation that neglects the implicit temperature dependence of the electronic DOS of the self-consistent formalism, or (c) a further approximation that considers only the effective, temperature independent DOS at the Fermi level (Sommerfeld approximation) [11]. These approaches are introduced in detail in Sec. 7.2. The literature survey in Tab. 7.1 reveals that the two approximate methods (DOS and SOM) prevail in actual applications over the SCF method. This is understandable because the latter requires multiple self-consistent cycles to derive the full temperature dependence of the electronic free energy, even if the atoms are restricted to their ideal lattice sites. The other two methods are computationally more appealing because either a single self-consistent calculation (fixed DOS approximation) or even a single value of the DOS at the Fermi level (Sommerfeld approximation) are sufficient. Despite the widespread use of these two approximate methods over the last decades, their actual, quantitative performance is not known.

Besides the fixed DOS and Sommerfeld approximation, a typical implicit assumption is that the atoms are restricted to their ideal T=0 K lattice positions. At high temperatures, however, lattice vibrations become significant and may alter the electronic states and thus the electronic free energy [5]. In order to fully incorporate the impact of lattice vibrations on the electronic free energy, compuationally expensive *ab initio* molecular dynamic (AIMD) simulations are required. This fact has drastically limited the number of corresponding studies [28, 29], and so far the importance of explicit vibrations remains elusive.

In the present work we address these issues by performing a study of *ab initio* electronic free energies and heat capacities for all $3d$, $4d$, and $5d$ transition elements on the ideal lattices of the bcc, fcc, and hcp phases. For a subset of relevant elements and phases we perform explicit AIMD calculations. We provide an analysis of the observed chemical trends in terms of the electronic DOS and the canonical d band model [30–32], and quantify the error introduced by the different approximations.

7.2. Theory

7.2.1. SCF finite temperature DFT approach

The finite temperature extension to DFT was developed by Mermin [33]. Mermin [33] extended the original Hohenberg-Kohn theorem [34] by proving the existence of a functional of the electronic density which uniquely determines the thermodynamic equilibrium ensemble at finite temperatures. This theorem implies that—given the exact temperature-dependent exchange-correlation functional—the free energy contribution due to the electronic degrees of freedom is exactly determined for a fixed set of atomic coordinates. In practice one is presently restricted to approximations which only implicitly depend on temperature, via the charge density, but which do not include explicit temperature effects [35].

Despite this inherent approximation, finite temperature DFT has been shown to capture a major part of the electronic contribution to the free energy and thus to thermodynamic properties [21, 36]. Therefore it can be considered as a highly accurate *ab initio* method. The key quantity in such an approach is the electronic charge density,

$$\rho(\mathbf{r},T) \;=\; \sum_i f(\varepsilon_i,T)\,|\phi_i(\mathbf{r})|^2, \tag{7.1}$$

where **r** is a 3-dimensional real space vector, T the temperature, and where the sum runs over

Kohn-Sham single particle orbitals ϕ_i [37] weighted with Fermi-Dirac occupation numbers,

$$f(\varepsilon_i, T) = \left[\exp\left(\frac{\varepsilon_i - \varepsilon_{\mathrm{F}}}{k_B T}\right) + 1\right]^{-1}, \tag{7.2}$$

where ε_i is the energy of ϕ_i, ε_{F} the Fermi energy or level, and k_B the Boltzmann constant. The temperature dependent charge density, $\rho(\mathbf{r}, T)$, enters the self-consistency cycle by determining the effective potential, thereby the Hamiltonian, and thus the ϕ_i, i.e., $\phi_i = \phi_i[\rho(\mathbf{r}, T)]$. The electronic free energy is given by

$$F^{\mathrm{el}}(T) = U^{\mathrm{el}}(T) - TS^{\mathrm{el}}(T), \tag{7.3}$$

with the internal energy $U^{\mathrm{el}}(T)$ often written as [38] $U^{\mathrm{el}}(T) = \sum_i f_i \varepsilon_i - E_{\mathrm{dc}}$, where $f_i = f(\varepsilon_i, T)$ and E_{dc} are double counting corrections, and with the configurational entropy

$$S^{\mathrm{el}}(T) = -\gamma k_B \sum_i \left[f_i \ln f_i + (1 - f_i) \ln(1 - f_i)\right], \tag{7.4}$$

where γ equals 1 for spin-polarized systems and 2 for spin-unpolarized systems.

The above self-consistency procedure yields eigenvalues that, as the $\phi_i = \phi_i[\rho(\mathbf{r}, T)]$, are implicitly depending on temperature, $\varepsilon_i = \varepsilon_i[\rho(\mathbf{r}, T)]$, and therefore an implicitly temperature dependent electronic DOS:

$$D(\varepsilon)[\rho(\mathbf{r}, T)] = \sum_i \delta(\varepsilon - \varepsilon_i[\rho(\mathbf{r}, T)]). \tag{7.5}$$

7.2.2. Fixed density-of-states approximation

If one assumes that the electronic DOS is temperature independent, the electronic free energy can be approximately computed via Eq. (7.3) by utilizing the T=0 K electronic DOS, $D(\varepsilon) = D(\varepsilon)[\rho(\mathbf{r}, T = 0\,\mathrm{K})]$, as

$$\begin{aligned}
\widetilde{F}^{\mathrm{el}}_{\mathrm{DOS}}(T) &= \widetilde{U}^{\mathrm{el}}_{\mathrm{DOS}}(T) - T\widetilde{S}^{\mathrm{el}}_{\mathrm{DOS}}(T), && (7.6)\\
\widetilde{U}^{\mathrm{el}}_{\mathrm{DOS}}(T) &= \int_{-\infty}^{\infty} D(\varepsilon)\, f\, \varepsilon\, \mathrm{d}\varepsilon - \int_{-\infty}^{\varepsilon_{\mathrm{F}}} D(\varepsilon)\, \varepsilon\, \mathrm{d}\varepsilon, && (7.7)\\
\widetilde{S}^{\mathrm{el}}_{\mathrm{DOS}}(T) &= \gamma k_B \int_{-\infty}^{\infty} D(\varepsilon)\, s(\varepsilon, T)\, \mathrm{d}\varepsilon, && (7.8)
\end{aligned}$$

where

$$s(\varepsilon, T) = -\left[f \ln f + (1 - f) \ln(1 - f)\right] \tag{7.9}$$

and $f = f(\varepsilon, T)$ [Eq. (7.2)]. The tilde over the thermodynamic variables indicates the approximate evaluation. Note that in practical calculations often an artificial electronic temperature, such as for example in the Methfessel-Paxton scheme [39], is used to stabilize the electronic charge self-consistency when calculating $D(\varepsilon)[\rho(\mathbf{r}, T = 0\,\mathrm{K})]$.

7.2.3. Sommerfeld approximation

For low temperatures, the first integral of Eq. (7.7) can be expanded following the Sommerfeld expansion [40], yielding an even more simplified expression for the internal energy

$$\widetilde{U}^{\mathrm{el}}_{\mathrm{SOM}}(T) \;=\; \frac{\pi^2}{6}k_B^2T^2D(\varepsilon_{\mathrm{F}})+O(T^4), \tag{7.10}$$

with the subscript "SOM" indicating the Sommerfeld approximation. The electronic entropy and free energy are then obtained from their fundamental thermodynamic relations to the internal energy [41]:

$$\widetilde{S}^{\mathrm{el}}_{\mathrm{SOM}}(T) \;=\; \int dT\frac{1}{T}\frac{\partial\widetilde{U}^{\mathrm{el}}_{\mathrm{SOM}}}{\partial T}=\frac{\pi^2}{3}k_B^2TD(\varepsilon_{\mathrm{F}})+O(T^3), \tag{7.11}$$

$$\widetilde{F}^{\mathrm{el}}_{\mathrm{SOM}}(T) \;=\; -\frac{\pi^2}{6}k_B^2T^2D(\varepsilon_{\mathrm{F}})+O(T^4). \tag{7.12}$$

The electronic contribution to the heat capacity (at constant volume), $\widetilde{C}^{\mathrm{el}}_{V,\mathrm{SOM}}$, can be computed as:

$$\widetilde{C}^{\mathrm{el}}_{V,\mathrm{SOM}}(T)=\frac{\partial\widetilde{U}^{\mathrm{el}}_{\mathrm{SOM}}}{\partial T}=\frac{\pi^2}{3}k_B^2TD(\varepsilon_{\mathrm{F}})+O(T^3). \tag{7.13}$$

7.2.4. Electronic free energies including lattice vibrations

The methodology discussed in Secs. 7.2.1 to 7.2.3 applies to a set of fixed atomic coordinates. A convenient choice are the ideal lattice sites (e.g., bcc, fcc, or hcp lattice) that correspond to the T=0 K equilibrium positions of the atoms. Such an ideal lattice approximation yields the electronic free energy neglecting a possible impact of explicit thermal vibrations of the atoms.

To go beyond one needs to consider the electronic free energy derived from AIMD simulations. The formal background is provided by the free energy Born-Oppenheimer approximation [8, 9], in which the atomic motion is determined adiabatically by the electronic free energy surface. For each AIMD snapshot, the electronic free energy, F^{el}_i, is calculated by the SCF procedure from Sec. 7.2.1 averaged according to

$$F^{\mathrm{el-vib}}(T)=\frac{1}{N}\sum_i^N\Delta F^{\mathrm{el}}_i(T), \tag{7.14}$$

with

$$\Delta F^{\mathrm{el}}_i(T)=F^{\mathrm{el}}_i(T)-U^{\mathrm{el}}_i(T=0\,\mathrm{K}), \tag{7.15}$$

and i running over N AIMD snapshots representing a statistically converged thermal distribution at T. In Eq. (7.15), $U^{\mathrm{el}}_i(T=0\,\mathrm{K})$ is the potential energy of snapshot i at an electronic temperature of T=0 K. With this reference, $F^{\mathrm{el-vib}}$ gives the electronic free energy including the coupling to explicit vibrations, but excluding the potential energy of the lattice degrees of freedom. Note that, in principle, ΔF^{el}_i could be also computed using either the fixed DOS or Sommerfeld approximation (as done below in Sec. 7.4.4 for test purposes). However, since AIMD requires a self-consistent cycle in any case, these approximations are not computationally beneficial.

7.3. Methodological details

We used the projector augmented wave method [42] and the PBE functional [43] as implemented in VASP [44, 45], in combination with the provided potentials [38]. For the early transition metals (up to Mn, Tc, and Re), the p states were treated as valence states [46]. For the ideal static lattice calculations, the plane-wave cutoff was set to twice the suggested maximum value, and the k-point meshes were set to $40 \times 40 \times 40$ for the 1-atom bcc and fcc cells (64,000 k-points · atom), and to $40 \times 40 \times 24$ for the 2-atom hcp cell (76,800 k-points · atom). For all the T=0 K calculations, the tetrahedron method with Blöchl corrections [47] was used to improve the convergence with respect to the k-point sampling. For the hcp structure an ideal c/a ratio was used. For comparing the different levels of approximations, the volume was set to 1.08 times the equilibrium volume at T=0 K, V_0, to approximately incorporate the thermal expansion at the temperatures of interest (1500 K and melting temperature). The actual dependence of the electronic excitations on the volume is discussed in Sec. 7.4.1.2. We determined V_0 by fitting the Vinet equation [48] to at least 12 energy-volume points in a range of $\pm 5\%$ around V_0. Most of the calculations were performed without spin-polarization to enable an interpretation of chemical trends. Bcc Fe, fcc Co and fcc Ni were additionally computed in the ferromagnetic state to elucidate the impact of magnetism. In order to obtain a smooth DOS $D(\varepsilon)$ from the discrete set of computed eigenvalues ε_i for visualization purposes and for deriving the DOS at the Fermi level $D(\varepsilon_F)$ for the Sommerfeld approximation, we replaced the delta function in Eq. (7.5) by smooth Gaussian functions:

$$D(\varepsilon) = \frac{1}{\sigma\sqrt{\pi}} \sum_i \exp\left(-\frac{(\varepsilon - \varepsilon_i)^2}{\sigma^2}\right), \tag{7.16}$$

with the broadening/smearing parameter σ set generally to 0.1 eV. For the Sommerfeld approximation we also used $\sigma = 0.2$ eV to test the influence on $D(\varepsilon_F)$.

For a subset of elements, namely bcc Nb, W; fcc Rh, Pt and hcp Re, Ru, we performed explicit AIMD simulations at different temperatures to investigate the impact of lattice vibrations. We used supercells with 54, 32, and 36 atoms for bcc, fcc, and hcp, respectively. Following the concept of the upsampled thermodynamic integration using Langevin dynamics (UP-TILD) method [49], in a first step these calculations were performed based on relatively low DFT convergence parameters to provide an efficient, but still accurate enough sampling of the configuration space. The cutoff energy was set to the default value of the potential from the VASP library and a $2 \times 2 \times 2$ k-point mesh was used (432, 256, 288 k-points · atom for bcc, fcc, hcp, respectively). The AIMD simulations were performed for about 5000 steps with a time step of 5 fs. The Langevin thermostat was used with a friction parameter of 0.01 fs^{-1}. In a following step, uncorrelated snapshots were extracted from the trajectories and recalculated with a denser k-point mesh ($8 \times 8 \times 8$; 27,648, 16,384, 18,432 k-points · atom for bcc, fcc, hcp) to determine accurate electronic free energies for the averaging. For each element and at each temperature, ten uncorrelated snapshots extracted from well equilibrated AIMD simulations were sufficient for a statistical error below 1 meV/atom in Eq. (7.14). The reason for this is that each supercell in itself is the average over many distinct atomic sites.

7.4. Results and discussion

7.4.1. SCF electronic free energies for ideal lattices

7.4.1.1. Temperature dependence

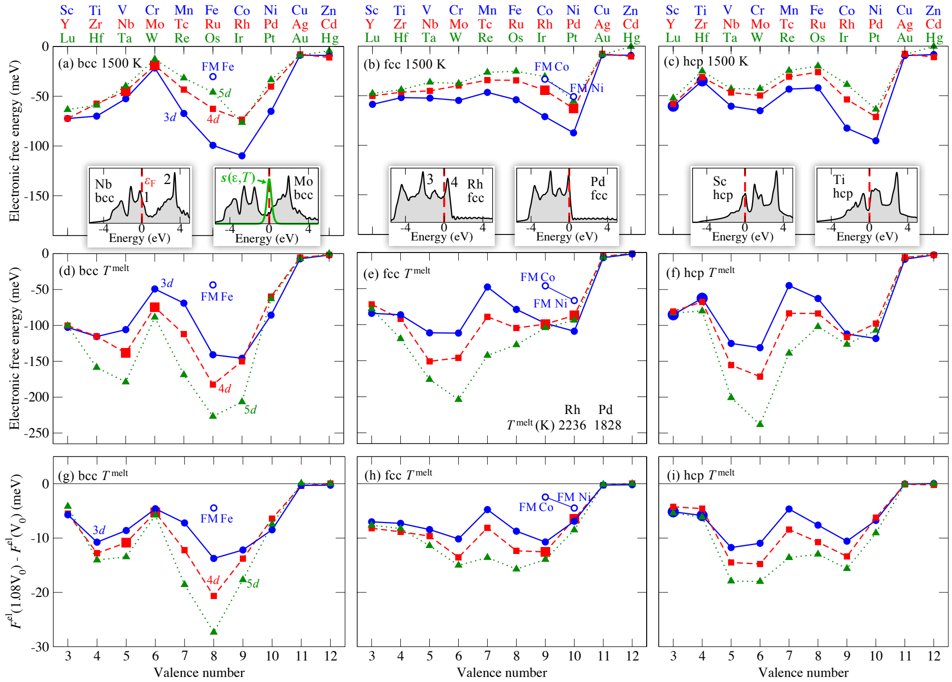

Figure 7.1: Ideal lattice SCF electronic free energies in meV/atom at (a-c) 1500 K and (d-f) the respective melting points (T^{melt}, cf. Tab. 7.3) referenced with respect to the internal energy at T=0 K. (g-i) show the electronic free energy change upon a volume increase of 8% with respect to the equilibrium volume V_0. The insets in (a-c) show the electronic DOS (arbitrary units) for some of the elements (emphasized by slightly larger symbols in the respective plots) in the three different structures (bcc, fcc, hcp). The Fermi levels ε_F are indicated by the red dashed lines. For bcc Nb and fcc Rh, the numbers 1-4 indicate peaks that are relevant for the discussion in the text. For bcc Mo, the entropy distribution $s(\varepsilon, T = 1500\,\text{K})$ [Eq. (7.9)] is plotted (green line). Throughout the figure, results correspond to non-magnetic calculations, except for the ferromagnetic (FM) results for bcc Fe, fcc Co, and fcc Ni (blue open circles). Exact numbers for all free energy values shown in (a-f) are given in Tab. 7.3.

Figure 7.1(a-c) shows the electronic free energies for all investigated elements and structures with atoms on the ideal lattice sites at an electronic temperature of 1500 K, calculated self-consistently using Eq. (7.3), but referenced to the extrapolated internal energy at T=0 K, i.e., showing $F^{\text{el}} - U^{\text{el}}(T\text{=}0\,\text{K})$. For interpreting the observed trends, the fixed DOS approximation is helpful. From Eqs. (7.6–7.8) it is apparent that the electronic free energy is directly linked to the electronic DOS. In fact, a closer look reveals that only the DOS close to the Fermi level contributes to F^{el}. For the internal energy, this can be seen by considering that the first integral in Eq. (7.7) is cancelled by the second one whenever $f \approx 1$, i.e., at energies sufficiently below the Fermi level. For energies sufficiently above the Fermi level, i.e., $f \approx 0$, both integrals give a negligible contribution. Regarding the entropy, note that the function $s(\varepsilon, T)$ in Eq. (7.9) is only peaked around the Fermi level as exemplified by the green line in the inset of Fig. 7.1(a). The Sommerfeld approximation, Eq. (7.12), gives an even more specific relation between the electronic DOS and electronic free energy: a *large* DOS at the Fermi energy implies a *largely negative* free energy.

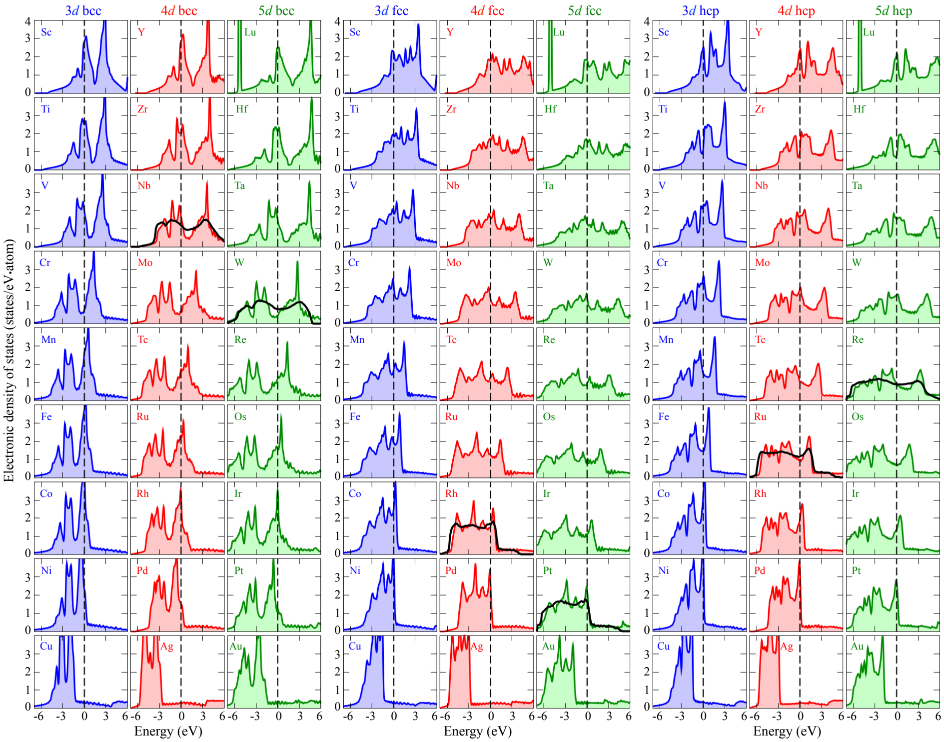

Figure 7.2: Electronic densities of states for all $3d$ (blue), $4d$ (red), and $5d$ (green) elements on the ideal lattices of bcc, fcc, and hcp in the non-magnetic state, and at an electronic temperature of T=0 K and a volume of $1.08V_0$, referenced with respect to the Fermi level (marked by the vertical dashed lines). The shift due to an increase in the electronic temperature up to the melting point is negligible on the shown scale. The black solid lines show the effective mean DOS' from the AIMD simulations at the melting temperature for the investigated cases. All DOS' were obtained with a smoothing parameter of $\sigma = 0.1$ eV.

Consider the two examples shown in the insets of Fig. 7.1(a), bcc Nb and Mo. The DOS is higher at the Fermi level for bcc Nb than for bcc Mo yielding a more negative free energy at 1500 K for Nb: -47 vs. Mo: -20 meV/atom [cf. large red squares in Fig. 7.1(a)]. For the subsequent $4d$ bcc elements [see Fig. 7.1(a)], the free energy decreases strongly to the right of Mo. This enhancement in magnitude is related to the peak in the DOS located above the Fermi level for Nb and Mo (marked with “2” in the Nb inset).

Indeed, according to the canonical d band model [30–32], the DOS does not significantly change across the d elements. We can therefore employ the DOS of Nb and Mo for statements about the other d elements. Increasing the number of valence electrons [i.e., going from left to right in Fig. 7.1(a)] only shifts the Fermi level to higher energies. The dependence of the electronic free energy for the bcc elements as a function of the d valence number hence reflects the peak structure of a generic bcc DOS. This applies to the $3d$, $4d$, and $5d$ transition elements, all having a very similar generic DOS and consequently a similar electronic free energy dependence [Fig. 7.1(a)].

The canonical d band model can similarly be used to correlate the dependence of the electronic free energy for the fcc and hcp elements with their generic DOS. As each geometry (bcc, fcc, hcp) leads to a different specific generic DOS [insets in Fig. 7.1(a-c)], the corresponding electronic free energy trends [Fig. 7.1(a-c)] likewise differ from each other. (See Fig. 7.2 for the complete set of the computed non-magnetic densities of states. The corresponding DOS values at the Fermi level are given in Tab. 7.2.)

The electronic free energy at a fixed absolute (electronic) temperature is, as just discussed, useful for analyzing the correlation to the DOS. When computing free energies one is, however, often interested in temperatures up to the respective melting point. The corresponding electronic free energies (still within the ideal lattice approximation) are shown in Fig. 7.1(d-f). The dependencies clearly change with respect to those at a fixed absolute temperature, because of the strongly varying melting points across the d elements (see Tab. 7.3). This is nicely illustrated for the example of Rh fcc and Pd fcc. At 1500K, the relative magnitude of the free energy for Pd and Rh is determined exclusively by the DOS near the Fermi level, and hence the free energy of Pd has a magnitude 38% larger compared to Rh. At the respective (experimental) melting temperature, the trend reverses: Rh has a melting temperature of 2236 K [50], larger by 22% than that of Pd (1828 K [50]). As the free energy scales approximately quadratically with temperature, the temperature effect dominates and reverts the order of relative magnitudes.

Figure 7.1(d-f) clearly shows that the magnitude of the electronic free energy at the melting point can be significant, ≈ -250 meV/atom (bcc Os, T^{melt}=3306 K). Comparing the data for the same element but for different structures reveals that the magnitudes can be quite different, e.g., Ir bcc: -218, Ir fcc: -113, Ir hcp: -136 meV/atom. This highlights the importance of electronic contributions for determining phase stabilities and transition temperatures as the latter are known to strongly depend even on changes in the range of a few meV/atom in the free energy [25, 51, 52].

7.4.1.2. Volume dependence

Since at high temperatures, especially at the melting point, the volume change of the system can be significant, the impact of volume on the electronic free energy needs to be carefully addressed. In Fig. 7.1(g-i) we show the change in the ideal lattice SCF electronic free energies at the melting point upon increasing the volume from the equilibrium volume at T=0 K, V_0, to a volume of $1.08V_0$, which reflects a reasonable estimate of the thermal expansion at the melting point. An important finding is that the electronic free energy decreases with increasing volume for all investigated elements. The overall magnitude

Table 7.2: Electronic densities of states at the Fermi level in states/eV·atom for all investigated elements and structures in the non-magnetic state at a volume of $1.08V_0$. The first row for each element shows the DOS for the ideal static lattice at an electronic temperature of T=0 K and the second row at an electronic temperature corresponding to the respective melting point. For a few selected elements and phases, the third row indicates the effective DOS at the Fermi level including the impact of thermal vibrations at the melting point. The subscripts "sv" and "pv" indicate the inclusion of semi-core s and p electrons into the valence of the employed potentials.

$3d$	bcc	fcc	hcp	$4d$	bcc	fcc	hcp	$5d$	bcc	fcc	hcp
$\mathrm{Sc_{sv}}$	2.8	2.3	2.5	$\mathrm{Y_{sv}}$	2.9	1.8	2.4	Lu	2.5	1.8	2.1
	2.8	2.2	2.5		2.8	1.8	2.4		2.5	1.8	2.1
$\mathrm{Ti_{pv}}$	2.5	1.9	1.1	$\mathrm{Zr_{sv}}$	2.0	1.7	1.1	$\mathrm{Hf_{pv}}$	2.1	1.6	0.8
	2.5	1.9	0.9		2.0	1.7	0.8		2.1	1.6	0.7
$\mathrm{V_{pv}}$	2.0	1.9	2.3	$\mathrm{Nb_{pv}}$	1.7	1.6	1.7	$\mathrm{Ta_{pv}}$	1.5	1.3	1.5
	1.8	1.8	2.2		1.4	1.6	1.7		1.2	1.3	1.5
					1.2						
$\mathrm{Cr_{pv}}$	0.8	2.2	2.6	$\mathrm{Mo_{pv}}$	0.7	1.4	1.9	$\mathrm{W_{sv}}$	0.5	1.6	1.6
	0.6	1.9	2.6		0.6	1.3	1.9		0.4	1.3	1.6
									0.8		
$\mathrm{Mn_{pv}}$	2.7	1.7	1.5	$\mathrm{Tc_{pv}}$	1.7	1.3	1.1	Re	1.3	1.0	0.8
	2.4	1.7	1.5		1.5	1.3	1.0		1.0	0.9	0.8
											0.9
Fe	3.7	1.9	1.5	Ru	2.3	1.2	1.0	Os	1.6	1.0	0.7
	3.6	1.9	1.4		2.3	1.2	0.9		1.6	0.8	0.7
							1.1				
Co	5.0	2.5	3.2	Rh	3.3	1.5	1.9	Ir	3.6	1.0	1.4
	3.9	2.4	2.9		2.2	1.5	1.8		3.2	1.1	1.3
						1.7					
Ni	2.3	4.4	5.0	Pd	1.5	3.0	3.5	Pt	1.2	2.4	2.8
	2.2	3.0	2.8		1.5	2.0	2.3		1.2	2.1	2.6
										1.6	
Cu	0.4	0.4	0.4	Ag	0.3	0.3	0.3	Au	0.3	0.3	0.3
	0.3	0.3	0.4		0.3	0.3	0.3		0.3	0.3	0.3
Zn	0.4	0.3	0.3	Cd	0.4	0.4	0.4	Hg	0.2	0.1	0.0
	0.3	0.3	0.3		0.4	0.3	0.4		0.2	0.0	0.0

Table 7.3: Ideal lattice electronic free energies in meV/atom at 1500 K and at the indicated melting points (T^{melt}=experimental melting point in K from Ref. [50]) for all $3d$, $4d$, and $5d$ transition metals for the bcc, fcc, and hcp structures computed using the SCF approach, Eqs. (7.1–7.4). Values correspond to non-magnetic calculations except for the ferromagnetic (FM) results for bcc Fe, fcc Co, and fcc Ni. The subscripts "sv" and "pv" indicate the inclusion of semi-core s and p electrons into the valence of the employed potentials.

Element	T^{melt}	bcc		fcc		hcp	
		1500 K	T^{melt}	1500 K	T^{melt}	1500 K	T^{melt}
$\mathrm{Sc_{sv}}$	1814	-72	-103	-59	-84	-61	-85
$\mathrm{Ti_{pv}}$	1943	-70	-116	-52	-86	-35	-62
$\mathrm{V_{pv}}$	2183	-53	-106	-52	-111	-61	-125
$\mathrm{Cr_{pv}}$	2180	-22	-49	-55	-112	-65	-131
$\mathrm{Mn_{pv}}$	1519	-67	-69	-47	-48	-43	-44
Fe	1811	-99	-141	-54	-79	-42	-63
Fe(FM)	1811	-30	-44				
Co	1768	-110	-146	-71	-98	-83	-112
Co(FM)	1768			-33	-46		
Ni	1728	-65	-86	-87	-109	-95	-118
Ni(FM)	1728			-51	-67		
Cu	1358	-9	-7	-9	-7	-9	-8
Zn	693	-9	-2	-9	-2	-8	-2
$\mathrm{Y_{sv}}$	1795	-72	-100	-50	-72	-58	-81
$\mathrm{Zr_{sv}}$	2127	-58	-115	-46	-92	-31	-67
$\mathrm{Nb_{pv}}$	2750	-45	-138	-45	-151	-47	-155
$\mathrm{Mo_{pv}}$	2895	-19	-75	-40	-146	-50	-171
$\mathrm{Tc_{pv}}$	2430	-43	-112	-34	-89	-31	-83
Ru	2606	-63	-182	-34	-105	-26	-83
Rh	2236	-73	-150	-44	-99	-54	-116
Pd	1828	-40	-60	-63	-87	-71	-97
Ag	1235	-8	-5	-8	-5	-8	-5
Cd	594	-11	-2	-10	-1	-11	-2
Lu	1936	-63	-101	-48	-78	-52	-83
$\mathrm{Hf_{pv}}$	2506	-59	-159	-44	-120	-25	-80
$\mathrm{Ta_{pv}}$	3290	-40	-179	-36	-176	-43	-201
$\mathrm{W_{sv}}$	3687	-13	-89	-38	-204	-43	-238
Re	3458	-32	-169	-26	-143	-25	-139
Os	3306	-46	-227	-25	-128	-20	-102
Ir	2719	-76	-207	-31	-104	-39	-126
Pt	2041	-34	-63	-55	-94	-64	-107
Au	1337	-9	-7	-8	-7	-8	-7
Hg	234	-5	0	0	0	0	0

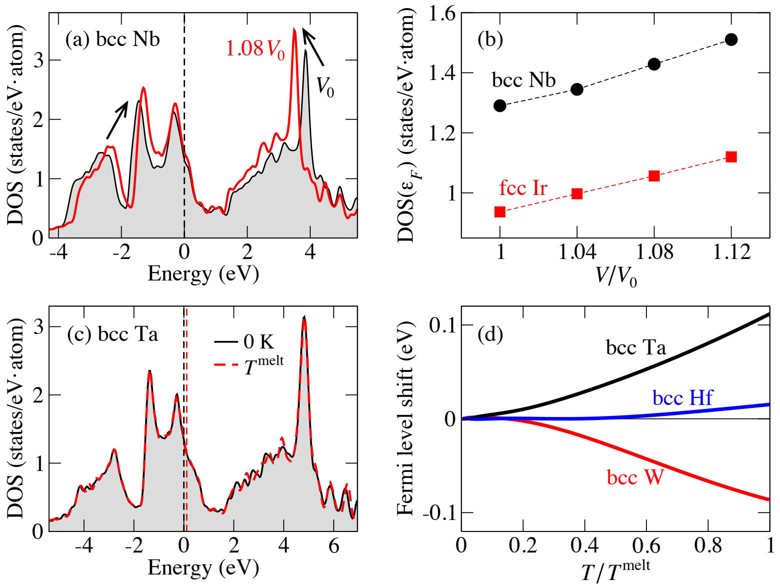

Figure 7.3: Influence of volume and temperature on the electronic DOS. (a) Change of the DOS for bcc Nb upon increasing the volume from V_0 (equilibrium volume at T=0 K, black line and gray shading) to $1.08V_0$ (red line). The resulting compression is emphasized by the arrows, and the Fermi level (the same for both DOS') is marked by the black dashed line. (b) Change of the DOS directly at the Fermi level, ε_F, with volume for two examples. (c) Change of the DOS for bcc Ta upon increasing the (electronic) temperature from T=0 K (black line and gray shading) to $T^{\text{melt}} = 3290$ K (red dashed line) within the self-consistent finite temperature DFT calculation. The black and red dashed lines mark the respective Fermi levels; the red line for the T^{melt} calculation being shifted by about 0.1 eV with respect to the black one. (d) Fermi level shift with temperature for three examples showing different dependencies (positive, small, negative).

of the free energy decrease due to the 8% volume change is for most of the investigated elements about 10% of the total electronic free energy [Fig. 7.1(d-f)], and consequently the general chemical trends are similar.

The negative dependence of the electronic free energy on the volume can be understood by examining the variation of the electronic DOS with volume. As a representative example, the electronic DOS of bcc Nb is shown in Fig. 7.3(a) at V_0 (black line and gray shading) and $1.08V_0$ (red line). As the volume increases, the generic features of the electronic DOS do not change except for an overall compression of the d band (exemplified by the arrows), centered around the Fermi level. This compression is a consequence of the well-known reduction of d-band width as the d-orbital overlap decreases with increasing distance between the atoms. Since the Fermi level is determined by the conservation of the number of electrons, it remains in a similar relative position after the volume change, as compared, e.g., to the neighboring peak. Further, since the total spectral weight of the d-band must remain the same the compression leads to an overall increase of the DOS, inversely proportional to the reduction in d-band width, as can be observed by comparing the heights of the peaks in Fig. 7.3(a). In consequence, increasing the volume leads to an increase of the DOS at the Fermi level [Fig. 7.3(b)] and hence to an increase in entropy and a corresponding lowering

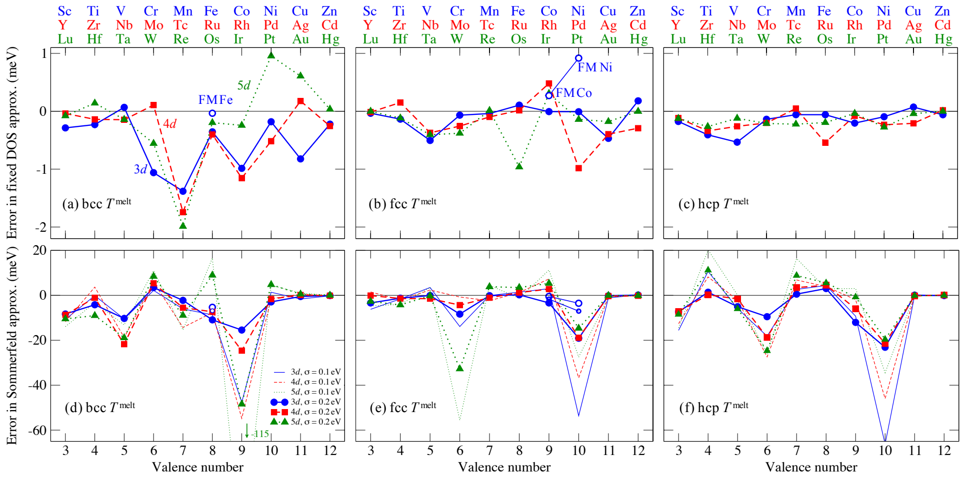

Figure 7.4: (a-c) Error in the fixed DOS and (d-f) Sommerfeld approximation at an electronic temperature corresponding to the respective melting point $T^{\rm melt}$ for all $3d$ (blue dots), $4d$ (red squares), and $5d$ (green triangles) transition metals in the (a, d) bcc, (b, e) fcc, and (c, f) hcp structures. The error is defined as the deviation from the SCF electronic free energy for an ideal lattice. In (d-f) the thick lines with symbols correspond to a smearing parameter $\sigma = 0.2$ eV and the thin lines without symbols to $\sigma = 0.1$ eV, used to obtain the corresponding DOS at the Fermi level. Throughout the figure, results correspond to non-magnetic calculations, except for the data shown by the blue open circles which represent ferromagnetic (FM) calculations for bcc Fe, fcc Co, and fcc Ni.

of the free energy.

7.4.2. Fixed density-of-states approximation

We now turn to the error introduced by the fixed DOS approximation [Eqs. (7.6–7.8)]. We focus on the deviation from the ideal lattice SCF electronic free energy at the melting point which can be considered as the most severe condition for the validation. As shown in Fig. 7.4(a-c), for most of the elements the corresponding error is below 1 meV/atom. Only a few cases, e.g., bcc Tc and Re, show a slightly higher error, up to 2 meV/atom. The performance of this approximation is best for hcp structures, with errors of less than 0.5 meV/atom. Noting that all errors will decrease upon lowering the temperature, we can safely conclude that the fixed DOS approximation is in general an excellent approximation to calculate electronic free energies.

Compared with the SCF method, the fixed DOS approximation neglects the variation of the electronic DOS with temperature. The validity of this assumption is illustrated in Fig. 7.3(c) for bcc Ta, showing a comparison of the DOS at T=0 K (black line) and at the melting temperature (red dashed line) using the identical volume. As the temperature is increased, the profile of the DOS remains almost the same (i.e., the red dashed curve and the black solid curve overlap) except for a shift of the Fermi energy (cf. distance between the vertical black and red lines). The Fermi energy shift, $\varepsilon_{\rm shift}$, can be determined by

$$\int_{-\infty}^{\infty} D(\varepsilon)\, f(\varepsilon - \varepsilon_{\rm shift}, T)\, {\rm d}\varepsilon \;=\; \int_{-\infty}^{\varepsilon_{\rm F}} D(\varepsilon)\, {\rm d}\varepsilon \;=\; N_{\rm el}, \qquad (7.17)$$

which ensures the preservation of the total number of electrons, N_{el}. The shift will be small [bcc Hf in Fig. 7.3(d)] when the DOS can be expanded reasonably well in even functions around the Fermi level. In this case, excited electrons will be able to populate energy states symmetrically around the (original, T=0 K) Fermi level. The shift will be larger [$\approx \pm 0.1$ eV; see bcc Ta and bcc W in Fig. 7.3(d)] for DOS' that are strongly deviating from an even description around the Fermi level, because then excited electrons will asymmetrically populate the empty energy states.

7.4.3. Sommerfeld approximation

The virtue of the Sommerfeld model is that it provides simple analytical formulas for the thermodynamic potentials [Eqs. (7.10–7.12)], which are for example important for parameterizations in thermodynamic modeling approaches (such as, e.g., the calphad approach [53, 54]). Since the Sommerfeld model is based on a low temperature expansion it is critical to know its performance up to the melting point. Figure 7.4(d-f) shows that the error in the electronic free energy caused by the Sommerfeld approximation can reach several tenths of meV/atom at T^{melt}. An additional difficulty is that the error critically depends on the technical details of the DOS calculation. The value of the electronic DOS at the Fermi level, which solely determines the electronic free energy in the Sommerfeld model, can sensitively depend on the broadening (aka smearing) parameter used to derive a smooth DOS from the discrete set of eigenvalues [Eq. (7.16)]. As an example, errors for two different smearing parameters of 0.1 and 0.2 eV are shown in Fig. 7.4(d-f) (thin and thick lines), indicating that a smaller error is generally associated with a larger smearing parameter. For a fixed smearing parameter, e.g., 0.2 eV, the magnitude of the error varies significantly across the d series, ranging from less than 1 meV (e.g., for bcc Zr, fcc V) to several tens of meV (e.g., for bcc Ir, fcc W) per atom.

It is useful to elucidate the origin of the deviations exhibited by the Sommerfeld model. For that purpose we compare in Fig. 7.5 the DOS of an element revealing a small error (1 meV/atom, fcc Ru) to an element revealing a large error (48 meV/atom, bcc Ir). One simplification within the Sommerfeld model is the assumption that the DOS close to the Fermi energy varies smoothly. It can be seen in Fig. 7.5(a) that the DOS of fcc Ru exhibits comparably small fluctuations close to the Fermi energy. The Fermi energy (vertical dashed line) is located close to a shallow valley where the DOS is not sensitive to the employed smearing parameter (cf. black solid line and blue dashed line). In contrast, as shown in Fig. 7.5(b), the DOS of bcc Ir has a sharp peak directly at the Fermi energy, the height of which changes dramatically with the smearing parameter. The observation that the Sommerfeld approximation exhibits large and sensitive errors when the Fermi energy is located at a sharp DOS peak is general. The bcc elements with 5 (V, Nb, and Ta) and 9 (Co, Rh, and Ir) valence electrons have large errors, because their Fermi level hits the peaks labeled 1 and 2 in the inset of Fig. 7.1(a). Similarly, the large errors for fcc Cr, Mo, and W are connected to the peak labeled 3 in the inset of Fig. 7.1(b) and the errors for fcc Ni, Pd, and Pt with the peak labeled 4.

A second simplification within the Sommerfeld model is the neglect of the higher-order terms in the expansions Eqs. (7.10–7.12). To elucidate the importance of these terms we plot in Fig. 7.6 the temperature dependence of the internal energy and free energy for fcc

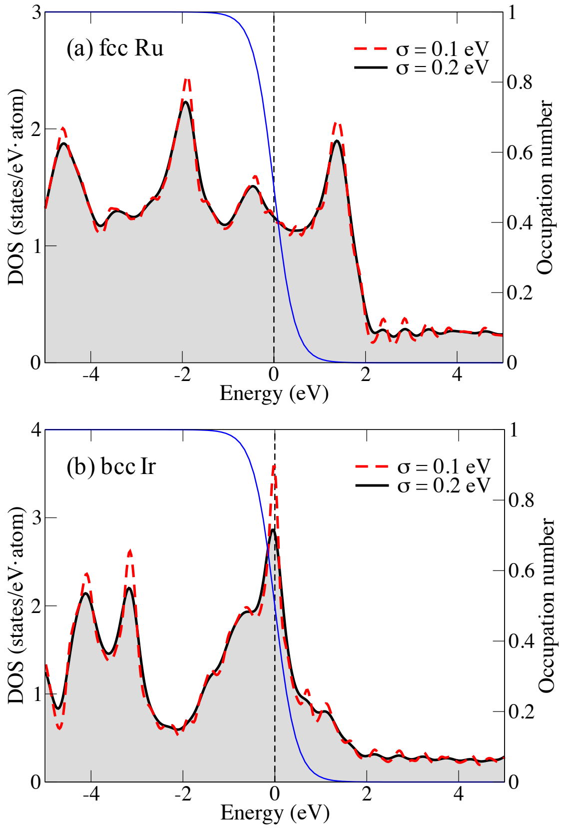

Figure 7.5: Electronic DOS for (a) fcc Ru and (b) bcc Ir at T=0 K, obtained with two different smearing parameters, σ, of 0.1 eV (red dashed lines) and 0.2 eV (black lines and gray shading) in Eq. (7.16). The blue solid lines indicate the Fermi-Dirac occupation function at the respective melting points (Ru: 2606 K and Ir: 2719 K).

Ru and bcc Ir up to the respective T^{melt}. All solid lines have been calculated using the SCF procedure, i.e., using Eqs. (7.1–7.4) and performing a full self-consistency cycle at each temperature. Figure 7.6 also includes the results from the Sommerfeld approximation (dashed and dash-dotted lines), using Eqs. (7.10) and (7.12), and neglecting all but the lowest-order term ($\sim T^2$ term). For fcc Ru shown in Fig. 7.6(a), the Sommerfeld model nicely reproduces the SCF dependence even up to the melting point of 2606 K [50], revealing that the electronic internal energy and free energy of fcc Ru depend quadratically on temperature. However, fcc Ru is a rare case and many elements such as, e.g., bcc Ir reveal rather strong deviations from the quadratic dependence. In Fig. 7.6(b), the $\widetilde{U}^{\mathrm{el}}_{\mathrm{SOM}}$ curve (dashed line above zero) deviates significantly from the SCF U^{el} curve at about 30% of the melting point. The $\widetilde{F}^{\mathrm{el}}_{\mathrm{SOM}}$ curve (dashed line below zero) starts to deviate from F^{el} at about 10% of the melting point, with the error changing the sign. For most of the $3d$, $4d$ and $5d$ elements the assumption of a quadratic T-dependence is thus not justified for an accurate determination of the electronic free energy.

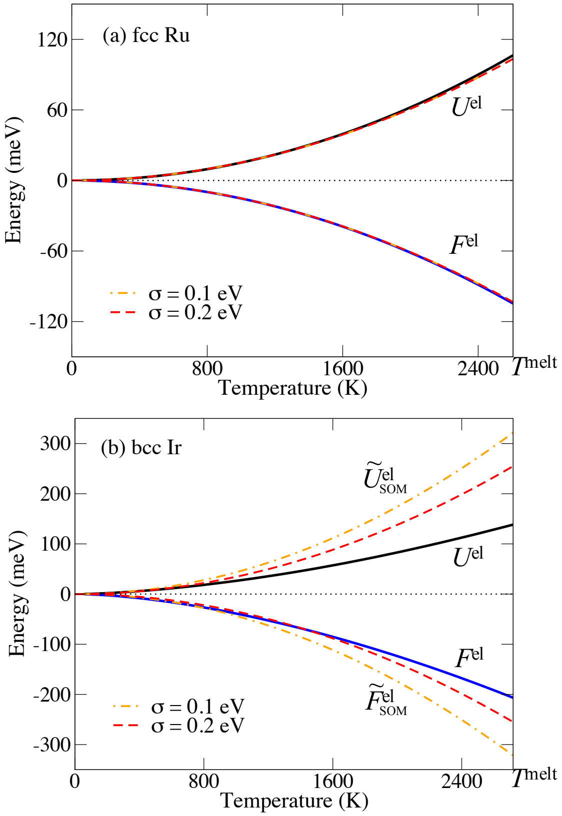

Figure 7.6: Temperature dependence of the SCF electronic internal energy U^{el} (black lines) and the SCF electronic free energy F^{el} (blue lines) for (a) fcc Ru and (b) bcc Ir up to the respective melting points, T^{melt}. The red dashed lines and orange dash-dotted lines show results of the corresponding Sommerfeld approximation [Eqs. (7.10) and (7.12)] for two different smearing parameters ($\sigma = 0.1$ eV and $\sigma = 0.2$ eV).

7.4.4. Impact of explicit lattice vibrations

All results discussed so far have been obtained with the atoms placed on their ideal lattice sites. This assumption neglects the impact of atomic vibrations on the electronic free energy. Investigating the corresponding error requires expensive AIMD simulations and we therefore restricted our attention to a few representative elements: bcc Nb, W; fcc Rh, Pt; hcp Re, Ru. This choice represents elements in their experimentally observed, stable phases, it covers the three investigated lattices and also the $4d$ and $5d$ elements. See the study on Fe in Ref. [29] for an example of a $3d$ element.

Figure 7.7 shows the change in the electronic free energy upon including the thermal vibrations at the melting point, where the highest impact can be expected. The black bars correspond to our reference computed by the SCF procedure for an ideal lattice (more precisely $F^{el} - U^{el}(T{=}0\,\text{K})$ as in Sec. 7.4.1) and the red bars show the AIMD results including explicit vibrations according to Eq. (7.14). The changes induced by the atomic

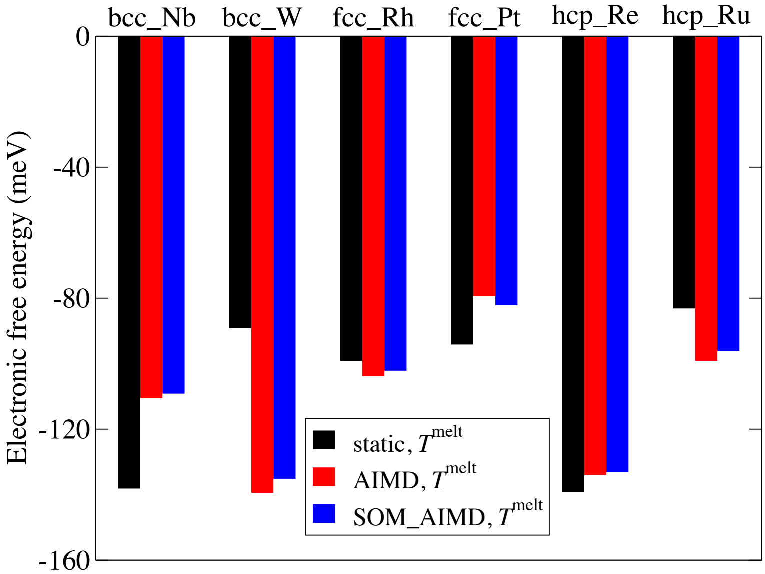

Figure 7.7: Comparison of the electronic free energies in meV/atom extracted from AIMD simulations (red bars) with those computed via the SCF finite temperature DFT approach for an ideal static lattice (black bars). The blue bars correspond to the Sommerfeld approximation, but using the effective DOS from the AIMD simulations as input.

motion can be positive or negative, with a substantial magnitude ranging from a few meV/atom (e.g., fcc Rh: –4) to a few tens of meV/atom (e.g., bcc W: –50).

The observed behavior can be understood by analyzing the averaged electronic DOS' obtained from the AIMD simulations, as shown in Fig. 7.8 by the black solid lines. A significant broadening and smoothening is visible when compared to the T=0 K electronic DOS' represented by the white solid curves. Sharp peaks are strongly smeared out and damped, and valleys are filled up with electronic states. These findings are consistent with previous studies for Mo [28] and Fe [29]. The reason for such a behavior is the loss of the crystal symmetry—a main ingredient to the pronounced peak profiles of the T=0 K DOS'—induced by the thermal vibrations. The disordered atomic positions result in a much more homogeneous distribution of the energy levels compared to the perfect static lattice. The homogeneous distribution applies already to each single snapshot and the differences between the DOS' of (uncorrelated) snapshots are small as evidenced by the small standard deviation (orange gradient in Fig. 7.8). This finding suggests that the number of k-points required to sample the Brillouin zone could be reduced for high temperature calculations. Future studies are required to quantify this statement.

The strong smoothening of the electronic DOS has a considerable effect on the electronic free energy, in full analogy to the discussions of the previous sections. Whenever the Fermi level is located close to a sharp peak in the original T=0 K electronic DOS, as for bcc Nb, the damping of the peak leads to a reduction of the effective DOS at the Fermi level and consequently to a reduction of the magnitude of the electronic free energy. When the Fermi level is located inside a valley of the original T=0 K electronic DOS, as for bcc

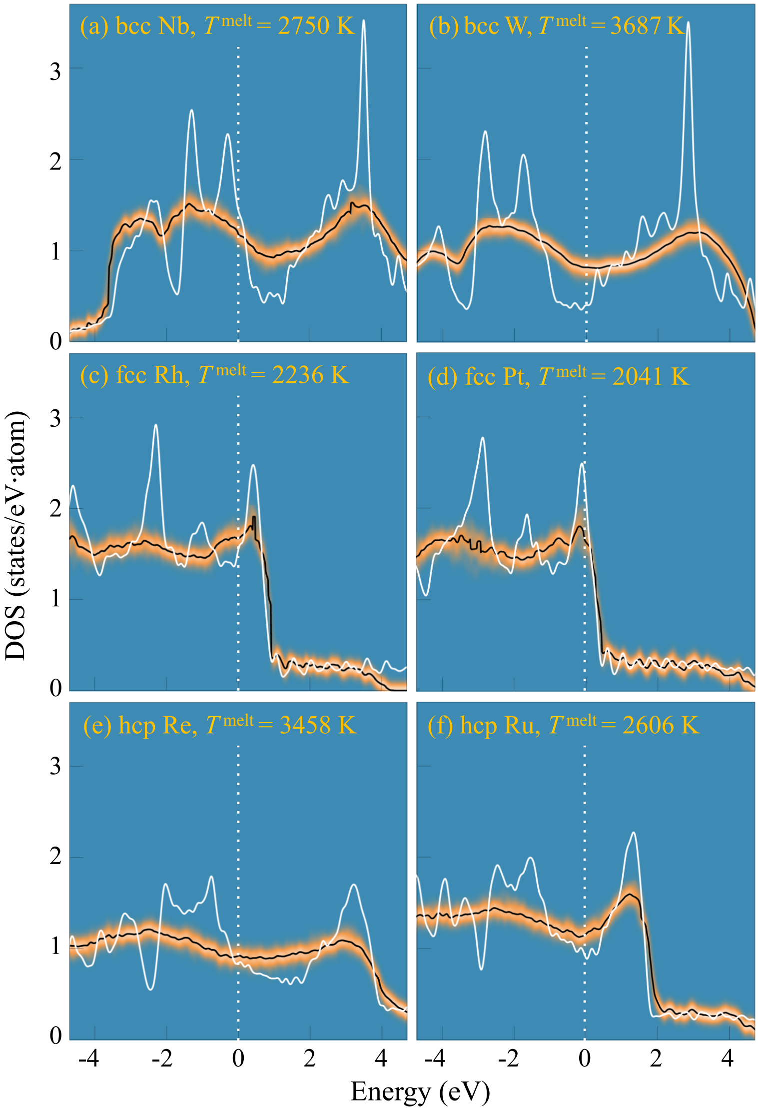

Figure 7.8: Influence of lattice vibrations on the electronic DOS for a few selected elements at their respective melting temperatures, extracted from AIMD simulations. The black lines indicate the mean value from a statistically converged set of uncorrelated AIMD snapshots and the orange gradient shows the corresponding standard variance. The white solid lines show the DOS obtained from static calculations for the ideal lattices at an electronic temperature corresponding to the melting point. The white dotted lines indicate the Fermi level.

W, the broadening leads to an increase of the effective DOS at the Fermi level and of the magnitude of the electronic free energy. An interesting side effect of the thermal broadening is an increase in the accuracy of the Sommerfeld model, provided one employs the high temperature effective DOS as input. The differences with respect to the full AIMD based

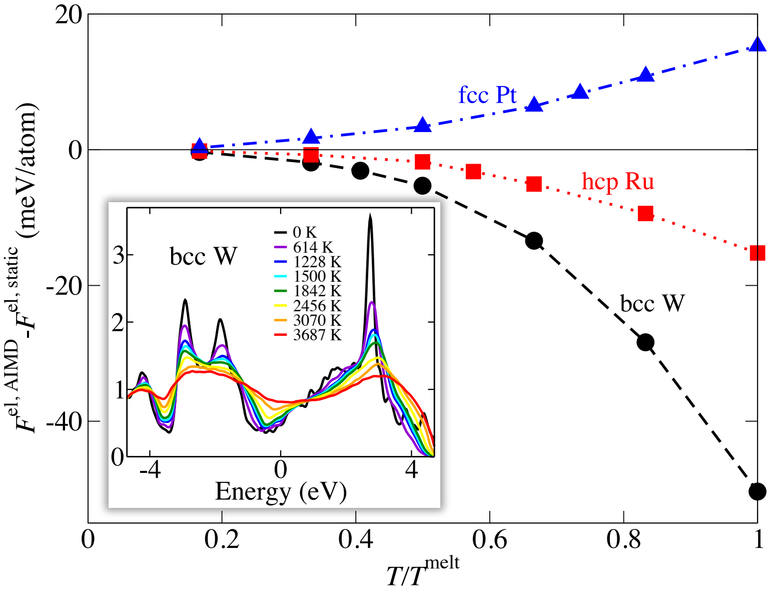

Figure 7.9: Temperature dependence of the change in the electronic free energy due to thermal lattice vibrations for bcc W (black circles), fcc Pt (blue triangles) and hcp Ru (red squares). The temperature axis has been normalized by the respective melting temperature. The inset shows the temperature dependence of the effective electronic DOS (in units of states/eV· atom) for bcc W from the AIMD simulations.

electronic free energy are in the range of a few meV/atom (blue vs. red bars in Fig. 7.7).

We have also investigated the temperature dependence of the impact of thermal vibrations on the electronic free energy. Figure 7.9 shows respective results for bcc W, fcc Pt and hcp Ru. A nonlinear temperature dependence can be observed for all three elements. The changes in the electronic free energy can be again traced back to the broadening of the electronic DOS with temperature as exemplified for bcc W in the inset. The exact type of the temperature dependence of the electronic free energy is difficult to deduce, but it is conceivable that a linear dependence is unlikely to occur due to the complex changes in the electronic DOS with temperature.

7.4.5. Electronic contribution to the heat capacity

As one of the key thermodynamic properties, heat capacities can be either measured experimentally or calculated theoretically. They are an important ingredient to thermodynamic modelling approaches of phase stabilities and phase diagrams, such as the calphad approach [53, 54]. For such a modelling it is useful to have a good estimate of the magnitude and of the temperature dependence of the different heat capacity contributions. For low temperatures, it is well-known that the electronic heat capacity contribution depends linearly on temperature as can be derived from the Sommerfeld model [cf. Eq. (7.13)] [16, 20, 23, 55]. We focus here on the electronic heat capacity at high temperatures.

Figure 7.10(a-c) shows the electronic heat capacities calculated by the SCF method

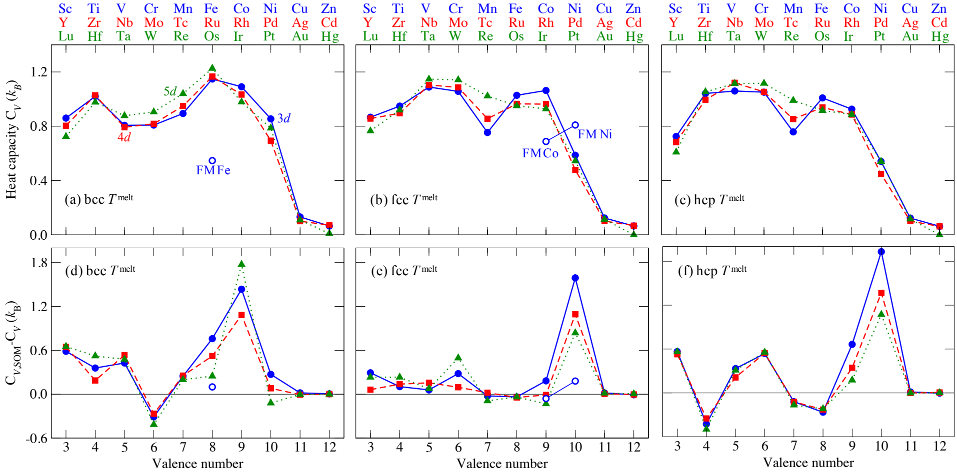

Figure 7.10: (a-c) Ideal lattice SCF electronic contribution to the constant volume heat capacity and (d-f) error of the Sommerfeld approximation at the melting point ($T^{\rm melt}$) and $1.08V_0$ for all $3d$ (blue dots), $4d$ (red squares), and $5d$ (green triangles) transition metals in the (a, d) bcc, (b, e) fcc, and (c, f) hcp structures. The ideal lattice SCF heat capacity was obtained from a finite difference of the temperature dependence of the electronic internal energy (using 1 K steps). The Sommerfeld heat capacity was calculated with Eq. (**??**), using $\sigma = 0.1$ eV for smoothing the required DOS at the Fermi level. Throughout the figure, results correspond to non-magnetic calculations, except for the data shown by the blue open circles which represent ferromagnetic (FM) calculations for bcc Fe, fcc Co, and fcc Ni.

for all investigated elements at the respective melting temperatures within the ideal, static lattice approximation. The magnitude of the electronic heat capacities is in the order of $\sim$1 k_B with the exception of the late transition elements (valence numbers 11 and 12). A contribution of $\sim$1 k_B is significant and is also in the order of other contributions (e.g., due to thermal expansion or anharmonic vibrations [7]). In fact, one should note that the electronic contribution to the heat capacity at constant pressure, which corresponds to the typical experimental conditions, will be 30 % larger than the here considered contribution to the constant volume heat capacity [56].

The fixed DOS approximation provides very accurate electronic heat capacities (not shown) with a maximum error of 0.03 k_B and most of the errors well below 0.01 k_B. One should be however cautious when using the linear Sommerfeld extrapolation up to the melting temperature. From Fig. 7.10(d-f) it is apparent that the corresponding errors can be significant, mostly overestimating the SCF heat capacity values. The maximum deviation can even reach up to a factor of 2 of the corresponding absolute value (e.g., fcc Ni). The critical cases are characterized by sharp peaks or dips in the DOS near the Fermi level.

Another source of error is the ideal lattice approximation, similarly as for the electronic free energies. The importance of lattice vibrations on the electronic heat capacity is shown in Fig. 7.11 for three representative elements bcc W, fcc Pt and hcp Ru. Dashed lines represent the electronic heat capacity from the SCF procedure for the ideal lattices, and solid lines the AIMD computed heat capacities. For fcc Pt and hcp Ru the impact of lattice vibrations is comparably small. In contrast, bcc W shows a strong impact with more than a factor of two

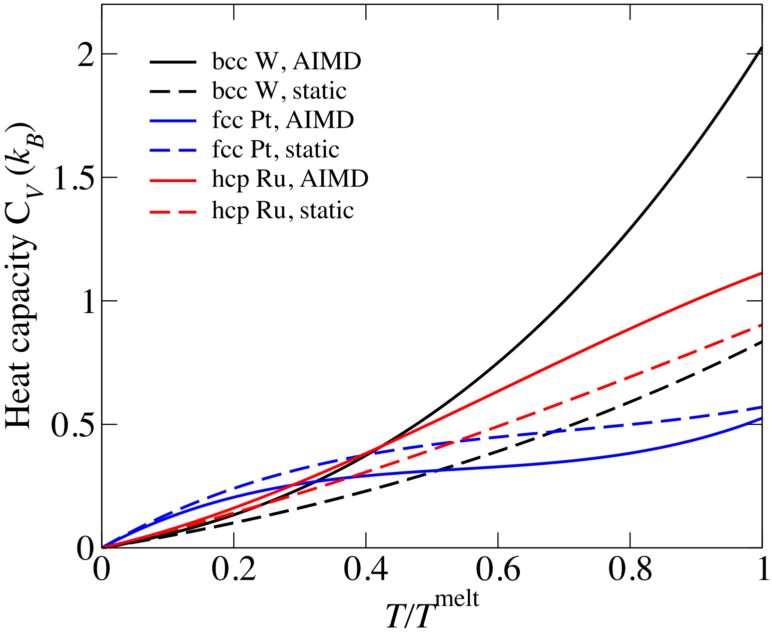

Figure 7.11: Temperature dependence of the constant volume electronic heat capacity for bcc W (black), fcc Pt (blue), hcp Ru (red) with (solid lines) and without (dashed lines) the impact of vibrations. To obtain an accurate heat capacity from the coarse set of free energies (see Fig. 7.9), we used a physically motivated fit as introduced in Ref. [25] with a second-order polynomial for the energy independent electronic density of states. For consistency, the same fit was used to obtain the temperature dependence of the ideal lattice SCF heat capacities (dashed lines). The temperature axis has been normalized by the respective melting temperature.

increase arising from the vibrations at the melting point. This behavior can be traced back to the significant non-linear temperature dependence of the electronic free energy including lattice vibrations (Fig. 7.9).

7.5. Conclusions

By conducting a wide-range investigation for all d transition elements for various ideal, static crystal lattices using finite temperature density-functional-theory calculations, we have systematically quantified general chemical trends of the electronic free energy and its relation to the electronic density of states. In agreement with previous knowledge, a high electronic density of states close to the Fermi energy results in a significant, negative electronic free energy contribution, in qualitative agreement with the Sommerfeld prediction. The dependence of the electronic free energy on the valence number therefore reflects the shape of a generic density of states, determined by the geometry of the crystal structure (bcc, fcc, hcp). The magnitude of the calculated electronic free energies as well as electronic heat capacities at high temperatures highlights the importance of electronic contributions in determining phase stabilities and phase diagrams.

Using this set of data and additional *ab initio* molecular dynamics simulations for selected cases allowed us to quantitatively assess the performance of three widely used approximations for computing electronic free energies. (1) The fixed density of states approximation, which neglects the temperature dependence of the density of states, performs extremely well for all investigated elements and structures, with errors in the electronic free energy of mostly below 1 meV/atom at the melting point. Electronic heat capacities are likewise very well predicted. (2) The Sommerfeld approximation—when fed with the electronic density of states computed for the ideal static lattice—makes much more drastic assumptions and thus the corresponding error at high temperatures is about an order of magnitude larger. (3) The ideal lattice approximation neglects the impact of thermal atomic vibrations. The latter have a significant smoothening effect on the electronic density of states, and the resulting thermally averaged electronic free energy can change with respect to the ideal lattice electronic free energy by several tens of meV/atom. The details of these changes depend on the original location of the Fermi level with respect to peaks and valleys in the ideal, static electronic density of states.

Interestingly, the accuracy of the Sommerfeld approximation increases substantially when the effective electronic density of states from the molecular dynamics simulations is employed as input. Such an effective Sommerfeld model offers an interesting possibility for relatively simple, but accurate parameterizations of the electronic free energy *including* the impact of thermal vibrations for calphad based phase diagram approaches.

The smoothening of the effective electronic density of states by the thermal vibrations destroys the crystal structure specific peak profile inherent to the ideal static lattice density of states. The thermal disorder thus drives the electronic density of states towards a generic profile, weakly dependent on the crystal structure. We have shown this for a few selected elements but we believe that this holds for all d transition elements.

We expect the insights and results of our study to be an important step towards the development of high accuracy databases of *ab initio* free energies for metals.

References

[1] G. Grimvall, B. Magyari-Köpe, V. Ozoliņš, and K. A. Persson, *Lattice instabilities in metallic elements,* Review of Modern Physics **84**, 945 (2012).

[2] O. Hellman, P. Steneteg, I. A. Abrikosov, and S. I. Simak, *Temperature dependent effective potential method for accurate free energy calculations of solids,* Physical Review B **87**, 104111 (2013).

[3] M. Pozzo and D. Alfè, *Melting curve of face-centered-cubic nickel from first-principles calculations,* Physical Review B **88**, 024111 (2013).

[4] C. Freysoldt, B. Grabowski, T. Hickel, J. Neugebauer, G. Kresse, A. Janotti, and C. G. Van de Walle, *First-principles calculations for point defects in solids,* Review of Modern Physics **86**, 253 (2014).

[5] M. Palumbo, B. Burton, A. C. E. Silva, B. Fultz, B. Grabowski, G. Grimvall, B. Hallstedt, O. Hellman, B. Lindahl, A. Schneider, P. E. A. Turchi, and W. Xiong, *Thermodynamic modelling of crystalline unary phases,* Physica Status Solidi B **251**, 14 (2014).

[6] F. Körmann, A. A. H. Breidi, S. L. Dudarev, N. Dupin, G. Ghosh, T. Hickel, P. Korzhavyi, J. A. Muñoz, and I. Ohnuma, *Lambda transitions in materials science: Recent advances in calphad and first-principles modelling,* Physica Status Solidi B **251**, 53 (2014).

[7] A. Glensk, B. Grabowski, T. Hickel, and J. Neugebauer, *Understanding anharmonicity in fcc materials: From its origin to ab initio strategies beyond the quasiharmonic approximation,* Physical Review Letters **114**, 195901 (2015).

[8] J. Cao and B. J. Berne, *A Born-Oppenheimer approximation for path integrals with an application to electron solvation in polarizable fluids* , Journal of Chemical Physics **99**, 2902 (1993).

[9] B. Grabowski, T. Hickel, and J. Neugebauer, *Formation energies of point defects at finite temperatures,* Physica Status Solidi B **248**, 1295 (2011).

[10] D. A. Boness, J. Brown, and A. McMahan, *The electronic thermodynamics of iron under earth core conditions,* Physics of the Earth and Planetary Interiors **42**, 227 (1986).

[11] C. Wolverton and A. Zunger, *First-principles theory of short-range order, electronic excitations, and spin polarization in Ni-V and Pd-V alloys,* Physical Review B **52**, 8813 (1995).

[12] E. Wasserman, L. Stixrude, and R. E. Cohen, *Thermal properties of iron at high pressures and temperatures,* Physical Review B **53**, 8296 (1996).

[13] E. G. Moroni, G. Grimvall, and T. Jarlborg, *Free energy contributions to the hcp-bcc transformation in transition metals,* Physical Review Letters **76**, 2758 (1996).

[14] C. Wälti, E. Felder, M. A. Chernikov, H. R. Ott, M. de Boissieu, and C. Janot, *Lattice excitations in icosahedral Al-Mn-Pd and Al-Re-Pd,* Physical Review B **57**, 10504 (1998).

[15] B. Sadigh and V. Ozoliņš, *Structural instability and electronic excitations in* Nb_3Sn*,* Physical Review B **57**, 2793 (1998).

[16] M. E. Manley, R. J. McQueeney, B. Fultz, R. Osborn, G. H. Kwei, and P. D. Bogdanoff, *Vibrational and electronic entropy of* β*-cerium and* γ*-cerium measured by inelastic neutron scattering,* Physical Review B **65**, 144111 (2002).

[17] Y. Wang, Z.-K. Liu, and L.-Q. Chen, *Thermodynamic properties of Al, Ni, NiAl, and* Ni_3Al *from first-principles calculations,* Acta Materialia **52**, 2665 (2004).

[18] R. Arroyave, D. Shin, and Z.-K. Liu, *Ab initio thermodynamic properties of stoichiometric phases in the ni–al system,* Acta Materialia **53**, 1809 (2005).

[19] H. Y. Geng, M. H. F. Sluiter, and N. X. Chen, *Cluster expansion of electronic excitations: Application to fcc Ni-Al alloys,* The Journal of Chemical Physics **122**, 214706 (2005).

[20] R. Lortz, Y. Wang, U. Tutsch, S. Abe, C. Meingast, P. Popovich, W. Knafo, N. Shitsevalova, Y. B. Paderno, and A. Junod, *Superconductivity mediated by a soft phonon mode: Specific heat, resistivity, thermal expansion, and magnetization of* YB_6, Physical Review B **73**, 024512 (2006).

[21] B. Grabowski, T. Hickel, and J. Neugebauer, *Ab initio study of the thermodynamic properties of nonmagnetic elementary fcc metals: Exchange-correlation-related error bars and chemical trends,* Physical Review B **76**, 024309 (2007).

[22] P. Souvatzis, O. Eriksson, and M. I. Katsnelson, *Anomalous thermal expansion in* α*-titanium,* Physical Review Letters **99**, 015901 (2007).

[23] Z. Lin, L. V. Zhigilei, and V. Celli, *Electron-phonon coupling and electron heat capacity of metals under conditions of strong electron-phonon nonequilibrium,* Physical Review B **77**, 075133 (2008).

[24] Y. Wang, J. J. Wang, H. Zhang, V. R. Manga, S. L. Shang, L.-Q. Chen, and Z.-K. Liu, *A first-principles approach to finite temperature elastic constants,* Journal of Physics: Condensed Matter **22**, 225404 (2010).

[25] B. Grabowski, P. Söderlind, T. Hickel, and J. Neugebauer, *Temperature-driven phase transitions from first principles including all relevant excitations: The fcc-to-bcc transition in Ca,* Physical Review B **84**, 214107 (2011).

[26] B. Kollmitzer and P. Hadley, *Thermodynamic properties of separable square-wave potentials,* Physica B: Condensed Matter **406**, 4373 (2011).

[27] M. Widom, *Prediction of structure and phase transformations,* in *High-Entropy Alloys: Fundamentals and Applications*, edited by C. M. Gao, J.-W. Yeh, K. P. Liaw, and Y. Zhang (Springer International Publishing, Cham, 2016) pp. 267–298.

[28] C. Asker, A. B. Belonoshko, A. S. Mikhaylushkin, and I. A. Abrikosov, *First-principles solution to the problem of Mo lattice stability,* Physical Review B **77**, 220102 (2008).

[29] B. Alling, F. Körmann, B. Grabowski, A. Glensk, I. A. Abrikosov, and J. Neugebauer, *Strong impact of lattice vibrations on electronic and magnetic properties of paramagnetic Fe revealed by disordered local moments molecular dynamics,* Physical Review B **93**, 224411 (2016).

[30] O. K. Andersen, *Linear methods in band theory,* Physical Review B **12**, 3060 (1975).

[31] J. Madsen, O. K. Andersen, U. K. Poulsen, and O. Jepsen, *Canonical band theory of the volume and structure dependence of the iron magnetic moment,* AIP Conf. Proc. **29**, 327 (1976).

[32] D. G. Pettifor, *Theory of energy bands and related properties of 4d transition metals. I. Band parameters and their volume dependence,* Journal of Physics F: Metal Physics **7**, 613 (1977).

[33] N. D. Mermin, *Thermal Properties of the Inhomogeneous Electron Gas,* Physical Review **137**, A1441 (1965).

[34] P. Hohenberg and W. Kohn, *Inhomogeneous electron gas,* Physical Review **136**, B864 (1964).

[35] S. Pittalis, C. R. Proetto, A. Floris, A. Sanna, C. Bersier, K. Burke, and E. K. U. Gross, *Exact conditions in finite-temperature density-functional theory,* Physical Review Letters **107**, 163001 (2011).

[36] F. Körmann, A. Dick, B. Grabowski, B. Hallstedt, T. Hickel, and J. Neugebauer, *Free energy of bcc iron: Integrated ab initio derivation of vibrational, electronic, and magnetic contributions,* Physical Review B **78**, 033102 (2008).

[37] W. Kohn and L. J. Sham, *Self-consistent equations including exchange and correlation effects,* Physical Review **140**, A1133 (1965).

[38] G. Kresse and D. Joubert, *From ultrasoft pseudopotentials to the projector augmented-wave method,* Physical Review B **59**, 1758 (1999).

[39] M. Methfessel and A. T. Paxton, *High-precision sampling for Brillouin-zone integration in metals,* Physical Review B **40**, 3616 (1989).

[40] N. W. Ashcroft and N. D. Mermin, *Solid State Physics,* (Harcourt College Publishers, Orlando, 1976) Chap. 2, pp. 29–56, 1st ed.

[41] D. C. Wallace, *Thermodynamics of Crystals* (Dover, New York, 1998).

[42] P. E. Blöchl, *Projector augmented-wave method,* Physical Review B **50**, 17953 (1994).

[43] J. P. Perdew, K. Burke, and M. Ernzerhof, *Generalized gradient approximation made simple,* Physical Review Letters **77**, 3865 (1996).

[44] G. Kresse and J. Furthmüller, *Efficient iterative schemes for ab initio total-energy calculations using a plane-wave basis set,* Physical Review B **54**, 11169 (1996).

[45] G. Kresse and J. Furthmüller, *Efficiency of ab-initio total energy calculations for metals and semiconductors using a plane-wave basis set,* Computational Materials Science **6**, 15 (1996).

[46] Note1, For W, s and p states were treated as valence states since the W_pv potential suffered from ghost states at higher energies.

[47] P. E. Blöchl, O. Jepsen, and O. K. Andersen, *Improved tetrahedron method for brillouin-zone integrations,* Physical Review B **49**, 16223 (1994).

[48] P. Vinet, J. Ferrante, J. H. Rose, and J. R. Smith, *Compressibility of solids,* Journal of Geophysical Research: Solid Earth **92**, 9319 (1987).

[49] B. Grabowski, L. Ismer, T. Hickel, and J. Neugebauer, *Ab initio up to the melting point: Anharmonicity and vacancies in aluminum,* Physical Review B **79**, 134106 (2009).

[50] W. M. Haynes, *CRC handbook of chemistry and physics* (CRC Press, Taylor & Francis Group, Boca Raton, 2015).

[51] C. Engin and H. M. Urbassek, *Molecular-dynamics investigation of the fcc→bcc phase transformation in Fe,* Computational Materials Science **41**, 297 (2008).

[52] F. Körmann, T. Hickel, and J. Neugebauer, *Influence of magnetic excitations on the phase stability of metals and steels,* Current Opinion in Solid State and Materials Science **20**, 77 (2015).

[53] L. Kaufman and H. Bernstein, *Computer Calculation of Phase Diagrams* (Academic Press, New York, 1970).

[54] N. Saunders and A. P. Miodownik, *Calphad (Calculation of Phase Diagrams): A Comprehensive Guide* (Pergamon, Oxford, 1998).

[55] C. Kittel, *Introduction to solid state physics,* (Wiley, New Jersey, 2004) Chap. 6, p. 145, 8th ed.

[56] T. Hickel, B. Grabowski, F. Körmann, and J. Neugebauer, *Advancing density functional theory to finite temperatures: methods and applications in steel design,* Journal of Physics: Condensed Matter **24**, 053202 (2012).

A

XKMC program

In order to efficiently perform kinetic Monte Carlo simulations in conjunction with CE, a program temporarily called "XKMC" was developed for fcc multicomponent alloys. One can easily implement either the conventional or the kinetic Monte Carlo simulations for fcc alloys once a good multicomponent CE is obtained. For kinetic Monte Carlo studies, if necessary, calculations for local environment dependent kinetically resolved activation (KRA) barriers are also implemented in the program. It is then possible to study the real kinetics, i.e., realistic evolution of order parameters as a function of time. As one of the output results, structures of the precipitates in real space can be readily observed in various visualization softwares such as, e.g., Ovito. Diffraction intensity data in reciprocal space are also available, which can be exported to other plotting tools, e.g., Techplot. Moreover, configurational thermodynamic properties at finite temperature, e.g., heat capacity, entropy and Gibbs energy etc. can also be obtained in the current program.

A.1. Introduction

Without relying on experimental results, *ab* initio predictions of materials properties are widely applied in many areas for materials design in recent years. With a dramatic increase of the computation power, challenge nevertheless remains for *ab* initio supercell calculations to treat arbitrary atomic arrangements. The cluster expansion technique provides an efficient parametrization of the *ab* initio supercell energies, which enables a quick evaluation of the energy for arbitrary configurations. With the recently developed multicomponent CEs, early stage precipitation in alloys can be monitored through kinetic Monte Carlo (kMC) simulations. In order to describe the realistic diffusion kinetics, it is crucial to use the realistic activation barriers when estimating different atom-vacancy swapping rates, i.e., local-atomic-environment dependent KRA barriers. It will be shown in the current program that multiple KRA barriers can also be efficiently computed from local cluster expansions.

This appendix provides details concerning the XKMC program, e.g., the background, example calculations, the input and output files etc., which facilitates users to get a quick start with the XKMC program.

A.2. Background of the program

The basic theory behind the XKMC program has been introduced in chapter 2. The main concepts, e.g., cluster expansion (Sec. 2.4), statistical thermodynamics (Sec. 2.5.1 and 2.5.2) and the (k)MC algorithms (Sec. 2.5.4 and 2.5.5), have been discussed in detail. Readers can refer to the corresponding sections for definitions or equations if necessary.

A.3. Capabilities

Presently, the program has the following capabilities:

- Currently designed only for fcc structures.
- Two algorithms are implemented in the code, Metropolis Monte Carlo and kinetic Monte Carlo.
- Cluster expansions for local environment dependent KRA barriers can be implemented in KMC to study realistic kinetics.
- The program can automatically terminate when the preset accuracy is reached or the preset number of steps is reached.
- For the current version, the following thermodynamic quantities can also be calculated:
    - total energy
    - heat capacity
    - entropy(if switch on)

  - correlation functions for each ECIs
  - Warren-Cowley SRO parameters
  - structure factors

- Visualize the microstructure evolution via the Ovito software

- Visualize the diffuse scattering contour for 3-D via the Tecplot software.

A.4. General notes on usage

Before using the XKMC program, the user is assumed to have experience on how to use the iCVM code since the input files of the current program are partly obtained from iCVM.

A.4.1. Metropolis MC

- For Metropolis MC, program execution is controlled by just 4 input files (not interactive):

  1. an input file [**INPUT.txt**]
  2. a correlation function list file [**corrfuntable.txt**]
  3. a file with cluster information [**clusters.txt**]
  4. a file includes ECIs [**eci.txt**]

  (For KMC, where CEs for KRA barriers are included, extra files are required(see section A.4.2).

- One can also define the initial configuration from an extra input file, [**rebuild.txt**], instead of random configuration.

- All of the writing format for input files should exactly follow the example files described in section A.5 in case error happens.

- Output files:

  1. log file [**log.txt**] which includes simulation parameters information and energy data.
  2. file for storing correlation functions data[**prob.txt**]
  3. files for visualizing precipitates in ovito software [**ovito_#**] and [**ovitoall_xxxx**]
  4. file for plotting SRO diffuse scattering [**isro.dat**]
  5. file for plotting diffraction pattern in reciprocal space [**strfact.dat**]
  6. file for entropy data [**entropy.txt**] (if switch on).

- a hyperlinked manual in PDF and postscript formats (this document) is provided.

- extra softwares or code package are required to implement the following functions:

1. iCVM software: to generate [**corrfuntable.txt**] file as one of the input files and to supply ECIs for [**eci.txt**] file.
2. code package [**getvari**]: to generate [**clusters.txt**] file as one of the input files.
3. ovito software: visualize the microstructure evolution. Output file from XKMC used: [**ovito_#**].
4. Tecplot software: visualize the diffuse scattering or diffraction intensity contour in 3-D. Output files from XKMC used: [**isro.dat**] and [**strfact.dat**].

Before performing simulations, all of the required input files must be included in the same directory.

- The file [**INPUT.txt**] includes all of the required parameters for a simulation, i.e. simulation box size, temperature, composition... the value of which are at the beginning of each line, followed by a "/" and the annotation for this parameter. The user cannot modify the sequence of lines in the current version. What one needs to do is just to modify the value before "/". For multiple values, a space or tab is required between each value.

- The second input file [**corrfuntable.txt**] is generated from iCVM software which includes correlation functions information related to all the clusters in the current approximation in iCVM, i.e. N4R8, meaning clusters with at most 4 sites and no interatomic distance is beyond 8th neighbor. This table also depends on the number of species because under the same approximation, say "N4R8", more species means a longer correlation function list. Therefore this file should be consistent with both the approximation used in iCVM and [**csp**] in the [**INPUT.txt**] file.

- The input file [**clusters.txt**] is generated from an extra package called [**getvari**]. This package is from a revised lite version of iCVM code which supplies the coordinate information of clusters used in the current simulation. In the [**getvari**] package, one only needs to modify (a) the type of approximation by setting TOKEN "NAME=" under CLASS "CLUST" and (b) the # of ECI by setting TOKEN "ECICLUSTERS=" under CLASS "ECLI" and run the code. The type of approximation defined after TOKEN "NAME=" should also be specified in IN.CVM or default file. Then the output file [**clusters.txt**] will be generated.

- The input file [**eci.txt**] includes all of the value(in the unit of meV/cluster) of ECIs.

After running the program, the information of the system will be written in the [**log.txt**] file, followed by the energy of each step. In the end, the equilibrium information and data will also be written if [**automatic stop**] setting is switched on. Correlation functions of the initial state and that of each block are written in [**prob.txt**] file. Ovito information of user specified element will be written in [**ovito_#**] file(# means the #th element) separately. The program can automatically terminate when accuracy specified by user is reached. At the same time, the information for diffuse scattering diffraction analysis and diffraction intensity are written in [**isro.dat**] file and [**strfact.dat**] file. If the [**entropy calculation**] is switched on, the program will calculate the entropy for each temperature at the end of the simulation and store the values in [**entropy.txt**] file.

A.4.2. KMC simulation

Besides all the input files required for conventional MC, additional files are needed for calculation of KRA barriers in KMC simulation.

1. a file for storing input parameters: [**INPUTkra.txt**].
2. a file includes information of correlation functions for all clusters: [**corrfunkra.txt**].
3. files supply the coordinates information of all clusters: [**clusterskra_xx.txt**](“xx” refers to the name of each species which should be consistent with the name in [**INPUTkra.txt**] file).
4. files contain ECIs: [**ecikra_xx.txt**].

A.5. Example calculation

As an example, the calculation of binary Al-Cu system with 2 $at\%$ Cu at 300 K has been provided. The ECIs are obtained from an “N4R8” CE. CE for KRA barriers are obtained from “N4R5”. The user can reproduce the simulation as following:

1. prepare [**corrfuntable.txt**] file from log file of iCVM “N4R8” calculation. If one performs KMC, additional similar file [**corrfunkra.txt**] can also be prepared from iCVM “N4R5” calculation.
2. prepare [**clusters.txt**] file as follows:
   - open IN.CVM file of the [**getvari**] package and find

     ```
     CLUST   NAME=N4R8
     N4R8    RMAX=2.01 NSMAX=4 PRNTMAXCL=T NMAX=0
     *N3R21    RMAX=3.01 NSMAX=3 PRNTMAXCL=T NMAX=0
     .................................
     ECLI    ECICLUSTERS=1-32,34-43,45-64...........
     ................
     ```

   - modefy the setting for “NAME=” and “ECICLUSTERS=” (number of ECIs should start from 1). do not forget to add the corresponding description lines for the approximation in IN.CVM or default file, i.e.,

     ```
     N4R8    RMAX=2.01 NSMAX=4 PRNTMAXCL=T NMAX=0
     ```

   - run the [**getvari**] code and get output file [**clusters.txt**].
   - If one performs KMC, additional similar files [**clusterskra_xx.txt**] can also be obtained in the way described above.
3. prepare the [**eci.txt**] file. If one performs KMC, additional similar files [**ecikra_xx.txt**] are also necessary.
4. modify the [**INPUT.txt**] file with your own parameters. If one performs KMC, additional similar file [**INPUTkra.txt**] should also be modified.
5. [**compile**] and run the code.

A.5.1. Example file: [INPUT.txt]

```
***********************************************

40   / size of simulation box
100  /number of blocks
3    /current number of species
4    /maximum size of the cluster used
100 /number of MC step in one block
0.0001  /accuracy value(eV)
3.29  /ratio of accuracy and sigma
300   /low temperature limit(K)
300   /high temperature limit(K)
100   /temperature interval(K)
Cu Va Al /name of each species
0.02 0.0 /composition of each species: A B C...
.true.   /MC=.false.;KMC=.ture.
.false.  /CTKRA=.true.;EDKRA=.false.
1  /number of vacancy
.true.  /if output the ovito file for all the minor species
1    /output the ovito file for which species
1.0 0.0 0.0/ prefactor for structure factors
.false.   /if entropy calculation
10  /number of data used for extrapolation in entropy calculation
.true.  /if use different random seed
.false. /if automatically stop
400   /user defined number of blocks for simulation
.true. /if re-build the simulation box from user defined file
.true. /if remove the oscillation
1.67875d13  4.63599d13  /vibrational frequency(Hz)

************************************************
```

At the beginning of each line, a velue is specified to the corresponding parameter required in the simulation, followed by the note for this value. Detailed explanation and suggestion for these settings will be introduced in section A.7.1. None of these lines can be eliminated in case of errors. Users only need to modify the value to their own settings.

A.5.2. Example file: [INPUTkra.txt]

```
***********************************************

2   /total number of CE used
Cu Al  /type of the diffusing atom
4 4 /maximal size of clusters used in each CE

************************************************
```

Detailed explanation and suggestion for these settings will be introduced in section A.7.2

A.5.3. Example file: [corrfuntable.txt]

```
*********************

S4N4R8
171 486 31049
1 1 1 1
2 1 2 1
3 1 3 1
1 2 4 6
2 2 5 12
5 2 5 12
3 2 6 12
9 2 6 12
6 2 7 6
7 2 8 12
10 2 8 12
11 2 9 6
..........
..........
154 486 31047 12
107 486 31048 24
167 486 31048 24
170 486 31048 24
155 486 31048 24
171 486 31049 6

*********************
```

- The first line is specified with a compact description of CE, i.e.,“S4” number of species is 4; “N4” maximal cluster—4-body cluster; “R8” maximal distance 8th neighbor.
- The second line gives three maximal values of: (1)decoration number, (2)serial number of clusters and (3)number of correlation functions. These value can generally be found at the end of the list.
- From the second line on, there are four columns. First column is the possible decoration number for each cluster, the second column is the serial number of each cluster, the third and fourth columns show the serial number and degeneracy of each variant(ECIs).
- User should make the [**corrfuntable.txt**] file as described above. These informations can be generally found in the log file of CMAT calculation in iCVM.

A.5.4. Example file: [corrfunkra.txt]

```
*********************
```

```
S3N4R5
41      52      467
1       1       1       1
2       1       2       1
1       2       3       6
2       2       4       12
4       2       4       12
5       2       5       6
1       3       6       3
2       3       7       6
4       3       7       6
......
......

*********************
```

A.5.5. Example file: [clusters.txt]

```
*********************

168 192 20392
1 1 1
0.0 0.0 0.0
2 2 12
0.0 0.0 0.0
-0.5 -0.5 0.0
0.0 0.0 0.0
-0.5 0.5 0.0
0.0 0.0 0.0
-0.5 0.0 -0.5
........
........
1.0 -1.0 -1.0
2.0 0.0 0.0
1.0 1.0 -1.0
0.0 0.0 0.0

**********************
```

- The first line gives the maximal value of : (1)number of clusters used in current simulation; (2)number of variants associated with one cluster; (3)total number of variants.

- From the second line on, information of each cluster is listed as: one line with (a)serial number of the cluster, (b)number of sites, (c)number of variants, and the following few lines with the coordinates (x,y,z) of each variant.

A.5.6. Example file: [clusterskra_xx.txt]

```
**********************

6 144 528
6 3 24
0.0 0.0 0.0
-0.5 -0.5 0.0
-0.5 0.0 0.5
0.0 0.0 0.0
-0.5 0.5 0.0
-0.5 0.0 -0.5
0.0 0.0 0.0
0.5 -0.5 0.0
0.5 0.0 -0.5
0.0 0.0 0.0
0.5 0.5 0.0
0.5 0.0 0.5
......
......

***********************
```

A.5.7. Example file: [eci.txt]

```
**********************

0       1.51702942
1       -500.311276
2       619.57476
3       -328.115498
4       -944.698674
6       39.3430231
9       195.952595
..........
..........
125     179.880285
133     -41.327839
134     138.717311
139     68.1532473
140     -122.538447
147     136.086282

**********************
```

- The left column is the serial number of correlation function used in the present simulation(consistent with the third column of [**corrfuntable.txt**] file). The right column is the value of ECIs(unit: meV/lattice site)

A.5.8. Example file: [ecikra_xx.txt]

```
**********************

0       579.260921
17      -163.925695
29      63.0109916
63      -39.9586824
256     -78.5686417
265     120.833756
343     -49.5893516
......
......
**********************
```

A.5.9. Example file: [rebuild.txt]

```
**********************

639 1
Cu  0.000 0.000 0.350
Cu  0.025 0.025 0.400
Cu  0.025 0.000 0.425
Cu  0.025 0.075 0.050
Cu  0.025 0.075 0.350
Cu  0.000 0.125 0.725
Cu  0.025 0.175 0.100
Cu  0.000 0.175 0.425
Cu  0.000 0.150 0.800
Cu  0.000 0.200 0.550
Cu  0.025 0.225 0.550
......
......
Va  0.000 0.675 0.925
```

- This file is for users who want to specify the initial configuration as their will from a file.
- The first line includes the number of atoms for each minority species, i.e., for Al-Cu-vac system, one only needs to specify the number of Cu atoms and Vac.
- The following lines list the type of each atom and their (x,y,z) positions.

A.6. Output files

A.6.1. Example file: [log.txt]

```
====================================================
```

```
                      XKMC
   Kinetic Monte Carlo for multi-component system
                   2011 - 2015
             Xi Zhang & Marcel Sluiter
              X.Zhang-3@TUDelft.NL
           Dept. MSE, 3ME, T.U. Delft
    Mekelweg 2, 2628CD Delft, the Netherlands
                Version: xxxxxxxx
     Date:xx-xx-xx,Time:xx:xx:xx, Zone:xxxx
====================================================
      Information of the present simulation
-Simulation box size: 20x20x20
-Total number of atoms: 32000
-Elements: Cu Va Al
-Composition:    0.020   0.000
-Kinetic Monte Carlo: T
-CE for energy: S3N4R8
-CE for KRA: S3N4R5
~~~~~~~~~~~~~~~~~~~~~~~~~~~~~~~~~~~~~~~~~~~~~~~~~~~~
-Temperature:   300.00 K
-Initial random state: T
~~~~~~~~~~~~~~~~~~~~~~~~~~~~~~~~~~~~~~~~~~~~~~~~~~~~
The initial energy is:      -0.00896158 eV/atom
The error bar is +(-)          0.00127359 eV/atom
~~~~~~~~~~~~~~~~~~~~~~~~~~~~~~~~~~~~~~~~~~~~~~~~~~~~
################# block    1 ###################
1     -0.00908592
2     -0.00927557
3     -0.00936294
4     -0.00938473
5     -0.00941431
............
............
............
======================================================
Block average E(eV/atom): -0.00982452  delta: -0.00086294
======================================================
################# block    2 ###################
.........
.........
.........
***************** Equilibrium state ******************
              Final system information
******************************************************
-(k)MC steps to equilibrium state: 23767
```

```
-Steps for average: 3432
-Final energy(eV/atom): -0.0112542
-Heat capacity: 0.14121E-09
~~~~~~~~~~~~~~~~~~~~~~~~~~~~~~~~~~~~~~~~~~~~~~~~~~~~~~
                 Normal termination
~~~~~~~~~~~~~~~~~~~~~~~~~~~~~~~~~~~~~~~~~~~~~~~~~~~~~~
     Date:xx-xx-xx,Time:xx:xx:xx, Zone:xxxx
TIMER: Total time cost: total =  xxxxx ms
~~~~~~~~~~~~~~~~~~~~~~~~~~~~~~~~~~~~~~~~~~~~~~~~~~~~~~
```

- following the title section, information about the present simulation are listed, then the initial energy and error bar.
- the energy of each (k)MC step will be written after the block number.
- when the program finishes the iteration of one block, the block average energy is shown as well as the value of the energy change compared with the last block .
- finally, equilibrium state information is written at the end of the file if [**auto**] setting is switched on.

A.6.2. Example file: [prob.txt]

```
====================================================
    The initial correlation function of ECIs
-Elements: Cu Al
-Composition:    0.020
-Temperature:   300.00 K
====================================================
  1 0.20000000E-01
  2 0.41666667E-03
  3 0.41666667E-03
  4 0.40364583E-03
  5 0.39583333E-03
  6 0.42187500E-03
  7 0.35937500E-03
  8 0.39322917E-03
  9 0.25000000E-03
 10 0.00000000E+00
 11 0.10416667E-04
 12 0.26041667E-05
 13 0.14322917E-04
 .......
 .......
=====================================================
 The average correlation function of ECIs of block 1
=====================================================
```

```
 1  0.20000E-01  0.00000E+00
 2  0.55302E-03  0.23010E-03
 3  0.39885E-03  0.55104E-04
 4  0.22747E-03 -0.17617E-03
 5  0.27552E-03 -0.12031E-03
 6  0.33609E-03 -0.76563E-05
 7  0.78104E-03  0.40604E-03
 8  0.30299E-03 -0.85026E-04
 9  0.42854E-03 -0.50625E-04
10  0.39331E-03 -0.25260E-05
11  0.42839E-03 -0.19531E-04
12  0.39516E-03 -0.50156E-04
........
........
***************** Equilibrium state *****************
      Equilibrium correlation function of ECIs
*******************************************************
 1  0.20000E-01  0.00000E-00
 2  0.57543E-03  0.45430E-03
 3  0.32344E-03  0.54354E-04
 4  0.22344E-03 -0.53244E-03
 5  0.23424E-03 -0.66345E-03
 6  0.35459E-03 -0.42421E-05
 7  0.78434E-03  0.65344E-03
 8  0.23453E-03 -0.86550E-04
.........
.........
```

- This file gives the correlation function variation for each block in the simulation.
- Each group of correlation function includes three columns: (1)sequence number of ECIs, (2)correlation function, (3)the difference between the current block and the last block.

A.6.3. Example file: [ovito_#]

```
*************************************************

640
The composition of species 1 is  0.020;T=  300.00
 0.00000 0.00000 0.60000
 0.02500 0.12500 0.75000
 0.00000 0.12500 0.92500
 0.02500 0.17500 0.20000
 0.00000 0.52500 0.07500
 0.02500 0.52500 0.05000
 0.00000 0.57500 0.02500
```

```
 0.00000 0.62500 0.57500
 0.00000 0.60000 0.80000
 .........
 .........
```

```
*************************************************
```

- The first line is the number of atoms of the #th species, followed by a line including composition and temperature information.
- for each step, all of the atomic positions of the #th species are listed in (x,y,z).
- This file can be opened in ovito software and one can visualize the microstructure evolution during the simulation(see Fig. A.1).

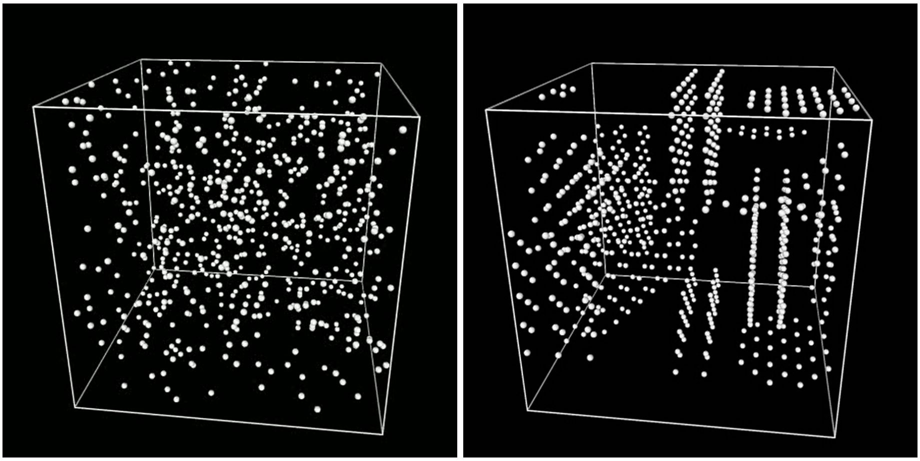

Figure A.1: Visualization of microstructure evolution in ovito software (a) inital random state. (b) equilibrium state.

A.6.4. Example file: [ovitoall_xxxx]

```
*************************************************

640
The composition is  0.020 0.000;T=  300.00
Cu  0.025 0.025 0.500
Cu  0.000 0.050 0.150
Cu  0.025 0.075 0.800
Cu  0.000 0.150 0.200
Cu  0.025 0.150 0.225
...........
...........
Va  0.050 0.500 0.000
```

****

- a similar file as [**ovito_#]** except for an extra column which includes the type of the atom. “xxxx” here refers to a four-digit number indicating the simulation temperature, i.e., if the simulation temperature is 300 K, the name of this file will be [ovitoall_0300].
- This file stores the atomic positions of all types of the minority atoms.
- This file can also be opened in ovito software and each type of atom will be shown in different colors.

A.6.5. Example file: [isro.dat]

****

```
TITLE = ″Diffuse scattering intensity plot″
VARIABLES = ″X″, ″Y″, ″Z″, ″Intensity″
ZONE I=41, J=41, K=41, F=POINT
0.000 0.000 0.000    10.46362
0.050 0.000 0.000    10.17516
0.100 0.000 0.000     9.34720
0.150 0.000 0.000     8.08587
0.200 0.000 0.000     6.54887
0.250 0.000 0.000     4.92020
0.300 0.000 0.000     3.38120
0.350 0.000 0.000     2.08296
0.400 0.000 0.000     1.12506
0.450 0.000 0.000     0.54427
0.500 0.000 0.000     0.31517
...........
...........
```

****

- This file is written following the requirement of the Tecplot solftware.
- Coordinates in reciprocal lattice associated with diffuse scattering intensity value are listed.
- This file can be opened in Tecplot software and one can visualize the 3-D diffuse scattering contour results(see Fig. A.2).

A.6.6. Example file: [strfact.dat]

- Exact the same format as [**isro.dat**] file.
- This file gives the calculated diffraction intensity for the selected minority species.

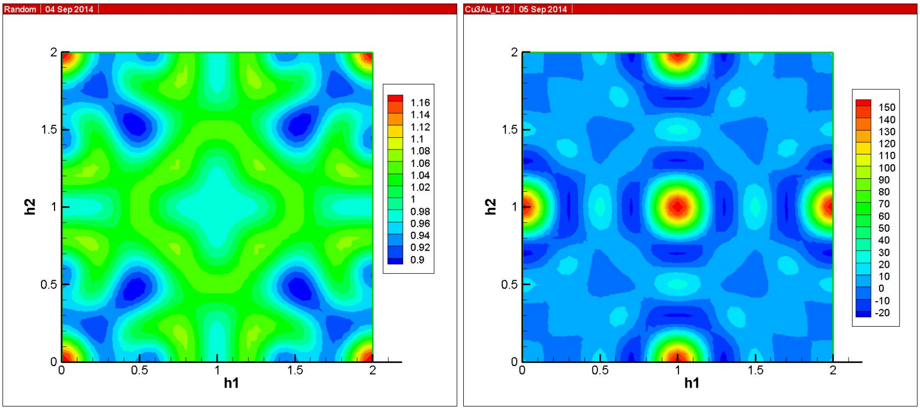

Figure A.2: Visualization of diffuse scattering contour in Tecplot software (a) random alloys, (b) $L1_2$-Cu_3Au ordered structure.

- This file can also be opened in Tecplot software and one can visualize the diffraction intensity contour(see Fig. A.3).

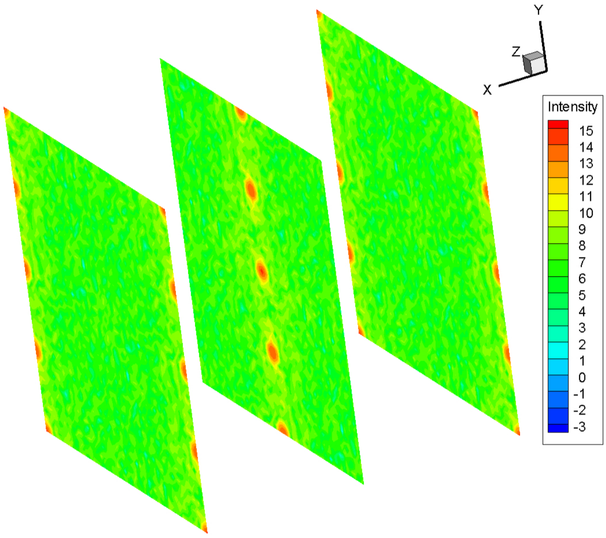

Figure A.3: Visualization of diffraction intensity contour in Tecplot software: GPII zones in Al-Cu alloys.

A.6.7. Example file: [entropy.txt]

```
********************************************

temperature(K)     entropy(kB)
```

```
1500.00        0.59693
1600.00        0.61994
1700.00        0.63471
1800.00        0.64504
1900.00        0.65267
2000.00        0.65851
2100.00        0.66311
2200.00        0.66681
2300.00        0.66984
2400.00        0.67236
2500.00        0.67448
2600.00        0.67628
2700.00        0.67783
.........
.........
**************************************************
```

- The first column gives the temperature while the second lists the entropy value in unit of k_B.

A.7. Description of required input parameters

A.7.1. Conventional MC

1. **nx: The size of simulation box**
   - Integer, even number, typically greater than 2. For fcc, size 2 is equal to one lattice constant a which yields all integer coordinates.
   - Example: 40 means the the simulation box is $20 \times 20 \times 20$ and the total number of atoms is $4 \times 20 \times 20 \times 20 = 32000$
   - This parameter also determines the number of movements in one (k)MC step. So it costs longer CPU time for larger size of simulation box.
2. **nblock: The number of blocks**
   - Integer, even number preferred, typically not smaller than 10.
   - This parameter determines the space one would like to open for storing the data points in the memory.
   - Example: 50 means if the [**nblstep**] equals 100, the space for storing total number of $50 \times 100 = 5000$ (k)MC step data is opened.
   - Suggestion: 50-200
3. **csp: current number of species**
   - Integer.

- Vacancy should be considered as an additional species, which means for A-B-vac system, this value should be 3.

4. **maxcl: maximum size of cluster used**
   - Integer
   - the maximal cluster used in [**clusters.txt**] file.
5. **nblstep: number of MC step in one block**
   - Integer, even number preferred.
   - Since correlation time is evaluated in one block, this parameter should go far beyond the correlation time. If the system is highly correlated or a large number of ECIs are used, one should set a large value to this item.
   - Suggestion: 100-1000
6. **prec: accuracy parameter**
   - Real, typically a small number.
   - The program will stop automatically if the energy is within the error bar $\pm$ this parameter, i.e. $\pm$ 0.001(eV/atom)
   - For large systems or complicated systems(a large number of ECIs), a proper accuracy parameter is necessary which means if this value is set too small the program will probably never stop.
   - Suggestion: 0.001 or even smaller depends on systems(best try first).
7. **zalfa: ratio of prec and sigma**
   - Real, set for the certainty of error.
   - calculated via
     $$\sqrt{2}\mathrm{erf}^{-1}(a) \tag{A.1}$$
     where a is 0.99 for 99% certainty; 0.999 for 99.9% certainty and so on.
8. **tlow(tup): low(up) temperature limit**
   - Real, in unit of Kelvin.
   - If ONLY one temperature is needed, these two limit should be set to be equal.
9. **tstep: temperature interval**
   - Real, in unit of Kelvin, simulation for multiple temperatures.
   - i.e., if tstep=10, tlow=100 and tup=1000, the program will do calculations for 100 K, 200 K, 300 K,..., 1000 K.
10. **elename: name of each element**

- Character, for each element, the name is capitalized.
- Sequence is consistent with [**fatom**]

11. **fatom: composition of each element**
    - Real, describe the atomic concentration for each MINORITY species only.
    - The number of values here should equal to [**csp**]-1.
12. **kmc: switch bewteen mc and kmc**
    - logical value(.true. or .false.), if kmc algorithm is implemented, .true. otherwise it is .false.
13. **conskra: switch between EDKRA and CTKRA**
    - logical value, if constant KRA barriers are used, .true. otherwise it is .false.
14. **nvac: number of vacancy**
    - Integer, set the number of vacancy in the simulation box, typically 1.
15. **ovta: ovito output setting**
    - logical value, if one needs [ovitoall_xxxx] file as one of the output files, .true., then the [**iov**] tag will become invalid, otherwise .false.
16. **iov: output the ovito file for which species**
    - Integer number(s), require the program output the ovito file for the #th species in [**elename**] when [**ovta**] is set to be .false.. Then files [**ovito_#**] will be generated.
    - For multiple values, sequence should be consistent with [**fatom**]
    - Example: 1(space)2 means the $1st$ and $2nd$ species.
17. **pref: prefactor for structure factors**
    - Real numbers, define the prefactors for diffraction intensity calculations.
    - For multiple values, sequence should be consistent with [**fatom**]
    - Suggestion: zero for majority atoms, unity for minority atoms.
18. **calcetp: switch on or off the entropy calculation**
    - logical value, if entropy calculation is needed, .true. otherwise it is .false.
19. **nextra: # of heat capacity data for entropy calculation**
    - Integer number, for the number of heat capacity data selected to extrapolate the value at infinite temperature.

- can not be larger than the number of calculated heat capacity data.

20. **newseed: use different random seed**
    - logical value, when generate initial random configuration, use a different random seed, .true. otherwise .false.
21. **auto: switch on or off automatically stop**
    - logical value, when one prefers to stop simulation by accuracy criterion, .true. otherwise .false.
22. **ublk: user defined number of block for termination**
    - Integer, when the [**auto**] is set to be .false., user can specify the total number of blocks for termination criterion.
    - This value should be [**nblock**]$\times 2^n$(n is an integer and $n \geq 0$),i.e., if [**nblock**]=100, then this value should be 100, 200, 400, 800,...
23. **rebuild: initialize the configuration from user defined file**
    - logical value, sometimes user wants to continue the simulation for more steps from last run, the last configuration when the program stops last time needs to be stored in [rebuild.txt] file and this tag is set to be .true., otherwise .false.
24. **remove: switch on or off the vacancy oscillations**
    - logical value, if removing the inefficiency from vacancy oscillations is required, this tag is set to be .true., otherwise .false.
25. **omega: vibrational frequency**
    - Real, set the vibrational frequency for each element, in unit of Hz.

A.7.2. For KMC

1. **ices: number of CEs for KRA barriers**
    - Integer, specify how many CEs are used for KRA barriers, generally it equals to the number of elements.
2. **diffname: the name for each diffusing element**
    - character, specify the name for each diffusing element, i.e., Cu Al.
3. **maxclk: maximal size of cluster used for each CE**
    - Integer, define maximal clusters used for each CE.

A.8. Compilation

Makefile is included in the source package for compilation. On unix/linux based machines with Intel fortran compiler, an executable file named “XKMC” is created by typing:

```
make XKMC [return]
```

The Makefile can also be used to concatenate the complete source into a single file named “all.f90” by entering the command:

```
make all [return]
```

When an archive (tar file) is desired of all essential files, simply enter the command:

```
make tar [return]
```

then a file named “XKMC.tar” is created.

After creating the executable “XKMC”, it can be run from the prompt by typing “XKMC” in the appropriate directory where input files are located.

B

Inheritance of ECIs: A derivation

Eq. 3.7 in chapter 3 shows the formulism that ECIs of high order systems can be obtained from their subsystems, i.e. one can model a ternary alloy A-B-C via reusing the ECIs of the A-C and B-C binaries. Typically ECIs in terms of pure elements can be trivially inherited just by copy whereas it is not the case for ECIs among different species. It is shown in chapter 3 that, for N-component system, the latter case can still benefit from the inheritance if all N atomic species are not present in one cluster. In this appendix, we will give a derivation to show that, for a ternary alloy A-B-C with C as the eliminated species, the A-B binary ECIs can be exactly preserved provided that the ECIs are limited to pair interactions.

For a binary P-Q (P and Q designate two different species), the energy can be expanded in the context of CE by up to 3-body clusters as, i.e.,

$$\begin{aligned} E &= \sum_{\alpha} \xi_{(\alpha)} J_{(\alpha)} \\ &= J_0 + \xi_{(P)} J_{(P)} + \xi_{(Q)} J_{(Q)} \\ &\quad + \xi_{(PP)} J_{(PP)} + 2\xi_{(PQ)} J_{(PQ)} + \xi_{(QQ)} J_{(QQ)} \\ &\quad + \xi_{(PPP)} J_{(PPP)} + 3\xi_{(PPQ)} J_{(PPQ)} + 3\xi_{(PQQ)} J_{(PQQ)} \\ &\quad + \xi_{(QQQ)} J_{(QQQ)} \end{aligned} \tag{B.1}$$

where $\xi_{(\alpha)}$ and $J_{(\alpha)}$ are correlation functions and the corresponding ECIs associated with a cluster α. It should be noticed that the basis used in Eq. B.1, or rather the Js, are not independent because of the following sum rules,

$$\begin{aligned} \xi_{(Q)} &= 1 - \xi_{(P)} \\ \xi_{(PQ)} &= \xi_{(P)} - \xi_{(PP)} \\ \xi_{(QQ)} &= 1 - \xi_{(PP)} - 2\xi_{(PQ)} \\ \xi_{(PPQ)} &= \xi_{(PP)} - \xi_{(PPP)} \\ \xi_{(PQQ)} &= \xi_{(PQ)} - \xi_{(PPQ)} \\ \xi_{(QQQ)} &= 1 - \xi_{(PPP)} - 3\xi_{(PPQ)} - 3\xi_{(PQQ)} \end{aligned} \tag{B.2}$$

Redundancy can be eliminated by substitution of these sum rules into Eq. B.1, which yields an expansion in terms of an independent basis,

$$\begin{aligned} E &= \sum_{\alpha} \xi_{(\alpha)} \tilde{J}_{(\alpha)/P(Q)} \\ &= [J_0 + J_{(Q)} + J_{(QQ)} + J_{(QQQ)}] \\ &\quad + [J_{(P)} + 2J_{(PQ)} + 3J_{(PQQ)} - J_{(Q)} - 2J_{(QQ)} - 3J_{(QQQ)}]\xi_{(P)} \\ &\quad + [J_{(PP)} + 3J_{(PPQ)} - 2J_{(PQ)} - 6J_{(PQQ)} + J_{(QQ)} + 3J_{(QQQ)}]\xi_{(PP)} \\ &\quad + [J_{(PPP)} - 3J_{(PPQ)} + 3J_{(PQQ)} - J_{(QQQ)}]\xi_{(PPP)} \end{aligned} \tag{B.3}$$

where $\tilde{J}_{(\alpha)/P(Q)}$ ($\alpha = 0, P, PP, PPP$) are independent with each other. It is apparent that

$\tilde{J}_{(\alpha)/P(Q)}$ and $J_{(\alpha)}$ has the following relations:

$$\begin{aligned}
\tilde{J}_{0/P(Q)} &= J_0 + J_{(Q)} + J_{(QQ)} + J_{(QQQ)} \\
\tilde{J}_{(P)/P(Q)} &= J_{(P)} + 2J_{(PQ)} + 3J_{(PQQ)} - J_{(Q)} - 2J_{(QQ)} - 3J_{(QQQ)} \\
\tilde{J}_{(PP)/P(Q)} &= J_{(PP)} + 3J_{(PPQ)} - 2J_{(PQ)} - 6J_{(PQQ)} + J_{(QQ)} + 3J_{(QQQ)} \\
\tilde{J}_{(PPP)/P(Q)} &= J_{(PPP)} - 3J_{(PPQ)} + 3J_{(PQQ)} - J_{(QQQ)} \qquad \text{(B.4)}
\end{aligned}$$

where the notation $(\alpha)/P(Q)$ refers to the ECI of cluster type α in the binary P-Q alloy with the species Q as eliminated species. Generally, in an alloy with N species, the cluster decoration probabilities involving $N-1$ species can be used as an independent basis to fully describe the configurational order.

Similarly, in A-B-C ternary alloys, we can find an independent basis $\tilde{J}_{(\alpha)/AB(C)}$ by eliminating ECIs involving one of the three species, e.g., "C". Then, as we did for binaries, we can derive the similar relations between independent basis $\tilde{J}_{(\alpha)/AB(C)}$ and basis $J_{(\alpha)}$ with redundant terms involving species C:

$$\begin{aligned}
\tilde{J}_{0/AB(C)} &= J_0 + J_{(C)} + J_{(CC)} + J_{(CCC)} \\
\tilde{J}_{(A)/AB(C)} &= J_{(A)} + 2J_{(AC)} + 3J_{(ACC)} - J_{(C)} - 2J_{(CC)} - 3J_{(CCC)} \\
\tilde{J}_{(B)/AB(C)} &= J_{(B)} + 2J_{(BC)} + 3J_{(BCC)} - J_{(C)} - 2J_{(CC)} - 3J_{(CCC)} \\
\tilde{J}_{(AA)/AB(C)} &= J_{(AA)} + 3J_{(AAC)} - 2J_{(AC)} - 6J_{(ACC)} + J_{(CC)} + 3J_{(CCC)} \\
\tilde{J}_{(BB)/AB(C)} &= J_{(BB)} + 3J_{(BBC)} - 2J_{(BC)} - 6J_{(BCC)} + J_{(CC)} + 3J_{(CCC)} \\
\tilde{J}_{(AB)/AB(C)} &= 2J_{(AB)} + 2J_{(CC)} - 2J_{(AC)} - 2J_{(BC)} + 6J_{(CCC)} \\
&\quad + 6\mathbf{J}_{(\mathbf{ABC})} - 6J_{(ACC)} - 6J_{(BCC)} \\
\tilde{J}_{(AAA)/AB(C)} &= J_{(AAA)} - 3J_{(AAC)} + 3J_{(ACC)} - J_{(CCC)} \\
\tilde{J}_{(AAB)/AB(C)} &= 3J_{(AAB)} - 3J_{(CCC)} - 3J_{(AAC)} - 6\mathbf{J}_{(\mathbf{ABC})} + 6J_{(ACC)} \\
&\quad + 3J_{(BCC)} \\
\tilde{J}_{(ABB)/AB(C)} &= 3J_{(ABB)} - 3J_{(CCC)} - 6\mathbf{J}_{(\mathbf{ABC})} + 3J_{(ACC)} - 3J_{(BBC)} \\
&\quad + 6J_{(BCC)} \\
\tilde{J}_{(BBB)/AB(C)} &= J_{(BBB)} - 3J_{(BBC)} + 3J_{(BCC)} - J_{(CCC)} \qquad \text{(B.5)}
\end{aligned}$$

Particular interest lies in a comparison of Eq. B.4 and Eq. B.5. The similar relations for all three subsystems of the ternary A-B-C are trivially obtained by replacing P and Q in Eq. B.4 with A, B or C. It is then evident that the pure A ECIs (i.e.,$\tilde{J}_{(A_n)/AB(C)}$) can be copied from the A-C binary (i.e.,$\tilde{J}_{(A_n)/A(C)}$) and the pure B ECIs (i.e.,$\tilde{J}_{(B_n)/AB(C)}$) can be copied from the B-C binary (i.e.,$\tilde{J}_{(B_n)/B(C)}$), where subscript n means it is valid for all n-body pure A and pure B clusters. Therefore, Eq. 3.8 is valid.

If we limit ourselves to pair ECIs, Eq. B.4 and Eq. B.5 will be further simplified to,

$$\begin{aligned}
\tilde{J}_{0/P(Q)} &= J_0 + J_{(Q)} + J_{(QQ)} \\
\tilde{J}_{(P)/P(Q)} &= J_{(P)} + 2J_{(PQ)} - J_{(Q)} - 2J_{(QQ)} \\
\tilde{J}_{(PP)/P(Q)} &= J_{(PP)} - 2J_{(PQ)} + J_{(QQ)}
\end{aligned} \tag{B.6}$$

and

$$\begin{aligned}
\tilde{J}_{0/AB(C)} &= J_0 + J_{(C)} + J_{(CC)} \\
\tilde{J}_{(A)/AB(C)} &= J_{(A)} + 2J_{(AC)} - J_{(C)} - 2J_{(CC)} \\
\tilde{J}_{(B)/AB(C)} &= J_{(B)} + 2J_{(BC)} - J_{(C)} - 2J_{(CC)} \\
\tilde{J}_{(AA)/AB(C)} &= J_{(AA)} - 2J_{(AC)} + J_{(CC)} \\
\tilde{J}_{(BB)/AB(C)} &= J_{(BB)} - 2J_{(BC)} + J_{(CC)} \\
\tilde{J}_{(AB)/AB(C)} &= 2J_{(AB)} + 2J_{(CC)} - 2J_{(AC)} - 2J_{(BC)}
\end{aligned} \tag{B.7}$$

where we can derive the relation

$$\tilde{J}_{(AB)/AB(C)} = \tilde{J}_{(AA)/A(C)} + \tilde{J}_{(BB)/B(C)} - \tilde{J}_{(AA)/A(B)}. \tag{B.8}$$

Unfortunately, if 3-body or larger clusters are included in a ternary alloy the inheritance seems to be intractable because ECIs mixed with AB type all contain energy terms that include all three species ABC (see terms in bold in Eq. B.5). Such energy terms cannot originate from a description of any binaries.

C

Calculation of the configurational entropy via thermodynamic integration

As mentioned in Sec. 2.5.2, the configurational entropy is not as trivially accessible as the internal energy or the heat capacity from MC. According to thermodynamic relations, the entropy can be obtained by integration of the heat capacity or the internal energy as a function of temperature (see Eqs. 2.45 and 2.46) where an integration path should be in prior defined. The value of the entropy at one end of the path should also be known. For the case that interested temperature is above the transition temperature, a path from the infinite temperature to a finite value is preferred because the entropy of the high-temperature limit is known as

$$S(\infty) = -k_B[x\ln x + (1-x)\ln(1-x)] \tag{C.1}$$

which takes the value $k_B\ln 2$ at equatomic composition for binary alloys, x is the composition. Then Eq. 2.45 will be written as,

$$S(T) = S(\infty) - \int_T^\infty \frac{C_\mathrm{p}}{\tau}\mathrm{d}\tau \tag{C.2}$$

It is numerically impractical, however, to do the integration if one of the integration limits is infinity. It is then necessary to substitute the variable to be integrated with one that makes both integration limits finite values. Moreover, since only finite-temperature heat capacity data are available from simulations, there must be a cutoff temperature above which the heat capacity data are extrapolated from the available data. Therefore it is of great interest to investigate the asymptotic behavior of the integrand going towards $T = \infty$ in Eq. C.2, $F(\tau) = C_\mathrm{p}/\tau$.

One can resort to one of the simplest solvable cases, a two-state Ising-like model: $\uparrow\uparrow$ represents $U = 0$ while $\downarrow\uparrow$ is associated with $U = J$. The partition function of such a simple model is straightforwardly written as

$$Z = 1 + e^{-\beta J}. \tag{C.3}$$

Combining the following relation,

$$C_\mathrm{p} = \frac{\beta}{T}\frac{\partial^2 \ln Z}{\partial \beta^2} \tag{C.4}$$

we can derive the expression of the integrand as a function of τ,

$$\begin{aligned} F(\tau) &= C_\mathrm{p}/\tau \\ &= \frac{J^2 e^{-\frac{J}{k_B\tau}}}{k_B\tau^3(1+e^{-\frac{J}{k_B\tau}})^2} \end{aligned} \tag{C.5}$$

The asymptotic behavior of $F(\tau)$ is indicated by the series expansion at $T = \infty$,

$$F(\tau) \sim \frac{J^2}{4k_B}\tau^{-3} - \frac{J^4}{16k_B^3}\tau^{-5} + O(\tau^{-7}). \tag{C.6}$$

We wish to replace τ by a variable in such a way that (a) both of the integration limits are finite values and (b) the integrand $F(\tau)$ changes as constant as possible. The reason is that integrating a constant is the easiest (and the most accurate) numerical integration one can perform. Apparently, if we only consider the first order term of $F(\tau)$ in Eq. C.6, an approximate τ^{-3} behavior can be found, which gives us a hint to do the following substitution,

$$\tau^{-3}\mathrm{d}\tau = \mathrm{d}x \tag{C.7}$$

which is also equal to

$$x = -\frac{1}{2}\tau^{-2} \tag{C.8}$$

Substitution of Eqs. C.7 and C.8 into Eq. C.2 yields,

$$\begin{aligned} S(X) &= S(0) - \int_X^0 F(x)\mathrm{d}x \\ &= S(0) - \int_{-\frac{1}{2}T^{-2}}^0 \frac{C_\mathrm{p}(x)}{-2x}\mathrm{d}x \end{aligned} \tag{C.9}$$

The validation of the substitution is shown in Fig. C.1 where $F(x)$ is plotted for the simplest two-state model. From Fig. C.1, we can see that the present transformation makes sense for both at the high temperature limit and the low temperature limit. As τ going towards infinity ($x \to 0$), the value of F goes, as expected, towards a constant. At the low τ limit ($x \to -\infty$) the value of $F(x)$ approaches 0, which means that the entropy is a finite value.

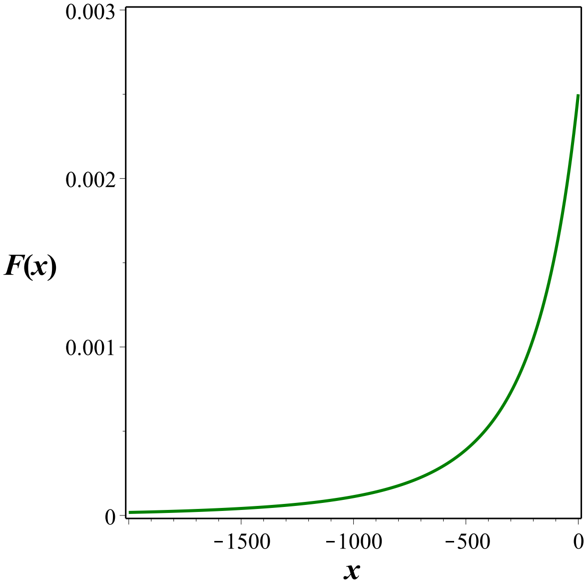

Figure C.1: Two-state Ising-like model: $F(x)$ as a function of x, $x \to 0$ indicates $\tau \to \infty$ while $x \to -\infty$ indicates $\tau \to 0$. $J = 0.1$ and $k_B = 1$ for simplicity.

We implemented the above integration method to our XKMC program and selected a simple toy fcc system for test. The input parameters for the toy A-B binary fcc system include: (a) composition $x_A = 0.5$ (b) point cluster interaction $J_{(A)} = 0.3265$ and nearest-neighbor-pair interaction $J_{(AA)} = -0.0544$(unit: eV/cluster). The interactions used are simply extracted from a cluster expansion for energies of five common structures—fcc pure A(B), L1$_2$-AB$_3$(A$_3$B) and L1$_0$-AB (see Fig. C.2. The calculated $F(x)$ as a function of x is shown in Fig. C.3.

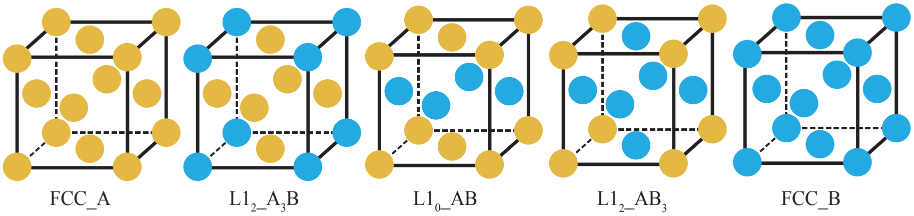

Figure C.2: Five common structures in fcc alloys. The energy associated with each structure in the present calculation is 0, 0.006, 0.008, 0.006, 0 (eV/atom).

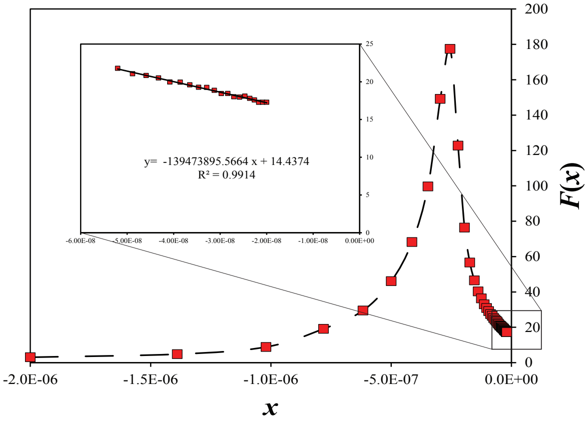

Figure C.3: A test calculation for entropy of a toy binary A-B alloy: $F(x)$ as a function of x. The inset shows the linear fitting of the data near $x = 0$.

The available heat capacity data from MC are up to 5000 K (corresponding to $x = -2\times10^8$), which means the extrapolation to $x = 0$ is necessary to obtain the whole integrand curve. In the present calculation, data points of $\tau \geq 3000$ K are linearly fitted to obtain the integrand function between $x = -2 \times 10^8$ and $x = 0$. The validation of linear extrapolation is justified by checking the slope of function $F(x)$ at $x \to 0$,

$$\begin{aligned}
\lim_{x\to 0}\frac{\partial F(x)}{\partial x} &= \lim_{x\to 0}\left[\frac{\partial F(x)}{\partial \tau}\frac{\partial \tau}{\partial x}\right] \\
&= \lim_{x\to 0}\left[\left(\lim_{\tau\to+\infty}\frac{\partial F(-\frac{c}{2}\tau^{-2})}{\partial \tau}\right)\frac{\partial \tau}{\partial x}\right] \\
&= c \qquad\qquad \text{(C.10)}
\end{aligned}$$

where c is a constant.

Fig. C.4 shows the calculated configurational entropy from 1500 K to 3000 K (above the transition temperature) in MC (solid triangle). As a comparison, the CVM results with a tetrahedron-octahedron (TO) approximation are also shown (open square). A nice agreement has been found especially at high temperature range.

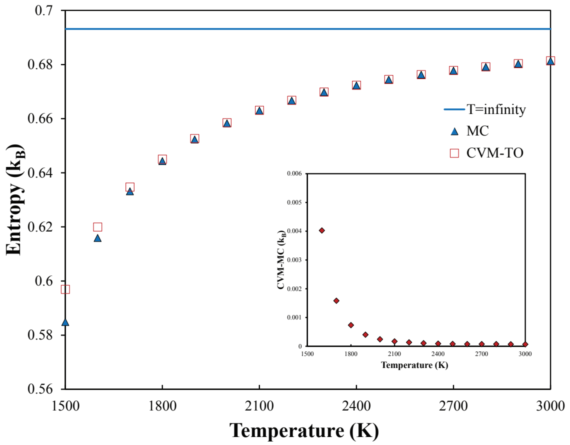

Figure C.4: Calculated configurational entropy (in unit of k_B) from MC and CVM as a function of temperature. The inset shows the difference of the CVM values and the MC values.

Summary

In the present thesis, an *ab initio* simulation method for the early stages of clustering and precipitation in substitutional alloys is developed and applied to aluminum alloys. There are strong indications that the currently achievable mechanical properties of light-weight aluminum alloys processed via age hardening can be significantly improved. Understanding precipitation thermodynamics and kinetics in Al-based alloys is thus of tremendous importance. The formation of the metastable Guinier-Preston (GP) zones at the early stages of precipitation improves the strength of the alloys and influences the growth of the final precipitates. It therefore deserves a comprehensive study (chapter 1). Despite the rapid development of advanced experimental techniques, robust *ab initio* simulations at the atomic level are important to relate the materials properties to underlying atomistic and physical mechanisms.

In the present work we focus ourselves not only on precipitation thermodynamics (e.g., morphology) but also on the underlying kinetics since under practical experimental conditions thermodynamic equilibrium might not be reached. For this purpose, a multiscale computational method is used where the underlying energetics is accurately described from density functional theory (DFT) and the configuration evolution is monitored employing atomic kinetic Monte Carlo (kMC) simulations (chapter 2). After a brief introduction to density functional theory in the first part of chapter 2, various Monte Carlo algorithms are discussed in detail. The convergence of the MC and the efficiency issues arising from the KMC are also discussed.

In order to efficiently describe properties in terms of configuration order, the cluster expansion (CE) method which provides an efficient coupling between *ab initio* DFT calculations and configurational thermodynamics is applied. Cluster expansions have proven to be an efficient and accurate method to investigate alloys thermodynamics. However, there are various challenges associated with obtaining a reliable CE, e.g., how to efficiently select the most relevant input structures and correlation functions for an adequate description of the energy, how to optimize a CE from a limited set of *ab initio* energies, etc. While these issues are already significant for binary alloys, they become even more serious when dealing with multicomponent alloys. In chapter 3, we address these issues by properly defining the correlation functions and the “cluster pool”, and by introducing efficient algorithms for determining CEs. With the current definition of correlation functions, effective cluster interactions (ECIs) of multicomponent systems can be inherited from their subsystems, i.e., ECIs from the constituent systems can be directly re-used.

Since diffusion in substitutional alloys is typically driven by vacancies, vacancy properties in concentrated alloys must be carefully addressed. This is usually a highly non-trivial task for *ab initio* computations. As shown in chapter 4, a simple model based on CE and statistical analysis is derived and applied to extract vacancy properties of concentrated Cu-Ni alloys. An Arrhenius analysis shows that the heat of vacancy formation is well represented by a linear function of temperature. The effective vacancy formation free energies deviate from the linear interpolation between that of the terminal pure elements. The positive slope of the temperature dependence implies a *negative* configurational entropy contribution to the vacancy formation free energy in the alloy.

It is shown in this work that diffusion activation barriers for many alloys are sensitive to local atomic arrangements around the vacancy and the diffusing atom. To realistically describe the precipitation kinetics, a local cluster expansion formalism which reproduces the substitutional diffusion energetics at transition states (saddle points) is also developed in the present work (chapter 5). We implement the local CE for activation barriers and CE for configurational energies into kMC simulations to monitor the morphology of GP zones and the their formation kinetics in a dilute Al-Cu alloy. The kinetics and evolution of clustering and precipitation differs significantly when modeled using constant or local configuration dependent activation barriers for diffusion. Motivated by these findings, further studies for investigating the impact of local atomic environment dependent activation barriers on thermodynamics and kinetics are performed with two model alloy systems (chapter 6). The remarkable finding is that in substitutional alloys peculiar ordered patterns can result from diffusion activation barriers depending on different local environment even in purely phase-separating alloys. Such ordered patterns can exist and appear stable for extended time periods and thus can be considered transient phases.

For describing finite temperature properties, energetics from DFT calculations at zero temperature can be improved by adding finite temperature excitation corrections. Among the important contributions is the electronic contribution which can be significant at high temperatures. In chapter 7, electronic free energies are computed for all transition elements on the ideal lattices of the bcc, fcc, and hcp structures using finite-temperature density functional theory. For a subset of elements the impact of explicit thermal vibrations on the electronic free energies are explored by using *ab initio* molecular dynamics simulations (AIMD). In agreement with previous knowledge, a high electronic density of states (DOS) close to the Fermi level results in a significant, negative electronic free energy. The performance of three widely used approximations for computing electronic free energies is also quantitatively assessed. At high temperatures, from the AIMD results, strong lattice vibrations alter the electronic energy states and therefore increase or decrease the electronic free energies. Since these thermal excitations at finite temperatures might significantly alter the $T = 0$ K energetics and hence the quality of the CE, the inclusion of finite-temperature excitations in the follow-up studies thus promises more accurate and realistic modeling.

The author hopes the present work may shed light on developing new computational methods for studying alloy precipitation thermodynamics and kinetics or similar phenomena in materials in the future.

Samenvatting

In dit proefschrift is een ab initio model ontwikkeld voor de vroege stadia van clustering en precipitatie in substitutionele legeringen en vervolgens toegepast op aluminiumlegeringen. Er zijn sterke aanwijzingen dat de momenteel haalbare mechanische eigenschappen van lichtgewicht aluminiumlegeringen, die hun eigenschappen verkrijgen via precipitatie, nog aanzienlijk kunnen worden verbeterd. Het begrijpen van de thermodynamica en kinetiek van precipitatie is daarom van groot belang. De vorming van metastabiele Guinier-Preston (GP) zones tijdens de vroege stadia van precipitatie verbetert de sterkte van de legeringen en beïnvloedt ook de vorming van latere precipitaten. Dit onderwerp is daarom uitvoerig behandeld in hoofdstuk 1. Ondanks de snelle ontwikkeling van geavanceerde experimentele technieken, zijn robuuste ab initio-simulaties op atoomschaal belangrijk om de materiaaleigenschappen te kunnen relateren aan onderliggende atomaire mechanismen.

In het huidige werk concentreren we ons niet alleen op de thermodynamica van precipitatie, zoals bijv. morfologische kenmerken, maar ook op de onderliggende kinetiek, aangezien onder praktische experimentele omstandigheden zelden thermodynamisch evenwicht bereikt wordt. Voor dit doel wordt een meerschalige computationele methode gebruikt waarbij de onderliggende energetica nauwkeurig wordt beschreven via dichtheidsfunctionaaltheorie (DFT) en de configuratie-evolutie wordt gevolgd met behulp van roostergas kinetische Monte Carlo (kMC) -simulaties op atomair niveau (hoofdstuk 2). Na een korte inleiding tot de dichtheidsfunctionaaltheorie in het eerste deel van hoofdstuk 2, worden verschillende Monte Carlo-algoritmen in detail besproken. De convergentie van de Monte Carlo (MC) simulaties en de efficiëntiekwesties die voortvloeien uit het gebruik van de kMC worden ook besproken.

Om eigenschappen efficiënt te beschrijven in termen van roostergasconfiguratie, wordt de clusterexpansie (CE) methode (CE) toegepast die een efficiënte koppeling tussen ab initio DFT-energieberekeningen en statistische thermodynamica biedt. CEs hebben bewezen een efficiënte en nauwkeurige methode te zijn om de thermodynamica van legeringen te onderzoeken. Er zijn echter verschillende uitdagingen verbonden aan het verkrijgen van een betrouwbare CE, bijv. hoe men efficiënt de meest relevante inputstructuren en correlatiefuncties kunt selecteren voor een nauwkeurige beschrijving van de energie, hoe een CE te optimaliseren als slechts een beperkt aantal ab initio-energieën beschikbaar is, enz. Hoewel deze problemen al significant zijn voor binaire legeringen, worden ze nog belangrijker als het gaat om multicomponentenlegeringen. In hoofdstuk 3 behandelen we deze problemen door de correlatiefuncties en de 'cluster-verzameling' goed te definiëren en door efficiënte algoritmen voor het bepalen van CE's in te voeren. Met de huidige definitie van correlatiefuncties kunnen effectieve clusterinteracties (ECI's) van multicomponentensystemen worden overgenomen van hun subsystemen, d.w.z. ECI's van de samenstellende systemen kunnen direct worden hergebruikt.

Aangezien diffusie in substitutionele legeringen meestal verloopt met tussenkomst van vacatures, moeten vacature-eigenschappen in geconcentreerde legeringen zorgvuldig worden behandeld. Dit is een hoogst niet-triviale taak voor ab initio beschrijvingen. In hoofdstuk 4 wordt een eenvoudig model afgeleid gebaseerd op CE- en statistische analyse. Het model wordt toegepast om vacature-eigenschappen van geconcentreerde Cu-Ni-legeringen te beschrijven. Een Arrhenius-analyse laat zien dat de energie van vacaturevorming goed wordt weergegeven als een lineaire functie van temperatuur. De vrije energie van vacaturevorming wijkt af van een lineaire interpolatie tussen die van de zuivere eindelementen. De positieve helling van de temperatuurafhankelijkheid van de vrije energie van vacaturevorming impliceert een negatieve configurationele entropiebijdrage in een legering.

In dit werk wordt aangetoond dat voor veel legeringen energiebarrières voor diffusie gevoelig zijn voor lokale atomaire configuraties rond de vacature en het diffunderende atoom. Om de precipitatiekinetiek realistisch te beschrijven, is in het huidige werk (hoofdstuk 5) ook een formalism uitgewerkt voor lokale CEs met het doel om de energieën van overgangstoestanden, d.w.z. zadelpunten van de potentiële energie, te reproduceren. We implementeren de lokale CE voor activeringsbarrières en de gebruikelijke CE voor configurationele energieën in kMC-simulaties om de morfologie van GP-zones en hun formatiekinetiek in een verdunde Al-Cu-legering te volgen. De kinetiek en evolutie van clustering en precipitatie verschilt aanzienlijk wanneer deze gemodelleerd wordt met behulp van constante of lokale configuratie afhankelijke activeringsbarrières voor diffusie. Gemotiveerd door deze bevindingen, wordt verder onderzoek van locale atomaire omgevingsafhankelijke activeringsbarrières op thermodynamica en kinetiek uitgevoerd met twee model-legeringssystemen (hoofdstuk 6). De opmerkelijke bevinding is dat in substitutionele legeringen eigenaardige geordende patronen kunnen ontstaan uit omgevingsafhankelijke diffusie-activeringsbarrières, zelfs in zuiver fase scheidende legeringen. Dergelijke geordende patronen lijken stabiel gedurende langere tijdsperioden en kunnen dus als tussenfasen worden beschouwd.

Om de materiaaleigenschappen bij eindige, d.w.z. niet nul, temperatuur te beschrijven kunnen DFT-berekende energieën worden aangevuld met bijdragen ten gevolge van temperatuur afhankelijke excitaties. Een van de bijdragen is de elektronische excitatie bijdrage die vooral significant zijn bij hoge temperaturen. In hoofdstuk 7 worden elektronische vrije energieën berekend voor alle overgangselementen op de ideale roosters van de bcc-, fcc- en hcp-structuren met behulp van eindige-temperatuur DFT. Voor een kleinere groep van elementen wordt ook de invloed van thermische trillingen op de elektronische vrije energieën onderzocht door middel van ab initio moleculaire dynamica simulaties (AIMD). In overeenstemming met theoretische voorspellingen resulteert een hoge elektronische dichtheid van toestanden (density of states, DOS) dicht bij het Fermi-niveau in een significante, negatieve elektronische vrije energie. De nauwkeurigheid van drie veel gebruikte benaderingen voor het berekenen van elektronische vrije energieën worden ook kwantitatief beoordeeld. De AIMD resultaten laten zien dat bij hoge temperaturen de sterke roostervibraties de elektronische energietoestanden aanzienlijk veranderen waarbij de elektronische vrije energieën zowel groter als kleiner kunnen worden. Omdat deze thermische excitaties bij eindige temperaturen de DFT berekende, T = 0 K, energieën sterk beïnvloeden, en daarmee ook de kwaliteit van de CE aanzienlijk kunnen veranderen, belooft de opname van eindige temperatuur excitaties te resulteren in een meer accurate en realistische modellering. De auteur hoopt dat het huidige werk licht kan werpen op de ontwikkeling van nieuwe computationele methoden voor het bestuderen van de thermodynamica en kinetiek van precipitatie in legeringen of van soortgelijke fenomenen in toekomstige materialen.

Acknowledgements

It has been more than six years since 2011... I clearly remember that when I started my first day of Ph.D research someone told me that getting a Ph.D within four years in our department is a “mission impossible”. I replied to him then with a confident smile indicating the saying “nothing impossible” due to my naivete at that time. As a result..., anyway, I finally made it, regardless of the time I spent. I solaced myself by thinking that intelligent and diligent Ph.D students need more time to get their Ph.D degree than other students.

I love the present thesis very much because it is exactly the product of the effort from myself and many other people. First of all, I would like to thank Marcel Sluiter, my supervisor as well as my friend. I really learned a lot from him—not only the expertise in computational materials science but also the necessary qualities that an excellent scientific researcher should have. I will never forget about what he told me when I felt confused in doing research, e.g., “one can never use a formula or a theory without rigorous proof”, “you should be patient enough in writing scientific programs”, “you should have a wide-ranging academic interest in topics beyond your own expertise”... Gradually I got a huge personal development with Marcel’s help. There is no doubt that I will benefit from Marcel’s cultivation—from those mathematical derivations in his office and from his criticism and comments on my poor presentations—in my future scientific career. I would also like to thank my promoter, Prof. Barend Thijsse, for carefully reading the thesis and his constructive comments on every aspect of the present thesis including structure, figures as well as writing issues. All his suggestions made the thesis much better.

I would like to thank the colleagues and friends from the fourth flour of 3ME department. Thank our famous “5ME” meetings members: Prof. Lucia Nicola, Casper, Robbert-Jan, Kelvin, Astrid, Darko etc. for the fruitful discussions on scientific issues and how to improve our presenting ability. Several friends on the fourth flour, e.g., Fengwei, Weichen, Casper, Qiyu, Yunhe, provided me much help on daily life. I would like to show my special appreciation to them. Life in Delft can never be so colorful without so many Chinese colleagues in TU Delft. Some of them have been my roommates and given me much company, e.g., Hongkai, Peijian, Wenhao, Tiantian, Jianbin, Weichen, Chao. Some of them, Zhenpei, Lixia, Jinglang, Le, Yue, have given me much help on tackling problems in life . Thank you all very much. I would also like to express my gratitude to Blazej and Fritz from Max-Planck-Institut für Eisenforschung (MPIE). They helped me a lot on finalizing the thesis and on my daily life.

Finally I sincerely express my gratitude to my family, my parents and my wife, for their thoughtful care and support. I love you so much!

Curriculum Vitæ

Xi ZHANG

22-01-1986	Born in Anyang, China.

Education

2004–2008	Bachelor of Materials Science and Engineering School of Materials Science and Engineering Central South University, Changsha, China
2008–2011	Master of Materials Science and Engineering School of Materials Science and Engineering Central South University, Changsha, China
2011–	Ph.D. candidate Department of Materials Science and Engineering Delft University of Technology, Delft, Netherlands.

Awards

2014	STT Student Fellowship offered by the Foundation for Applied Thermodynamics, KTH, Sweden (STT , Stiftelsen för Tillämpad Termodynamik)
2010	Best paper award The 15th National Conference of Phase Diagrams of China and International Symposium on Phase Diagrams and Materials Design Shenyang, China

List of Publications

Journals:

6. **Xi Zhang**, Blazej Grabowski, Tilmann Hickel and Jörg Neugebauer *Calculating free energies of point defects from ab initio*, submitted to Computational Materials Science.
5. **Xi Zhang** and Marcel H. F. Sluiter, *Kinetically driven ordering in phase separating alloy*, submitted to Physical Review Materials (Chapter 6).
4. **Xi Zhang** and Marcel H. F. Sluiter, *Cluster expansions for realistic precipitation kinetics: An application to Guinier-Preston zone formation in an Al-Cu alloy*, to be submitted (Chapter 5).
3. **Xi Zhang**, Blazej Grabowski, Fritz Körmann, Christoph Freysoldt, and Jörg Neugebauer, *Accurate electronic free energies of the 3d, 4d, and 5d transition metals at high temperatures*, Physical Review B **95**, 165126 (2017) (Chapter 7).
2. **Xi Zhang** and Marcel H. F. Sluiter, *Cluster expansions for thermodynamics and kinetics of multicomponent alloys*, Journal of Phase Equilibria and Diffusion **37**, 44 (2016) (Chapter 3).
1. **Xi Zhang** and Marcel H. F. Sluiter, *Ab initio prediction of vacancy properties in concentrated alloys: the case of fcc Cu-Ni*, Physical Review B **91**, 174107 (2015) (Chapter 4).

Conference Abstracts:

5. Marcel Sluiter, **Xi Zhang**, *Cluster Expansions for Thermodynamics and Kinetics of Multicomponent Mixtures on Fixed Lattices*, **TMS2015**, Florida, USA (2015).
4. **Xi Zhang**, Marcel Sluiter, *Earliest Stages of Precipitation in fcc Al-Rich Alloys with Realistic Compositions*, **TMS2015**, Florida, USA (2015).
3. **Xi Zhang**, Marcel H. F. Sluiter, *Ab initio modelling of precipitation in multicomponent aluminium alloys with realistic compositions*, **CALPHAD XLIV**, Loano, Italy (2015).
2. Marcel H. F. Sluiter, **Xi Zhang**, *Cluster expansions for configuration dependent kinetics in substitutional alloys* **CALPHAD XLIV**, Loano, Italy (2015).
1. **Xi Zhang** and Marcel H. F. Sluiter, *Ab initio prediction of vacancy properties in concentrated alloys: the case of fcc Cu-Ni*, **CALPHAD XLIII**, Changsha, China (2014).